DOE/MC/30097 -- 4090
(DE96000579)

Energy and Environmental Research Emphasizing Low-Rank Coal

Semi-Annual Report
January - June 1994

September 1994

Work Performed Under Contract No.: DE-FC21-93MC30097

For
U.S. Department of Energy
Office of Fossil Energy
Morgantown Energy Technology Center
Morgantown, West Virginia

By
University of North Dakota
Grand Forks, North Dakota

DISCLAIMER

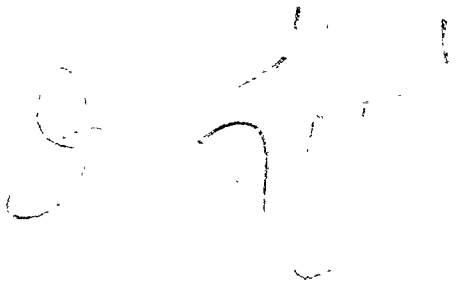

DOE/MC/30097 -- 4090
(DE96000579)
Distribution Category UC-113

Energy and Environmental Research Emphasizing Low-Rank Coal

Semi-Annual Report
January - June 1994

Work Performed Under Contract No.: DE-FC21-93MC30097

For
U.S. Department of Energy
Office of Fossil Energy
Morgantown Energy Technology Center
P.O. Box 880
Morgantown, West Virginia 26507-0880

By
University of North Dakota
Energy Research Center
P.O. Box 9018
Grand Forks, North Dakota 58202

September 1994

TASK 1.6

MIXED WASTE TREATMENT

Prepared by:

John R. Rindt
Jo Ann Fain

August 1994

TABLE OF CONTENTS

TASK 1.6 MIXED WASTE TREATMENT

1.0 INTRODUCTION/OBJECTIVES

Mixed waste sites make up the majority of contaminated sites, yet remediation techniques used at such sites often target only the most prevalent contaminant. A better understanding of site situation (i.e., most common types of contamination), current remediation techniques, and combinations of techniques would provide insight into areas in which further research should be performed.

The first objective for this task is to perform a comprehensive study of the most common types of mixed waste contamination as well as the remediation techniques that have been developed (or are under development) for the treatment of various wastes. Preliminary investigation of some promising research areas (as indicated by the study) will be performed during the last half of the subtask. Specific steps required to meet the first objective include the following:

- Investigation of common types of mixed waste sites
- Performance of a detailed literature search of the remediation techniques and combinations currently available
- Assessment of each of the techniques, combining them in various ways appropriate to mixed waste protocol

2.0 ACCOMPLISHMENTS

During the previous quarter, a literature search was conducted, focusing on site remediation as well as methods of treatment for mixed wastes, organic solvents, radio nuclides, polychlorinated biphenyls (PCBs), chlorinated hydrocarbons, and other waste stream problems. The search was conducted via DIALOG on-line computer search. Databases parsed in the search included CA selects, Engineering Info Inc., ENVIROLINE, Dialog Information Service, American Chemical Society, and EPRI. Nearly 800 pertinent abstracts were collected. These data are being entered into a database which can be used to sort the articles by waste type, process type, site characteristics, and other factors. Upon completion, this database should prove to be a useful tool for determining treatment or remediation techniques so that complete site remediation is possible.

Frank Beaver, Associate Director of the Energy & Environmental Research Center (EERC), attended the Fifth Annual Weapons Complex Conference in Phoenix, Arizona, April 4–7, 1994. The purpose of this trip was twofold: 1) to evaluate existing obstacles between DOE agencies and laboratories and industry in the area of mixed waste and 2) to define a role for the EERC in mixed waste research. Concerns expressed included the matching of technologies with problems and the need for innovative remediation technology development. This presents an opportunity for the EERC to help to develop a communication base with a better definition of problems in order to obtain better results. The EERC can serve as the link needed to develop technology and enhance communication between government and industry.

Frank Beaver also attended the U.S. Department of Energy (DOE) Stakeholder/ Roundtable Meeting in Denver, Colorado on June 29, 1994. The U.S. DOE Denver Regional Office cosponsored the meeting with The Rocky Mountain Oil Field Test Center in Casper, Wyoming. The focus of the meeting was the off-the-shelf technology and near-term technology transfer programs designed to help the independent oil and gas industry producers lower their production costs. This trip afforded the opportunity to gain a better understanding of the problems that exist between government programs and the independent oil and gas producers. Independent producers have expressed their frustration with the results of past efforts to supply the information and technologies they need. An opportunity exists for the EERC to assist in the technology development and transfer process focused on specific problems found by independent oil and gas producers.

3.0 FUTURE WORK

Investigation of common types of mixed waste sites is continuing. The literature search that was performed and each of the technologies will be evaluated. John Rindt, Research Supervisor, Advanced Technologies Group, will be attending AIChE's 1994 Summer National Meeting, August 14–18, in Denver, Colorado. The theme of the 1994 conference is "Stewardship of the Environment" and issues to be addressed include separations, safety and health, nuclear engineering, and fuels and petrochemicals; however, most of the programs will focus on environmental concerns. John Rindt will also visit the National Environmental Waste Technology Testing Evaluation Center (NEWTTEC) at DOE's Component Development and Integration Facility (CDIF) in Butte, Montana. The Resource Recovery Project (RRP) is directed from this facility. The RRP is a 5-year effort established by the Office of Technology Development to evaluate and demonstrate multiple technologies for recovering water, metals, and other industrial resources from contaminated surface and groundwaters. He will also attempt to visit mixed waste sites in Colorado.

TASK 1.7

HOT-WATER EXTRACTION OF NONPOLAR ORGANIC POLLUTANT FROM SOILS

Prepared by:

Steven B. Hawthorne

August 1994

TABLE OF CONTENTS

TASK 1.7 HOT-WATER EXTRACTION OF NONPOLAR ORGANIC POLLUTANT FROM SOILS

1.0 INTRODUCTION

Water has been used to extract solids contaminated with organic pollutants either by steam stripping (which is limited to relatively volatile species) or under supercritical conditions (i.e., temperatures > 374°C and pressure > 218 atm). Both techniques are severely limited for environmental remediation; i.e., steam stripping is effective only on relatively volatile organics, and the high corrosivity and high temperature and pressure requirements of supercritical water make its use unrealistic. However, the conditions that make supercritical water effective (e.g., lowering of the water's dielectric constant so that it behaves like an organic solvent) do not require supercritical conditions, and can be achieved at relatively "engineering-friendly" conditions of only a few atmospheres pressure and temperatures as low as 200° to 250°C. Surprisingly, these mild conditions have not been investigated as a remediation technique. Preliminary studies in our laboratory using water at 50 atm and 250°C have shown nearly quantitative removal of creosote polycyclic aromatic hydrocarbons (PAHs) from a contaminated soil. This study will determine the feasibility of subcritical water to extract nonpolar organic pollutants from contaminated soils.

2.0 OBJECTIVES

The ability of hot water (not steam) to extract PAHs from contaminated soils will be determined. Specific objectives are as follows:

- To determine the optimal pressure and temperature for removal of PAHs from real-world contaminated soils
- To determine the minimum pressure and temperature required for reasonable removal rates
- To perform preliminary determinations of the use of hot (subcritical) water to remove other organic contaminants, i.e., polychlorinated biphenyls (PCBs) from contaminated soils

3.0 ACCOMPLISHMENTS

A laboratory system for extracting organics from small (gram) solid samples has been built and tested. Hot-water extraction conditions have been investigated for the extraction of polar and nonpolar organics spiked on sand. Polars (e.g., chlorinated phenols) were efficiently extracted at low temperatures (e.g., 50°C), while more nonpolars (PAHs) were efficiently extracted at 250°C. The pressure of the extraction does not seem to be important (other than to maintain the liquid state), which is fortuitous, since the use of hot-water extraction for remediation would be much simpler if the pressure requirements were minimal. Hot water was also used to extract PAHs from two real-

world samples, air particulate matter and soil. Water at 250°C and 50 bar was sufficient to quantitatively remove all regulated PAHs from both samples in only 15 minutes.

The details of these results are described in the enclosed manuscript, which has been accepted for publication in Analytical Chemistry.

4.0 FUTURE WORK

The laboratory hot-water extraction system is presently being evaluated to determine if extraction conditions can be developed to remove PCBs from soil.

APPENDIX A

EXTRACTION OF ORGANIC POLLUTANTS FROM ENVIRONMENTAL SOLIDS WITH SUB- AND SUPERCRITICAL WATER

MSC: ac9402945 BATCH: ac9m38 USER: eap69 PAGE: 1
DIV: @xyldr/data7/CLS_pj/GRP_ac/JOB_i17/DIV_ac9402945 DATE: 06/29/94

Extraction of Organic Pollutants from Environmental Solids with Sub- and Supercritical Water

Steven B. Hawthorne,* Yu Yang, and David J. Miller
Energy and Environmental Research Center, University of North Dakota, Campus Box 9018, Grand Forks, North Dakota 58202

Low-polarity organic pollutants such as polycyclic aromatic hydrocarbons (PAHs) typically have very low solubilities (e.g., ppb) in water at ambient conditions because of water's high polarity (dielectric constant, $\epsilon = 80$). However, the dielectric constant can be drastically lowered by raising the temperature of the water under moderate pressure with dramatic increases (e.g., to percent levels) in the solubility of low-polarity organics. For example, subcritical water at 250 °C and 50 bar has $\epsilon = 27$, which allowed quantitative extractions of PAHs in 15 min from soil and urban air particulates. Decreasing the polarity of water by sequentially raising the extraction temperature from 50 to 250 °C (subcritical water) and finally to 400 °C (supercritical water if $P > 221$ bar) allowed class-selective extractions of polar organics (e.g., chlorinated phenols), low-polarity organics (e.g., PAHs), and nonpolar organics (alkanes) to be performed. Simple methods for using sub- and supercritical water for quantitative extraction of organics from environmental solids are presented.

The recent interest in reducing the use of organic solvents has lead to the rapid development of supercritical fluid extraction (SFE) methods for analytical extractions.[1-3] The vast majority of analytical SFE has focused on the use of supercritical CO_2, primarily because it has low toxicity and is environmentally acceptable, and reports of quantitative SFE methods have increased dramatically in recent years. While an excellent solvent for nonpolar organics, the most frequent limitation in using CO_2 as an analytical extraction solvent is that its polarity is often too low to obtain efficient extractions, either because the analytes lack sufficient solubility or because (e.g., in the case of relatively soluble molecules such as polycyclic aromatic hydrocarbons (PAHs) or PCBs) of a poor ability to displace pollutant organics from matrix active sites.[4-13] Thus, many recent SFE papers have focused on increasing the solvent strength of CO_2, primarily by adding organic modifiers.[6-12]

Like CO_2, water is an environmentally acceptable solvent, but has not yet received attention as an analytical extraction solvent for environmental solids because (in contrast to the low polarity of supercritical CO_2) water is too polar to efficiently dissolve most nonionic organics that are associated with environmental solids. Indeed, if a particular organic has a high water solubility, it will tend to partition into water in the environment rather than remain associated with a solid such as soil or air particulate matter, with the result that aged environmental solids tend to be left with less polar pollutants. At ambient temperature and pressure, water has a dielectric constant (ϵ) of ca. 80,[14] which is much too polar to efficiently solvate low-polarity organic pollutants such as fuel hydrocarbons, PAHs, and PCBs.[15-17] For example, PAHs associated with contaminated solids typically have solubilities in ambient water which decrease rapidly with molecular weight from micrograms per milliliter to less than nanograms per milliliter (e.g., the solubility of naphthalene is 32 μg/mL, phenanthrene is 1.3 μg/mL, pyrene is 0.14 μg/mL, chrysene is 0.002 μg/mL, and benzo[*ghi*]perylene is 0.0003 μg/mL).[15] Similarly, PCBs range from ~1 (dichlorobiphenyls) to ~0.0005 μg/mL (heptachlorobiphenyls),[16] and alkanes from 0.009 (for *n*-decane) to 0.0008 μg/mL (for *n*-octadecane).[17]

Although low-polarity organics do not have high water solubilities at ambient conditions, supercritical water ($T >$ 374 °C and $P > 221$ bar) has a much lower dielectric constant (ϵ = ~5–15, depending on temperature and pressure)[14] and is, therefore, an extremely effective solvent for organic pollutants.[18-25] However, the high temperature and pressure requirements of supercritical water make its routine use for sample preparation unlikely from a practical standpoint, and

(1) Hawthorne, S. B. *Anal. Chem.* 1990, *62*, 633A.
(2) Vannoort, R. W.; Chervet, J.-P.; Lingeman, H.; DeJong, G. J.; Brinkman, U. A. Th. *J. Chromatogr.* 1990, *505*, 45.
(3) Chester, T. L.; Pinkston, J. D.; Raynie, D. E. *Anal. Chem.* 1992, *64*, 153R.
(4) Langenfeld, J. J.; Hawthorne, S. B.; Miller, D. J.; Pawliszyn, J. *Anal. Chem.* 1993, *65*, 338.
(5) Hawthorne, S. B.; Langenfeld, J. J.; Miller, D. J.; Burford, M. D. *Anal. Chem.* 1992, *64*, 1614.
(6) Alexandrou, N.; Pawliszyn, J. *Anal. Chem.* 1989, *61*, 2770.
(7) Alexandrou, N.; Pawliszyn, J. *Anal. Chem.* 1992, *64*, 301.
(8) Paschke, T.; Hawthorne, S. B.; Miller, D. J.; Wenclawiak, B. *J. Chromatogr.* 1992, *609*, 333.
(9) Onuska, F. I.; Terry, K. A. *J. High Resolut. Chromatogr.* 1989, *12*, 357.
(10) Wright, B. W.; Wright, C. W.; Gale, R. W.; Smith, R. D. *Anal. Chem.* 1987, *59*, 38.
(11) Wheeler, J. R.; McNally, M. E. *J. Chromatogr. Sci.* 1989, *27*, 534.
(12) Langenfeld, J. J.; Hawthorne, S. B.; Miller, D. J.; Pawliszyn, J. *Anal. Chem.* 1994, *66*, 909.
(13) Pawliszyn, J. *J. Chromatogr. Sci.* 1993, *31*, 31.
(14) Haar, L.; Gallagher, J. S.; Kell, G. S. *National Bureau of Standards/National Research Council Steam Tables*; Hemisphere Publishing Corp.: Bristol, PA, 1984.
(15) Mackay, D.; Shiu, W. Y. *J. Chem. Eng. Data* 1977, *22*, 399.
(16) Erickson, M. D. *Analytical Chemistry of PCBs*; Butterworth Publishers: Stoneham, MA, 1986.
(17) Verschueren, K. *Handbook of Environmental Data on Organic Chemicals*; Van Nostrand Reinhold Co.: New York, 1977.
(18) Shaw, R. W.; Brill, T. B.; Clifford, A. A.; Eckert, C. A.; Franck, E. U. *Chem. Eng. News* 1991, 26.
(19) Jain, V. K. *Environ. Sci. Technol.* 1993, *27*, 806.
(20) Kocher, B. S.; Azzam, F. O.; Lee, S. *Prepr. Pap.—Am. Chem. Soc., Div. Fuel Chem.* 1993, *38*, 339–342.
(21) Franck, E. U.; Rosenzweig, S.; Christoforakos, M. *Ber. Bunsenges. Phys. Chem.* 1990, *94*, 199.
(22) Uematsu, M.; Franck, E. U. *J. Phys. Chem. Ref. Data* 1980, *9*, 1291.
(23) Heger, K.; Uematsu, M.; Franck, E. U. *Ber. Bunsenges. Phys. Chem.* 1980, *84*, 758.
(24) Gupta, R. B.; Panayiotou, C. G.; Sanchez, I. C.; Johnston, K. P. *AIChE J.* 1992, *38*, 1243.
(25) Siskin, M.; Katritzky, A. R. *NATO ASI.*

0003-2700/xx/0300-0001$04.50/0

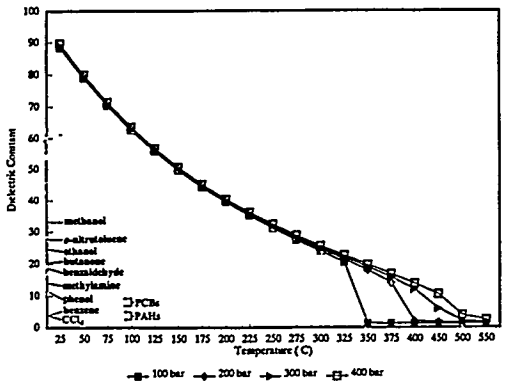

Figure 1. Effect of temperature and pressure on the dielectric constant (ϵ) of water compared to the dielectric constants of some representative organic compounds. Water data are adapted from ref 14.

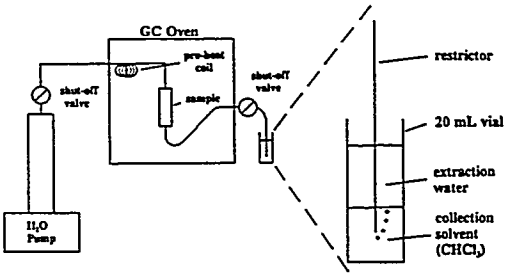

Figure 2. Schematic diagram of the water extraction system. System components are described in the text.

its use for analytical applications is further reduced by its reactive nature in terms of both analyte degradation and corrosivity. Because of these limitations, supercritical water is most likely to be used for the extraction and destruction of high-cost organics such as chemical warfare agents.[18] Fortunately, the dielectric constant of water can be dramatically lowered at much milder (and potentially useful) conditions by simply increasing the temperature at moderate pressures, as shown in Figure 1. Thus, by changing temperature, a tremendous range in the solvent polarity of water can be achieved (e.g., ϵ changes from about 90 to 20 by raising the temperature from ambient to 300 °C, Figure 1). In contrast, ϵ for supercritical CO_2 ranges only from about 1 to 1.6.[26] Therefore, the solubility of low-polarity organics can be dramatically increased by heating the water under moderate pressure. For example, at 350 °C and ~100 bar, the solubility of benzo[*e*]pyrene has been reported to increase from its ambient solubility of ~4 ng/mL[15] to ~10 wt %,[27] an increase of ~25 million-fold.

The purpose of the present investigations was to exploit the changes in the polarity of water which occur by raising its temperature for extracting moderate- and low-polarity organic pollutants from environmental solids. The possibility of sequentially extracting polar, moderately polar, and nonpolar organic pollutants by sequentially raising the extraction temperature (thereby lowering the extracting water's polarity) is investigated. The effects of temperature, pressure, and flow rate on recoveries are determined, and methodology for performing quantitative extractions of PAHs from soil and urban air particulates with sub- and supercritical water are described.

EXPERIMENTAL SECTION

Water Extractions. All extractions were performed in a manner similar to conventional SFE using the apparatus shown in Figure 2. HPLC-grade water (Fisher Scientific, Fair Lawn, NJ) was first purged for several hours with nitrogen to remove dissolved oxygen and filled into an ISCO Model μLC-500 syringe pump. The pump was operated in the constant-pressure mode (except for the 5-bar extractions as described below) to supply water through the $^1/_{16}$-in. o.d. (0.020-in.-i.d.) stainless steel tubing (including a 1-m preheating coil placed inside the Hewlett-Packard Model 5890 GC oven) to the extraction cell. SFE cells (4.6-mm i.d., 50-mm length, 0.8 mL) from Keystone Scientific (Bellefonte, PA) were used for all temperatures up to 250 °C. Because the polyimide seals in the SFE cells failed at higher temperatures, HPLC columns (30-mm length, 4.6-mm i.d.) from the same supplier were used as SFE cells for the 300 and 400 °C extractions. Extraction cells were mounted vertically in the GC oven with the water flowing from top to bottom so that any extracted analytes were immediately swept from the cell. The outlet of the extraction cells were connected by stainless steel tubing to an HIP Model 15-11AF1 shut-off valve (High Pressure Equipment Co., Erie, PA) mounted just outside the oven wall. The outlet of the valve was connected via stainless steel tubing and a $^1/_{16} \times {}^1/_{16}$ in. Parker tubing union to flow restrictors constructed from ~10-cm lengths of fused silica tubing (Polymicro Technologies, Phoenix, AZ). The majority of the extractions were performed at 350 bar, using a 30-μm-i.d. restrictor to yield a flow of ~1 mL/min, or at 50 bar, using a 50-μm i.d. restrictor (also for a flow rate of ~1 mL/min). For the flow rate study, (performed at 250 °C and 350 bar) restrictors with inner diameters of 20, 25, 28, and 30 μm were used to yield flow rates of 0.1, 0.3, 0.7, and 1.1 mL/min, respectively. For the pressure study, flow rates were maintained at ~1 mL/min using restrictors with inner diameters of 25 (for 600 bar), 30 (350 bar), and 50 μm (50 bar). For the extractions performed at 5 bar, the flow was difficult to control at 1 mL/min using the fused silica restrictors. Therefore, the pump for these extractions was set in the constant-flow mode at 1 mL/min, and a 150-μm-i.d. restrictor were used. This resulted in pressures of about 4–6 bar during the extraction. All flow rates are as liquid water measured at the pump.

Since heating the GC required several minutes at the higher extraction temperatures (up to ~11 min for the 400 °C extractions), the outlet valve of the extraction cell was not opened until the heating was completed. Therefore, the following sequence was used for all extractions. After the extraction cell was assembled in the GC oven, the cell was pressurized with ~50 bar of water (except for the 5-bar extractions, where the initial pressure was ~3 bar) by opening the inlet valve from the pump (outlet valve closed). The inlet valve was then closed, and the GC oven was heated to the

(26) Drake, B. D.; Smith, R. L., Jr. *J. Supercrit. Fluids* 1990, *3*, 162.

desired temperature. (Note: pressurization to the full extraction pressure is not done prior to heating to avoid high-pressure buildup during the heating step.) After the GC oven reached full temperature, the outlet and inlet valves were opened and the cell was immediately pressurized to the desired pressure. This sequence assured that the sample cell was always full of water and that dangerously high pressures were avoided during the heating step. (Note that, since the outlet valve was located outside of the oven, some deposition of analytes in the valve might occur. However, the lack of detectable analytes in system blank extractions, and the quantitative collection of spiked analytes, demonstrated that no detectable analyte losses occurred.)

Collection of the extracted analytes was performed by inserting the outlet of the restrictor into a 22-mL glass vial containing 5 mL of chloroform. Thus, the water percolated through the chloroform (allowing the extracted analytes to partition into the organic solvent) and formed a layer on top of the chloroform. At the higher extraction temperatures (300 and 400 °C), the collection chloroform evaporated and therefore the chloroform volume was maintained at about 4–5 mL by small additions during the extraction. For some of the analytes (particularly the organics with higher water solubility), quantitative transfer from the water to the collection solvent did not occur by this simple percolation technique. Therefore, the water layer from each extraction was extracted with a second 2–3-mL aliquot of chloroform, the two chloroform aliquots were combined, and finally appropriate internal standards were added to the chloroform solution.

After extraction with water, selected residues were again extracted by sonication (bath sonicator) for 14 h in 5 mL of chloroform.

Extract Analysis. All extracts were analyzed by GC-FID (Hewlett-Packard 5890) or GC/MS (Hewlett-Packard 5988) using a 25 m × 250 μm i.d. (0.17-μm film thickness) HP-5 column (Hewlett-Packard) and either split or splitless injection, as appropriate. Quantitation of the spiked test compounds was based on GC-FID analysis, and standards were prepared from the same stock solution as that used for spiking the clean sand matrix (washed sea sand, Fisher Scientific). Octahydroanthracene was used as the internal standard for these analyses. Quantitation of the PAHs from the highly contaminated soil was based on GC-FID analysis of gravimetrically prepared PAH calibration standards and octahydroanthracene added to both standards and sample extracts as the internal standard. (Peak identities and the absence of any coeluting organics that could interfere with FID quantitation was confirmed by GC/MS.) Quantitation of the PAHs from the urban air particulate matter was based on the addition of deuterated internal standards representing each molecular weight of PAH including phenanthrene-d_{10}, pyrene-d_{12}, benz-[*a*]anthracene-d_{12}, benzo[*b*]fluoranthene-d_{12}, and benzo[*ghi*]-perylene-d_{12} as well as standard curves generated from appropriate dilutions of NIST SRM 1647b (PAHs in acetonitrile). GC/MS was run in the selected ion monitoring mode (SIM) by monitoring the molecular ion of each PAH and m/z = 85 for the alkanes. All internal standards were added after the extractions to ensure that any analyte losses that might occur at any step in the extraction and collection steps were observed.

Samples. Two real-world samples available as certified reference materials were selected for the determination of PAH extraction efficiencies: urban air particulate matter (NIST SRM 1649, National Institute of Standards and Technology, Gaithersburg, MD) and PAHs from a highly contaminated soil (US EPA Certified PAH Contaminated Soil, Lot No. AQ103, Fisher Scientific). Both samples contained environmentally aged or "native" (not spiked) PAHs ranging from low microgram per gram of individual PAHs (SRM 1649) to high microgram per gram concentrations (Fisher Scientific soil). Based on thermal gravimetric analysis (weight loss up to 105 °C), the water contents of the samples (for the urban air particulates and soil, respectively) were about 4% and 5%, and the organic contents were about 38% and 8%. Extractions of the contaminated soil and urban air particulate matter used 200-mg samples.

RESULTS AND DISCUSSION

Extraction of Spiked semivolatile Organics from Sand. Initial studies were performed to determine the temperature conditions at which significant solubilization of a range of polar to nonpolar organics would occur by spiking several organics onto sand for subsequent extraction with water. (Please note that the spike studies were performed only to investigate the solubilization effect of water and may not represent the extraction of aged environmental matrices since the extraction behavior of spiked and environmentally aged organics can be very different, as has been demonstrated with SFE using CO_2).[28] Several members of the U.S. Environmental Protection Agency's Semi-Volatile Priority Pollutant list (including chlorinated phenols, amines, and PAHs) as well as several *n*-alkanes were spiked onto sand (ca. 40 μg each component onto 0.5 g of sand) and extracted sequentially for 10 min each at 50, 150, and 250 °C (all subcritical) and 400 °C (supercritical) as described in the Experimental Section. These conditions sequentially lowered the ϵ value of the extraction water from 71 (at 50 °C) to 45 (150 °C), 29 (250 °C), and 8 (400 °C).[14] Since pressure has only a small effect on ϵ (Figure 1), 350 bar was arbitrarily chosen for these initial experiments.

The results of these initial extractions are shown in Table 1. At 50 °C (ϵ = 71), as might be expected, the extraction efficiencies parallel the water solubility at ambient conditions for the test organics, and water efficiently extracted the more polar components (e.g., the chlorinated phenols and *N*-nitroso-di-*n*-propylamine). In addition, nonpolar compounds with low molecular weights (e.g., naphthalene, MW = 128) also showed significant extraction. As the temperature was raised to 150 °C, the PAHs ranging from MW = 178 to MW = 228 showed significant extraction, as did moderately polar compounds such as 4-chlorophenyl phenyl ether. After the 250 °C extractions, virtually all of the test organics (except the *n*-alkanes) had been quantitatively extracted. These extraction efficiencies were all achieved with subcritical water. When supercritical water was used (400 °C), the remaining traces of the organics (including the *n*-alkanes) were removed.

(27) Sanders, N. D. *Ind. Eng. Chem. Fundam.* **1986**, *25*, 171.
(28) Burford, M. D.; Hawthorne, S. B.; Miller, D. J. *Anal. Chem.* **1993**, *65*, 1497.

Table 1. Water Extraction of Polar and Nonpolar Organics from Spiked Sand Using Sequentially Higher Temperatures

	cumulative % extracted in 15 min[a]			
	50 °C	150 °C (plus 50 °C)	250 °C (plus 50 and 150 °C)	400 °C (plus 50, 150, and 250 °C)
2,4-dichlorophenol	96	99	100	100
2,4,5-trichlorophenol	96	100	100	100
2,3,4,6-tetrachlorophenol	98	100	100	100
N-nitroso-di-*n*-propylamine	99	100	100	100
3-nitroaniline	17	92	100	100
2-aminofluorene	70	100	100	100
4-chlorophenyl phenyl ether	9	86	95	100
dibenzofuran	26	82	96	100
naphthalene	75	97	100	100
phenanthrene	6	81	96	100
anthracene	2	79	95	100
chrysene	1	56	90	100
benzo[*a*]pyrene	0	35	86	100
benzo[*ghi*]perylene	0	6	94	100
tridecane (C-13)[b]	4	34	90	100
heptadecane (C-17)[b]	2	20	50	100
docosane (C-22)[b]	1	6	14	100
hexacosane (C-26)[b]	1	4	10	100
triacontane (C-30)[b]	1	3	5	100

[a] The results in Table 1 are based on 100% removal, defined by the lack of any detectable species in a chloroform extract (14-h sonication) of the residues after water extraction. The percent recoveries based on recovery of the spiked analytes agree well with the results shown in Table 1, i.e., percent recoveries versus the spiked value were >90% for all of the test species except those that were highly soluble in ambient water. For such species (the chlorinated phenols, naphthalene, and *N*-nitroso-di-*n*-propylamine), the total recoveries were ranged from 82% to 86%. These losses were shown to be a result of the partitioning step between the collection chloroform and the extraction water and were not because of subquantitative extraction (as demonstrated by the lack of detectable species after chloroform sonication of the residues). All values are based on triplicate extractions. Standard deviations in percent recovery were typically less than ±4. [b] Estimated values are given because the collection efficiencies in the chloroform trapping solvent were low for the *n*-alkanes (ranging from 75% for *n*-heptadecane to 50% for *n*-triacontane). The percentage in each fraction was determined by comparing the quantity collected in that fraction to the total quantity collected in the four fractions.

Although the more polar species do extract at 50 °C (Table 1) there is no apparent advantage in using the lower temperature conditions for the more polar species (other than the potential for class-selective extractions), since the dielectric constant of the water is still much higher than those of all of the test species listed in Table 1. This is confirmed by the fact that, when the same test mix is extracted beginning at 250 °C, all of the species listed in Table 1 (except the *n*-alkanes) were quantitatively extracted (>97%) after 10 min.

While virtually all of the semivolatile pollutants listed in Table 1 were quantitatively extracted in subcritical water at a temperature of 250 °C, *n*-alkanes showed poor extraction efficiencies at all subcritical conditions. The more volatile (and more water soluble) alkanes (C-13 and C-17) showed some extraction in subcritical water, but neither were quantitative and all of the higher molecular weight alkanes required supercritical water for efficient extraction (Table 1). It is interesting to note that, for water, alkanes are the most difficult species to extract, while for supercritical CO_2, alkanes are among the easiest organics to extract (as would be expected on the basis of the polarity considerations discussed above).

Extraction of PAHs from Contaminated Soil. The extraction of the spiked semivolatile pollutants from sand demonstrates that subcritical water is capable of solubilizing a wide range of organic pollutants in sufficient quantities for analytical-scale extractions and that the more polar organics (e.g, chlorophenols) extract at lower temperatures than low-polarity organics (e.g., PAHs). However, the results of a spike study do not necessarily reflect the ability of an extraction method to quantitatively extract organics from real-world samples since the spiked analytes are not likely to reflect the interactions between the organic pollutants and matrix active sites.[28] The extraction of PAHs was chosen to investigate the use of water for analytical extractions from real-world samples. PAHs were selected since they were the most difficult organics to extract of all of the hazardous semivolatile pollutants studied above (except the alkanes, which are not generally considered hazardous), and since they are present as contaminants in several different environmental matrices ranging from air particulate matter and exhaust particulates to soils and sludges.

Two real-world samples available as certified reference standards, a highly contaminated soil and urban air particulate matter, were selected for further study. The soil is highly contaminated with PAHs (>500 μg/g for several individual PAHs) and has been shown to be relatively "easy" to extract with supercritical CO_2.[4] This sample should reflect the ability of water to extract very high concentrations of PAHs where the majority of the contaminants are not tightly bound to the sample matrix. In contrast, the urban air particulate matter has much lower concentrations of the individual PAHs (typically low micrograms per gram), and the sample has been one of the more difficult to extract with supercritical CO_2.[4,12] Therefore, the air particulates should reflect the ability of water to extract PAHs which have strong matrix/analyte interactions.

Effect of Extraction Temperature. The effects of water temperature (at a constant pressure of 350 bar and a flow rate of ca. 1 mL/min) on the extraction of PAHs from the contaminated soil are summarized in Table 2. As would be expected on the basis of the high dielectric constant of water, and on the spike extractions (Table 1), extractions at 50 °C failed to yield significant recovery of any of the PAHs. As the temperature was increased to 200 °C, the recoveries of all of the PAHs increased substantially, and the recoveries of the low molecular weight PAHs (up to phenanthrene and anthracene) were quantitative compared to those certified on the basis of Soxhlet and sonication extraction. Further increases in recoveries were achieved by increasing the temperature to 250 °C, and the recoveries at 250 °C compared very favorably with the certified concentrations. Note that, despite the fact that the water dielectric constant of 29 was still quite high compared to those of PAHs of ca. 3 (Figure 1), the polarity of water was sufficiently reduced at 250 °C so that water was a very effective extraction solvent.

Additional increases to 300 (still subcritical conditions) and 400 °C (supercritical water) did not increase the recoveries significantly despite lowering ε to about 22 and 8, respectively. In fact, the recoveries obtained using supercritical water were slightly lower than the subcritical water recoveries. The lower recoveries obtained using supercritical water are a result of lower collection efficiencies in the chloroform trap, rather than lower extraction efficiencies as was described above for the larger *n*-alkanes (chemical degradation under these conditions may be possible, but seems unlikely because of the lack of oxygen in the system and the thermal stability of PAHs.

Table 2. Effect of Water Temperature on PAH Recoveries from Soil at 350 bar in 15 Minutes

		recovery (% RSD)[a]					
		subcritical water					
	cert conc, μg/g (% RSD)	50 °C ε = 71	120 °C ε = 52	200 °C ε = 36	250 °C ε = 29	300 °C ε = 22	supercritical water 400 °C ε = 8
naphthalene	24 (119)	23 (11)	64 (23)	151 (15)	150 (11)	165 (9)	132 (19)
2-methylnaphthalene	57 (37)	5.7 (9)	20 (19)	118 (7)	127 (14)	120 (26)	104 (23)
acenaphthene	16 (68)	2.9 (9)	14 (11)	99 (6)	94 (12)	93 (24)	~~131 (16)~~ 81 (30)
dibenzofuran	306 (25)	2.8 (11)	16 (13)	117 (6)	152 (11)	129 (14)	151 (16)
fluorene	476 (21)	2.9 (5)	11 (14)	93 (11)	94 (15)	95 (22)	84 (21)
phenanthrene	1450 (39)	4.5 (15)	18 (33)	116 (12)	110 (13)	111 (22)	92 (14)
anthracene	425 (16)	2.9 (3)	13 (18)	93 (11)	96 (16)	107 (19)	90 (16)
fluoranthene	1307 (30)	0.2 (24)	4.6 (24)	73 (20)	96 (20)	97 (22)	74 (16)
pyrene	961 (45)	0.3 (11)	4.5 (23)	79 (19)	106 (13)	114 (21)	86 (17)
benz[*a*]anthracene	249 (23)	ND[b]	3.5 (33)	36 (15)	79 (17)	96 (11)	73 (41)
chrysene	311 (20)	ND	3.9 (37)	36 (17)	85 (24)	111 (13)	75 (14)
benzo[*b*+*k*]fluoranthene[c]	156 (26)	ND	1.9 (19)	29 (13)	115 (18)	132 (25)	92 (20)
benzo[*a*]pyrene	98 (27)	ND	1.9 (19)	27 (14)	103 (19)	120 (18)	84 (40)

[a] Percent recovery versus certified value based on Soxhlet and sonication performed according to EPA SW-846, methods 3540 and 3550. Relative standard deviations are based on triplicate water extractions at each condition. [b] ND, not detected. [c] The sum of benzo[*b*]- and benzo[*k*]fluoranthene is reported because these two species were not adequately resolved by the GC conditions used.

Also, no PAH degradation products were detected during GC/MS analysis). This problem exists because the high temperature of the effluent water causes the chloroform collection solvent to evaporate rapidly (5 mL evaporates in ca. 3 min), which likely leads to analyte losses despite constant addition of new chloroform to maintain a reasonable volume of collection solvent.

The initial extractions were performed on the contaminated soil for 15 min using 350 bar pressure with different temperatures. Figure 3 shows the effect of temperature on the extraction rates of representative PAHs over longer extraction times. As shown in Figure 3, the lowest molecular weight PAH, naphthalene, shows a significant extraction rate even at 50 °C, although the extraction rate increases substantially with temperature. As the molecular weight of the PAH increases, the extraction rates at lower temperatures decrease dramatically, as shown in Figure 3 for pyrene (MW = 202) and benzo[*a*]pyrene (MW = 252). For all of the PAHs, raising the extraction temperature from 250 to 300 °C (both below the critical temperature of water) only yielded a small increase in the extraction rate (Figure 3). (Note that the extraction rate curves for 400 °C are not shown in Figure 3 because of the poor collection efficiencies, as discussed above.) Figure 3 also demonstrates that the largest quantities of the PAHs were extracted during the first 15 min and that increasing the extraction time to 60 min yielded only small increases in the recoveries. In addition, as shown in Table 2, the recoveries that were achieved in 15 min generally exceeded the certified values based on conventional Soxhlet and sonication extraction.

In addition to the rapid loss of collection solvent that occurs at the higher extraction temperatures (discussed above), the observation that 250 °C is sufficient for quantitative PAH extractions is fortunate, because the technical performance of the extractions is much easier at 250 °C than at either 300 or 400 °C. At 250 °C the Keystone SFE cells were very reliable; however, at any higher temperatures cells relying on stainless/stainless sealing surfaces (i.e., the HPLC columns from Keystone Scientific) were needed. The Keystone SFE cells depend on a polyimide ring that surrounds the entrance and exit frit to form the pressure seals. At 250 °C, these seals were reliable as long as care was taken that no foreign substance (e.g., sand from the sample) was on the sealing surfaces before tightening, and as long as they were tightened with slightly more torque than would be used for the same cells used for normal SFE. Under these conditions, the cells could be used for 10–20 extractions before replacing the end caps and frits). However, with the 300 and 400 °C extractions, the entire HPLC column had to be replaced after only a few uses and at a substantially higher cost. Obviously, proper care to shield the operator should be taken during these extractions, particularly since a leak could spray steam, resulting in scalding. It should also be noted that supercritical water that has not been purged to remove oxygen may be corrosive to stainless steel vessels. Since water extractions at 250 °C yielded recoveries similar to those achieved using higher temperatures (and were much simpler to perform), all subsequent PAH extractions were performed at 250 °C.

Effect of Water Flow Rate. The effect of the water flow rate on the extraction rate of PAHs from the soil sample (250 °C and 350 bar for 15 min) is shown in Figure 4. For the lower molecular weight PAHs (e.g., naphthalene), flow rate had little effect on the recoveries, while the recoveries of the higher molecular weight PAHs (e.g., benzo[*a*]pyrene) increased substantially with increasing flow rates up to 1.1 mL/min (measured at the pump). Therefore, all subsequent extractions were performed at a flow of ~1 mL/min. The lack of effect of flow rate for the lower molecular weight PAHs demonstrates that their extraction is not limited by their solubility at 250 °C and 350 bar (or partitioning onto the matrix during the elution process[12,13]), while the dependence on flow rate for the higher molecular weight PAHs does indicate that higher solubility conditions may increase the extraction rates. For SFE with CO_2, organic modifiers are often added in the range of 10 vol % in an attempt to increase the polarity of CO_2 (and thus increase the solubility of target analytes). Our results suggest that adding modifiers to *decrease* the polarity of water may be an effective strategy to obtain high extraction efficiencies of nonpolar organics (and possibly at lower temperatures).

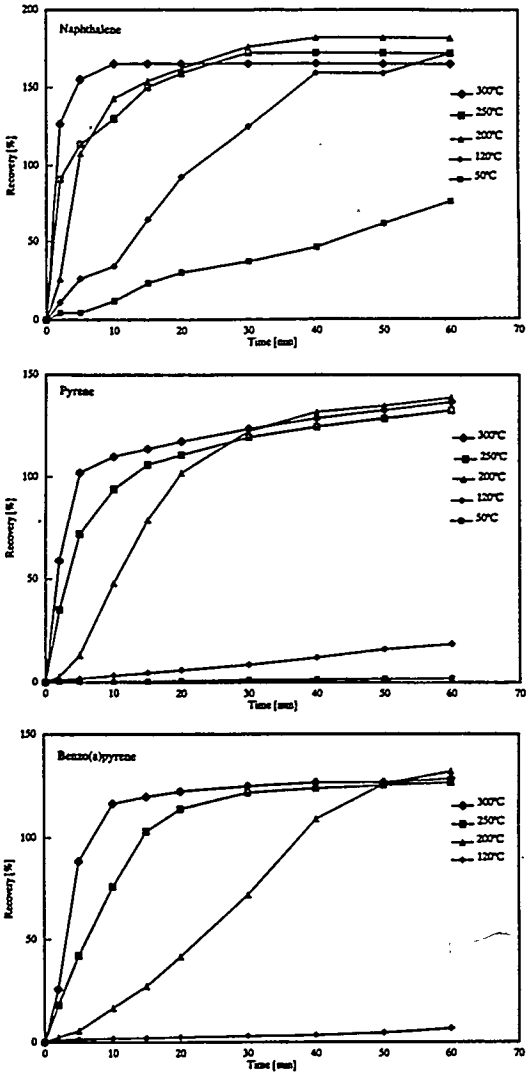

Figure 3. Effect of extraction temperature on the extraction rates of representative PAHs from a highly contaminated soil using water at 350 bar. Percent recoveries are compared to the certified values based on Soxhlet and sonication extraction.

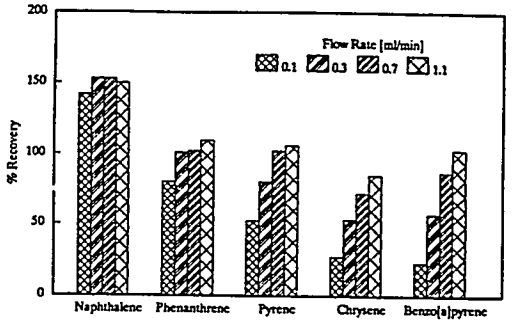

Figure 4. Effect of water flow rate on the extraction efficiencies of representative PAHs from a highly contaminated soil at 350 bar and 250 °C for 15 min. Percent recoveries are compared to the certified values based on Soxhlet and sonication extraction.

Effect of Pressure. Extraction efficiencies using SFE with CO_2 can show substantial changes with extraction pressure since the solubility of most organics increases with increasing CO_2 density (assuming a constant temperature). However, this may not be the case for water since, as shown in Figure 1, the dielectric constant of water depends primarily on temperature and much less on the pressure. In fact, an increase in pressure causes a small increase in ϵ, which could possibly inhibit the extraction of low-polarity organics. The most obvious change in extraction conditions that occurs with pressure is the change of the water density, most notably in determining whether the extraction is performed with liquid water or with steam. To determine the effect of pressure on the extraction efficiencies of PAHs, the soil sample was extracted using pressures of 5 (steam) and 50 and 600 bar (liquid). (Recoveries at 350 bar are already reported in Table 2.) Water densities at 250 °C were 2.1, 800, 830, and 850 mg/mL, respectively, at 5, 50, 350, and 600 bar.[14] All extractions were performed at 250 °C with a flow rate of ca. 1 mL/min for 15 min.

As shown in Table 3, the extraction efficiencies had very little dependence on pressure when the temperature was 250 °C, with the exception that the steam extraction (5 bar) yielded significantly lower recoveries than the liquid water extractions. The lower recoveries for steam could be a result of lower extraction efficiencies, but this does not seem likely since 14 h of sonication with chloroform of the steam-extracted residues failed to show significant concentrations of any of the PAHs. The steam extractions were more difficult to perform than the liquid water conditions because (like the supercritical water extractions) the chloroform solvent evaporated more rapidly. Therefore, a more likely explanation for the lower recoveries is that the PAHs were efficiently extracted, but not as efficiently collected from the steam extracts as from the liquid water extracts.

The recoveries shown in Tables 2 and 3 are typically higher than the certified values based on conventional liquid solvent extraction. These differences may be partially due to the high relative standard deviations associated with the extractions (note that the RSDs of the water extractions are generally substantially better than those of the conventional extractions), and in general, the higher recoveries obtained by the water extractions are not statistically significant based on the high variance in the conventional solvent extraction data. The results of the 15-min water extractions also compare well with the recoveries previously reported by Langenfeld et al. for this sample based on extraction with supercritical CO_2[4,12] as shown in Table 3. Similarly high recoveries were reported in that study for the low and middle molecular weight PAHs, although the optimized water extractions did appear to give significantly higher recoveries of the high molecular weight PAHs (e.g., benzo[*a*]pyrene).

Extraction of PAHs from Air Particulate Matter. Based on the discussions above, the optimal conditions (both for recoveries and ease of performance) for the extraction of PAHs from the highly contaminated soil were 250 °C, 50 bar, and a water flow rate of ca. 1 mL/min. Therefore, these conditions

Table 3. Effect of Water Pressure on PAH Recoveries from Soil at 250 °C in 15 Minutes

		% recovery (% RSD)				
		water[a]			CO_2[b]	
	cert conc, μg/g (% RSD)	5 bar	50 bar	600 bar	659 bar 50 °C	659 bar 200 °C
naphthalene	24 (119)	109 (18)	187 (20)	160 (17)	207 (21)	165 (10)
2-methylnaphthalene	57 (37)	80 (8)	136 (10)	108 (3)	152 (4)	146 (10)
acenaphthene	16 (68)	74 (5)	110 (2)	84 (3)	135 (12)	134 (15)
dibenzofuran	306 (25)	91 (6)	100 (19)	128 (3)	147 (10)	119 (17)
fluorene	476 (21)	65 (5)	102 (3)	81 (6)	127 (14)	125 (12)
phenanthrene	1450 (39)	110 (4)	159 (15)	108 (10)	121 (10)	135 (8)
anthracene	425 (16)	82 (5)	135 (12)	109 (10)	97 (14)	107 (16)
fluoranthene	1307 (30)	74 (6)	123 (16)	81 (7)	144 (6)	146 (9)
pyrene	961 (45)	100 (5)	146 (23)	107 (10)	132 (12)	137 (7)
benz[*a*]anthracene	249 (23)	49 (11)	107 (8)	77 (22)	97 (14)	98 (15)
chrysene	311 (20)	80 (10)	119 (8)	85 (19)	103 (17)	98 (12)
benzo[*b*+*k*]fluoranthene[c]	156 (26)	142 (8)	182 (10)	140 (27)	119 (8)	85 (4)
benzo[*a*]pyrene	98 (27)	76 (12)	176 (13)	126 (24)	98 (6)	65 (8)

[a] Percent recovery versus certified value based on Soxhlet and sonication performed according to EPA SW-846, methods 3540 and 3550. Relative standard deviations are based on triplicate water extractions at each condition. [b] Recoveries resulting from triplicate SFE extractions with CO_2. Data adapted from ref 4. [c] The sum of benzo[*b*]- and benzo[*k*]fluoranthene is reported because these two species were not adequately resolved by the GC conditions used.

Table 4. Recoveries of PAHs from Urban Air Particulates (NIST 1649)

		% recovery (% RSD)		
	cert conc, μg/g (% RSD)	water 250 °C 50 bar	CO_2[a] 200 °C 659 bar	CO_2[b] 10% toluene 80 °C 405 bar
phenanthrene	4.5 (7)	112 (6)	99 (10)	100 (2)
fluoranthene	7.1 (7)	100 (6)	155 (13)	96 (2)
pyrene	7.2 (7)	95 (6)	109 (6)	81 (2)
benz[*a*]anthracene	2.6 (12)	89 (9)	111 (5)	94 (4)
chrysene + triphenylene[c]	5.2	95 (7)	96 (3)	129 (4)
benzo[*b*+*k*]fluoranthene[c]	8.2	100 (7.6)		
benzo[*a*]pyrene	2.9 (17)	73 (15)	95 (3)	60 (8)
indeno[1,2,3-*cd*]pyrene	3.3 (15)	57 (11)	45 (21)	57 (13)
benzo[*ghi*]perylene	4.5 (24)	68 (7)	60 (18)	26 (11)

[a] Recoveries based on triplicate 40-min extractions with CO_2. Data taken from ref 4. [b] Recoveries based on triplicate 20-min extractions (10 min static/10 min dynamic) with CO_2 modified with 10 vol % toluene. Data taken from ref 12. [c] The sum of chrysene and triphenylene and of benzo[*b*]- and benzo[*k*]fluoranthene is reported because these two species were not adequately resolved by the GC conditions used. Concentrations are certified for fluoranthene, benz[*a*]anthracene, benzo[*a*]pyrene, benzo[*ghi*]perylene, and indeno[1,2,3-*cd*]pyrene. All other concentrations are informational values supplied by NIST.

were used to determine the extraction efficiencies of PAHs from the urban air particulate matter. While the individual PAH concentrations on the soil were typically several hundred to thousands of micrograms per gram, the concentrations of individual PAHs on the air particulate matter were in the low microgram per gram range. Quantitative recoveries from this sample using conventional SFE have also been much more difficult to obtain than from the soil used above,[4,12] indicating that the PAHs are more tightly bound to matrix active sites on the air particulates.

The extraction efficiencies obtained in 15 min using 250 °C and 50 bar (compared to the values certified by NIST based on 48-h Soxhlet extractions) are shown in Table 4. For most of the PAHs, the water extractions gave good quantitative reproducibilities, and the recoveries obtained were in good agreement with the certified values. However, the concentrations of the higher molecular weight PAHs (e.g., indeno[1,2,3-*cd*]pyrene and benzo[*ghi*]perylene) were significantly lower than those reported by NIST. Since the lower concentrations of these species could be a result of either lower extraction efficiencies or differences in the methods used to determine the PAH concentrations in the extracts (the extracts of this material contain a very complex mixture of PAH and non-PAH hydrocarbons, which greatly complicates the quantitation of the individual PAH components), the residues from the water extractions were sonicated for 14 h in chloroform in an attempt to extract any remaining indeno[1,2,3-*cd*]pyrene and benzo[*ghi*]perylene. However, none of the PAHs could be detected in the sonication extracts, indicating that the water extractions were quantitatively efficient. In addition, earlier studies performed in our laboratory using SFE have obtained recoveries for the higher molecular PAHs similar to those we obtained with subcritical water as shown in Table 4, which further indicates that the differences in recoveries are an artifact of the analysis and not the extraction procedures.

Since the recoveries shown in Table 4 were based only on 15-min extractions, the effect of extraction time on the extraction rates was also determined for the air particulate sample. As shown in Figure 5, the extraction of all of the lower molecular weight PAHs was essentially complete after ~10 min, and additional extraction time above 15 min (even up to 90 min) yielded no increase in recoveries. For the higher molecular weight PAHs, there was a slight increase in recoveries with extraction time, but even after 90 min the increase in recoveries were only from 57% to 70% (for indeno-[1,2,3-*cd*]pyrene) and 73% to 86% (for benzo[*a*]pyrene), which does not account for the differences between the certified and our values.

Selectivity of Water Extractions. As mentioned above, extracts of urban air particulates (and exhaust particulates)

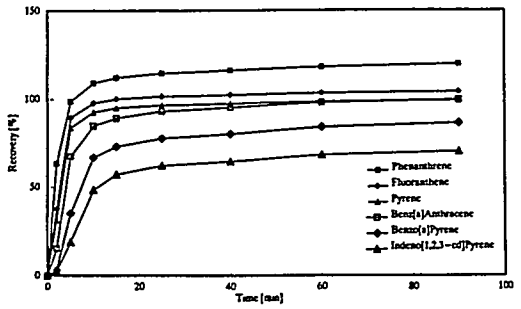

Figure 5. Extraction rates of representative PAHs from urban air particulate matter (SRM 1649) using water at 250 °C and 50 bar. Percent recoveries are compared to the values reported by NIST based on 48-h Soxhlet extractions.

are typically very complex since they contain high concentrations of branched and normal alkanes in the same volatility range as the PAHs of toxicological interest. The bulk of these alkanes are from about C-18 to C-30 and elute in the same chromatographic region as the PAHs of interest. Therefore, reducing the amounts of alkanes that are extracted with the PAHs would simplify the chromatographic determination. Organic solvent extractions are typically nonselective. SFE with CO_2 has been used to sequentially extract alkanes (at low pressure) followed by PAHs (at high pressure),[29] although the alkanes must be removed prior to the PAHs since (as CO_2 is a low-polarity solvent) any SFE condition used to extract PAHs will be even better for alkanes. In contrast (as shown in Table 1), water is too polar of a solvent, and therefore it is easier to extract PAHs than alkanes.

Although no attempts were made to optimize selective extractions from the urban air particulate matter, the conditions used for the extractions listed in Table 4 (i.e., 50 bar, 250 °C, and 15 min) did yield highly selective extractions, particularly for the higher molecular weight alkanes. Comparison of the mass of each alkane extracted by water to the mass extracted from the water-extracted residue by sonication (14 h) showed that the majority of the alkanes were found in the water extract up to ~C-20 (Table 5). (For brevity, only even-numbered *n*-alkanes are listed since the same trend holds for the odd-numbered *n*-alkanes). However, only 5–10% of the alkanes from C-24 and larger were found in the water extract while the remainder stayed on the particulates until extracted with chloroform. While the alkanes that were extracted by water fall in the same chromatographic range as the PAHs with molecular weights of 178 and 202, all of the PAHs with higher molecular weights have *n*-alkane retention indexes of >2400 (i.e., elute after the C-24 *n*-alkane),[30] and thus have very little chromatographic interference from alkanes, as shown in Figure 6. These results emphasize the ability of water to extract more polar organics in favor of less polar organics, while more conventional SFE and liquid solvent extractions typically extract less polar organics in favor of more polar organics.

(29) Hawthorne, S. B.; Miller, D. J. *J. Chromatogr. Sci.* **1986**, *24*, 258.
(30) Rostad, C. E.; Pereira, W. E. *J. High Resolut. Chromatogr. Chromatogr. Commun.* **1986**, *9*, 328.

Table 5. Selectivity of Water Extractions at 50 bar and 250 °C against *n*-Alkanes

	% extracted by water + SD[a]
dodecane (C-12)	91 ± 6
tetradecane (C-14)	91 ± 4
hexadecane (C-16)	90 ± 2
octadecane (C-18)	90 ± 5
eicosane (C-20)	77 ± 8
docosane (C-22)	53 ± 12
tetracosane (C-24)	10 ± 3
hexacosane (C-26)	6 ± 1
octacosane (C-28)	5 ± 2
triacontane (C-30)	6 ± 2
dotriacontane (C-32)	6 ± 2
tetratriacontane (C-34)	5 ± 2

[a] The percentage extracted by water for each alkane was calculated from the total quantities extracted by water and by chloroform (14-h sonication) of the residues from the water extractions. Standard deviations were based on triplicate sequential (water followed by chloroform) extractions.

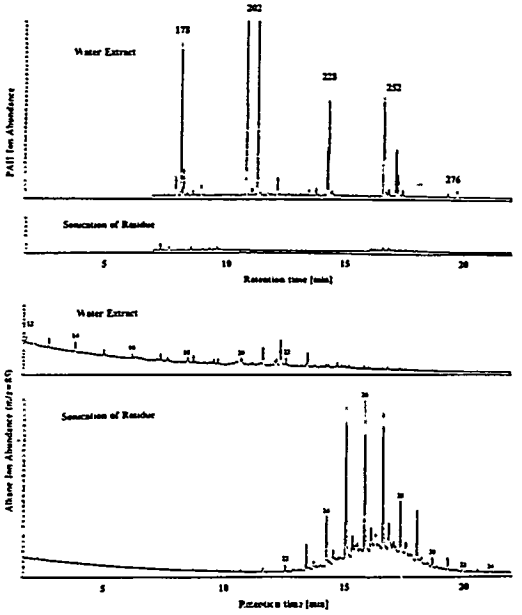

Figure 6. Selectivity of water extractions (250 °C, 50 bar, 15 min) for PAHs versus alkanes from urban air particulate matter (SRM 1649). The chromatograms show the selected ion chromatogram for alkanes at $m/z = 85$ (the numbers above the peaks indicate the chain length of the *n*-alkane), and for PAHs based on their molecular ions. The chloroform extractions (14-h sonications) were performed on the residues after the water extractions.

CONCLUSIONS

The polarity (dielectric constant) of water can be lowered dramatically by simply raising its temperature. Therefore, water can be used to sequentially extract polar, moderately polar, and nonpolar organics from environmental solids by sequentially increasing the extraction temperature from 50 (for polar organics, e.g., chlorophenols) to 400 °C (for very nonpolar organics, e.g., >C-20 alkanes). Extraction efficiencies depend primarily on extraction temperature, but there is little dependence on pressure. Although polar organics are the easiest to extract with water, quantitative extractions of low-polarity organics such as PAHs can be achieved at

MSC: ac9402945 BATCH: ac9m38 USER: eap69 PAGE: 9
DIV: @xy1dr/data7/CLS_pj/GRP_ac/JOB_i17/DIV_ac9402945 DATE: 06/29/94

relatively mild conditions (e.g., 250 °C and 50 bar) in 15 min without extracting the bulk of alkanes (>~C-22) that interfere with GC determinations of the PAHs. Since water is the extraction solvent, the presence of water in the sample (which often requires drying steps prior to extraction using liquid solvents or SFE) does not matter. The results of this study demonstrate that water is a potentially useful analytical extraction solvent for the entire range of polar and nonpolar organics from environmental solids.

ACKNOWLEDGMENT

The financial support of the U.S. Department of Energy (Morgantown Energy Technology Center) and Chevron Oil Co. is gratefully acknowledged.

Received for review March 29, 1994. Accepted June 1, 1994.•

• Abstract published in *Advance ACS Abstracts*, Xxxxxxxx YY, ZZZZ.

USER: PAGE: 1 DATE: 06/24/94 TIME: 14:23:02
DIV: @xy2dr/data3/CLS_ pj/GRP_ ainprt/JOB_ ainprt/DIV_ ainsoftin

AUTHOR INDEX ENTRIES

MSC: ac9402945 BATCH: ac9m38 VOLUME: 066 ISSUE: 017

Hawthorne, S. B.

Yang, Y.

Miller, D. J.

TASK 1.8

AQUEOUS-PHASE THERMAL OXIDATION WASTEWATER TREATMENT

Prepared by:

John R. Rindt
Jo Ann Fain

August 1994

TABLE OF CONTENTS

TASK 1.8 AQUEOUS-PHASE THERMAL OXIDATION WASTEWATER TREATMENT

1.0 INTRODUCTION/OBJECTIVE

A novel aqueous-phase thermal (APT) oxidation apparatus has been designed for the cost-effective treatment of organically contaminated aqueous streams. During the research for this task, the specific components will be integrated and tested to evaluate their operability. A determination will also be made as to the ability of the integrated system to adequately remediate an organically contaminated aqueous stream.

The overall objective of this task is to perform a sequentially integrated test of the critical components of the novel APT oxidation apparatus to evaluate the ability of this system to remediate an organically contaminated aqueous stream. Steps required to meet this objective are as follows:

- Selection of an appropriate aqueous waste stream
- Operation of the integrated system using actual aqueous waste stream
- Analysis of all feeds and products
- Calculation of mass and material balances for the tests
- Interpretation of the data and determination of the viability of using this type of system for contaminated aqueous streams

2.0 ACCOMPLISHMENTS

Evaluation of streams that have the potential to be remediated by the technology is currently under way.

3.0 FUTURE WORK

A stream will be selected for the experimental testing in this program.

TASK 2.3

REVIEW AND ASSESSMENT OF RESULTS FROM COMPREHENSIVE CHARACTERIZATION OF AIR TOXIC EMISSIONS FROM COAL-FIRED POWER PLANTS

Prepared by:

Stanley J. Miller
Sumitra R. Ness

August 1994

TABLE OF CONTENTS

TASK 2.3 REVIEW AND ASSESSMENT OF RESULTS FROM THE COMPREHENSIVE CHARACTERIZATION OF AIR TOXIC EMISSIONS FROM COAL-FIRED POWER PLANTS

1.0 INTRODUCTION

Significant concern exits over the impact of increasing energy consumption on ambient air quality. Acid rain and the passage of legislation to reduce emissions of acid rain precursors continue to be prominent issues in the United States, Canada, Europe, and Japan. Emissions of fine particles are of concern because these particles can be deposited in the lower respiratory system through normal breathing. The potential problem is further compounded because hazardous trace elements such as selenium and arsenic are known to be concentrated on such fine particles. Recent studies indicate that the current ambient air quality standard for particulate matter less than 10 microns (PM10) may not adequately protect public health. In addition to potentially causing adverse health effects, fine particles, including secondary sulfates, are the primary cause of visibility impairment in the atmosphere. The 1990 Clean Air Act Amendments address the issue of emission of acid rain precursors, require study of air toxic emissions, and provide for possible expansion of visibility protection measures.

Hazardous air pollutants (HAPs) emissions from eight different power plants, each with different process configurations, were characterized by U.S. Department of Energy Pittsburgh Energy Technology Center (DOE/PETC) contractors during Phase I of a study entitled "Comprehensive Characterization of Air Toxic Emissions from Coal-Fired Power Plants." Results from the study are intended to provide the U.S. Environmental Protection Agency (EPA) with data to help decide whether regulation of air toxic emissions from coal-fired power plants is necessary. The Energy & Environmental Research Center (EERC) acted as an independent technical reviewer of the final draft reports submitted by the DOE/PETC contractors.

2.0 OBJECTIVES AND DELIVERABLES

The objectives of this task are to provide an independent review of reports produced from the air toxic emissions study, evaluate the scientific validity of the conclusions, identify significant correlations between emissions and fuel or process parameters, compare the data with available results from Electric Power Research Institute (EPRI) studies, and make recommendations for possible future studies.

The deliverables for this task were to be 1) a work plan describing the approach for detailed assessment of the reports, and 2) review comments for each of the individual reports, to be used by the individual contractors in preparing their respective final reports.

The work plan was submitted to DOE/PETC in May. The exact work plan for further review and summary is still pending with DOE.

3.0 RESULTS AND ACCOMPLISHMENTS

Subtask 1 of this project, which is the only portion of the project funded to date, consisted of review of the first eight draft field reports by the EERC review team. Comments were compiled for each report to serve as a guide for the individual contractors to prepare their final reports. Conference calls were held between the EERC, DOE, and the respective contractors for each of these reports to discuss comments and form a consensus as to required changes for the final contractor reports.

Eight of ten reports were reviewed by each of the EERC team members. Two contractors have not completed Phase I reports. During the follow-up conference calls, the EERC reviewers suggested formatting and technical changes for the final reports. The DOE representative then directed the contractors to either take action on or disregard the suggestions. In general, most of the technical suggestions involved 1) alterations to standard analytical methods, 2) consistent formatting for data, especially emission factor data, and 3) mass balance and uncertainty analysis calculations. Review of the first eight reports for Phase I was completed in early June.

Additional work planned under this project, but not yet funded, is as follows:

Subtask 2 will provide DOE with a summary of recommendations for improving the quality of data in a second phase of field tests based on review of the Phase I reports and past EERC experience.

Subtask 3 will consist of preparation of a summary report of the eight individual Phase I reports to provide a clear, concise overview of the important findings.

Subtask 4 will consist of comparison of the trace element emissions data from Phase I of the Comprehensive Characterization of Air Toxic Emissions from Coal-Fired Power Plants study, with the trace element emissions data that are available from EPRI-sponsored field tests; evaluation of correlations between emission factors and the coal, process, and operating conditions for the combined data set; and forming general conclusions from the combined data set.

In Subtask 5, relevant DOE and EPRI data will be incorporated into the database on air toxic metals that is part of the National Center for Excellence on Air Toxic Metals, which the EERC has established for the EPA. Upon completion, the database will supply well-organized information on toxic metals to DOE, EPA, EPRI, and the general public.

TASK 2.4

AIR TOXIC FINE PARTICULATE CONTROL

Prepared by:

Grant E. Dunham
Marlys Heidt
Stanley J. Miller

August 1994

TABLE OF CONTENTS

LIST OF FIGURES

LIST OF FIGURES (continued)

LIST OF TABLES

TASK 2.4 AIR TOXIC FINE PARTICULATE CONTROL

1.0 INTRODUCTION

Significant concerns exist over the impact of increasing energy consumption on ambient air quality. Acid rain and the passage of legislation to reduce emissions of acid rain precursors continue to be prominent issues in the United States, Canada, Europe, and Japan. Emissions of fine particles are of concern because these particles can be deposited in the lower respiratory system through normal breathing. The potential problem is further compounded because hazardous trace elements, such as selenium and arsenic, are known to be concentrated on such fine particles. Recent studies indicate that current levels of fine particles in the atmosphere are causing up to 60,000 excess deaths per year and the current ambient air quality standard for PM10 may not adequately protect public health. In addition to potentially causing adverse health effects, fine particles, including secondary sulfates, are the primary cause of visibility impairment in the atmosphere. The 1990 Clean Air Act Amendments address the issue of emissions of acid rain precursors, require the study of air toxic emissions, and provide for possible expansion of visibility protection measures. Therefore, a current need exists to develop superior, but economical, methods to control emissions of SO_2, NO_x, and air toxics.

Recent particulate research at the Energy & Environmental Research Center (EERC) has focused on two areas: 1) bench-scale investigation of the relationships between fine-particle emissions from fabric filters and electrostatic precipitators (ESPs) and the cohesive properties of fly ash and 2) investigation of the impact of coal combustion on atmospheric visibility. Control of fine-particle emissions from coal-fired boilers is an issue because of the current concern over atmospheric air toxics, which contain high concentrations of trace elements. The best method to minimize the emission of these air toxic trace elements into the atmosphere is to install high-efficiency fine-particle control devices. After collection, the dust must be removed from the filter bags or ESP plates and transferred to the hopper without significant redispersion. Since it is more difficult to collect fine particles, the extent to which the dust is redispersed into its original particle-size distribution will have a major impact on the overall fine-particle collection efficiency of the filter or ESP and, subsequently, the collection efficiency of air toxic metals. The application is not only to conventional particulate control technologies such as fabric filters and ESPs, but also to advanced filtration methods such as the CeraMem® ceramic filter and ceramic candle filters. Previous research has shown that the collectability of fine particles from coal combustion is highly dependent upon the cohesive properties of the fly ash. Cohesive properties are also important in dust cake release, rapping or pulsing reentrainment, and hopper reentrainment.

2.0 OBJECTIVES

The goal of Task 2.4 is to evaluate redispersion of dust in particulate control devices so that the appropriate methods to minimize redispersion can be implemented. The primary objective is to determine the extent to which fly ash is redispersed as individual particles upon cleaning of the filters or ESP plates. Past research has focused on the development of reliable methods to measure the cohesive properties of fly ash in an effort to develop a model that relates cohesive properties to fine-particle emissions. The current

research will determine whether the level of redispersion of fly ash correlates with measurable cohesive dust properties. This will contribute to the long-term project goal of developing models to the point where they can be used to help design particulate control devices for the lowest level of fine-particle emissions at a reasonable cost.

3.0 SCOPE OF WORK

The planned work, as stated in the Annual Research Plan, consists of bench-scale tests to determine the extent of fly ash redispersion upon the cleaning of filters or ESP plates. Work for this reporting period included ESP redispersion tests, some data reduction and interpretation, and pulse-jet baghouse redispersion tests.

In ESPs, an ideal dust would readily release from the plates upon rapping and fall to the hopper with minimum redispersion. In the worst-case scenario, ash would release from the ESP plates, be completely redispersed by the incoming flue gas, and either be re-collected on the ESP plates or be carried out the stack by the flue gas. To achieve good dust cake release, a minimum cohesive or tensile strength would appear desirable, but to minimize redispersion of the dust into its original particle-size distribution, high dust tensile strength is preferred. Since these two factors are in direct opposition, a balance between good dust release and minimum redispersion must be achieved for optimum ESP performance.

For fabric filters, the cake should release from the fabric with a minimum energy input, without significant redispersion of the dust, while maintaining some minimum residual dust cake to achieve a high collection efficiency. Under nonideal conditions, the dust would release from the fabric, including the residual dust cake, and be redispersed to its original size distribution. Lacking a residual dust cake, the fine particles would pass through the bag, resulting in a very low collection efficiency for the fine particles. The relationship between dust redispersion and dust cohesive properties in fabric filters is analogous to that in an ESP. Low cohesive strength appears to facilitate good cake release and low residual dust cake thickness, while high cohesive strength seems necessary to maintain high dust cake porosity (low pressure drop) and prevent dust reentrainment upon cleaning. Obviously, there must be a proper balance between these factors to optimize particulate collection efficiency, pressure drop, and dust redispersion.

The level of reentrainment of submicron particles is important, because they are the most difficult to collect and because hazardous trace elements are known to be concentrated on such fine particles. Documentation and quantifying of the level of reentrainment will help to determine the importance of such filtering parameters as ash layer thickness, cleaning energy, and dust characteristics. This information can then be used to optimize the collection efficiency of the fine particles.

The approach was to look at several variables and how they affected the amount and size distribution of ash redispersed when cleaning a filter or ESP plate. Table 1 presents the completed ESP test matrix and the ambient conditions at the time of the test. It was planned to look at three independent variables for the ESP reentrainment tests: ash layer thickness, ash type, and cleaning energy. Ash layer thickness affects the amount of ash reentrained, but it may also affect the extent to which the ash is redispersed. A thicker ash layer may form larger agglomerates which will reach the hopper without

TABLE 1

ESP Reentrainment Test Matrix

Date	Coal Run No.	Ash Type	Ash Collection Time, min	Relative Humidity, %	ESP Voltage, kV	Gas Flow, scfm	Grain Loading, gr/scf
4/27/94	AB-445	Absaloka	15	11	55	129.8	6.1
4/27/94	BB-386	Big Brown (baseline)	15	14	55	129.8	6.3
4/28/94	BB-386	Big Brown (baseline)	60	14	55	130.3	5.9
4/28/94	AB-445	Absaloka	60	14	55	130.4	5.6
4/29/94	BB-384	Big Brown (conditioned)	60	14	55	130.1	6.7
4/29/94	BB-384	Big Brown (conditioned)	15	16	55	130.1	6.5
6/02/94	BV-473	Blacksville	60	19	55	130.1	5.9
6/13/94	BV-473	Blacksville	15	41	55	129.8	4.9

being redispersed. Four fly ash samples were selected from our stored fly ash sample inventory, based on previous ESP and fabric filtration experiments at the Energy & Environmental Research Center (EERC). The ashes evaluated included a Big Brown Texas lignite, a Big Brown Texas lignite conditioned with SO_3 and ammonia, an Absaloka subbituminous coal fly ash, and a Blacksville bituminous coal fly ash. The coal fly ash composition as measured by x-ray fluorescence analyses is given in Table 2. As shown in the table, the Blacksville coal had a much higher iron content (23.6%) than either the Big Brown (4.5%) or Absaloka (3.5%) coals. Ashes were selected with a range of cohesive properties in order to evaluate their effect on dispersibility or reentrainment. Previous tensile strength measurements on similar ash samples showed that the Big Brown baseline (unconditioned) ash had the lowest measured cohesive tensile strength at constant porosity and the Big Brown conditioned ash had the highest tensile strength. The Absaloka and Blacksville ashes had intermediate tensile strengths. Tests were also planned to determine the effect of cleaning energy intensity, but the cleaning mechanism did not provide any adjustment.

The dependent variables that were used to determine the effects of the ash layer thickness and ash type included the size distribution of the injected ash; the size distribution of the ash after ESP plate cleaning, the concentration of particles in the submicron size range for both the inlet ash and the ash redispersed when the ESP plate was cleaned; and the cohesive properties of the ash. The change in the size distribution of the ash redispersed after the ESP plate was cleaned was also measured as a function of time.

TABLE 2

Analyses of Fly Ashes Tested

Major Elements as Oxides, wt% on a dry basis	Absaloka	Blacksville	Big Brown
SiO_4	34.3	40.2	46.5
Al_2O_3	20.3	18.8	15.7
Fe_2O_3	3.5	23.6	4.5
TiO_2	1.0	0.8	1.9
P_2O_5	2.6	0.7	0.3
CaO	14.2	7.3	17.6
MgO	6.7	0.7	3.5
Na_2O	1.9	1.1	0.4
K_2O	0.6	1.1	0.4
SO_3	15.6	5.4	9.2

4.0 EXPERIMENTAL FACILITY

The ESP reentrainment tests were performed with the ESP on the particulate test combustor (PTC) at the EERC. The ESP has a single wire (one field), and a 8.6 ft-long by 11-in.-diameter tubular plate. The nominal applied voltage was 55 kV for all tests. The induced-draft fan for the combustor was used to maintain a nominal gas flow of 130 scfm, which translates to a nominal gas velocity of 3.3 ft/sec in the ESP.

The baghouse reentrainment tests were performed with the three-bag pulse-jet baghouse on the PTC. A single Ryton bag 13 ft long and 5 in. in diameter was installed in the baghouse. Blanks were installed in the remaining tube sheet holes. Sight ports were installed in blanks for visual observation and recording of pulsing. The pulse-jet chamber is 20 in. in diameter and 21 ft long. The induced-draft fan for the combustor was used to maintain a nominal vertical gas flow of 130 scfm, which translates to a nominal gas velocity in the chamber of 0.99 ft/sec.

An AccuRate dry material feeder and an educator were used to feed ash into the inlet piping upstream of the ESP or the pulse-jet baghouse. A concern with using a dry material feeder was the ability to redisperse the ash into its original size distribution or into the submicron region. It was expected that submicron particles would not readily redisperse. However, results indicated that significant amounts of submicron particles in the ashes were redispersed, but not completely to their original size distributions.

In order to determine the effect of ash layer thicknesses on redispersion, ash was injected upstream of the ESP for 15 minutes or one hour before cleaning. Inlet sampling with a TSI model 3934 scanning mobility particle sizer (SMPS), a TSI model 33 aerodynamic particle sizer (APS), and a TSI model 3022A condensation particle counter (CPC) was completed during the 1-hr loading tests. Figure 1 is a diagram of the sampling system. When the plate loading was completed, the ash feed was turned off. The induced-draft fan remained on for approximately three minutes to clear any ash remaining in the inlet piping. After the induced-draft fan was shut off, the ESP field was turned off. Ash that was not collected on the ESP plate, but fell to the hopper, was removed and weighed prior to ESP rapping. The ESP field was activated after this to remove any particulate that was reentrained when the hopper valve was opened. With the ESP current off, a sample probe was inserted into the chamber just below the plate. When the ESP was rapped, most of the ash dropped to the hopper, but some was redispersed and suspended in the ESP chamber. It was the redispersed ash that was sampled. The SMPS sampled for 90 seconds immediately after the ESP plate was cleaned in order to determine the submicron size distribution. The APS sampled the redispersed ash for ten seconds immediately after the ESP plate cleaning, and the CPC sampled every two seconds throughout the cleaning process. The loaded ESP plate weight, after rap plate weight, hopper ash weight, weight of ash remaining in the inlet pipes, and weight of ash fed were recorded to determine an ash balance.

The size distributions of the injected ash and the ash redispersed upon cleaning the ESP plate were characterized by an SMPS, an APS, and a CPC. The SMPS system measures the number size distribution of particles using an electrical mobility detection technique. The SMPS uses a bipolar charger in the electrostatic classifier to charge particles to a known charge distribution. The particles are then classified according to

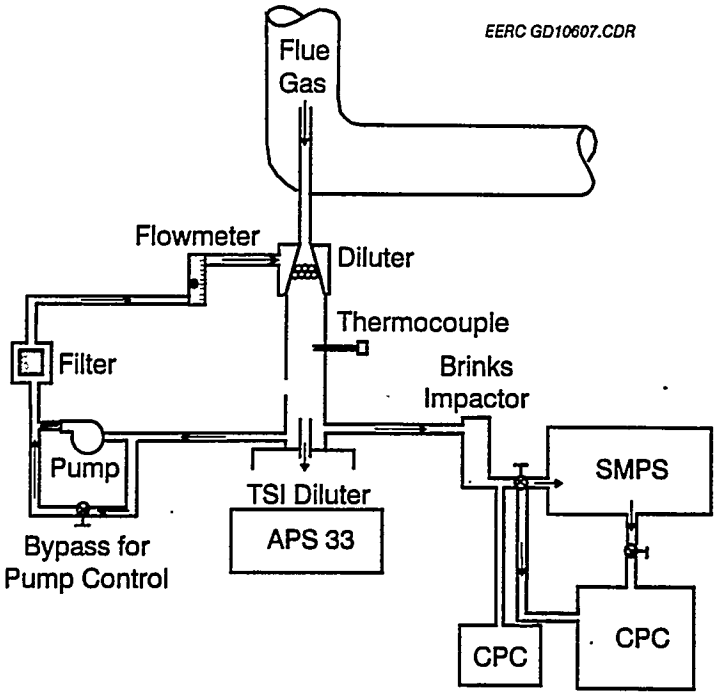

Figure 1. Schematic of particulate sampling equipment.

their ability to traverse an electrical field and counted with a CPC. The SMPS is capable of determining the size distribution of the fine particles from 0.01 μm to 1.0 μm in 90 seconds. The APS is a laser particle sizer used to characterize particles in the 0.5-μm to 30-μm range. The APS also measures respirable mass, which is defined by the American Council of Governmental and Industrial Hygienists as a weighted sum of particles between 1 and 10 μm, with greater weighting given to the smaller particles. A CPC separate from an electrostatic classifier was used for continuous on-line monitoring of the total concentration of particles from 0.01 μm to 4 μm. The particles entering the CPC are detected and counted by an optical detector after a supersaturated vapor condenses onto the particles, causing them to grow into larger droplets. The range of detection is from less than 0.007 particles/cm^3 to 9.99 $\times$ 10^6 particles/cm^3. From the data, it was possible to determine the size distribution of the injected ash and compare it to the size distribution of the original ash. Also, the size distribution of the redispersed ash was compared to the size distribution of the injected ash to determine the level of redispersion when the ESP plate was cleaned.

Video equipment was used to record some on-line operation of the ESP and the plate cleaning for each test condition. The video record was intended to provide qualitative information on the amount of material collected on the plate, the amount of material removed during the cleaning process, and the amount of ash reentrained during the cleaning process.

5.0 ACCOMPLISHMENTS/RESULTS

Hopper ash samples were submitted for Coulter counter analysis, and multicyclone samples were taken at the inlet of the pulse-jet baghouse for each ash. To determine a complete size distribution of the injected ash, the Coulter counter data and the multicyclone data were combined and plotted. The Coulter counter data, which are based on geometric particle diameter, were converted to aerodynamic particle diameter. The Coulter counter data were then normalized to include the multicyclone data, assuming the multicyclone data provides an absolute mass distribution for the smaller particles and the Coulter counter ignores particles smaller than a certain minimum size. Figures 2–5 present the combined Coulter counter/multicyclone inlet size distributions for each ash. The data are plotted on a log-probability plot because the size distribution is expected to follow a log-normal distribution, which is represented by a straight line on the log-probability plot. From the figures, it can be seen that the multicyclone and coulter Counter data do not agree exactly: the injected ash did not redisperse to completely its original size distribution. However, the agreement is fairly close, indicating a reasonable level of redispersions. Figure 6 plots the multicyclone distribution for each ash. The ashes were expected to redisperse into different distributions because they should each have somewhat different cohesive properties. However, there was little difference between the injected ashes which may be a limitation of the ash injection system. Multicyclone data for the original Big Brown ash were available, and Figure 7 plots the original multicyclone size distribution and the size distribution of the injected Big Brown ash. As expected the injected ash was not redispersed completely into its original size distribution, but there was a significant amount of ash redispersed into the submicron range.

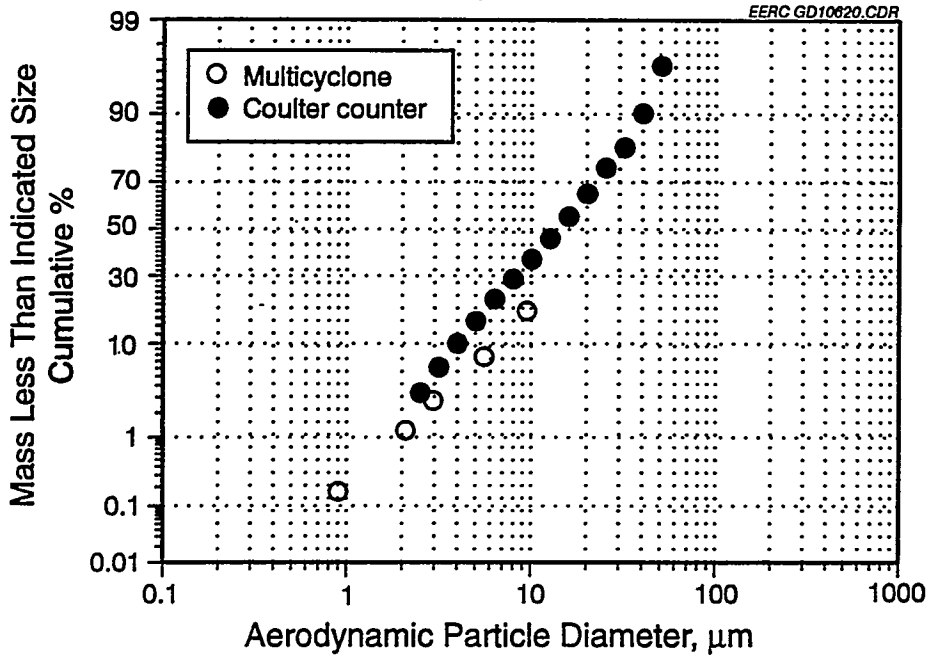

Figure 2. Combined multicyclone/Coulter counter size distribution for Absaloka ash.

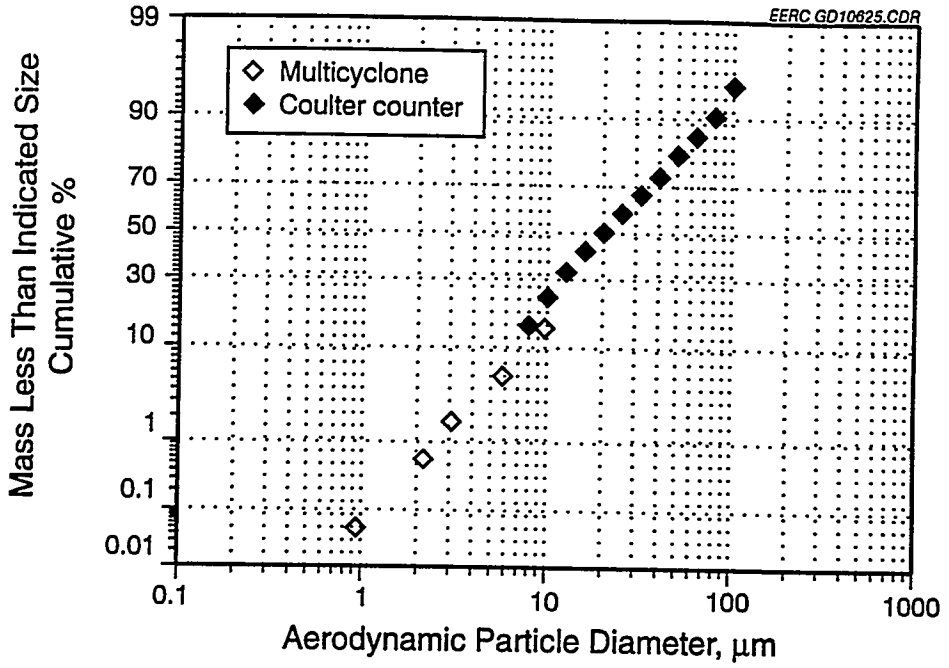

Figure 3. Combined multicyclone/Coulter counter size distribution for conditioned Big Brown ash.

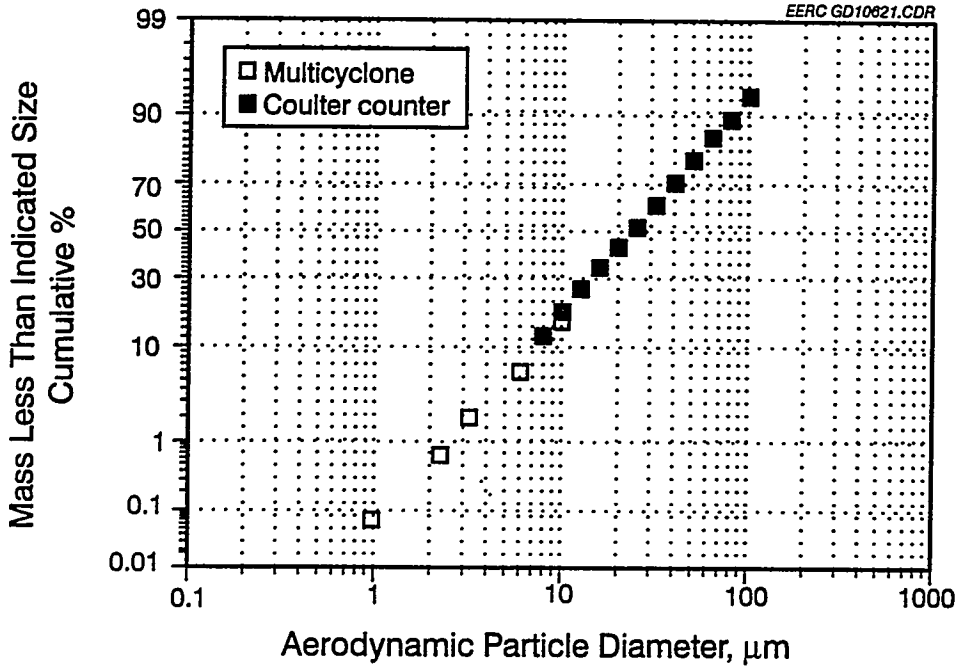

Figure 4. Combined multicyclone/Coulter counter size distribution for Big Brown Ash.

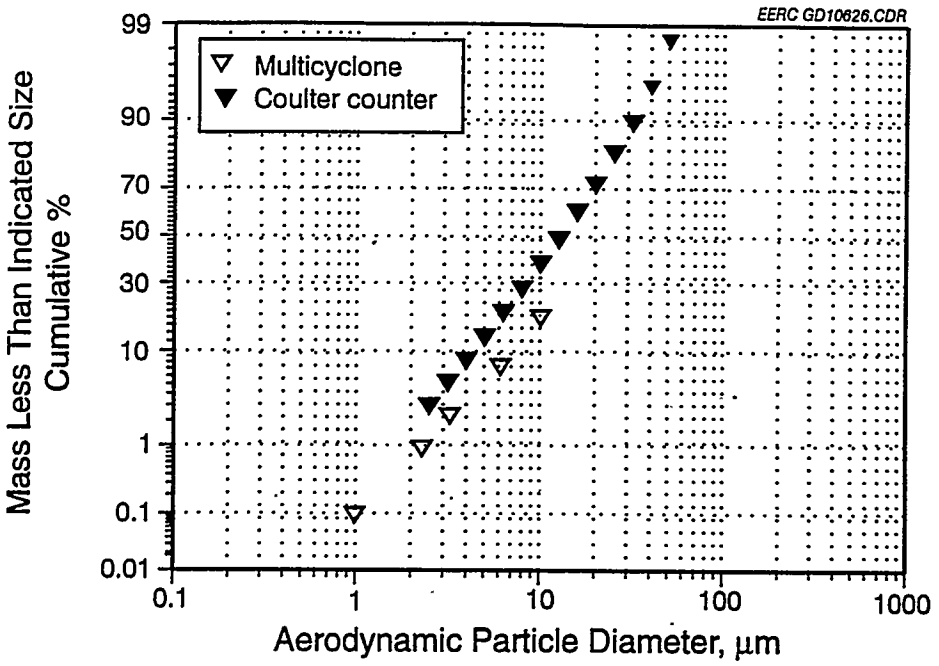

Figure 5. Combined multicyclone/Coulter counter size distribution for Blacksville ash.

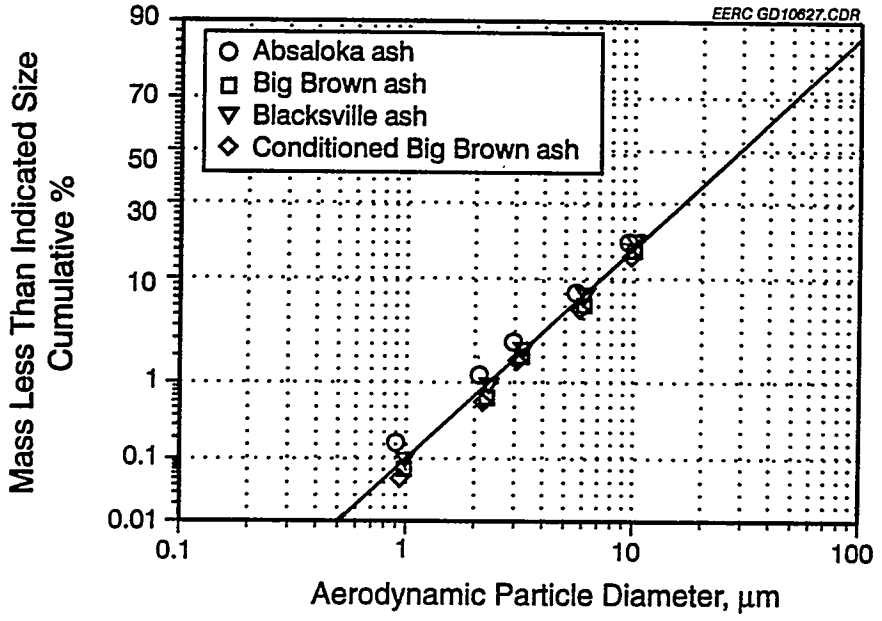

Figure 6. Multicyclone data for all ashes.

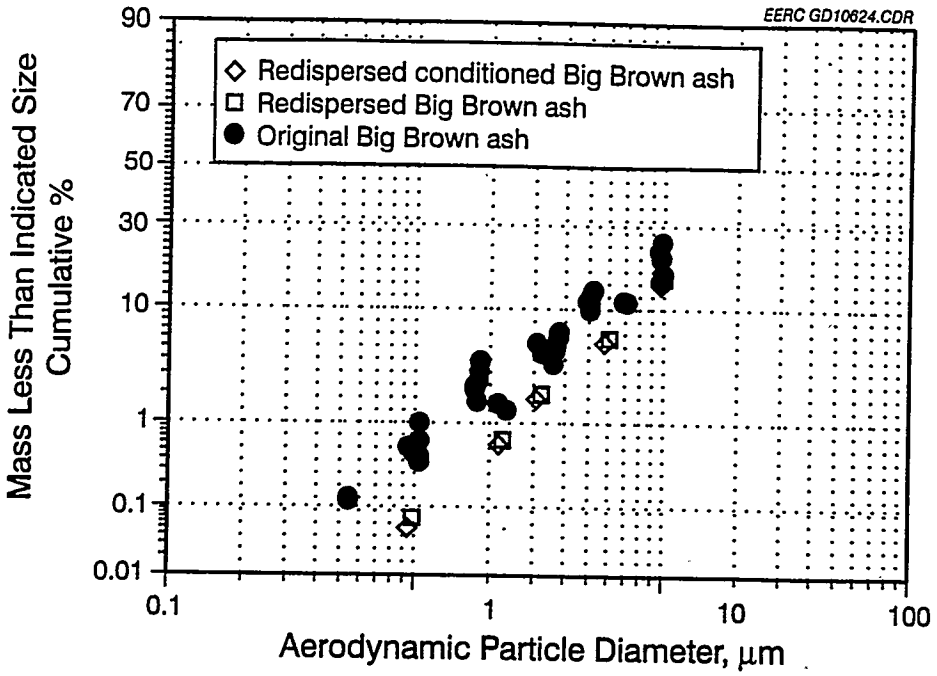

Figure 7. Multicyclone data for original and redispersed Big Brown Ash.

Table 3 presents the mass balance data for each test. The percent of the collected mass removed from the plate was fairly constant from ash to ash and for each loading condition. This may be a function of the cleaning energy. With a higher cleaning energy, perhaps a larger percent of the collected ash would be removed from the plate. However, the percent of ash fed that actually was collected on the plate was different for the two loading conditions. When the ESP plate was loaded for 15 minutes, most of the ash was retained on the plate, 90%–97%, and when the plate was loaded for 1 hour, only 36%–44% of the ash fed was retained on the plate. This indicates that during the 1-hr loading tests, some of the ash dropped from the ESP plate before it was cleaned. This affected the amount of ash available for reentrainment when the ESP plate was cleaned. The values for the Big Brown ash were reversed, 62% for the 15-min loading and 85% for the one 1-hr loading. The effect of ash type will be determined when cohesive strength data are available for each ash.

In order to determine the extent of the ash redispersed when the ESP plate was cleaned, the data were plotted a number of ways. Figures 8–15 present the combined SMPS and APS size distributions for the inlet ash and the ash immediately after cleaning the ESP plate, on a log-probability plot. The figures include data from the SMPS and APS, but do not represent the entire size distribution. Particles less than approximately 0.03 μm and larger than approximately 15 μm are not included. However, for the purpose of comparison, the figures are useful. The size distributions for each ash are similar, and it appears the ash type had little effect on the size distribution of the injected ashes. This was somewhat expected, since the injected ashes had similar inlet size distributions, based on the multicyclone data. Until cohesive data for each ash are available, no further conclusions can be made about the effect of ash type. It appears that the ash layer

TABLE 3

Mass Balance Data

Date	Coal Run No.	Ash Type	Relative Humidity, %	Ash Collection Time, min	Ash Fed, lb	Hopper Ash Weight		End-of-Test Ash Weight		% Ash Fed Collected	% Collected Ash Removed After 1 Rap
						Before Rap, lb	After 1 Rap, lb	Inlet Piping, lb	ESP, lb		
04/27/94	AB-445	Absaloka	11	15	1.7	0.10	1.20	0.07	0.38	96.9	75.9
04/27/94	BB-386	Big Brown (baseline)	14	15	1.75	0.08	0.81	0.07	0.23	61.9	77.9
04/28/94	BB-386	Big Brown (baseline)	14	60	6.6	0.92	4.46	0.07	1.10	85.1	80.2
04/28/94	AB-445	Absaloka	14	60	6.25	3.66	1.86	0.02	0.73	4 1.6	71.8
04/29/94	BB-384	Big Brown (conditioned)	14	60	7.45	4.16	2.06	0.02	0.60	35.8	77.4
04/29/94	BB-384	Big Brown (conditioned)	16	15	1.8	0.28	1.15	0.13	0.36	90.4	76.2
06/02/94	BV-473	Blacksville	19	60	6.6	2.48	2.33	0.36	0.41	43.9	85.0
06/13/94	BV-473	Blacksville	41	15	1.35	0.00	0.82	0.15	0.32	95.0	71.9

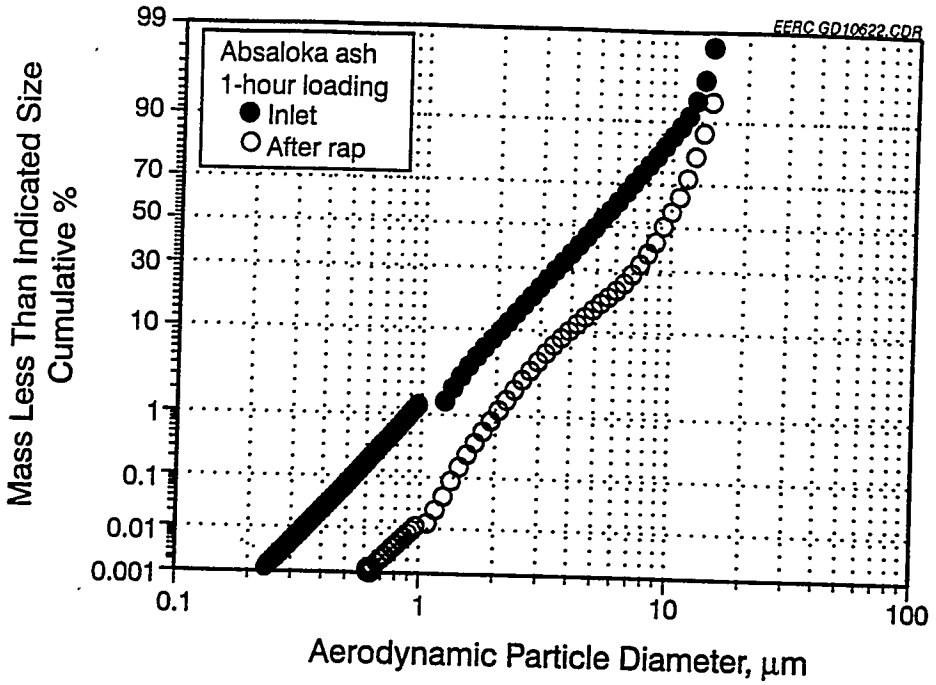

Figure 8. Combined inlet and after-ESP-cleaning SMPS/APS size distributions for Absaloka ash, 1-hr loading.

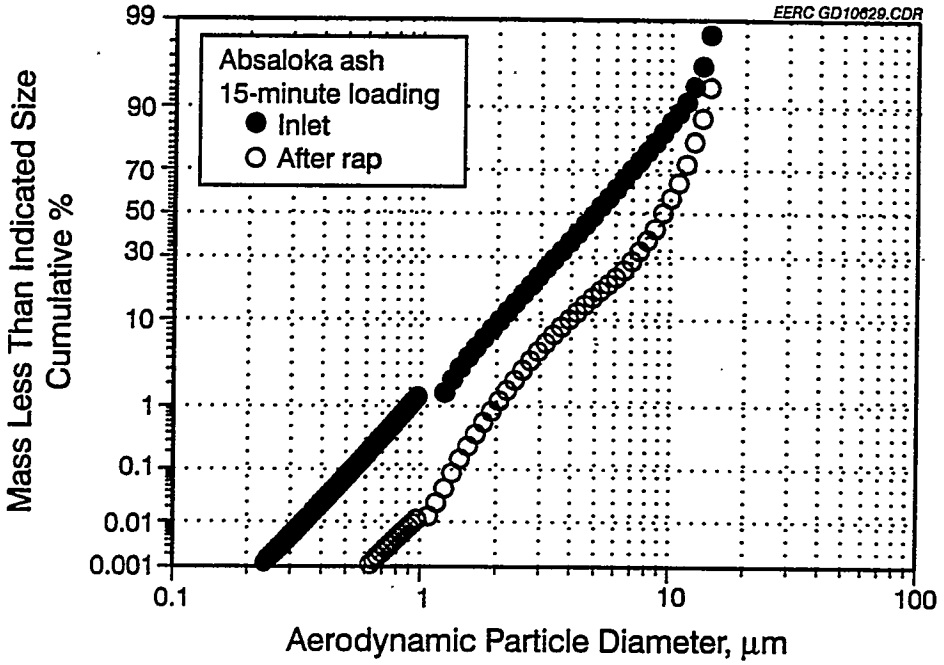

Figure 9. Combined inlet and after-ESP-cleaning SMPS/APS size distributions for Absaloka ash, 15-min loading.

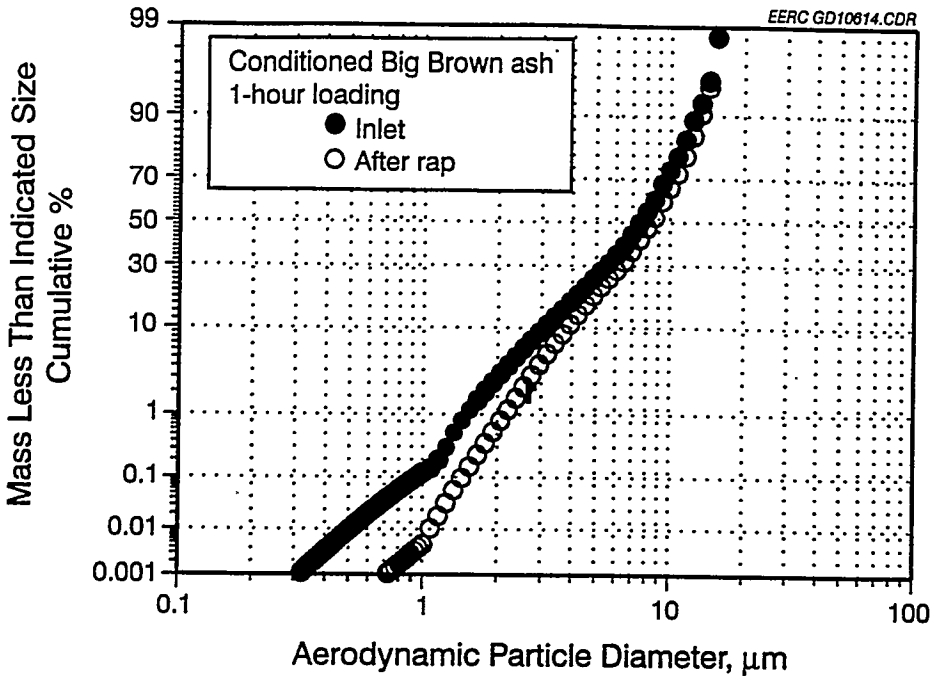

Figure 10. Combined inlet and after-ESP-cleaning SMPS/APS size distributions for conditioned Big Brown ash, 1-hr loading.

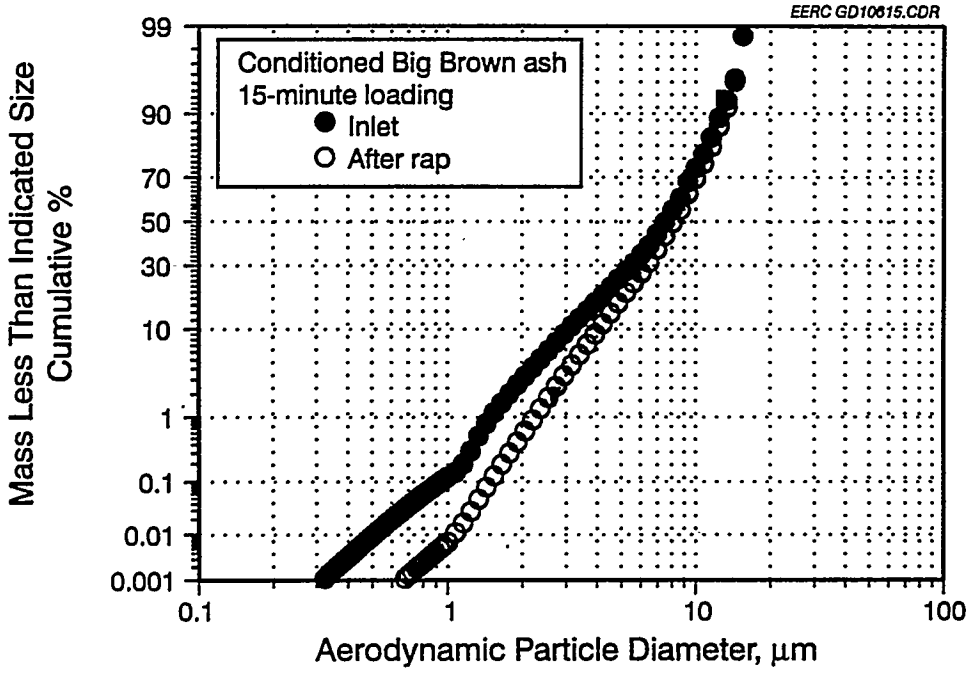

Figure 11. Combined inlet and after-ESP-cleaning SMPS/APS size distributions for conditioned Big Brown ash, 15-min loading.

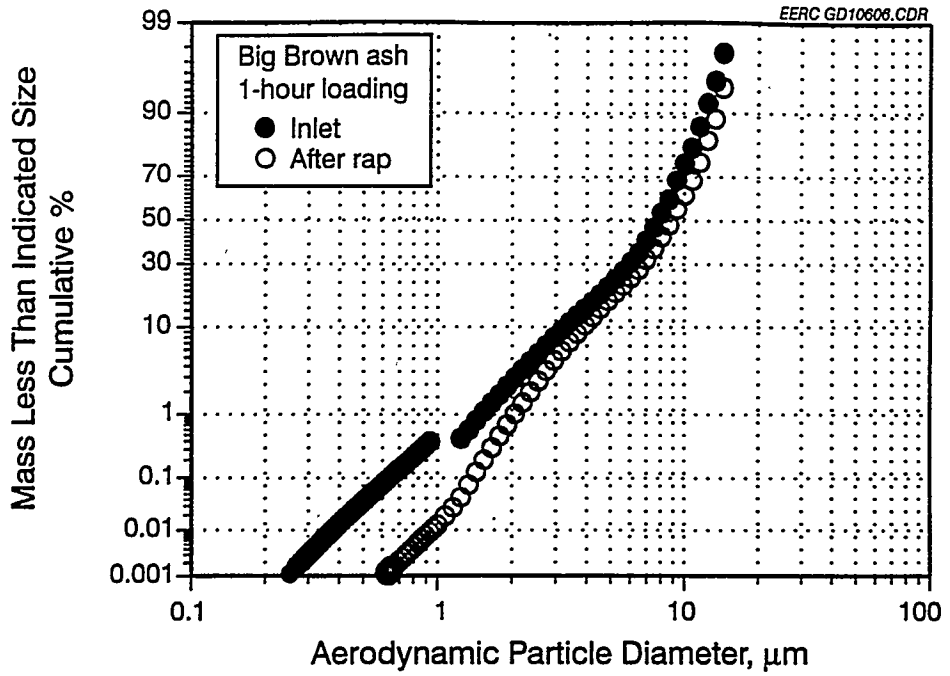

Figure 12. Combined inlet and after-ESP-cleaning SMPS/APS size distributions for Big Brown ash, 1-hr loading.

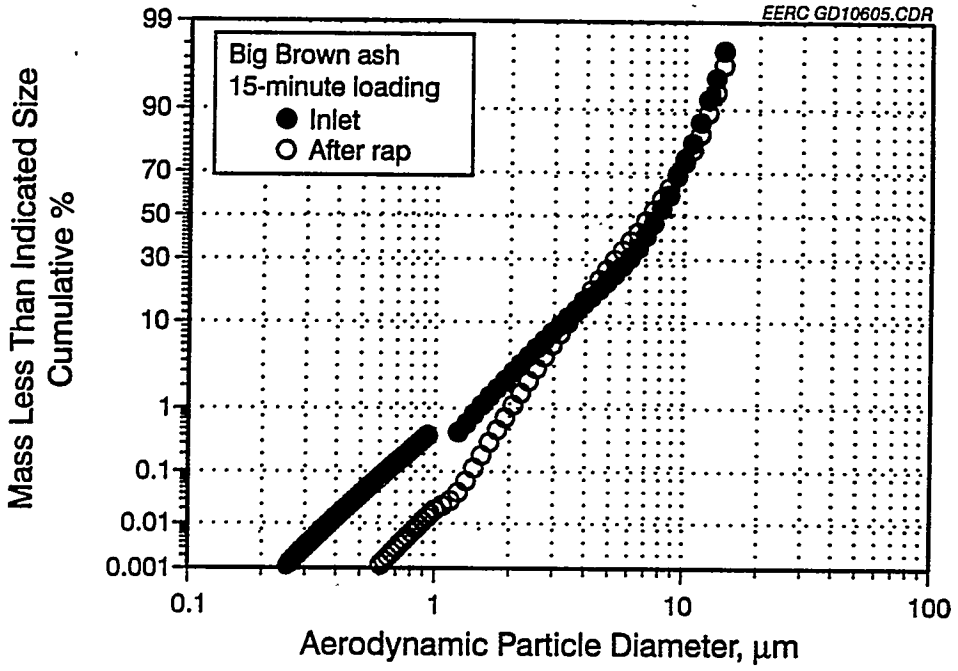

Figure 13. Combined inlet and after-ESP-cleaning SMPS/APS size distributions for Big Brown ash, 15-min loading.

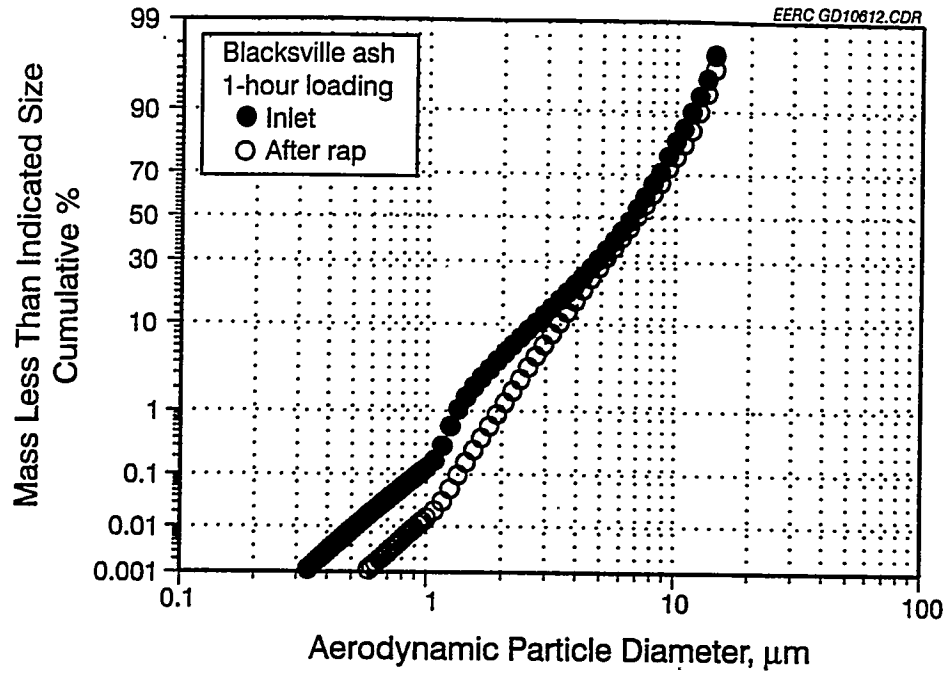

Figure 14. Combined inlet and after-ESP-cleaning SMPS/APS size distributions for Blacksville ash, 1-hr loading.

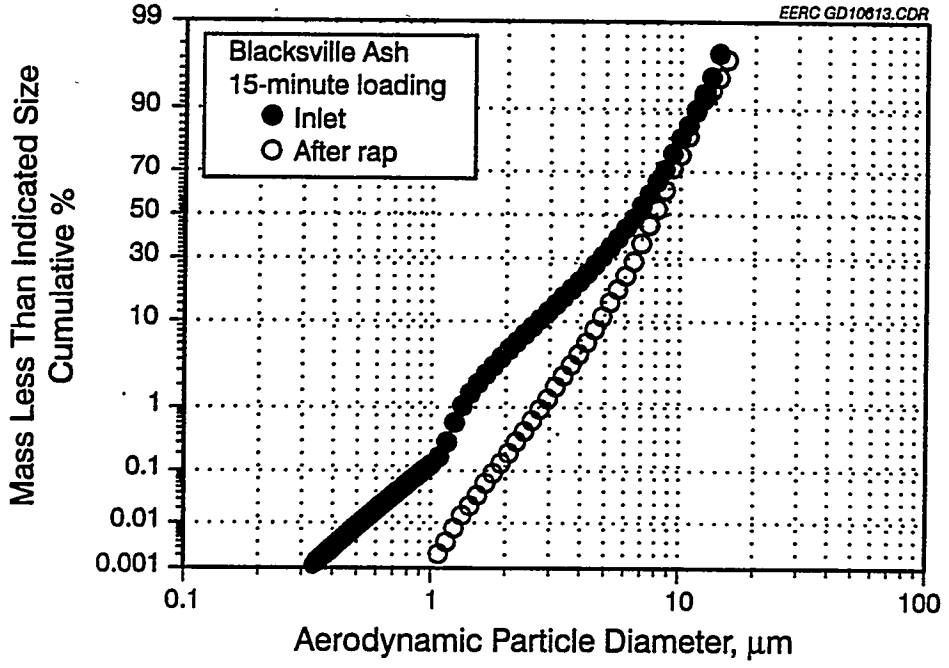

Figure 15. Combined inlet and after-ESP-cleaning SMPS\APS size distributions for Blacksville ash, 15-min loading.

thickness affects the size distribution of the reentrained ash. A thicker ash layer redisperses into a larger size distribution. The size distribution of the ash redispersed after the ESP plate was loaded for 15 minutes is larger than the inlet size distribution, but smaller than the size distribution for the 1-hr loading test.

The data from the SMPS, APS, and CPC were used to compare the particle concentrations of the inlet ash and the ash reentrained when the ESP plate was cleaned. The mass median diameter, total mass, and respirable mass, as determined by the APS for each inlet sample and after cleaning the ESP plate for each test are presented in Table 4. The average inlet concentration and the peak concentration after cleaning the ESP plate based on the CPC data is also presented. These values do not represent the entire size distribution, but they are representative and can be used for comparison. The mass median diameter data indicate the ash (after 1-hr loading) is redispersed to a larger size distribution than the inlet particle distribution. The mass median data for the 15-min loading of the ESP plate indicate that the ash is redispersed approximately into its original (inlet) size distribution. The total and respirable mass data show the effect of ash layer thickness on redispersion. As expected, more mass is redispersed from the thicker ash layer (1-hr loading). The exception was the Big Brown ash conditioned with NH_3 and SO_3, which showed no effect. The CPC data indicate that ash type affects the total concentration of particles 4.25 μm and smaller, but the effect of ash type cannot be completely determined without cohesive strength data.

Figures 16–23 plot the ratio of after-ESP-plate-cleaning particle concentration to inlet particle concentration for each test condition, based on the combined SMPS/APS data. Again, this does not represent the entire size distribution, but it is useful for comparison purposes. If the after-rapping particle distribution was exactly the same as the inlet particle-size distribution (PSD), the plate would be a straight horizontal line at 100%. For all but the 1-hr loading of the Blacksville ash, the concentrations of the redispersed submicron particles were lower than the inlet concentrations, while the concentrations of the particles larger than 1 μm were greater than the inlet concentration. This indicates the ash was redispersed upon ESP plate cleaning as larger particles, which are easier to recollect and less likely to be carried out the stack. Again, the effect of the ash layer thickness is evident for all but the conditioned Big Brown ash. Also evident from the plots, the overall concentration of particles increases with increasing ash layer thickness. The effect of the ash layer thickness is most pronounced for the Absaloka and Blacksville ashes.

Figure 24 plots the ratio of after-ESP-plate-cleaning particle concentration to inlet particle concentration as a function of time for the 1-hr loading of the Absaloka ash. Only APS data were used, because the APS sampled approximately once every ten seconds and the SMPS sampled once every 90 seconds. The main effect observed is the dilution of the ash cloud in the ESP chamber with time. To a smaller extent, the setting effect of larger particles is observed. The settling velocity of a 10-μm particle (unit density sphere) is approximately 0.3 cm/sec, and the settling velocity of a 1-μm particle is approximately 0.0035 cm/sec. The difference in settling velocities is almost two orders of magnitude. Therefore, if there is a unit change in the concentration of the 1-μm particles there should be a two orders of magnitude change in the concentration of the 10-μm particles. With increasing time the shape of the curve would change, with the ratio of the larger particles dropping off quickly and the concentration ratio of the smaller particles remaining high. The final curve might resemble an exponential decay. Instead, the plot shows an almost

TABLE 4

APS and CPC Statistical Data

Ash	Inlet Average				1-Hr Loading				15-Min Loading			
	Mass Median Diameter, μm	Total Mass, mg/m^3	Respirable Mass, mg/m^3	CPC Concentration, part./cm^3	Mass Median Diameter, μm	Total Mass, mg/m^3	Respirable Mass, mg/m^3	CPC Concentration, part./cm^3	Mass Median Diameter, μm	Total Mass, mg/m^3	Respirable Mass, mg/m^3	CPC Concentration, part./cm^3
Absaloka	5.00	7727	1363	365,000	9.28	121,000	14,140	271,791	7.16	38,710	---	90,194
Big Brown Conditioned	7.60	5922	1089	498,000	8.36	80,200	10,920	90,345	8.11	83,700	10,780	95,871
Big Brown	7.81	4169	690	193,000	8.84	107,000	13,500	194,304	7.22	24,600	4,414	98,481
Blacksville	6.62	5714	1407	524,000	6.88	39,100	7,467	88,071	8.05	5,480	561	35,280

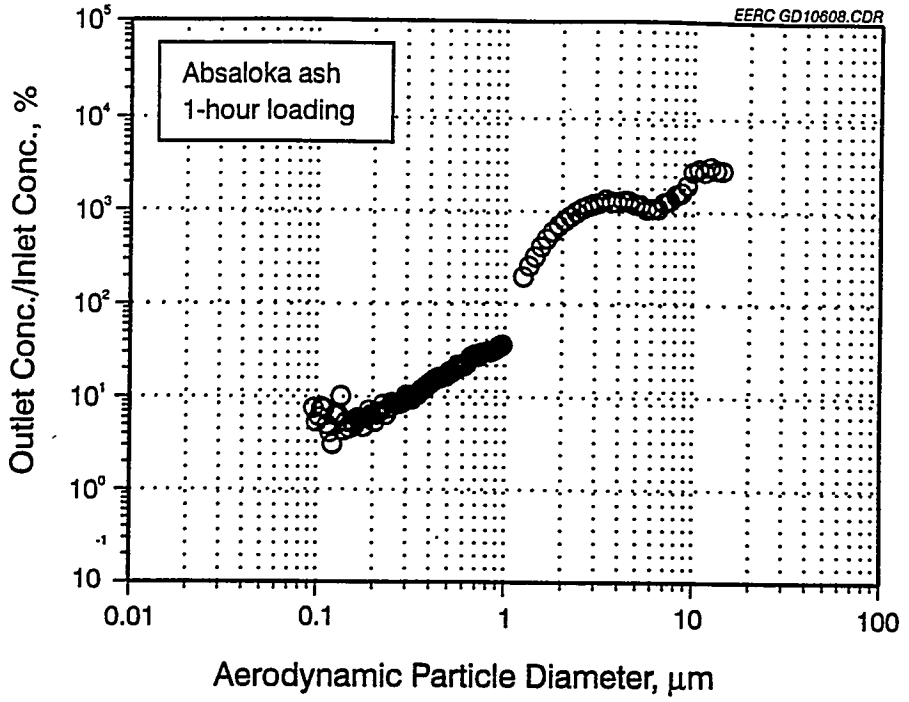

Figure 16. Ratio of after-ESP-plate-cleaning concentration to inlet concentration, based on the combined SMPS/APS data, 1-hr loading, Absaloka ash.

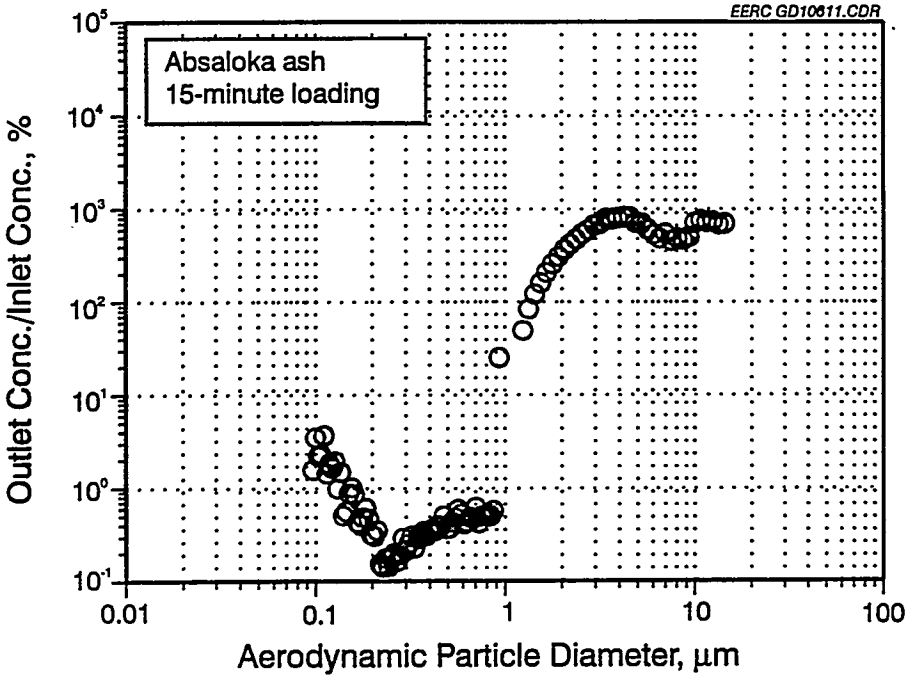

Figure 17. Ratio of after-ESP-plate-cleaning concentration to inlet concentration, based on the combined SMPS/APS data, 15-min loading, Absaloka ash.

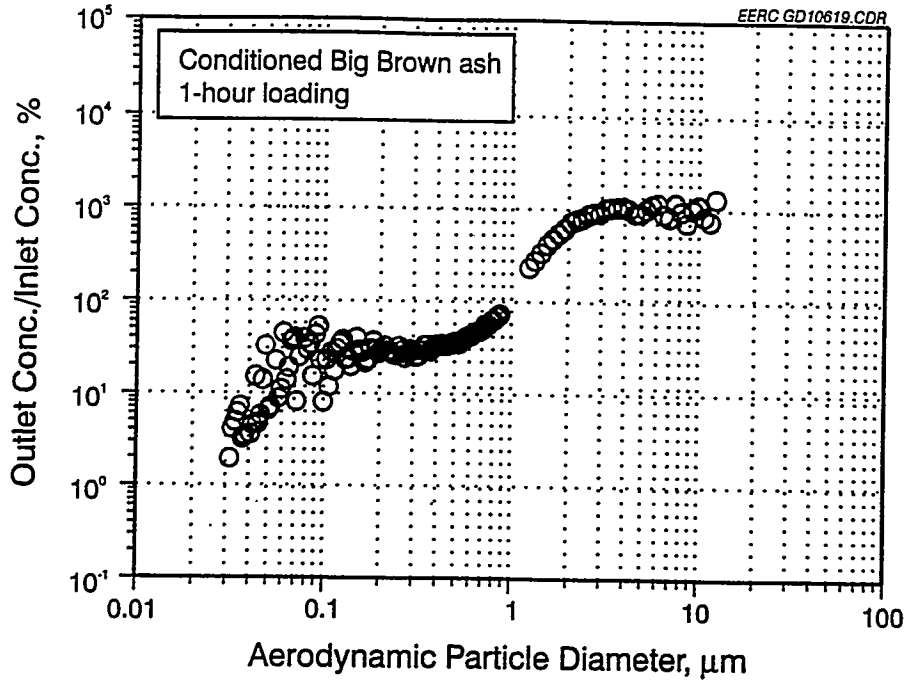

Figure 18. Ratio of after-ESP-plate-cleaning concentration to inlet concentration, based on the combined SMPS/APS data, 1-hr loading, conditioned Big Brown ash.

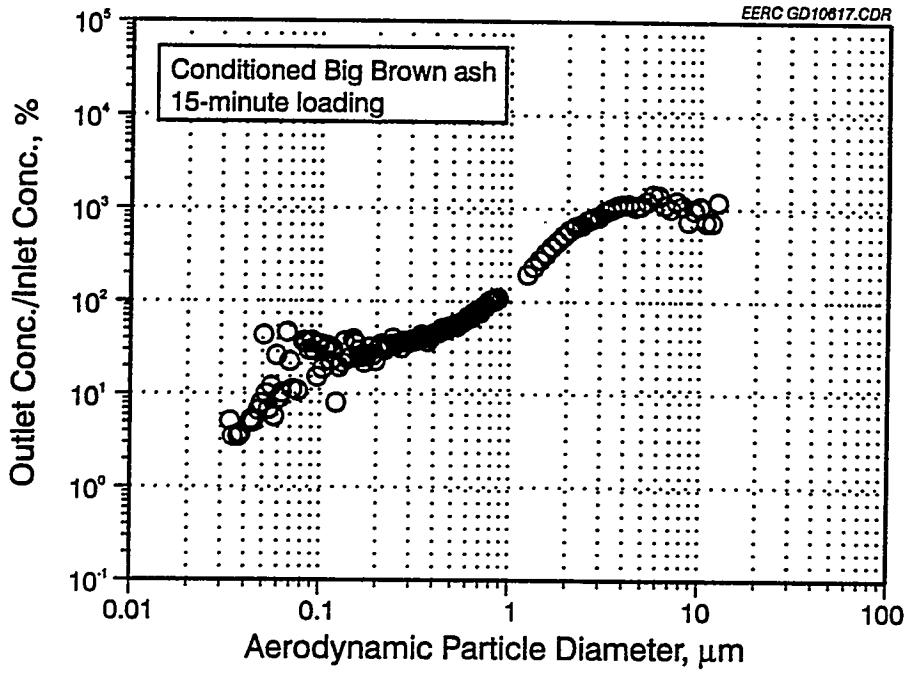

Figure 19. Ratio of after-ESP-plate-cleaning concentration to inlet concentration, based on the combined SMPS/APS data, 15-min loading, conditioned Big Brown ash.

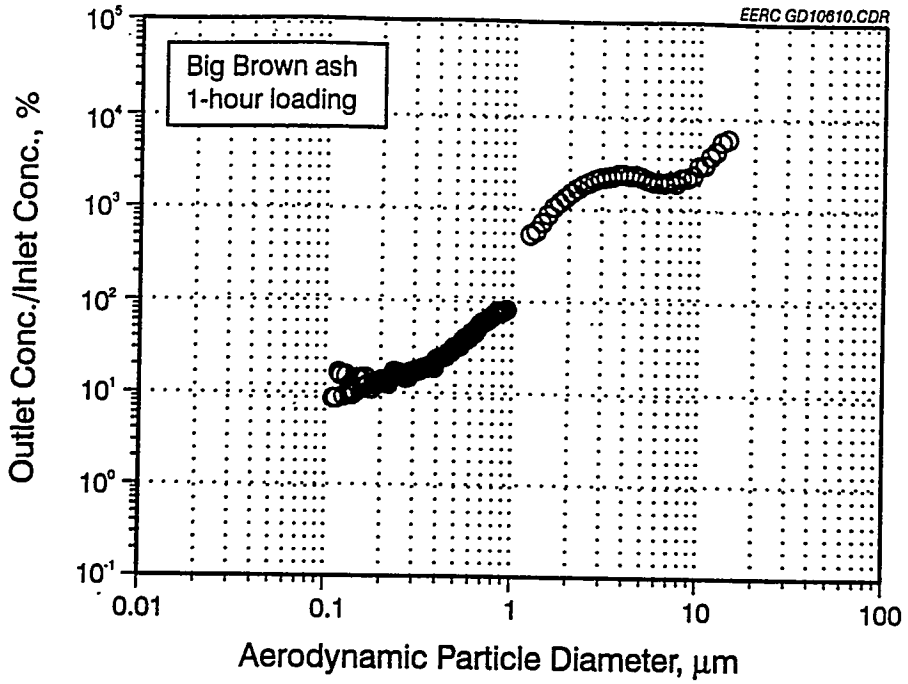

Figure 20. Ratio of after-ESP-plate-cleaning concentration to inlet concentration, based on the combined SMPS/APS data, 1-hr loading, Big Brown ash.

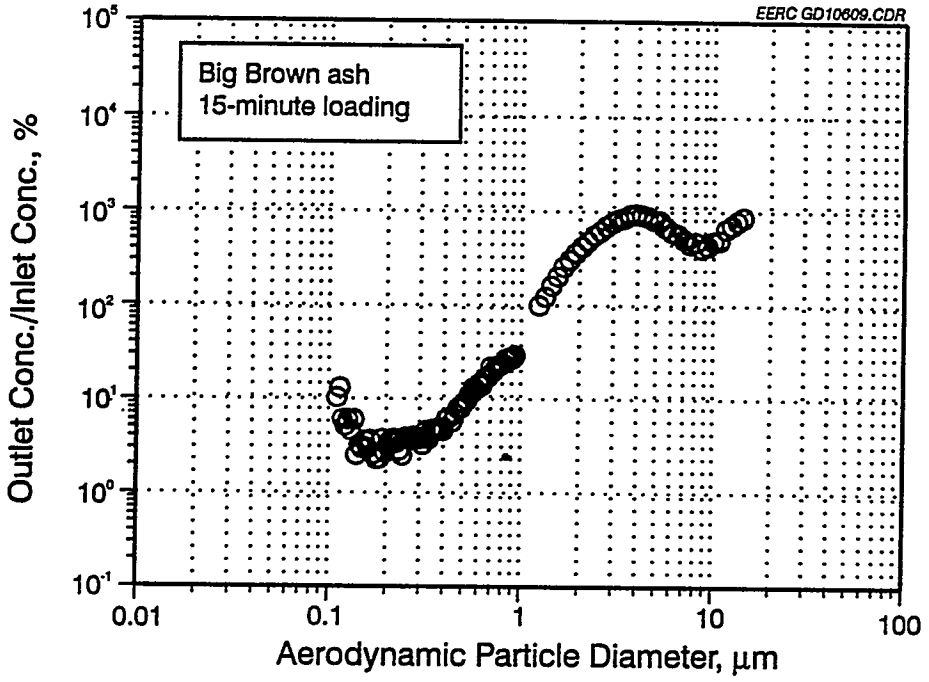

Figure 21. Ratio of after-ESP-plate-cleaning concentration to inlet concentration, based on the combined SMPS/APS data, 15-min loading, Big Brown ash.

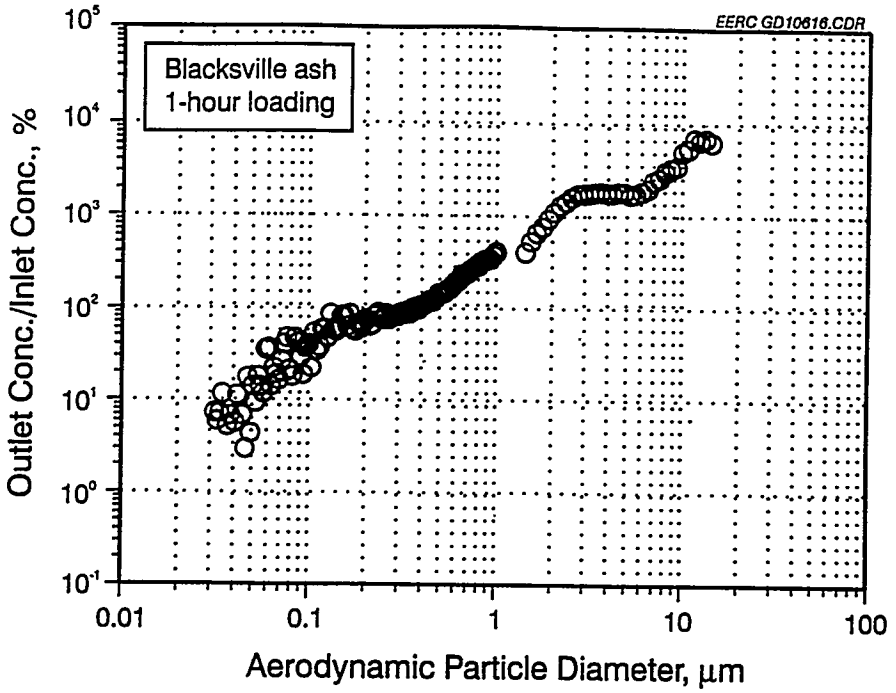

Figure 22. Ratio of after-ESP-plate-cleaning concentration to inlet concentration, based on the combined SMPS/APS data, 1-hr loading, Blacksville ash.

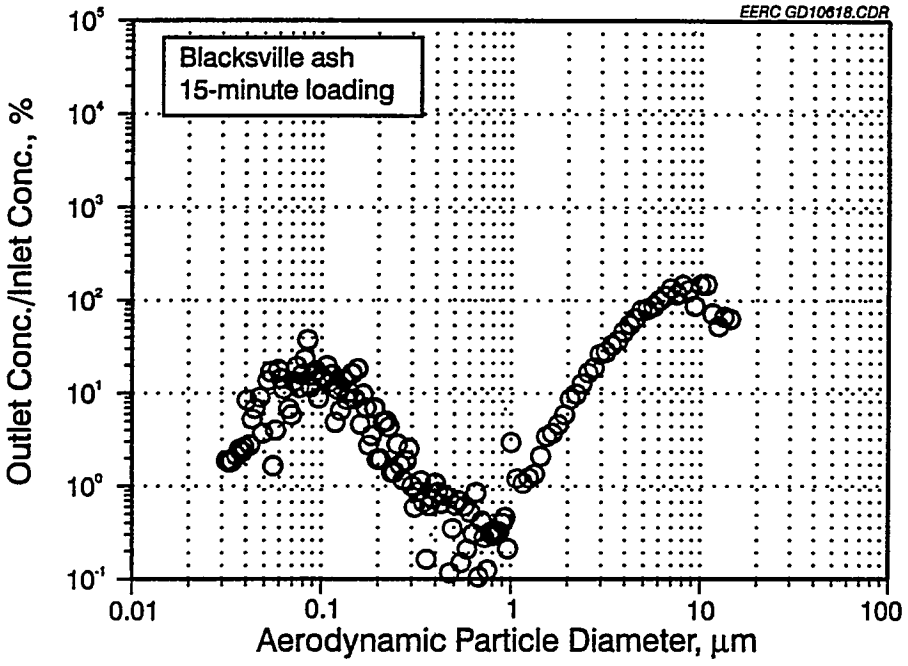

Figure 23. Ratio of after-ESP-plate-cleaning concentration to inlet concentration, based on the combined SMPS/APS data, 15-min loading, Blacksville ash.

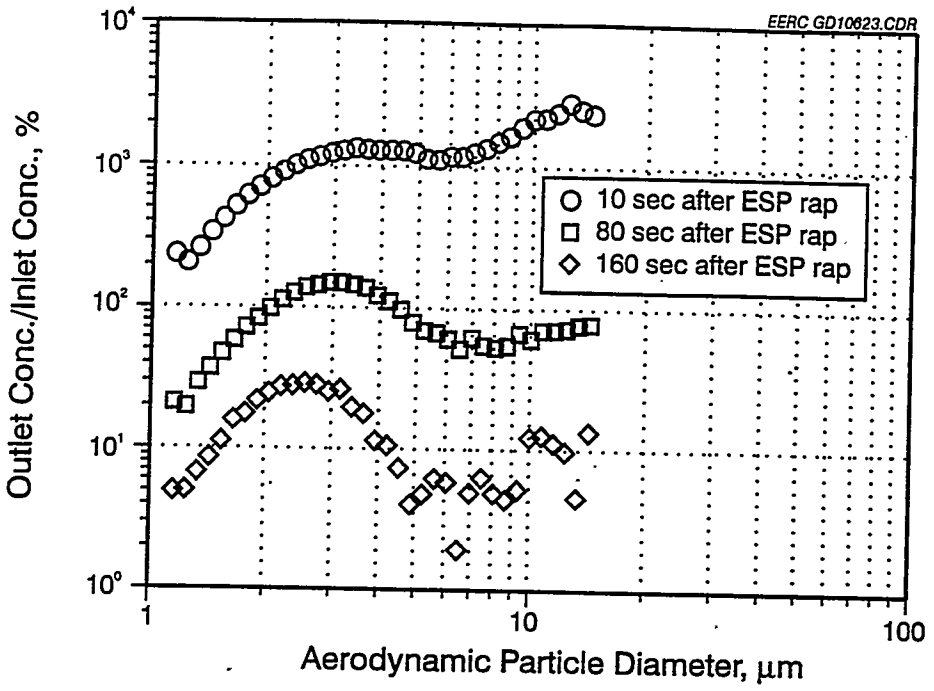

Figure 24. Ratio of after-ESP-plate-cleaning concentration to inlet concentration as a function of time, based on APS data, 1-hr loading, Absaloka ash.

equal drop in the concentration ratios for all particles. This is characteristic of the dust cloud becoming more dilute with time.

Video equipment was used to record the cleaning of the ESP plate. The video shows that ash was removed only from roughly the bottom third of the ESP plate. However, most of the ash that was removed fell to the hopper as large agglomerates. If the ESP had been on-line and there were airflow through the ESP (normal operating conditions) during plate cleaning, a certain amount of the large agglomerates that reached the hopper would have been redispersed by the airflow, increasing the amount of redispersed ash. The video also showed the ash cloud disperse and become more dilute shortly after the ESP plate was cleaned. This is consistent with the particle concentration data.

The pulse-jet baghouse tests were also completed during this reporting period. However, no data reduction has been performed at this time. Table 5 presents the completed pulse-jet test matrix.

From the data evaluated to this point, it appears the injected ash was redispersed adequately to determine the level of ash reentrainment when a filter or an ESP plate is cleaned. The difference in size distribution relating to ash type was not as pronounced as expected. This may be a limitation of the ash injection system and will be explored further when cohesive data are available for each ash. The mass balance indicated the ash type and the ash layer thickness did not affect the percent of the collected ash

TABLE 5

Pulse-Jet Fabric Filter Reentrainment Test Matrix

Date	Coal Run No.	Ash Type	Relative Humidity, %	Fabric	Nominal Pressure Drop, in. H_2O	Cleaning Energy, psig
6/21/94	AB-445	Absaloka	35	Ryton	7	20
6/22/94	AB-445	Absaloka	59	Ryton	7	60
6/22/94	AB-445	Absaloka	54	Ryton	2	20
6/22/94	AB-445	Absaloka	55	Ryton	2	60
6/23/94	BB-386	Big Brown (baseline)	55	Ryton	7	60
6/23/94	BB-386	Big Brown (baseline)	36	Ryton	7	20
6/24/94	BV-473	Blacksville	50	Ryton	7	20
6/24/94	BV-473	Blacksville	45	Ryton	7	60
7/06/94	BB-384	Big Brown	47	Ryton	7	20
7/06/94	BB-384	Big Brown	50	Ryton	7	60

removed from the plate during cleaning. It is expected that this is a function of the cleaning energy. The percent of ash fed retained on the plate was different for the two loading conditions. A shorter loading time would be adequate to develop a maximum ash layer thickness. It is unclear at this time if there was any effect as a result of ash type. Based on the combined SMPS/APS size distributions, ash type had little or no effect on the size distribution of the redispersed ash. Based on the same data, when the ESP plate after loading for 1 hour, the ash redispersed into a size distribution larger than the inlet ash. The concentration data show the same effect caused by ash layer thickness. Increasing the ash layer thickness increased the amount of ash redispersed. There may be an effect on particle concentration related to ash type, but until cohesive strength data is available, no conclusions can be made. Plotting the ratio of after-ESP-plate-cleaning particle concentration to inlet particle concentration showed the concentration of the redispersed submicron particles was less than the concentration of the inlet particles. This also indicates the ash is redispersed to a larger size distribution.

Video recordings of the ESP plate cleaning showed most of the ash removed from the ESP plate reached the hopper as large agglomerates. The video also showed the dilution of the dust cloud with time.

Future work will include data reduction and interpretation of the pulse-jet baghouse test results. The tests with the CeraMem® filters will be completed along with data reduction and interpretation.

TASK 2.5

EFFECTIVENESS OF SORBENTS FOR TRACE ELEMENTS

Prepared by:

Brian C. Young
Mark A. Musich

August 1994

TABLE OF CONTENTS

TASK 2.5 EFFECTIVENESS OF SORBENTS FOR TRACE ELEMENTS

1.0 INTRODUCTION/OBJECTIVES

Significant quantities of trace elements are emitted to the atmosphere each year as a result of the large volumes of coal used in combustion and gasification processes as well as from other industrial and commercial operations such as the waste incineration and chlorine and alkali production (1). Owing to their potentially harmful effects on the ecosystem, eleven trace elements have been identified for control action under the 1990 Clean Air Act Amendments. These elements are beryllium, chromium, manganese, cobalt, nickel, arsenic, selenium, cadmium, antimony, lead, and mercury. Although appearing as trace species, arsenic, selenium, and mercury are of particular concern, since they can occur in gaseous or submicron fume form; consequently, substantial amounts can pass through the conventional collection devices such as precipitators and baghouses.

Current trace element collection strategies focus on sorbents as a collection method. The sorbents generally consist of a large volume of inexpensive, disposable activated coke or char with modest sorption activity. An alternative approach is to use innovative technology to produce a regenerable sorbent material with enhanced sorption characteristics, from which trace metals are recovered.

Following the release of trace metals such as arsenic, selenium, and mercury from coal combustion and gasification, homogeneous and heterogeneous reactions can occur (2). Identifying and controlling these reactions are important in determining the effectiveness of sorbents to capture particular species, for example, metallic mercury and mercuric chloride. Activated carbon, alone and impregnated with sulfur or iodide, has been used as a capture sorbent. However, mercury in the presence of oxygen at elevated temperatures ($<500°C$) may form mercuric oxide, thus lessening the effectiveness of carbon as a capture agent. Other gases such as carbon monoxide, nitrogen dioxide, and sulfur dioxide have the potential to interfere also with the effective sorption of mercury species. In addition to activated carbon, fly ash has also been implicated in mercury reactions and mercury sorption (3, 4). Quantitative kinetic data regarding the sorption processes of trace elements in combustion and gasification gas streams are scarce and the sorption mechanisms not well understood. Hence, a research strategy to develop a basis for air quality control management of trace element emissions is timely.

The overall objective of the project is to identify the conditions for the most effective capture of trace elements by carbon sorbents and the controlling processes for trace element sorption in combustion and gasification systems. The specific objectives are as follows:

- To identify the parameters, including temperature, mercury species concentration, and flow rate in controlling the level of mercury sorption by activated carbons in a laminar flow combustion system.

- To identify the effects of various flue gas components, including oxygen, affecting mercury species sorption by carbon sorbents.

- To generate sorption kinetic data to assist in developing a preliminary understanding of the mechanism of mercury sorption by carbon-based materials.

2.0 ACCOMPLISHMENTS

During the previous quarter, a testing apparatus was constructed that will allow evaluation of select sorbents for removing elemental mercury and/or mercuric chloride from simulated utility or incinerator flue gas streams. Additionally, a tentative operating procedure and test matrix were established and shakedown testing was initiated.

2.1 Experimental Apparatus

Presently, the apparatus consists of five main subsystems: 1) flue gas generation, 2) mercury injection, 3) sorbent–flue gas contactor, 4) effluent gas analysis (with data logging), and 5) residual mercury scrubbing. Most of the components in contact with the mercury-laden gas are made of Teflon, glass, or quartz. The exception is the analyzer subsystem, which contains relatively short lengths of Tygon tubing; efforts continue to find a practical method for conversion to Teflon or glass tubing and connections. Additionally, all components downstream of the mercury injection point are heated to prevent mercury and water condensation.

The system is capable of generating a simulated flue gas containing N_2, O_2, CO_2, SO_2, HCl, NO_2, and water vapor, into which elemental mercury and mercuric chloride, as vapors, can be introduced. Permeation tubes, supplied by VICI Metronics, are presently being evaluated as a method to attain relatively precise mercury concentrations in the simulated flue gas.

An externally heated filter assembly, of the type typically used for in-stack particulate sampling, is being evaluated as a sorbent bed containment device. The interior of the assembly, including filter support grid, is Teflon-coated. A novel procedure, employing a vacuum, has been developed to deposit a uniform layer of sorbent onto the quartz filter paper and support grid. The filter assembly will employ a downflow configuration to minimize entrainment of the powdered activated carbon sorbents.

Presently, a Buck Scientific Model 400 cold-vapor ultraviolet (253.7 nanometer) analyzer is being evaluated for continuous monitoring of the elemental mercury concentration in the filter effluent gas stream. Shakedown and calibration testing has shown that the measured mercury concentration is affected by variations in the flowing gas pressure. Consequently, considerable effort has been expended to minimize this effect; the result has been the implementation of equipment and methods for achieving identical gas sample pressure from test to test.

Two methods to record mercury concentration values from the cold-vapor analyzer will be used: 1) continuous monitoring with a chart recorder, and 2) logging to personal computer (PC) via a GWBasic program. Subsequent to testing, the data can be edited and then subjected, as appropriate, to uptake rate or capacity computations.

Residual elemental mercury or mercuric chloride will be scrubbed from the sorbent filter effluent gas using an EPA Method 29 impinger train or activated carbon final filter.

The procedures for glassware cleaning and storage, as previously established at the EERC, will be followed.

2.2 Experimental Procedure

Briefly, the experimental procedure to be implemented is as follows: The desired mass of sorbent will be charged to the filter assembly, after which the filter assembly and system tubing will be heated to the desired temperatures under flowing simulated flue gas conditions. The sweep gas containing the mercury species of interest from the permeation tube will be introduced into the bulk gas stream. The effluent gas from the filter assembly will be monitored for breakthrough (<100% mercury capture) and complete sorbent loading (0% mercury capture). From the PC-recorded data, the sorption kinetics will be ascertained at the nonequilibrium conditions. The sorbent and Method 29 impinger solution will be analyzed (via atomic absorption [AA] spectrophotometric methods) to quantify mercury adsorption and to allow mercury mass-balance determination.

2.3 Test Matrix

The test matrix for the assessment of carbon sorbents for mercury species has been finalized to include testing of five sorbents. The sorbents are 1) American Norit Darco FGD, a steam-activated lignite carbon, 2) American Norit Darco KB, a chemical-activated hardwood, 3) American Norit PC 100, a steam-activated bituminous coal, 4) Barneby & Sutcliffe Corp. CB, an iodized steam-activated coconut shell, and 5) Alcoa Mersorb LH, a sulfur-impregnated steam-activated carbon.

Additional test variables include mercury species (elemental mercury and mercuric chloride), mercury concentration (15, 50, and 100 $\mu g/m^3$), filter gas temperature (120° and 150°C), gas velocity (baseline = 12.5 cm/sec), O_2 concentration (3 and 7 vol%), and sorbent mass (0.02 to 0.25 g). Fixed test parameters include SO_2 concentration (575 ppm). Later testing will entail investigating the effect of NO_2 and HCl on sorbent utilization. Replicate tests will be performed periodically to assure confidence in the test results.

2.4 Preliminary Results

During shakedown testing, breakthrough curves have been obtained for elemental mercury vapor adsorbed onto a lignite-based carbon and a sulfur-impregnated carbon tested at 100 $\mu g/m^3$ mercury, 120°C, and 0.25 g sorbent in a N_2-only atmosphere. Although no conclusions can be advanced at this time, it was observed that breakthrough was instantaneous with both sorbents. Further, the lignite-based carbon attained full loading after approximately 30 minutes; in comparison, the sulfur-impregnated carbon showed much greater capacity for retaining mercury vapor and was still absorbing mercury after 70 minutes.

A paper entitled "Carbon Sorption of Trace Mercury Species" by Brian C. Young, Stanley J. Miller, and Dennis L. Laudal has been submitted and accepted for the Eleventh Annual International Pittsburgh Coal Conference in September, 1994.

3.0 FUTURE WORK

1. Equipment shakedown and calibration will be completed using elemental mercury in N_2.

2. The five sorbents will be tested at 150°C and 100 $\mu g/m^3$ elemental mercury or mercuric chloride in a simulated flue gas at 3 vol% O_2 and 575 ppm SO_2.

3. Methods for converting mercuric chloride to elemental mercury in the filter effluent stream to allow continuous concentration monitoring will be explored.

4. The best sorbent for elemental mercury and mercuric chloride sorption at the conditions in Item 2 above (except for temperature) will be tested at 120°C and 150°C, mercury concentrations of 15 and 50 $\mu g/m^3$, and at gas velocities ranging between 0.75 and 1.25 cm/sec.

5. Preliminary evaluations will be performed concerning the influence of HCl and NO_2 on sorbent efficacy.

6. Brian Young will present a paper at the Pittsburgh Coal Conference.

4.0 REFERENCES

1. Hutchinson, T.C.; Meema, K.M., Eds.; *Lead, Mercury, Cadmium, and Arsenic in the Environment*; J. Wiley: Chichester, 1987.

2. Hall, B.; Schager, P.; Lindquist, O. "Chemical Reactions of Mercury in Combustion Flue Gases," *Water, Air, and Soil Pollution*, **1991**, *56*, 3–14.

3. Hall, B.; Schager, P.; Weesma, J. "A Qualitative Study of Heterogeneous Reactions of Elemental Mercury on Activated Carbon and Fly Ash in the Presence of Oxygen," *Chemosphere*, 1994; in review.

4. Otani, Y.; Kanoaka, C.; Usui, C.; Matsui, S.; Hitoshi, E. "Adsorption of Mercury Vapor on Particles," *Environ. Sci. Techol.* **1986**, 20, 735–738, 1986.

TASK 2.6

CATALYST FOR UTILIZATION OF METHANE IN SELECTIVE CATALYTIC REDUCTION OF NO_x

Prepared by:

Edwin S. Olson

August 1994

TABLE OF CONTENTS

TASK 2.6 CATALYST FOR UTILIZATION OF METHANE IN SELECTIVE CATALYTIC REDUCTION OF NO_X

1.0 INTRODUCTION

The selective catalytic reduction (SCR) of NO_x in flue gas or engine exhaust gas with hydrocarbons as the reductant has great potential for less expense, less pollution, and easier operation than SCR with ammonia. Methane is the preferred reducing gas because of its low cost and low toxicity. Stable, low-cost catalysts for the SCR with methane are required to demonstrate this technology for controlling NO_x emissions.

2.0 OBJECTIVES

The objective of the proposed work is to demonstrate that catalysts consisting of metal ions impregnated on a clay or pillared clay support or on a highly stable composite carbon support are effective for SCR of NO_x.

3.0 ACCOMPLISHMENTS

Because of the late start date for the contract, work on this task has not been initiated.

A selection of clays and pillared clays will be exchanged or impregnated with metal ions or cluster ions, such as copper, cobalt, iron, titanium, zirconium, and cerium. Catalysts will be tested in a small fixed-bed flow reactor with a reaction gas consisting of 5000 ppm NO, 5000 ppm methane, and 5% oxygen in an inert carrier (He). Initial tests will be performed in a matrix of varying temperatures. Product gases will be analyzed by Fourier transform infrared spectroscopy (FT-IR) or gas chromatography. Some testing will be performed with catalysts that have been exposed to SO_2. Some of the catalysts may improve as a result of the superacidity generated by sulfating the metals (Fe, Ti, Zr). Other catalysts may be deactivated by conversion of metal ions to the sulfide during the reduction. Work in subsequent years will examine catalyst stability in greater detail, since problems with coking and loss of metal ions may occur.

Similar methane SCR tests will be performed with metal-loaded carbon composites produced in another project. These thermally stable carbon composites will consist of boron, silicon, or titanium carbide layers deposited or formed on the surface of a coal-derived char or carbon.

TASK 3.1

FUEL UTILIZATION PROPERTIES

Prepared by:

Kevin C. Galbreath
Chris J. Zygarlicke
Donald P. McCollor

TABLE OF CONTENTS

LIST OF FIGURES

LIST OF TABLES

ADVANCED POWER SYSTEMS
TASK 3.1 FUEL UTILIZATION PROPERTIES

INTRODUCTION

The mission of the U.S. Department of Energy (DOE) and the Energy & Environmental Research Center (EERC) Cooperative Agreement is to promote the clean and efficient use of energy resources through a program of research and development efforts. These efforts include research characterization, air quality impacts and controls, advanced power systems, and advanced fuel forms. The goals of the Cooperative Agreement are energy efficiency, preserving the environment, securing the domestic energy supply, diversifying the coal industry, and fortifying foundations in research, education, and technology commercialization. Four major tasks were established for the EERC–DOE Cooperative Agreement. The Fuel Utilization Properties project is Task 3.1 of the Advanced Power Systems program. The overall goal is to determine the fundamental physical and chemical transformations of coal inorganic constituents and the relationship of the resulting ash intermediates to the formation of ash deposits in low-NO_x combustion and advanced power systems.

The overall objectives of Subtask 3.1 are 1) to determine the mechanisms of inorganic transformations during coal conversion processes, 2) to develop algorithms to predict the transport mechanisms of an ash–particulate flux to heat-transfer surfaces, 3) to study the effect of deposit characteristics on deposit strength and heat-transfer properties, and 4) to examine the effects of deposit characteristics on deposit removability. This report covers only the two outstanding activities within Task 3.1, Fuel Utilization Properties which were not reported in the Topical Report for Task 3.0 of the EERC–DOE Cooperative Agreement for 1993 (1). These activities include coordinating a round-robin collaborative testing of the computer-controlled scanning electron microscopy (CCSEM) method for measuring minerals in coal and determining a theoretical basis for establishing algorithms for describing the thermoconductive and reflective properties of entrained ash and ash deposits. The round-robin work was actually a continuation of work that began in 1990 under a different project that was entitled Combustion Inorganic Transformations (2).

ACCOMPLISHMENTS

Collaborative Study of The Computer-Controlled Scanning Electron Microscopy Method of Quantitative Coal Mineral Analysis

Introduction

The scanning electron microscope (SEM) equipped with an energy-dispersive x-ray spectrometer (EDS) is uniquely suited for coal mineral analysis because it provides both compositional and morphological information on a micro scale. Manual operation of the SEM has been used sparingly in coal mineral research because of the time required to acquire a statistically significant number of analyses to fully characterize the complex mineralogy of a coal sample. In the early 1970s, Noran Instruments, Inc. (formally Tracor Northern, Inc.) introduced the first commercially available digital electron beam control

system for SEMs combined with particle recognition and characterization (PRC), a computer program for controlling the electron beam and sample stage positioning and the EDS. This instrumentation enabled on-line image analysis to be performed to locate mineral grains and determine size, shape, and chemical information during unattended operation of the SEM. Thus, large numbers of mineral grains could be efficiently analyzed. This technology was developed specifically for quantitative coal mineral analysis in the early 1980s by Lee and Kelly (3) and Huggins et al. (4, 5) and marketed by Noran Instruments, Inc. (6). In subsequent years, this method of quantitative coal mineral analysis has been referred to as SEM-based automated image analysis (AIA), computerized SEM-AIA, and automated SEM, but most commonly as computer-controlled SEM (CCSEM).

Currently, CCSEM is a widely applied method for determining the size, association, composition, and abundance of minerals in coal. The method and its applications in coal mineral research were reviewed recently by Skorupska and Carpenter (7). Although CCSEM has been used extensively to analyze coal mineralogy, the available information required to evaluate the performance characteristics (i.e., precision, accuracy, sensitivity, and limitations) of this method is sparse. The evaluation process has been impeded because there are no certified coal mineral standards available, and there are a limited number of laboratories employing CCSEM available to perform collaborative testing. Nevertheless, an international collaborative study of the CCSEM method was conducted. Six laboratories participated in the study. Each laboratory was requested to perform a total of five analyses on three prepared coal samples: the Illinois No. 6 and Pittsburgh No. 8 coals from the Argonne Premium Coal Sample Program and the Prince coal from the European Centre for Coal Specimens. The collaborative study results were used to assess the intra- and interlaboratory precision of CCSEM.

Experimental

Ampules of 100-mesh Illinois No. 6 and Pittsburgh No. 8 high-volatile bituminous coals were obtained from the Argonne Premium Coal Sample Program (8, 9). The coal samples were pulverized to a standard utility combustion grind, i.e., 70% to 80% of the particles −200 mesh. A sample of −200 mesh Prince coal was obtained from the European Centre for Coal Specimens. Selected chemical properties of these coals (8, 10, 11) are presented in Table 1.

Three grams of each coal were mixed with two grams of Buehler epoxide resin in a 1.25 in. (3.18-cm) diameter mold and allowed to harden under ambient conditions. A single epoxy mount was prepared for each of the Illinois No. 6 and Prince coals. Six epoxy mounts of the Pittsburgh No. 8 coal were prepared. The coal–epoxy pellets were cross-sectioned using a slow-speed diamond saw. The sectioned pellet surfaces were polished using 6-μm, 1-μm, and 0.25-μm diamond pastes. The coal pellets were cleaned by sonication in trichlorotrifluoroethane after each polishing step. The polished pellet surfaces were then sputter-coated with a conductive layer of carbon to minimize the imaging artifacts caused by electron-beam charging.

TABLE 1

Chemical Properties of the Collaborative Test Coals

	Illinois No. 6	Pittsburgh No. 8	Prince
Ash, wt% dry	15.5	9.2	9.20
VM,[1] wt% dry	40.0	37.8	33.8
Sulfur, wt% dry	4.83	2.19	4.32
Pyritic Sulfur	2.81	1.37	1.80
Ash Analysis, wt%			
SiO_2	40.2	45.6	40.4
Al_2O_3	14.1	20.2	16.3
Fe_2O_3	23.8	22.4	33.7
TiO_2	0.7	1.1	1.12
CaO	7.8	3.0	1.16
MgO	0.9	0.6	0.4
Na_2O	1.0	0.5	0.6
K_2O	1.5	1.5	1.8
P_2O_5	0.1	0.2	0.8
SO_3	3.8	2.0	1.0

[1] Volatile matter.

The Illinois No. 6 and Prince coal pellets were submitted sequentially to the following laboratories and organizations for analysis: Commonwealth Scientific and Industrial Research Organization (CSIRO), Victoria, Australia (Lab A); Netherlands Energy Research Foundation (ECN), Petten, Netherlands (Lab B); Energy & Environmental Research Center, Grand Forks, ND (Lab C); RJ Lee Group, Inc., Monroeville, PA (Lab D); Sandia National Laboratories, Livermore, CA (Lab E); and the Consortium for Fossil Fuel Liquefaction Science, University of Kentucky, Lexington, KY (Lab F). The laboratories also received a prepared sample of the Pittsburgh No. 8 coal.

Analytical Methods

The instrumentation, software, and operating conditions employed by the various laboratories are summarized in Table 2. Five of the laboratories (B, C, D, E, and F) used conventional scanning electron microscopes equipped with an EDS. These laboratories also used similar digital electron beam control systems. A brief description of the CCSEM procedures for collecting and presenting data that are common to these five laboratories follows.

TABLE 2

Analytical Instrumentation and Operating Conditions

Laboratory	A	B	C	D	E	F
Accelerating Voltage, kV	25	20	15	20	15	20
Probe Current, nA	3.0	0.3	0.6	NR[1]	15	0.7
Magnifications, ×	22/32/48/64/100	50/150/450	50/240/500	50/240/500	100/860	25/100/500
Spectral Acquire Time, s	0.025	2 or 3	5	3	20	2
SEM	ISI SX-30	JEOL JXA 840	JEOL JSM-35U	NR	JEOL 733	ETEC-Autoscan
X-Ray Analyzer	Tracor Northern (TN)	TN-5500	TN-5502	NR	TN-5502	TN-2000
Software	QEM*SEM[2]	PRC[3]	PRC Partchar®[4]	NR	CMA[5]	CMA

[1] Not reported.
[2] Quantitative Evaluation of Materials by Scanning Electron Microscopy, developed by CSIRO.
[3] Particle Recognition and Characterization, marketed by NORAN Instruments, Inc. (formally, Tracor Northern, Inc.).
[4] Particle Characterization, developed by the EERC.
[5] Coal Mineral Analysis, marketed by Noran Instruments, Inc. (Hamburg, 1984).

In summary, the electron beam is digitally stepped in a raster pattern on the sample surface while the SEM is operating in a backscattered electron (BSE) imaging mode. A mineral grain is automatically detected by an increase in the BSE signal above a preset, operator-selected, video threshold. Digital beam control guides the beam through a programmed raster pattern, an iterative bisection of chords, to locate the particle's center and to determine physical dimensions (e.g., average diameter, area, perimeter). After the size analysis, an energy-dispersive x-ray spectrum of the particle is acquired and the characteristic x-ray emission intensities of common mineral-forming elements are measured. This sequence is repeated until a statistically significant number of mineral grains has been analyzed. The analysis is performed at several magnifications to provide the spatial resolution necessary for obtaining information on the distribution of various sizes of minerals. The particle analyses are classified based on compositional criteria into various mineral categories. The results are tabulated in terms of the number and proportions of various mineral categories in their respective size intervals. Mineral weight proportions can be calculated assuming that particle area is proportional to particle volume (the Delesse relation) (12,13).

Laboratory A employed a SEM-based image analysis system equipped with four EDSs. The four detectors are used simultaneously to greatly improve x-ray spectrum collection efficiency. This system, designated as quantitative evaluation of materials by scanning electron microscopy (QEM-SEM), was originally developed by CSIRO for the Australian mining industry to evaluate the mineralogy of ores and rocks for metallurgical purposes (14). Minerals are classified based on a combination of BSE brightness and elemental proportions. The development and application of this method for quantifying coal mineralogy is discussed by Creelman (15) and Gottlieb et al. (16).

Analysis Guidelines

Instrumentation characteristics, operating parameters, and procedures that are unique to the participating laboratories will affect the intra- and interlaboratory agreement of CCSEM analysis results. Many of the critical factors that affect CCSEM analysis results have been identified and tabulated by Birk (17). In the present study, the interlaboratory variability originating from coal sampling and preparation is virtually eliminated, because all participating laboratories analyzed identically prepared samples. A major concern, however, is the variability resulting from differences in instrumentation performance characteristics, operating parameters, data acquisition parameters, and data reduction procedures.

The participating laboratories were requested to perform the analyses at three magnifications with at least 1000 particles analyzed at each magnification, or until the entire sample surface had been analyzed. These operating and data acquisition guidelines were specifically designed to minimize the variability resulting from differences in particle detection sensitivity and counting statistics. As indicated in Tables 2 and 3, several of the laboratories were unable to comply with these guidelines because their systems did not have the stage automation required to efficiently analyze such large numbers of particles per magnification. Critical parameters that were not specified in the analysis guidelines include the BSE video threshold setting and the video-sampling signal value. These settings are largely dependent on sample characteristics and the BSE collection efficiency of the detector employed.

The accelerating voltages, probe currents, and energy-dispersive x-ray spectrum acquisition times employed by the laboratories varied greatly (Table 2). The settings of these operating parameters could not be specified because they are dependent on SEM geometry (working distance, specimen chamber dimensions, x-ray takeoff angle, etc.) and the performance characteristics of the energy-dispersive x-ray spectrometer employed. The relative x-ray intensity criteria used by most laboratories to classify particle analyses into mineral/chemical categories are affected by these parameters.

Interlaboratory comparison of CCSEM analysis results can be hindered because of differences in data reduction procedures. Data reduction involves the classification of the particle analyses into various user-specified mineral/chemical categories and size intervals. The classification categories are defined based on elemental x-ray intensities (% x-ray counts), relative intensity ratios, and stoichiometric criteria. The categories, category definitions, and size intervals are inconsistent among the participating laboratories. Consequently, the laboratories were requested to analyze minerals ranging in average diameter from 1 μm to 100 μm and to report only the total concentration of four common coal minerals. This reporting format facilitated the statistical comparison of results.

Results and Discussion

The laboratories were requested to perform a total of five analyses on the three coals. A single analysis was to be performed on the Illinois No. 6 coal pellet and Prince coal pellet by each laboratory. In addition, three analyses were to be performed on each laboratory's assigned Pittsburgh No. 8 coal pellet. Participants were requested to report the proportions of calcite, kaolinite, pyrite, and quartz on a percent by weight of total minerals basis. Three laboratories reported their results in volume percent, thus

TABLE 3

Total Number of Mineral Grains Analyzed

Laboratory	Illinois No. 6	Pittsburgh No. 8[1]	Prince
A	NR[2]	NR	NR
B	2937	1575	2855
C	3661	2666	2329
D	NR	2692	NR
E	NA[3]	679	NA
F	1200	1200	1200

[1] Average of three analyses.
[2] Not reported.
[3] Not analyzed.

precluding a direct comparison of the results. These results, however, were converted to weight percent using the appropriate mineral density values tabulated in Carmichael (18) and assuming an average density of 2.7 g/cm^3 for the minerals that were analyzed but not reported. This conversion was required to enable a direct comparison of results.

The Pittsburgh No. 8, Illinois No. 6, and Prince coal collaborative analysis results are presented in Tables 4, 5, and 6, respectively. These results were analyzed statistically using the American Society for Testing and Materials (ASTM) Interlaboratory Data Analysis Software (19,20) to provide a measure of intra- and interlaboratory precision and repeatability and reproducibility. The statistical parameters and their corresponding symbols used in this study are summarized in Table 7.

Repeatability

Repeatability was evaluated based on the Pittsburgh No. 8 coal mineral analysis results (Table 4). Unfortunately, Laboratory B analyzed the Pittsburgh coal only once and therefore their results could not be included in the statistical analysis. The intralaboratory statistics presented in Table 8 indicate that Laboratory A reported the most precise results. Consistency testing indicated that the pyrite analysis results reported by laboratory E were significantly more variable, i.e., k statistic exceeded critical value of 1.91, than those reported by the other laboratories. The greater imprecision may be attributable to the employment of only two magnifications (Table 2) and to the smaller number of mineral grains analyzed (Table 3). Although laboratory E did not comply with the analysis guidelines, their pyrite results were retained for additional statistical analysis because of the limited number of participants. Repeatability statistics for the Pittsburgh No. 8 coal are presented in Table 9. The RSD_r values in Table 9 are comparable, less than 20 %, for all four mineral categories. Similar repeatability statistics for CCSEM were reported by Casuccio et al. (21).

Reproducibility

Reproducibility of the CCSEM method was evaluated using the Pittsburgh No. 8, Illinois No. 6, and Prince coal mineral analysis results (Tables 4, 5, and 6). The reproducibility statistics determined from each coal are presented in Tables 10, 11, and 12. Kaolinite shows the poorest reproducibility for all three coal samples. The poor reproducibility of kaolinite analysis results was also documented in the study by Casuccio et al. (21) and attributed to differences in BSE and x-ray collection efficiencies. The poor reproducibility of the calcite results for the Pittsburgh No. 8 coal and of the quartz results for the Illinois No. 6 and Prince coals is attributable to poor counting statistics resulting from their relatively low concentrations in these coals. The reproducibility of calcite and quartz improves greatly, $RSD_R < 30\%$, in the Illinois No. 6 and Pittsburgh No. 8 coals, respectively, where their concentration levels are greater than 10 wt%. Reproducibility of the pyrite results is consistent (RSD_R values range from 21% to 23%) among the coals.

The average 95% reproducibility limits and their ranges determined from all the coals used in the collaborative study are presented in Table 13. The reproducibility limits for the selected mineral species in the three coals (Tables 10, 11, and 12) are generally

TABLE 4

Collaborative Analysis Results of Selected Minerals in the Pittsburgh No. 8 Coal (percent by weight of minerals)

Laboratory	Calcite	Kaolinite	Pyrite	Quartz	Total
A	3.8	15.1	43.4	15.6	77.9
	3.8	14.8	42.9	16.1	77.6
	4.2	14.3	42.8	15.6	76.9
B[1]	2.4	10.1	68.7	6.9	88.1
C	4.0	22.8	38.9	15.9	81.6
	3.2	21.6	35.3	17.7	77.8
	3.2	19.8	43.2	15.0	81.2
D	8.6	12.9	46.8	10.6	78.9
	8.6	8.8	52.2	9.2	78.8
	6.5	8.1	54.8	8.8	78.2
E	4.1	42.9	30.9	18.9	96.8
	4.9	35.4	42.6	13.7	96.6
	3.1	45.2	19.2	20.3	87.8
F	2.5	3.3	36.3	18.6	60.7
	2.1	1.7	36.8	13.0	53.6
	3.6	2.5	31.8	13.7	51.6

[1] Reported only one analysis result.

TABLE 5

Collaborative Analysis Results of Selected Minerals in the Illinois No. 6 Coal (percent by weight of minerals)

Laboratory	Calcite	Kaolinite	Pyrite	Quartz	Total
A	12.3	3.2	61.6	6.3	83.4
B	15.7	5.3	57.9	5.1	84.0
C	12.7	8.9	43.2	15.6	80.4
D	21.4	4.0	38.6	10.8	74.8
E	NR[1]	NR	NR	NR	NA[2]
F	11.5	3.8	42.5	10.8	68.6

[1] Not reported.
[2] Not applicable.

TABLE 6

Collaborative Analysis Results of Selected Minerals in the Prince Coal (percent by weight of minerals)

Laboratory	Calcite	Kaolinite	Pyrite	Quartz	Total
A	0.1	3.1	76.5	6.7	86.4
B	2.4	6.4	73.7	6.7	89.2
C	ND[1]	10.4	59.7	7.2	77.3
D	0.1	7.6	48.7	11.4	67.8
E	NR[2]	NR	NR	NR	NA[3]
F	ND	3.2	49.6	3.1	55.9

[1] Not detected.
[2] Not reported.
[3] Not applicable.

TABLE 7

Statistical Parameters and Symbols

Parameter	Symbol
Mean	X
Standard deviation	s
Relative standard deviation	RSD
Repeatability standard deviation	s_r
95% Repeatability limit ($2.8 \times s_r$)	r
Repeatability relative standard deviation	RSD_r
Reproducibility standard deviation	s_R
95% Reproducibility limit ($2.8 \times s_R$ or $2.8 \times RSD_R$)	R
Reproducibility relative standard deviation	RSD_R

TABLE 8

Intralaboratory Statistics of the Pittsburgh No. 8 Coal Mineral Analysis Results (percent by weight of minerals unless otherwise noted)

Laboratory	A			C			D			E			F		
Parameter	X	s	RSD	X	s	RSD	X	s	RSD	X	s	RSD	X	s	RSD
Calcite	3.9	0.2	6%	3.5	0.5	13%	7.9	1.2	15%	4.0	0.9	22%	2.7	0.8	28%
Kaolinite	14.7	0.4	3%	21.4	1.5	7%	9.9	2.6	26%	41.2	5.1	12%	2.5	0.8	32%
Pyrite	43.0	0.3	1%	39.1	4.0	10%	51.3	4.1	8%	30.9	11.7[1]	38%	35.0	2.8	8%
Quartz	15.8	0.3	2%	16.2	1.4	8%	9.5	0.9	10%	17.6	3.5	20%	15.1	3.1	20%

[1] Intralaboratory consistency statistic, k, exceeded critical value of 1.91.

TABLE 9

Repeatability Statistics for the Pittsburgh No. 8 Coal Mineral Analysis Results

Mineral/Level	Calcite	Kaolinite	Pyrite	Quartz
Number of Laboratories	6	6	6	6
Number of Results	16	16	16	16
Number of Laboratories Retained[1]	5	5	5	5
Number of Accepted Results	15	15	15	15
X, wt%	4.4	17.9	39.9	14.8
s_r, wt%	0.8	2.7	5.9	2.2
RSD_r, %	18	15	15	15
r, wt%	2.2	7.5	16.7	6.2

[1] Number of laboratories was insufficient to be in conformance with ASTM Standard E691-87.

TABLE 10

Reproducibility Statistics for the Pittsburgh No. 8 Coal Mineral Analysis Results

Mineral/Level	Calcite	Kaolinite	Pyrite	Quartz
Number of Laboratories	6	6	6	6
Number of Results	16	16	16	16
Number of Laboratories Retained[1]	5	5	5	5
Number of Accepted Results	15	15	15	15
X, wt%	4.4	17.9	39.9	14.8
s_R, wt%	2.1	14.9	9.2	3.6
RSD_R, %	48	83	23	24
R, wt%	5.9	41.6	25.8	10.1

[1] Number of laboratories was insufficient to be in conformance with ASTM Standard E691-87.

proportional to mineral concentration. Consequently, the limits presented in Table 13 for each mineral category are expressed as a percentage in accordance with ASTM Standard Practice E177. The reproducibility limit is the preferred index for expressing interlaboratory precision (20).

Summary and Conclusions

Six laboratories collaborated in a study of the CCSEM method of coal mineral analysis. Intralaboratory results agreed to within 20% RSD_r for the four mineral species analyzed. The repeatability of CCSEM is apparently independent of the mineral species analyzed. Reproducibility for the interlaboratory results was poor, especially the kaolinite determinations. Hopefully, the more advanced digital image analysis systems employed on current generation SEM instruments can provide improved quantitative coal mineral analysis results.

The Thermoconductive and Reflective Properties of Entrained Ash and Deposits.

Introduction

Very little in the form of credible data exists that describes the radiative properties of coal ash in a combustion or other conversion system, nor the impacts of these phenomenon on the heat balance of a boiler. A theoretical approach to developing algorithms that describe the heat reflection and conduction properties for entrained ash and ash deposits was initiated. This work was conducted as a collaboration between the EERC and a visiting scientist, Dr. Terry Wall from the University of Newcastle, Australia.

TABLE 11

Reproducibility Statistics for the Illinois No. 6 Coal Mineral Analysis Results

Mineral/Level	Calcite	Kaolinite	Pyrite	Quartz
Number of Laboratories	5	5	5	5
Number of Results	5	5	5	5
Number of Laboratories Retained[1]	5	5	5	5
Number of Accepted Results	5	5	5	5
X, wt%	14.7	5.0	48.8	9.7
s_R, wt%	4.1	2.3	10.3	4.2
RSD_R, %	28	45	21	43
R, wt%	11.4	6.4	28.8	11.7

[1] Number of laboratories was insufficient to be in conformance with ASTM Standard E691-87.

TABLE 12

Reproducibility Statistics for the Prince Coal Mineral Analysis Results

Mineral/Level	Calcite	Kaolinite	Pyrite	Quartz
Number of Laboratories	5	5	5	5
Number of Results	5	5	5	5
Number of Laboratories Retained[1]	NA[2]	5	5	5
Number of Accepted Results	NA	5	5	5
X, wt%	NA	6.1	61.6	7.0
s_R, wt%	NA	3.1	13.1	2.9
RSD_R, %	NA	50	21	42
R, wt%	NA	8.7	36.6	8.3

[1] Number of laboratories was insufficient to be in conformance with ASTM Standard E691-87.
[2] Not applicable because calcite was reported as below detection by two laboratories.

Radiative Properties and Impacts of Entrained Ash

The radiative properties of entrained ash and their significance on the operation of furnaces depends on coal properties, especially the distribution of minerals within the coal, as well as on the combustion system, in so far as this determines the character of the ash generated on combustion. As ash is only one of the species derived from combustion, its effect depends on these other components—the triatomic gases, unburnt char, and soot.

An outline is presented for techniques that allow prediction of the coefficients necessary to quantify the significance of ash, those being the factors used in mathematical codes for furnace prediction, and proposes factors based on coal and ash analyses that may be used to compare coals. The factors can be estimated with reasonable accuracy. They should be calculated for several coals for which plant data are available or used in predictive codes in order to identify the magnitudes associated with plant characteristics.

In pulverized coal (pc) systems, the components that absorb are the triatomic gases CO_2 and H_2O, entrained ash, soot and unburnt char. Entrained ash particles are the dominant scattering components, being of a size comparable to the wavelength of the thermal radiation. Fine unburnt char may scatter, but to an insignificant extent compared to ash. Soot radiation is important only in flame regions.

TABLE 13

Reproducibility Limits Based on Pittsburgh No. 8, Illinois No. 6, and Prince Coal Mineral Analysis Results

Mineral/Level	Calcite	Kaolinite	Pyrite	Quartz
Number of Laboratories[1]	5	5	5	5
Number of Accepted Results	20	25	25	25
X Range, wt%	4.4–14.7	5.0–17.9	39.9–61.6	7.0–14.8
R, % of test result[2]	106 (78, 134)	167 (127–232)	61 (59–65)	102 (68–121)

[1] Number of laboratories was insufficient to be in conformance with ASTM Standard E691-87.
[2] Average R ($2.8 \times RSD_R$) with range shown in parenthesis.

Illustrative trends of the component absorption coefficients (k_a) for pc burning in air at a given stoichiometry (20% excess air) are given in Figure 1. From the figure the following points may be noted.

- At complete combustion (approximating most of the volume of pc-fired furnaces) ash is the dominant emitter/absorber for bituminous coals and an important emitter/absorber for lignites.

- Ash is the dominant scattering component.

The magnitude of the points in the figure may be estimated from coal analysis, combustion calculations, and the size distributions of the coal and ash. These coefficients allow the direct comparison of the significance of the components and are the factors used in mathematical models of furnaces.

Factors are proposed that compare coals and quantify the effect of entrained ash as a furnace radiator. The factors are based on estimates of the coefficient (k) for the radiating components. To estimate those factors requires the following information on coal properties; no furnace information is required.

- For all factors, the amount (volume of mass) of radiator per unit volume of gas is required, from measurement or calculation based on combustion stoichiometry and coal ultimate analysis. Those amounts are estimated at a particular gas temperature, say 1800°K. Tabulated data and plots may be used to obtain the gas emissivity for a mixture of CO_2 and H_2O.

- For char, the mass of char and its size distribution is required, either from measurement or from a burnoff calculation.

- For ash, the mass and size distribution is again required. At complete combustion, the mass is obtained by calculation; the size may be measured or derived from the CCSEM analysis of the coal minerals. The ash factors also require absorption and scatter efficiencies, which depend on the ash size distribution and (to some extent) on ash chemistry.

Absorption of particles is determined by the proportion of a beam of radiation intercepted, considering particles to be spherical geometric interceptors, multiplied by the efficiency of this interception. Scatter coefficients are defined in a similar way.

Char particles may be approximated as black bodies and to estimate the number of char particles of size d per unit volume, a burnout calculation may be made. This will follow the char burning after devolatilization in a stream where the progressive oxygen partial pressure is reduced according to burnout (22). For most pc furnaces, the number of char particles present is sufficiently low for most of the furnace volume and the contribution may be neglected; for the fuel-rich region of slagging combustors this may not be the case.

Ash particles are of a similar dimension in the wavelengths of radiation involved at the temperatures of interest; they therefore both absorb and scatter. The dust burden may be determined by a combustion calculation and is inversely proportional to gas temperature. The projected surface area is weighted toward the fine end of the size distribution.

The absorption and scattering efficiencies are complex functions derived from Mie theory involving integration over the size distribution of ash as well as the black body spectrum defining the wavelength of importance (23). These efficiencies have a primary dependence on size and a secondary dependence on the chemical nature of the ash.

Calculations have been made to determine the magnitudes and sensitivities of ash properties on the coefficients. The hemispherical properties were calculated for a gas slab containing a cloud of ash particles, using a code based on the Mie theory. This calculation reveals that, for a given mass of per unit volume, the size distributions considered,

- The absorption coefficient k_a is essentially independent of mean size;
- The scattering coefficient k_s decreases continually with mean size with a value for the finest ash (70%<5μm) being three times that for the larger ash (70%<25μm).

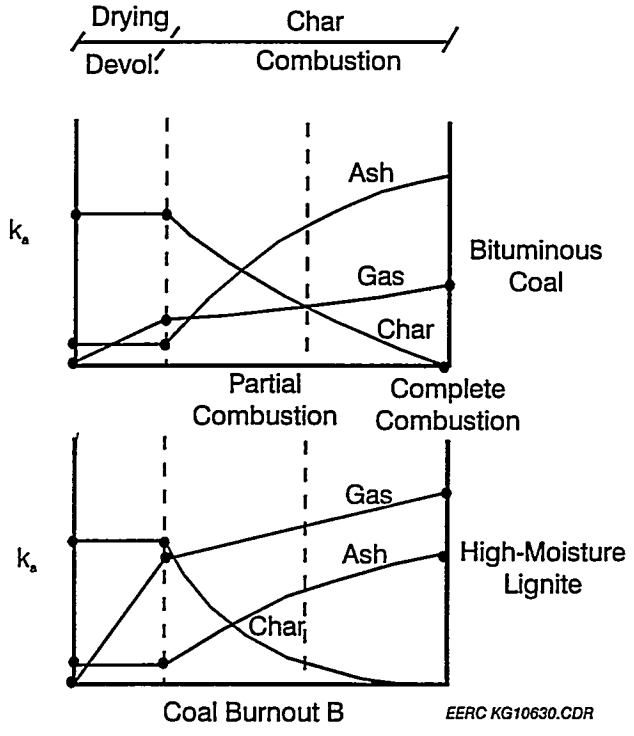

Figure 1. Illustrative trends for the magnitudes of component absorption coefficients with burnout.

Ash composition influences the optical properties of the fly ash by its influence on the complex refractive index, but the variation with composition is somewhat unclear. It is possible that the effect of particle size on the efficiencies is greater than the effect of composition.

Estimates of the hemispherical radiative properties of a slab containing a particle cloud allow the effect of the cloud to be evaluated. The optical properties of char result in a cloud being on absorber/emitter of radiation, with a small reflective effect. The estimate of the coefficient and factors for ash and the gases at complete combustion is a relatively simple matter, requiring only the dust burden and ash size distribution and the partial pressures of CO_2 and H_2O. These may be estimated by a combustion calculation requiring only the proximate and ultimate analysis of the coal, the excess air level, a typical gas temperature and a measured (or estimated) ash size distribution.

Radiative Properties of Deposited Ash

The insulating effect of ash deposits on furnace walls may occur by a restriction of radiative or conductive heat transfer. Trends in furnace efficiency as deposits grow are quantified by changes in the furnace exit gas temperature (FEGT). The properties influencing the efficiencies are

- The radiative property, the wall emittance (ϵ) or absorbance (α);
- The conductive property, the ratio of the unit thermal conductivity divided by the deposit thickness (k/x).

Illustrative trends (24) in the FEGT and deposit surface temperature of the deposit are given on Figure 1 as deposits grow and mature. The notation is a. clean tube; b. deposit of fine ash; c. coarse ash; d. thickened coarse ash; e. rough sintered ash; f. molten (slag) layer.

It is apparent that the initial changes are associated with radiative effects, and later changes are associated with conductive effects. The most severe effects are predicted for reflective and poorly conducting layers, for which increases of FEGT of 200°C are predicted, compared to a clean furnace.

The influence of physical and chemical character on the radiative properties of the ash deposits on furnace walls is now understood in general terms. For example, it has been stated that "radiative properties are highly dependent on the morphology of the deposit and have a minimal dependence on chemical composition" (25). This statement agrees with conclusions from a detailed review that "the properties depend principally on the physical ash character and whether the deposits have a particulate character or are sintered or fused" (23).

It is now clear that initial powdery deposits have low emissivities; that is, they are reflective. As they fuse and sinter, emissivity increases, reaching a limiting value of about 0.9 when the deposit slags (25). Any predictive technique for radiative properties must therefore predict this physical character. A further difficulty is that the outermost layer of the deposit is involved in the radiative interaction rather than the deposit as a whole. On the other hand, the conductive properties of deposits depend on the whole

deposit, particularly the physical paths established within the deposit that allow conductive heat transfer to occur, as well as the deposit thickness. Porosity has been used to characterize thermal conductivity.

The support for relating radiative properties with morphology comes from several experimental and theoretical sources. Recently, Markham et al. (25) have measured the spectral emittance of a sample of sintered slag, compared to the same sample after grinding and after fusion and melting. A continuous increase in spectral emittance was observed as the material passed through the physical changes from powdered, sintered, fused, and molten. A similar change was noted for a sample of fused fly ash.

Several trends are also noted in the experimental data of Boow and Goard (26) on layers of particles prepared from synthetic slags. These are similar to those of many other studies by Wall et al. (23) on powdery ash deposits and slag layers. The trends observed are as follows:

- A reduction of emittance of particulates with temperature until sintering and fusion occurs. On sintering, emittance increases.
- A systematic increase of emittance with particle size prior to sintering.
- An increase of emittance with iron content (Fe_2O_3) and carbon content (caused by unburnt coal in ash) prior to sintering. Measurements on slag layers suggest that the emittance attained on complete fusion is likely to exceed 0.9.

Recent theoretical predictions by Wall et al. (23) (based on Mie theory for the scatter of particles) support the concepts.

The trends expected for the properties are based on data from these references. For the deposit-free wall (or tube), the absorbance is high, about 0.8. The initial deposit layer is likely to be fine condensible salts or fine ash transported by the thermophorosis mechanism (23, 24). For a particulate layer of 2-μm ash, the absorbance may be less than 0.3. As the fine layer thickens and results in the collection of larger particles (which rebound from a thin layer), a layer of coarse ash develops with an absorbance of, perhaps, 0.4–0.5. As this particulate layer builds to a greater thickness, the absorbance will not change, but the conduction coefficient (k/x) will continue to decrease. During the development of this particulate layer, the temperature difference through the deposit and, therefore, the temperature of its surface, will continuously increase. Sintering and fusion will result. Also, a thick deposit is likely to leave an irregular (rough) surface. Therefore α and k/x will increase. Once the thickness builds and temperature increases further, a liquid slag will develop, causing α and k to increase; therefore, k/x may increase or decrease compared to its value for the sintered deposits. It is possible that an intermediate steady state may develop during deposit growth. For example, if the deposit does not sinter appreciably, the erosion rate of the deposit by large particles may balance the deposition rate and a permanent particulate character will result.

The processes leading to the changes are understood to the extent that models, or algorithms, may be used to predict them. The three processes of deposition, sintering, and melting are related to the chemical and physical character of ash (by properties such as particle size and viscosity), allowing comparisons between coals to be made. For a model,

the processes related to the deposition or transport of ash to walls are relatively well developed (27, 28). However, processes related to the reactions within the deposit, its development of strength, and transformation into slag are not well developed.

The appropriate way to progress further in modeling of deposit thermal properties is as follows:

- Review the literature on controlled experiments which monitor ash sintering and fusion (29, 30).
- Use sintering theory to attempt predictions of experimental results of 1.
- Examine the properties of deposits.

Summary and Conclusions

The radiative properties of furnace gases, entrained ash, and char may be predicted from scattering theory when combined with estimations of gas composition and particle composition, size distribution, and particulate loading. These factors can be calculated from existing combustion and ash transformation codes requiring only coal and ash analyses as input. The radiative properties predictions should be calculated for several coals for which plant data are available to identify the effects of plant physical characteristics on the model.

The radiative properties of deposited ash can be predicted, provided a critical piece of information about the deposit surface is available, i.e., the degree of sintering. The transport of ash to the surface can be modeled with a fair degree of confidence; however, sintering and slagging processes occurring in the deposit are less well understood. Crude first-order approximations of sintering can be made using sintering data in the literature, allowing predictions of deposit conductivity, surface temperature, surface morphology, and the radiative properties to be made also. More detailed predictions will require additional study of deposit properties and transformations and the development of an improved understanding of sintering behavior.

CONCLUSIONS

Work was initiated several years ago to perform a round-robin testing of the CCSEM technique to begin the process of standardizing it. Six laboratories collaborated in a study of the CCSEM method of coal mineral analysis. Intralaboratory results agreed to within 20% RSD_r for the four mineral species analyzed. The repeatability of CCSEM is apparently independent of the mineral species analyzed. Reproducibility of the interlaboratory results was poor, especially the kaolinite determinations. Hopefully, the more advanced digital image analysis systems employed on current-generation SEM instruments can provide improved quantitative coal mineral analysis results. This work completes the round-robin CCSEM program, and future steps may need to be taken to establish a second round of collaborative CCSEM analyses to establish a standard procedure for performing CCSEM analysis across various laboratories.

A theoretical approach to developing algorithms that describe the heat reflection and conduction properties for entrained ash and ash deposits was initiated. This work was conducted as a collaboration between the EERC and a visiting scientist, Dr. Terry Wall from the University of New Castle, Australia. The radiative properties of furnace gases, entrained ash, and char may be predicted from scattering theory when combined with estimations of gas composition and particle composition, size distribution, and particulate loading. These factors can be calculated from existing combustion and ash transformation codes that require only coal and ash analyses as input. The radiative properties predictions should be calculated for several coals for which plant data are available to identify the effects of plant physical characteristics on the model.

The radiative properties of deposited ash can be predicted provided a critical piece of information about the deposit surface is available, i.e. the degree of sintering. The transport of ash to the surface can be modeled with a fair degree of confidence; however, sintering and slagging processes occurring in the deposit are less well understood. Crude first-order approximations of sintering can be made using sintering data in the literature, allowing predictions of deposit conductivity, surface temperature, surface morphology, and the radiative properties to be made. More detailed predictions will require additional study of deposit properties and transformations and the development of an improved understanding of sintering behavior.

REFERENCES

1. Zygarlicke, C.J.; Katrinak, K.A. "Combustion Inorganic Transformations," final technical progress report for the period April 1, 1986, through December 31, 1992; U.S. Department of Energy, DE-FC21-86MC10637, 1992.

2. Zygarlicke, C.J.; McCollor, D.P. "Fuel Utilization Properties," in Advanced Power Systems, Topical Report Task No. 3.0 for the period January 12 to December 31, 1993; U.S. Department of Energy, DE-FC21-93MC30097, 1992.

3. Lee, R.J.; Kelly, J.F. "Overview of SEM-Based Automated Image Analysis," *Scanning Electron Microscopy* **1980**, *I*, 303–310.

4. Huggins, F.E.; Kosmack, D.A.; Huffman, G.P.; Lee, R.J. "Coal Mineralogies by SEM Automatic Image Analysis," *Scanning Electron Microscopy* **1980**, *I*, 531–540.

5. Huggins, F.E.; Huffman, G.P.; Lee, R.J. "Scanning Electron Microscope-Based Automated Image Analysis (SEM-AIA) and Mössbauer Spectroscopy: Quantitative Characterization of Coal Minerals," In *Coal and Coal Products: Analytical Characterization Techniques*; Fuller, E.L., Jr., Ed.; American Chemical Society Symposium Series 205, 1982, Chapter 12, pp 239–258.

6. Hamburg, G. "Description of the Tracor Northern Energy-Dispersive System as Applied to Coal Minerals Analysis," *Technology in Review* **1984**, *2* (1), 7–10.

7. Skorupska, N.M.; Carpenter, A.M. "Computer-Controlled Scanning Electron Microscopy of Minerals in Coal," In *Perspectives*; International Energy Agency Coal Research, IEAPER/07, 1993; p 21.

8. Vorres, K.S. *User's Handbook for the Argonne Premium Coal Sample Program*; Argonne National Laboratory, 1989; p 64.

9. Vorres, K.S. "The Argonne Premium Coal Sample Program," *Energy & Fuels* **1990**, *4* (5), 420–426.

10. Evans, J.R.; Sellers, G.A.; Johnson, D.V.; Kent, J. "Analysis of Eight Argonne Premium Coal Samples by X-Ray Fluorescence Spectrometry," U.S. Geological Survey Open-File Report 91-638 1991, pp 42–49.

11. European Centre for Coal Specimens SBN Coal Catalogue, Release E1, 1991.

12. Chayes, F. *Petrographic Modal Analysis—An Elementary Statistical Appraisal*; New York: Wiley, 1956; p 113.

13. DeHoff, R.T.; Rhines, F.N. *Quantitative Microscopy*; Materials Science and Engineering Series, McGraw-Hill Book Company, 1968; p 422.

14. Reid, A.F.; Gottlieb, P.J.; MacDonald, K.J.; Miller, P.R. "QEM*SEM Image Analysis of Ore Minerals: Volume Fraction, Liberation, and Observational Variances," *Applied Mineralogy* **1984**, 191–204.

15. Creelman, R.A.; Greenwood-Smith, R.; Gottlieb, P.; Paulson, C. "The Characterization of Mineral Matter in Coal and the Products of Coal Combustion Using QEM*SEM," *In* Proceedings of the Australian Coal Science Conference 2; Newcastle, Australia, Dec. 1–2, 1986, Vol. 1, p. 215–221.

16. Gottlieb, P.J.; Agron-Olshina, N.; Sutherland, D.N. "The Characterization of Mineral Matter in Coal and Fly Ash," *In* Proceedings of the Engineering Foundation Conference on Inorganic Transformations and Ash Deposition During Combustion; Benson, S.A., Ed.; Palm Coast, FL, March 10–15, 1991, pp 135–145.

17. Birk, D. "Coal Minerals: Quantitative and Descriptive SEM-EDX Analysis," *Journal of Coal Quality* **1989**, *8* (2), 55–62.

18. *Practical Handbook of Physical Properties of Rocks and Minerals*; Carmichael, R.S., Ed.; CRC Press, Inc., 1989; p. 741.

19. American Society for Testing and Materials. "Standard Practice for Conducting an Interlaboratory Study to Determine the Precision of a Test Method," *Annual Book of ASTM Standards*, Vol. 14.02, Designation E 691-87, 1992.

20. American Society for Testing and Materials. "Standard Practice for Use of the Terms Precision and Bias in ASTM Methods," *Annual Book of ASTM Standards*, Vol. 14.02, Designation E 177-86, 1992.

21. Casuccio, G.S.; Gruelich, F.A.; Hamburg, G.; Huggins, F.E.; Nissen, D.A.; Vleeskens, J.M. "Coal Mineral Analysis: A Check on Interlaboratory Agreement," *Scanning Microscopy* **1990**, *4* (2), 227–236.

22. Wall, T.F.; Phelan, W.: Bortz, S. *Comb. Flame* **1986**, *66*, 137–150.

23. Wall, T.F.; Bhattacharya, S.P.; Zhang, D.K.; Gupta, R.P.; He, X. "The Properties and Thermal Effect of Ash Deposits in Coal-Fired Furnaces," *Prog. Energy Combust. Sci.* **1993**, *19*, 487–504.

24. Wall, T.F.; Baxter, L.L.; Richards, G.; Harb, J. *In* Proceedings of the Conference on Coal Blending and Switching; Bryers, R.W.; Harding, N.S., Eds.; ASME, NY, 1994, pp 453–463.

25. Markham, J.R.; Best, P.E.; Soloman, P.R.; Yu, Z.Z. *J. Heat Transfer* **1992**, *114*, 458.

26. Boow, J.; Goard, P.R.C. *J. Inst. Fuel* **1969**, *42*, 412.

27. Beér, J.M.; Sarofim, A.F.; Barte, L.E. "From Coal Mineral Properties to Fly Ash Deposition Tendencies: A Modeling Route," *In* Proceedings of the Engineering Foundation Conference on Inorganic Transformations and Ash Deposition During Combustion; Benson, S.A., Ed.; ASME, 1992, pp 71–94.

28. Baxter, L.L.; Abbott, M.F.; Douglas, R.E. *In* Proceedings of the Engineering Foundation Conference on Inorganic Transformations and Ash Deposition During Combustion; Benson, S.A., Ed.; ASME, 1992, pp 679–698.

29. Raask, E. *Mineral Impurities in Combustion*; Hemisphere, 1985.

30. Sanyal, A.; Mehta, A.K. "Development of an Electrical Resistance-Based Ash Fusion Test," *In* Proceedings for the Impact of Ash Deposition on Coal-Fired Plants; Engineering Foundation Conference, Solihull, Birmingham, UK, June 20-25, 1993, Taylor and Francis, 1993, pp 445–460.

TASK 3.4

HOT-GAS CLEANING

Prepared by:

Greg F. Weber

August 1994

TABLE OF CONTENTS

LIST OF FIGURES

LIST OF TABLES

TASK 3.4 HOT-GAS CLEANING

1.0 BACKGROUND

Many prototype high-efficiency coal-fired power systems require stringent removal of particulate ash from the high-pressure/high-temperature gas stream to prevent erosion of turbine blades or plugging of fuel cells. At present, ceramic candle filters and cross-flow filters have shown the capability to reduce particle loadings in coal-fired gas streams to acceptable levels. However, long-term thermal and chemical degradation of the filters has prevented their reliable use at the relatively high temperatures required. One of the principal degradation mechanisms is vapor-phase alkali attack of aluminosilicate materials or the silicon in silicon carbide or silicon nitride materials. The alkali interaction usually leads to the formation of new phases that have different specific volumes or thermal expansion coefficients. The differences lead to spalling of surface reaction layers, permitting further attack of the underlying material. However, the research into the performance of ceramic materials in hot gases produced during coal firing has been limited. As yet, an adequate database that would permit material selection based on coal properties is not available. Also, no database is available on the rates of corrosion and strength loss of the materials, nor is a fundamental understanding of the mechanisms of vapor-phase alkali corrosion mechanisms developed.

2.0 OBJECTIVES

The overall objective of the hot-gas cleanup task is to develop reliable methods to remove particulate matter from high-temperature/high-pressure gas streams produced from coal combustion. The primary area of research will involve determinations of rates and mechanisms of filter blinding and alkali corrosion of ceramic filter materials.

Bench-scale hot-gas filter research will be performed with the pressurized fluid-bed reactor (PFBR) and a hot-gas filter vessel being built under this program. The objectives of this work are to determine particulate and vapor-phase alkali degradation of candidate ceramic filter structures. Finally, pilot-scale tests of alkali corrosion of ceramic materials will be performed with the hot-gas cleanup test loop attached to the EERC carbonizer gasification facility.

3.0 ACCOMPLISHMENTS

3.1 Bench-Scale Measurements

Originally a probe system that could be used for long-term ceramic filter testing in the pressurized drop-tube furnace (PDTF) was proposed. The probe system was originally proposed because it would be a low-cost method to expose ceramic filter elements to coal ash under high-temperature and high-pressure conditions over long operating periods. However, because of difficulties in controlling the temperature in the zone of the furnace where the ceramic filter would be operated and because the high workload on the PDTF makes it difficult to schedule long operating periods devoted strictly to ceramic filter testing, EERC personnel do not feel that assembly of a probe system for use in the PDTF would be appropriate at this time. Alternative approaches have been considered by EERC

personnel and discussed with the DOE METC Performance Monitor. Alternative approaches considered include building a bench-scale filter vessel to be used with bench-scale pressurized combustion and gasification reactor systems. A second option would involve building an extractive sampling system to pull a slipstream for testing small filter elements in conjunction with the operation of any EERC combustion or gasification system.

The design and construction of a bench-scale filter vessel that could be used in conjunction with the bench-scale pressurized fluid-bed reactor (PFBR, for combustion) and the continuous fluid-bed reactor (CFBR, for gasification/pyrolysis) was selected as the best option for obtaining high-temperature, high-pressure operational data on various filter elements. Also, it was decided that the filter vessel should be designed to be used as a slipstream device on other larger-scale pressurized combustion and gasification systems and atmospheric combustion systems at the EERC. The PFBR has been constructed to simulate the bed chemistry, ash interactions, emissions evaluation, and hot-gas cleanup testing from a PFB under closely controlled conditions. Typical operating conditions for this reactor are shown in Table 1. This 3-in.-ID by 4-ft-high, pressurized and heated reactor and 2-in.-ID hot cyclone nominally combusts 4 lb/hr of coal. The reactor is capable of operating at 1700°F and 11 atmospheres pressure. The CFBR is capable of nominally gasifying 4 lb/hr of coal. The bottom section of the CFBR is made of 3-in. pipe and is 33 in. in length. The top section is made of 4-in. pipe and is 18.75 in. in length. The reactor currently has two ceramic fiber heaters to maintain vessel temperature and eliminate hot spots. The CFBR and 3-in.-ID hot cyclone are capable of operation at a maximum of 11.5 atmospheres and 1550°F. Typical CFBR operating conditions are shown in Table 2.

Figure 1 is a drawing of the hot-gas cleanup (HGCU) bench-scale vessel for the testing of ceramic candle filters on the 3-in. PFBR currently available at the EERC. This vessel was designed to handle all of the gas flow from the PFBR at its nominal design conditions. The vessel will be approximately 10 in. ID and 66 in. long and would be designed to handle this gas flow (approximately 25 scfm) at 1550°F and 150 psig. The tube sheet will be interchangeable to handle different sized filters. The

TABLE 1

Typical PFBR Operating Conditions

Reactor Diameter	2.875 in. ID
Temperature	1400°–1700°F
Pressure	0–150 psig
Gas Flow Rate	1–30 scfm
Coal Feed Rates	1–8 lb/hr
Velocities	1–10 ft/sec
Cyclone Exit Temp.	1600°F maximum
Particulate Loading	200–9000 ppm

TABLE 2

Typical CFBR Operating Conditions

Reactor Diameter	2.9 in. ID
Temperature	1300°–1500°F
Pressure	0–175 psig
Gas Flow Rate	1–10 scfm
Coal Feed Rates	Nominal 4 lb/hr
Velocities	1.5–2 ft/sec
Cyclone Exit Temp.	1475°F
Particulate Loading	300–4000 ppm

Typical Gas Composition	Raw Gas	w/o Fluidizing N_2
CO_2	4.68	26.56
CO	2.67	15.16
H_2	7.69	43.62
CH_4	1.01	5.74
N_2	84.79	8.23

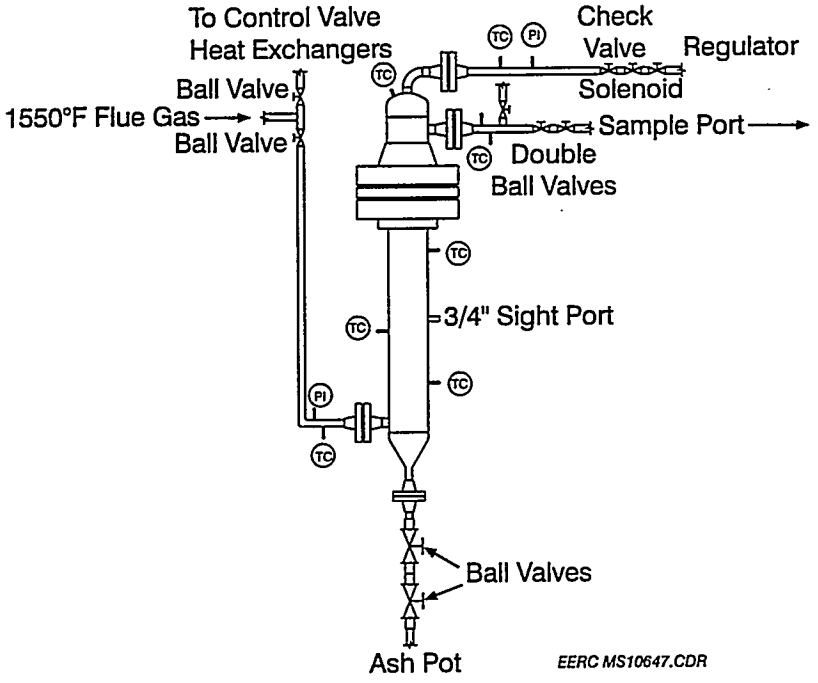

Figure 1. Schematic of high-temperature, high-pressure, bench-scale hot-gas filter vessel.

filters are sealed in the tubesheet with weighted metal donut rings which counteract the upward force imparted across the candle filter by the filter's differential pressure. The vessel is sized such that it could handle 3 candle filters up to 20 in. long and up to 2.75-in. OD. This would enable filter face velocities as low as 4 ft/min to be tested. Higher face velocities would be achieved by using shorter candles or higher gas flow rates. Proposed operating conditions for the filter vessel are shown in Table 3.

Ports are added in the filter vessel for allowing temperature and pressure measurements to be obtained. These same ports can be utilized to insert a water-cooled boroscope probe for visually inspecting the filter elements. The ash letdown station consists of two alternating high-temperature valves to act as lock hoppers.

The nitrogen backpulse system will be constructed from existing materials utilized from a previous hot-gas filter test system. The backpulse system is designed to supply a minimum of 3 candle volumes per pulse for the largest-volume candle and even higher for the smaller-candle filters. The system is capable of heating the nitrogen up to 1500°F before it enters the filter vessel. The length and volume of nitrogen displaced into the vessel is controlled by the regulated pressure (up to 800 psig) of the nitrogen reservoir and the solenoid valves used to control the timing of the cold-gas pulse that displaces the hot nitrogen in the nitrogen reservoir. Because of a height limitation, a heated 1-in. pipe is used to connect the 3-in. PFBR to the hot-gas filter vessel.

It is expected that this filter vessel will be used on other combustion and gasification equipment at the EERC. This equipment includes pulverized coal-fired furnaces, atmospheric fluid-bed combustors (both bubbling and circulating), and gasifiers including a 100-lb/hr carbonizer and the M.W. Kellogg transport reactor development unit (TRDU) at the EERC.

3.2 Pilot-Scale Measurements

To complement the laboratory- and bench-scale testing of alkali attack of ceramic filter materials, pilot-scale testing of the most inert candidate materials will be performed using the EERC test loop in conjunction with a pilot-scale carbonizer gasification facility

TABLE 3

High-Temperature High-Pressure Filter Vessel Operating Capabilities

Vessel Diameter	10 in. ID
Temperature	up to 1550°F
Pressure	
Gas Flow Rate	up to 30 scfm
Filter Sizes	2.75 in. OD by 20 in. long
Filter Face Velocities	4–15 ft/min
N_2	Backpulse system up to 1550°F inlet; both short high-pressure and long low-pressure pulses

that has been built and operated in support of other research programs. The system also includes a high-pressure, high-temperature particulate sampling system. Work in the first year will involve modifying the design of the particulate sampling system so that it can be employed on other, smaller, test systems and attaching and testing the test loop with the pilot-scale facilities.

3.2.1 High-Pressure and High-Temperature Sampling System

The High-Pressure and High-Temperature Sampling System (HPHTSS) was designed to extract dust-laden flue gas isokinetically from either an oxidizing or reducing environment. The maximum design temperature of the gas stream was specified as 1800°F for the HPHTSS. The maximum working pressure of the gas stream for the HPHTSS was specified as 150 psig.

The probe for the HPHTSS is a ⅜-in.-OD and ⅛-in.-ID 304 stainless steel tube. The probe is used for only one sampling test and then discarded. The key to the sampling system is the use of a vessel, designed to withstand high-pressure and high-temperature conditions, to enclose the low-pressure sampling devices. An illustration of the HPHTSS is found in Figure 2.

The vessel was constructed of 5-in. schedule 80 pipe and fitted with raised face 300-lb flanges. The material used for the HPHTSS pressure vessel was 316L stainless steel. The HPHTSS was designed to house both multicyclone assembly with backup filter as well as a backup filter alone.

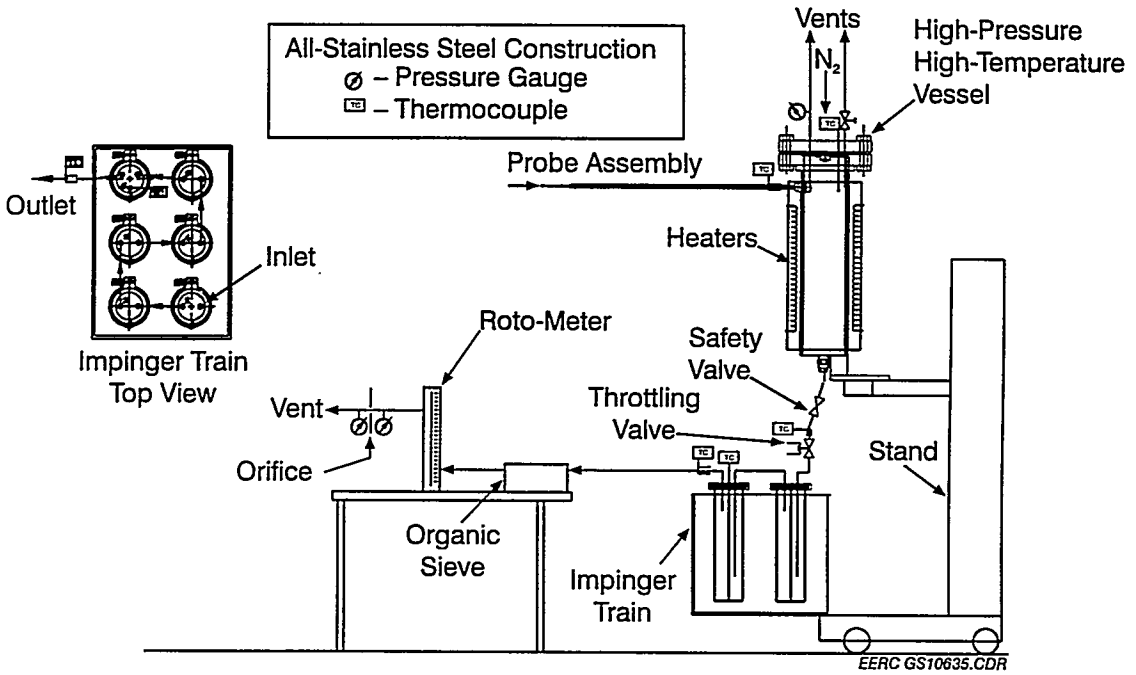

Figure 2. High-pressure, high-temperature sampling system.

The principle of operation is to pressurize the outside of the sampling device (i.e., multicyclone assembly or backup filter) with a slightly higher gas pressure then the system pressure of the flue gas. Bottled nitrogen gas will be used to pressurize the vessel. The pressure differential between the nitrogen gas within the pressure vessel and the flue gas within the sampling device will be maintained at 5 psig.

If the HPHTSS is operating in a reducing environment where the presence of organic vapors is a possibility, the pressure vessel is capable of operating at temperatures as high as 1000°F and maintaining nitrogen gas pressures up to 150 psig. Electric resistance heaters of sufficient wattage will be used to heat pressure vessel to specified temperatures.

Once the process gas exits the sampling assembly, the gas pressure is reduced through a throttling valve to approximately 50 psig. The throttling valve will also act as the flow control valve for the sampling system. A second valve was installed in series in the event that the primary throttling valve failed to close.

After the throttling valve, the process gas is cooled through a set of impingers to remove moisture and organic vapors if present. A set of up to six impingers may be used in this sampling system. These impingers are rated for 200 psig at 250°F maximum operating conditions. The impingers are made of 304 stainless steel with the interior surfaces coated with teflon. The teflon-coated surfaces allow the HPHTSS to be used for trace metal sampling.

The dry gas is then throttled to atmospheric pressure and metered through a roto-meter and orifice in order to measure total flow. The process gas then reenters the main gas stream for cleanup and disposal.

The HPHTSS is currently under final stages of construction and is scheduled for completion in mid-August 1994. This HPHTSS is the first of two systems to be built. When this prototype has been successfully tested a second HPHTSS is planned for construction. With the completion of the second HPHTSS, it will be possible to simultaneously sample the process gas from the inlet and outlet of high pressure particulate removal equipment.

3.2.2 Pilot-Scale Hot-Gas Filter Vessel

A new activity was added in September 1993 to Task 3.4, Subtask 3.4.5 Hot-Gas Filter Testing. The purpose of the new activity was to initiate an effort to design and construct a hot-gas filter vessel to be operated in conjunction with the TRDU. In the first quarter of 1994, work continued on this task. Efforts were directed at locating an existing pressure vessel which could be incorporated into a hot-gas filter system with minimal modification. Several vessels were located and the design of each was reviewed.

The first vessel was designed by the Allison Gas Turbine Division of General Motors Corporation. It was originally constructed for use as a hot barrier filter vessel to be used in Allison's direct coal-fired gas turbine project. Ownership of the vessel still remains with DOE, so cost associated with this vessel would entail only transportation to the EERC and modification of the vessel to meet our requirements.

The Allison filter vessel was designed and fabricated by Allison under DOE contract No. DE-AC21-86MC23165. It was designed to clean a gas stream containing <10 micron particles of frozen slag and ash. The filters and backpulse system were to be supplied by Industrial Pump and Filter. A water-cooled filter tube sheet was fabricated but never installed. The vessel itself is composed of 58.5 in. of 42-in.-diameter carbon steel pipe. Both ends of the pipe are capped with 48-in. torispherical heads. A number of nozzles penetrate the wall of the vessel. All flanged surfaces have been converted from raised face spiral-wound gasket designs to metal/metal seat applications. The head on the clean side of the filter tube sheet has been penetrated by twenty-six nozzles to accommodate the filter backpulse system, as well as the clean gas outlet nozzle. The vessel was used in a passthrough mode, without the tube sheet installed, in a test that exposed it to 1500°F reducing gas at 200 psig. The design limits were 2000°F and 300 psig.

A visit was made to Allison to inspect the vessel. It had been stored in an unprotected outside storage site. All carbon steel surfaces were slightly rusted, including the flange sealing surfaces. The refractory liner was cracked but had very little loss of material from spalling. It appeared that a number of the flanges would need to be resurfaced or replaced to return them to compatibility with the raised face design commonly used at the EERC. The refractory would probably have be removed and replaced to allow for modification to nozzles in the shell.

The second vessel selected for consideration was the C-121 vessel used on the KRW Gasifier. The vessel is of similar construction to that of the Allison vessel. The vessel holds an ASME stamp for 650°F shell temperature at 300 psig. The shell is 48-in.-diameter pipe 8 ft. 6 in. in length. The ends are torispherical heads. There are a number of nozzle penetrations in the head and shell in addition to the main gas inlet and outlet. This vessel, as well as the majority of equipment from the KRW Waltz Mill site is now owned by Stanton Energy Industry Consultants Inc. (SEIC). The vessel appears to be ideally suited to the application; however SEIC is not interested in selling the vessel and associated subsystems, preferring to enter into a lease arrangement, which at this time does not appear attractive to the EERC.

A third vessel has been discovered in the equipment storage area at the EERC. It was acquired several years ago as surplus equipment from the NASA Lewis Research facility. It was designed as a hot-gas filter vessel for use on a pressurized fluid-bed combustor. It holds an ASME stamp for 400°F shell temperature at 135 psig. It was designed by Aerodyne Development Corporation. The shell is fabricated from 36-in.-diameter carbon steel pipe. It has a torispherical head on the clean side of the filter tube sheet. The lower head of the shell is a cone which reduces to an 8-in. flanged ash discharge nozzle.

This vessel had set unused in an outdoor storage yard for a number of years. To assess its potential for the application, a certification report was obtained from the National Board. The vessel was brought into the shop and briefly inspected. The mineral wool insulation and stainless steel inner liner were removed from the interior of the vessel to allow inspection of the inner surface of the vessel. Minimal corrosion was found.

Heat-transfer calculations were performed on the vessel to determine what usable bore diameter would remain in the vessel after sufficient refractory had been installed to

keep the vessel skin temperatures below the 400°F rated maximum. It was determined that a 20-in. ID could be maintained using 1600°F inlet gas temperatures and mass flow rates matching the output of the carbonizer at the EERC. This would allow for installation of up to 16 candle filter elements. The number of elements could be varied to change the face velocities from 4-12 ft/minute. It may also be possible to operate this vessel in conjunction with the TRDU. The TRDU is a 200–300-lb/hr pressurized circulating fluid-bed gasifier. The TRDU has an exit gas temperature of 1800°F and a higher mass flow rate than the carbonizer. Heat-transfer calculations for this application have not been completed at this time.

The preliminary heat-transfer calculations also pointed out the need to modify one or more of the nozzles on the vessel. The dirty gas inlet nozzle must be increased in diameter to allow for a thicker layer of refractory if <400°F metal temperatures are to be maintained in the area of the nozzle. Additionally, a preheat natural gas burner will be required to prevent condensation from collecting in the vessel while the gasifier is starting up. The hot gas from the burner will enter the vessel via the same inlet as the dirty gas.

If no major problems are found in the initial inspection, the vessel will be bolted together and leak-checked prior to the start of any modifications. All modification work will be subcontracted to a stamped fabrication shop. At the completion of the modification work, the vessel will be rehydrotested to match the ASME stamp.

TASK 3.7

FUEL UTILIZATION PROPERTIES

Prepared by:

Christopher J. Zygarlicke
Donald P. McCollor
Thomas A. Erickson

August 1994

TABLE OF CONTENTS

LIST OF FIGURES

LIST OF TABLES

TASK 3.7 FUEL UTILIZATION PROPERTIES

1.0 INTRODUCTION

The Fuel Utilization Properties project will determine the impacts of specific coal properties and additives on ash formation and deposition in advanced power systems. The first year will focus on integrated gasification combined cycle (IGCC)-type systems, whereby small-scale furnaces will be employed to simulate gasification or highly reducing conditions in order to produce entrained ash and deposits for analysis. A lesser emphasis will be placed on analyzing deposits from a small-scale pressurized fluid-bed reactor (PFBR). Limited work will also be directed toward surveying the types of ash partitioning and ash deposition that could be occurring in PFB-type reactors.

2.0 OBJECTIVES

The overall objectives of this project are to determine key fuel properties and mechanisms that impact ash formation and deposition in advanced power systems and to propose and test measures for mitigating ash deposition. Specific goals for this years's work in the area of ash formation and deposition in advanced power systems include the following:

- Determining the general chemical and physical properties of simulated entrained ash and deposits that may lead to operational problems.
- Identifying and testing methods to mitigate deposition in IGCC-type systems.

3.0 ACCOMPLISHMENTS

3.1. Inorganic Transformations under Gasification or Highly Reducing Conditions

Determination of mechanisms of coal inorganic transformations under reducing or gasification conditions is being accomplished using a pressurized drop-tube furnace (PDTF). Entrained ash has been produced for several coals using gas compositions, temperatures, and pressures similar to those used in current IGCC systems. A first-generation model of inorganic transformations under gasification conditions is in the process of being formulated by revising an existing Energy & Environmental Research Center (EERC) model called ATRAN, which predicts entrained ash particle-size and composition distribution for a conventional pulverized coal combustion system. The ATRAN code will be enhanced with currently available data at the EERC as well as with data generated from the PDTF ash production tests.

Modifications were made to the existing ATRAN program by converting the original FORTRAN program to a more compact and faster C language program. Debugging and enhancements to some of the algorithms have also been completed. The major enhancement of ATRAN to include mechanisms of coal inorganic transformations under reducing or gasification conditions has been initiated. The database for ATRAN has been

expanded to include data from Illinois No. 6, Pittsburgh No. 8, and Sufco coals. Future work will focus on the kinetics of the decomposition of sulfides and carbonates.

Several important upgrades and enhancements were made to the PDTF to improve operating performance and to allow effective operation under simulated IGCC system conditions. A new lower furnace was installed and furnace insulation replaced in the upper three furnace zones, as was the central ceramic reaction tube. The load cell that monitors the coal feed rate was upgraded to 0.01-gram accuracy, allowing more precise control of sample feeding. Of particular importance was the installation of additional gas-handling equipment and mass-flow controllers to the PDTF facility. The PDTF now has the capacity to operate with gas mixtures of CO, CO_2, H_2, and water, which more closely simulates the reducing conditions encountered in advanced systems.

As a preliminary step, mineral transformations during the combustion of Black Thunder and Illinois No. 6 coals have been examined at atmospheric pressure under oxidizing conditions of 50% excess air and fuel-rich conditions of 0% and –50% excess air. These tests will provide a basis of comparison with subsequent tests under strongly reducing pressurized conditions. The fly ashes produced were analyzed by computer-controlled scanning electron microscopy (CCSEM) to determine particle-by-particle composition and mineral phases.

Mineral phases as determined by CCSEM analysis for the bulk fly ashes are given in Table 1. Because of the large percentage of "unknown" material (16.6% to 45.4%), specific trends of mineral transformations should be treated with caution. For the Black Thunder ash, the effect of fuel-rich conditions appears to be an increase in quartz, calcite, dolomite, and calcium-rich phases, along with a decrease in gypsum–aluminosilicate phases. This may be the effect of the lower particle temperature and oxygen-lean atmosphere reducing the interaction and assimilation of pure quartz and organically bound calcium into mixed calcium aluminosilicate phases. The large (45%) unknown category for the Black Thunder under full air conditions is indeed dominated by particles which are composed predominantly of calcium, silicon, and aluminum. For the Illinois No. 6 ash, the fuel-rich conditions give a decrease in iron oxide, iron and sodium aluminosilicates, and iron silicate. There is a corresponding increase in pyrite and pyrrhotite, which were absent under full air conditions. The fuel-rich conditions appear to prevent the oxidation of pyrite and pyrrhotite to iron oxide, along with less assimilation of iron into mixed phases because of the lower temperatures.

An alternative method of examining mineral matter transformations is given in Figures 1 and 2 for calcium and iron. Here, the cumulative percentage of the total particles by volume is plotted versus the elemental concentration for specific elements. This allows visualization of the general behavior of the element without using specific mineral categories, thus avoiding the problem of the "unknown" category.

For the Illinois No. 6, calcium shows little change between oxidizing and fuel-rich conditions. Approximately 85% of the particle volume contains less than 15% calcium, and 15% of the volume contains greater than 80% calcium, with very few intermediate particles. By contrast, the Black Thunder shows 60% of the particle volume with calcium concentrations between 40% and 70% under oxidizing conditions. At 0% excess air, 60% of the particle volumes have little or no calcium, with the remainder having an evenly distributed increasing calcium concentration. At –50% excess air, the calcium

TABLE 1

Mineralogy of the Bulk Filter Fly Ashes as Determined Using Computer-Controlled Scanning Electron Microscopy

	Black Thunder, full air	Black Thunder, 0% EA[1]	Black Thunder, –50% EA	Illinois No. 6, full air	Illinois No. 6, 0% EA	Illinois No. 6, –50% EA	Wyodak, full air
Quartz	9.8	16.8	17.0	19.4	18.2	18.8	13.0
Iron oxide	0.7	2.5	0.8	10.7	6.2	0.8	0.7
Periclase	0.0	0.0	0.0	0.0	0.0	0.0	0.0
Rutile	0.1	0.1	0.1	0.1	0.0	0.4	0.0
Alumina	0.0	0.0	0.0	0.0	0.0	0.0	0.0
Calcite	1.4	1.4	2.9	3.2	3.1	5.3	0.0
Dolomite	0.3	2.4	4.3	0.0	0.0	0.0	0.0
Ankerite	0.0	0.0	0.1	0.0	0.0	0.0	0.0
Kaolinite	4.5	11.5	7.0	4.4	7.1	4.8	1.9
Montmorillonite	1.1	2.8	0.7	6.6	7.6	4.9	2.5
K Al-Silicate	0.7	1.1	0.9	9.2	11.2	7.9	1.7
Fe Al-Silicate	0.2	0.1	0.1	7.9	6.0	3.0	0.3
Ca Al-Silicate	6.9	9.1	4.5	2.1	1.0	0.2	38.1
Na Al-Silicate	0.0	0.0	0.6	0.0	0.0	0.0	0.0
Aluminosilicate	0.7	2.6	0.8	3.1	3.0	0.8	1.5
Mixed Al-Silicate	0.7	0.4	1.2	4.4	2.8	6.8	2.7
Fe Silicate	0.0	0.0	0.0	1.9	1.0	0.3	0.1
Ca Silicate	4.7	6.0	5.7	0.1	0.4	0.5	1.2
Ca Aluminate	11.7	13.7	12.4	0.0	0.0	0.0	1.3
Pyrite	0.0	0.0	0.0	0.0	2.1	2.1	0.0
Pyrrhotite	0.0	0.1	0.0	0.0	3.1	7.6	0.0
Oxidized Pyrrhotite	0.0	0.0	0.4	0.1	0.8	2.0	0.0
Gypsum	0.0	0.0	0.0	0.4	0.0	0.3	0.0
Barite	0.0	0.0	0.0	0.0	0.0	0.0	0.0
Apatite	0.0	0.0	0.0	0.0	0.0	0.0	0.0
Ca–Al–P	0.0	0.3	0.5	0.0	0.0	0.0	0.1
KCl	0.0	0.0	0.0	0.0	0.0	0.0	0.0
Gypsum–Barite	0.0	0.0	0.0	0.0	0.0	0.0	0.0
Gypsum–Al-Silicate	4.8	0.0	0.7	0.0	0.0	0.0	0.8
Si-Rich	0.9	3.6	2.8	9.2	8.8	8.7	5.4
Ca-Rich	4.2	7.4	9.2	0.2	0.1	0.3	0.4
Ca–Si-Rich	1.3	1.2	1.0	0.2	0.2	0.1	0.1
Unknown	45.4	16.8	26.2	16.8	17.1	24.3	28.1

[1]Excess air.

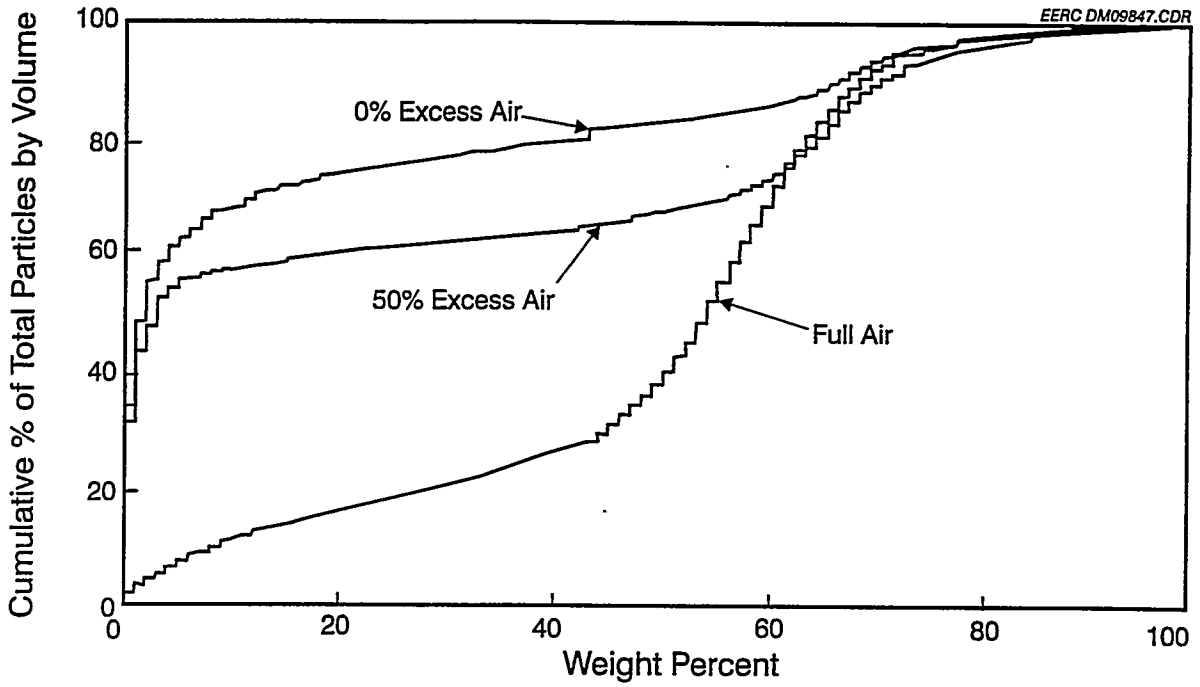

Figure 1a. Cumulative distribution of calcium in Black Thunder ash.

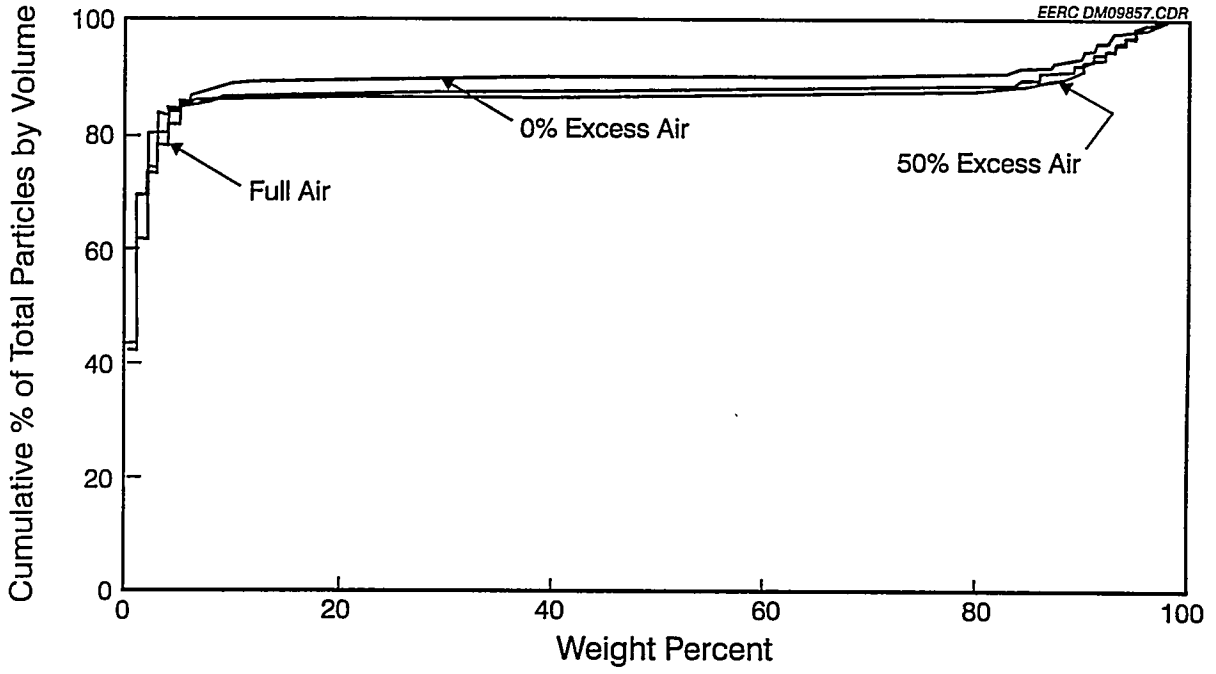

Figure 1b. Cumulative distribution of calcium in Illinois No. 6 ash.

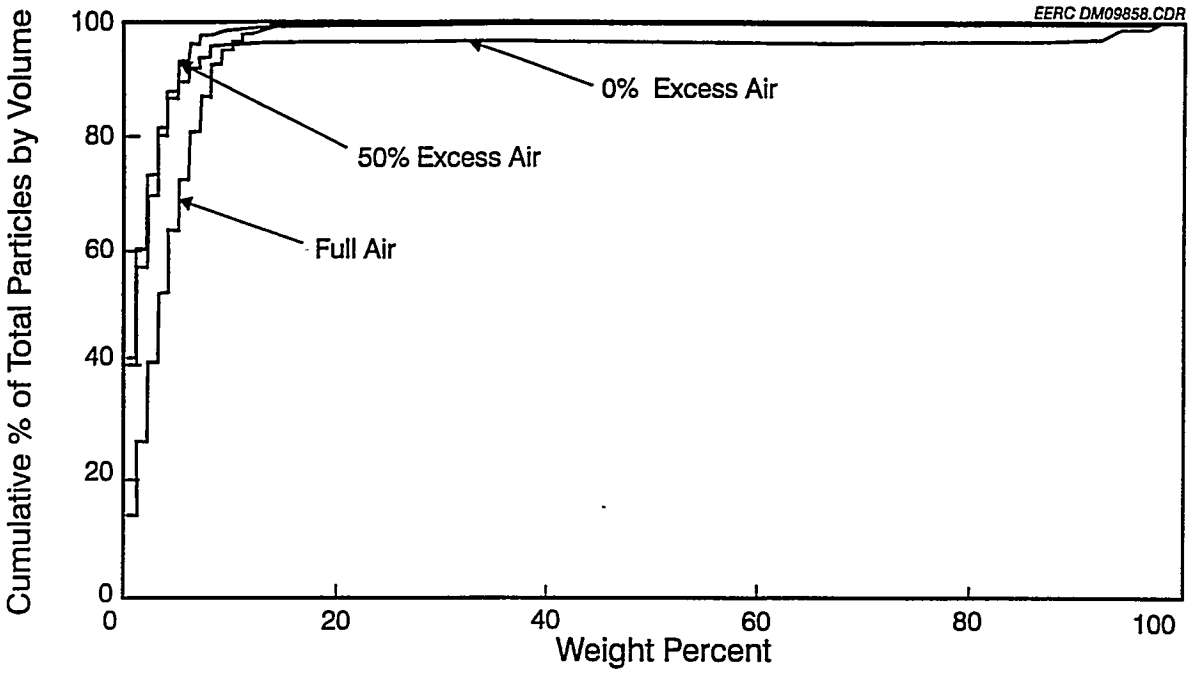

Figure 2a. Cumulative distribution of iron in Black Thunder ash.

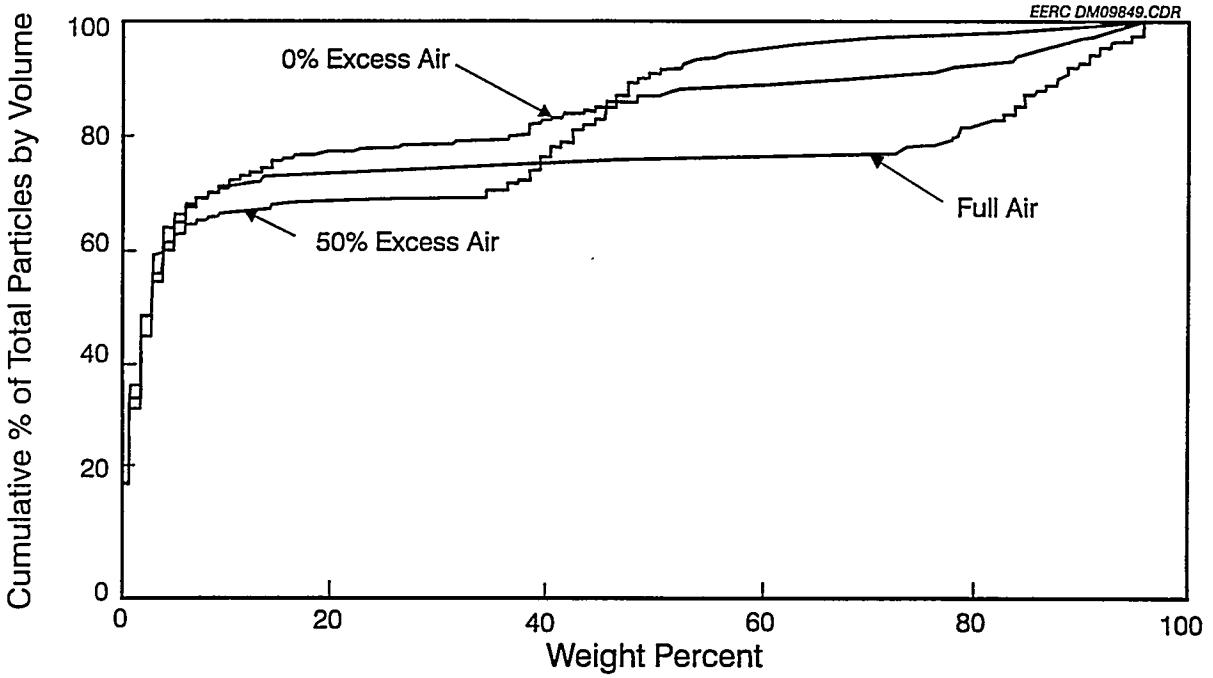

Figure 2b. Cumulative distribution of iron in Illinois No. 6 ash.

concentration is separated, with 60% of the particle volumes having little or none, and 25% having very high calcium concentrations of 60% or greater. The interpretation is that under oxidizing conditions (full air) in the Black Thunder ash there is extensive interaction of calcium with the aluminosilicates to form calcium aluminosilicates between 60% and 80% calcium. This is possibly a result of higher particle temperatures and the decomposition of calcium carbonates to calcium oxide. At more fuel-rich conditions of 0% excess air, some interaction still takes place, but to a lesser extent. Finally at –50% excess air, conditions are unfavorable for calcium–aluminosilicate interaction and favorable for the formation of calcium oxide and carbonates; hence the division into particles with very low and very high calcium levels.

Iron in the Black Thunder coal is a relatively minor component, and little change is seen between full air and fuel-rich conditions. For the Illinois No. 6 under full air, the iron concentration in the particle volumes is either quite low or quite high; less than 20% or greater than 80%. This is indicative of some interaction of iron with other species at low concentration along with the formation of iron oxide particles under the highly oxidizing conditions. Under fuel-rich conditions, the percentage of iron oxide decreases, with a concurrent increase in particles with intermediate (40%–80%) iron concentration, corresponding to pyrite and pyrrohotite.

3.2. Mechanisms of Deposit Formation in IGCC-Type Systems

Deposits will be generated in a drop-tube furnace to determine the effects of coal characteristics, system aerodynamics and transport mechanisms, pressure, temperature, and gas composition on the degree of deposit severity. Deposit severity will be assessed based on the hardness, growth rate, and liquid-phase viscosity of the deposits that are formed. The deposits will be analyzed using scanning electron microscopy, x-ray fluorescence, x-ray diffraction, and physical strength analysis. A minor part of this task will include characterizing the physical and chemical properties of deposits and fly ash generated in the EERC PFBR to assess ash partitioning and potential ash deposition problems.

A test matrix was planned for PDTF testing of Black Thunder subbituminous and Illinois No. 6 bituminous coals in the PDTF under gasification conditions. Deposits will be generated at 1500°C and collected from four different cooled collection zone temperatures: 550°, 700°, 850°, and 1000°C. Pressure for the systems will be 100–160 psi and O/C ratio will be 1.25. The deposits that are generated will hopefully simulate the silicate and sulfide types of deposits that form under different temperature regimes of gasifiers.

An initial set of shakedown tests have been performed to produce fly ash and deposits from a Drayton coal under pressurized reducing conditions. Although analysis of the fly ash is still in progress, preliminary results have been compiled herein.

The Drayton coal is a subbituminous coal, and the as-received proximate and ultimate analyses are given in Table 2. Fly ash and an ash deposit were produced in the PDTF at approximately 1500°C and 100 psig under reducing conditions. Details of the test conditions are given in Table 3.

The ash deposit was mounted in epoxy and cross-sectioned vertically for SEMPC and morphological analysis. The SEMPC analysis was performed in two separate areas, in

TABLE 2

Proximate and Ultimate Analysis of Drayton Coal	
Proximate Analysis, as-received, %	
Moisture	3.20
Volatile Matter	35.89
Fixed Carbon	47.88
Ash	13.03
Ultimate Analysis, as-received, %	
Hydrogen	4.56
Carbon	68.19
Nitrogen	1.52
Sulfur	0.87
Oxygen	11.82
Ash	13.03
Heating Value, Btu/lb	11830

the base and top region of the deposit, respectively. No significant differences were found in mineral species or average elemental concentrations between the two regions. Mineral composition as determined by SEMPC is given in Table 4. The deposit was collected in a gas temperature zone of about 1000°C and it was primarily a high-temperature silicate–rich deposit with no obvious reduced mineral species being identified. Analysis of the fly ash has not yet been performed.

3.3. Fouling Deposit Mitigation Measures

The PDTF will be used to test additives for mitigating ash deposition, also using Illinois No. 6 and Black Thunder coals. The test matrix will use the same system conditions described in activity 3.2 for deposit mechanism determination. The additives that are tested will be mixed with coal at some predetermined proportion and the coal–additive mixture will be fired under an O/C stoichiometry 1.25, an initial gas temperature of 1500°C, and a pressure of 100–160 psi. Four deposits will be collected at 550°, 700°, 850°, and 1000°C and the chemistry and physical strengths of the deposits will be compared to those deposits formed without the additive. The potential additives are zeolite, kaolinite, and limestone additives. Tests will be run to assess the effectiveness of the additives, and inorganic analysis of the particulate samples and deposits will examine the interaction of the additives with the coal ash and their effectiveness.

Additives will be selected using the knowledge gained previously in the study of deposit formation mechanisms. Additives will most likely be alkali and sulfide getters, acting to render these species ineffective for depressing melting points of entrained ash and deposit material. It is the lower-melting-point and lower-viscosity phases that can cause entrained ash to stick and deposits to form and acquire strength. Additives may also be selected that act to physically weaken deposits by diluting the bad-acting components or by creating a more porous and weakened deposit structure.

TABLE 3

Test Conditions for Fly Ash and Deposit Production Under Pressure in a Reducing Atmosphere

	Fly Ash Deposit	
Drayton Test Conditions, 7-26-94	DRAY 191	DRAY 192
Coal Feed Rate, g/min	0.1662	0.1458
Avg. Coal Feed Rate, g/min	0.1708	0.1441
Linear Coal Feed Rate, g/min	0.1650	0.1414
Total Weight Coal Fed, g	5.9	4.3
PDTF Pressure, psig	93.7	98.8
Zone 1 Tube Temp., °C	1478	1449
Zone 2 Tube Temp., °C	1498	1498
Zone 3 Tube Temp., °C	1499	1460
Optical Zone Temp., °C	–7	0
Zone 4 Tube Temp., °C	1152	939
Substrate Metal Temp., °C	101	735
Avg. Quench N_2 Flow Rate, slpm	1.93	1.14
Avg. Feeder Air Flow Rate, slpm	0.48	0.48
Avg. Feeder Gas Flow Rate, slpm	12.00	11.99
Avg. Secondary Air Flow Rate, slpm	0.00	0.00
Avg. N_2 Flow Rate, slpm	2.99	3.01
Initial O_2 Concentration, mol%	0.65	0.65
Exit Gas Equivalence Ratio	2.394	2.100
Excess Air, %	–58.24	–52.39
Excess Air, avg. %	–59.37	–51.83
Stoich. Fraction of O to C	1.06	1.20
Avg. Stoich. Fraction O to C	1.03	1.22
Primary Gas Velocity, m/s	1.767	1.693
Total Gas Velocity, m/s	0.2340	0.2207
Accelerator Gas Velocity, m/s	0.27	1.55
Avg. Residence Time, s	6.640	6.566
Residue Collected This Run, g	0.5326	0.0983
Composite Residue Collected, g	0.5326	0.0983
Weight of Ash Fed, g	0.7693	0.5607
Composite Percent Ash, %	62.22	62.22
Composite Carbon Burnout, %	90.55	90.55
Composite % Ash Closure	24.92	4.60
Oxygen Analyzer, mol%	–0.03	-0.07
Carbon Dioxide Analyzer, mol%	14.23	12.17
Carbon Monoxide Analyzer, ppm	20.0	20.0

TABLE 4

Mineral Composition of Drayton Deposit Base and Upper Portion

Mineral Name	Frequency, % Bottom	Top
Oxide Rich		
Aluminum Oxide	0.8	0.0
Calcium Oxide	1.6	0.0
Iron Oxide	1.6	1.6
Mixed Oxide-Rich	0.8	0.8
Total for group	4.8	2.4
Phosphorous-Rich		
Mixed Phosphorous-Rich	0.8	0.0
Total for Group	0.8	0.0
Silicon Rich		
Quartz	19.2	13.6
Anorthite	3.2	5.6
Kaolinite	29.6	28.0
Altered Kaolinite	8.0	12.0
Montmorillonite	16.0	23.2
Wollastonite	1.6	0.0
Mixed Silicon-Rich	16.0	13.6
Total for Group	93.6	96.0
Other	0.8	1.6

The coals that will be tested in the DTF additive evaluation tests will be Illinois No. 6 and Black Thunder. The reasons for selecting these coals are as follows:

- Black Thunder has levels of sodium, potassium, and calcium likely to cause deposition and fouling problems in an advanced gasification system and is already recognized as a problem coal in some conventional combustion systems. The level of calcium makes it likely that the lower-temperature calcium sulfide deposits will be formed. It also contains a low amount of kaolinite which reduces the propensity for inherent interfering sorbing action of the ash in the flame. Kaolinite has been proven to be a good getterer of certain coal minor elements such as sodium in conventional combustion systems.

- Illinois No. 6 coal has only small amounts of calcium, minimizing the likelihood of low-temperature calcium sulfide deposits forming. Instead, the high levels of iron, primarily as pyrite, and aluminosilicates should form primarily high-temperature iron sulfide and iron aluminosilicate deposits.

Previous work has shown that gasification-type deposits can consist of higher-temperature formations of alkali silicates or lower-temperature formations of iron and

alkali sulfides. Selection of additives for precombustion injection was made primarily on the basis of the potential for the additive to provide the following:

- Adequate surface and structure for entrapment or physical contact between low-melting alkali species and the additive, within or shortly after the coal flame.

- Chemical compatibility for reactions that will promote capture of alkali species within or shortly after the coal flame, primarily through chemical reaction between the components or nucleation of vapor-phase species. Capture of sulfur in a higher melting point phase may also be another mechanism of deposit mitigation.

Additive materials that work well for actual chemical reaction in the flame or shortly after the flame are aluminosilicates, especially those that can attain small particle sizes with some physical porosity or surface roughness. These characteristics allow for capture with subsequent chemical reaction. Potential candidate additives that meet these criterion are kaolinite, zeolite, vermiculite, emathlite, and bauxite. Unlike combustion, in the reducing environment of a gasification system, calcium-based materials such as limestone ($CaCO_3$) or lime ($Ca(OH)_2$) may actually aggravate rather than mitigate deposition.

Problems may arise in the area of operation and maintenance when coal with any of these additives is burned. Low-melting-point silicate-based eutectics may develop on the surface of entrained ash silicates when using the aluminosilicate additives are used causing fouling in the hotter sections of a gasifier heat-transfer zone. When calcium-based additives are used, calcium sulfide fouling may occur in the cooler regions of the heat-transfer areas pass because of increased availability of calcium to form calcium sulfide deposits. Other operational concerns include the handling and feeding of the additive material. Most of the silicate materials are fairly conducive to handling and feeding; however, calcium-based materials can cause serious dust problems if the particle sizes are too small.

Additives will be selected for DTF testing in this program in the near future. At this time, some candidates under consideration are zeolite, kaolinite, and limestone. These materials should be commercially available at reasonable costs. The zeolite material should provide maximum entrapment of alkali species in its layered and porous clay structure, while also providing an aluminosilicate matrix to react in the coal flame. Zeolite may also be tailored for desired chemical and physical properties if produced synthetically. Kaolinite is a good candidate for in-flame metal capture, primarily because of its fine size distribution and relatively pure inert composition, which adds only a minimum potential for detrimental boiler operation and maintenance side effects. Kaolinite has been shown to be effective in conventional combustion systems, but may perform differently under reducing conditions and may not have the physical entrapping effect of the zeolites. Lime will be used primarily as an additive to physically break up the deposits that form, or to combine with sulfur to circumvent formation of troublesome iron sulfides at intermediate temperature ranges of 800°–1100°C.

TASK 3.8

PRESSURIZED FLUIDIZED-BED COMBUSTION

Prepared by:

Michael Mann
Ann Henderson
Michael Swanson

August 1994

TABLE OF CONTENTS

LIST OF FIGURES

LIST OF TABLES

TASK 3.8 PRESSURIZED FLUIDIZED-BED COMBUSTION

1.0 INTRODUCTION

One of the overall goals of the U.S. Department of Energy (DOE) is the development of the technology necessary to provide for a secure, reliable, affordable, and environmentally sound source of energy. This is important in order to ensure economic stability and growth in the next century as well as to reduce current and minimize future environmental impacts associated with power generation in the United States and the world as a whole. The continued and potentially expanded use of abundant coal reserves is one key to a secure and affordable source of energy in the United States.

Throughout the world, coal will play an expanded role in the production of the affordable energy necessary to meet the demands of economic development and growth. The development of more efficient and environmentally sound technology in the United States may present export market opportunities throughout the world; specific examples include East Central Europe and the Pacific Rim. In East Central Europe, where substantial coal utilization has occurred for decades, an urgent need exists for commercial emissions control technology as well as for current clean coal technology. The lack of emissions control technology in East Central Europe is exacting a high price in terms of human health and long-term environmental damage. In contrast, the Pacific Rim has only recently begun to expand the use of coal to meet energy demands created by economic growth. Therefore, the need in that region is for commercial and developing technologies to allow new coal-fired plants to meet current and future energy demands in an environmentally sound manner.

In order for coal to play a key role in the U.S. energy mix, it will be necessary to develop and commercialize technologies capable of producing electricity at significantly higher overall system efficiencies than the 30%–35% levels currently observed in conventional coal-fired systems. Also, the production of liquid and gaseous fuels from coal will be necessary in order to effectively meet the broad spectrum of future energy needs. In order to achieve overall system efficiencies of 40% to 60% in an environmentally acceptable manner, development and demonstration of advanced second-generation utilization and conversion technology will be necessary. Examples include 1) advanced pulverized coal-fired combustion systems; 2) high-temperature heat exchangers for indirect firing of gas turbines; 3) pressurized combustion in staged, entrained, slagging, and fluidized-bed modes; and 4) integrated gasification and direct gas-fired turbines.

A number of barrier issues exist that are not unique to individual technologies but are in some manner common to all advanced power system processes for both oxidizing and reducing environments. Examples include materials issues, specifically ceramic and refractory components, and operational issues unique to high-temperature pressurized systems. The focus of the current work on pressurized fluidized-bed combustion is the development of sorbents for in-bed alkali control.

2.0 OBJECTIVES

The goal of the pressurized fluidized-bed combustion (PFBC) activity is to generate fundamental process information that will further the development of an economical and environmentally acceptable second-generation PFBC. The immediate objectives focus on generic issues, including the fate of alkali, the sulfide species in the carbonizer char, and the Resource Conservation and Recovery Act (RCRA) heavy metals in PFBC. A great deal of PFBC performance relates to the chemistry of the bed and the gas–solids contacting that occurs during combustion. These factors can be studied in a suitably designed bench-scale reactor. The present studies are focusing on the emission control strategies applying in the bed, rather than in hot-gas cleaning. Emissions include alkali and heavy metals in addition to SO_2, NO_x, N_2O, and CO.

3.0 ACCOMPLISHMENTS

3.1 Description of Pressurized Fluidized-Bed Reactor

A pressurized fluidized-bed reactor (PFBR) has been constructed at the Energy & Environmental Research Center (EERC) to simulate the bed chemistry, ash interactions, and emissions from a PFB under closely controlled conditions. This reactor is used for sorbent characterization, gaseous emissions including trace elements, agglomeration, and hot-gas cleanup testing in a cost-effective manner over a wide range of operational conditions. The 55-in.-tall reactor is constructed of 3-in. Schedule 80 pipe and is externally heated with three ceramic heaters. A hot cyclone collects the ash and bed material that is carried out of the reactor. The preheated fluidizing gas can be a mixture of air and nitrogen or just air; in addition, one additional gas such as carbon dioxide, carbon monoxide, sulfur dioxide, or a nitrogen oxide can be added to result in a fuel gas similar to that generated in a full-scale fluidized-bed combustor. Preheated gas at temperatures of up to 1400°F and pressures of up to 200 psig are supplied at the bottom of the reactor through a 1-in. Schedule 40 pipe. The fluidizing gas is supplied at sufficiently high velocities to prevent the sized bed material from dropping out during operation. Figure 1 shows the maximum allowable working pressure of the reactor at various temperatures.

The fluidizing gas enters the 3-in. Schedule 80 main section of the reactor through a conical transition. This conical section was designed without a distributor plate to allow quick removal and quench of the bed material after completion of a test. Bed material can be sampled or collected using a lock hopper system located at the bottom of the reactor. A sight port at the top of the reactor is fitted with a color video camera for on-line observation of the bed during either high-pressure or atmospheric operation. A recorder may be added to the camera at a later date. Figure 2 is a side view schematic of the reactor and cyclone. Figure 3 is a photograph of the actual reactor vessel, cyclone, air preheater, reactor collection pot and fuel feed hopper. Figure 4 is a photograph of the final system after the external heaters and other auxiliaries have been installed.

Temperatures in the reactor are measured with eleven Type K thermocouples. These are located at 0.25, 1.75, 3.5, 5, 7, 9, 11, 15, 23, 31, and 43.25 inches above the conical transition section. Thermocouples are also located at the gas inlet, the cyclone

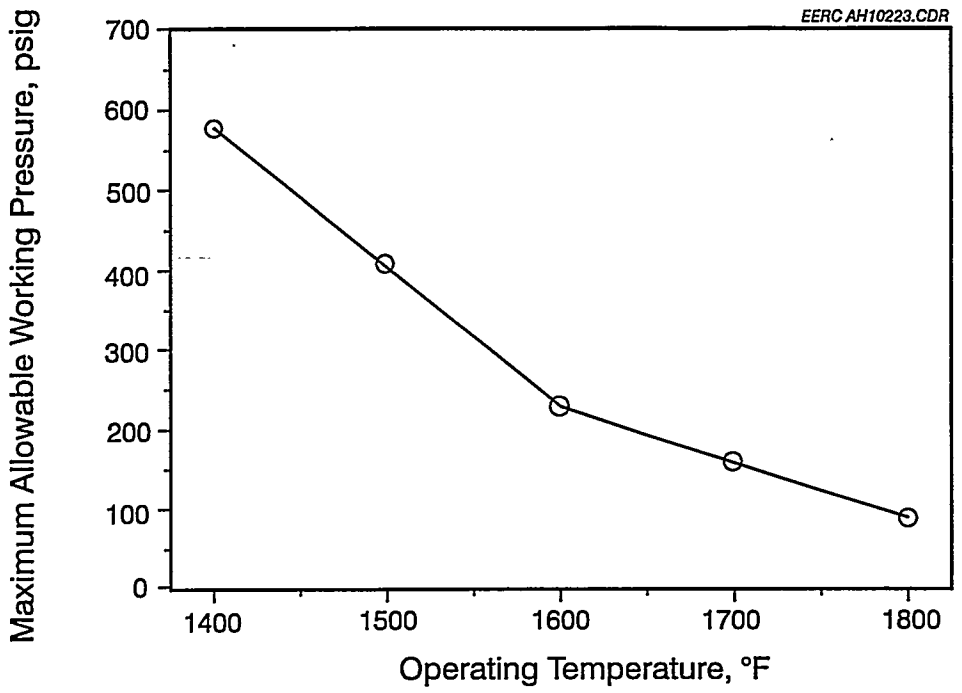

Figure 1. Reactor maximum allowable working pressure over a range of temperatures.

exit, and the pressure letdown valve inlet. A sampling port is located downstream of the pressure letdown valve.

The use of electric heaters provides the capability to match the fuel feed rate to the amount of bed material in the reactor. External heaters are used for heating and maintaining the reactor and hot cyclone at temperatures of up to 2000°F for atmospheric operation and up to 1700°F for operation at 150 psig. The external ceramic heaters on the gas preheater and the reactor itself are rated at 10.8 and 10.05 kW, respectively, with an upper temperature limit of 2200°F. In a full-scale system, the bed is deep relative to that in the PFBR. Therefore, to keep the coal feed rate-to-bed inventory similar between bench- and full-scale systems, the coal feed rate in the PFBR is kept low relative to full-scale systems, compared on a fuel feed rate per bed cross-sectional area basis. Therefore, additional heat is required to maintain the desired temperature. The high heat losses through the reactor walls inherent to small-scale systems also require either good insulation or reactor heating. This type of heating system provides very good control of the reactor temperature. At atmospheric pressure, an in-bed cooling coil can be used to remove excess heat from the high-temperature dense-bed region, allowing for higher fuel feed rates and providing a more uniform overall temperature distribution. The use of both air and nitrogen as fluidizing gas allows excess air and gas velocity to be matched to any design condition.

The bench-scale PFBR is equipped to feed either dry fuel or slurry. Slurry feed is metered with a variable-speed pump. Dry coal and sorbent are metered with separate augers that feed into a common water-cooled auger, which in turn carries the material

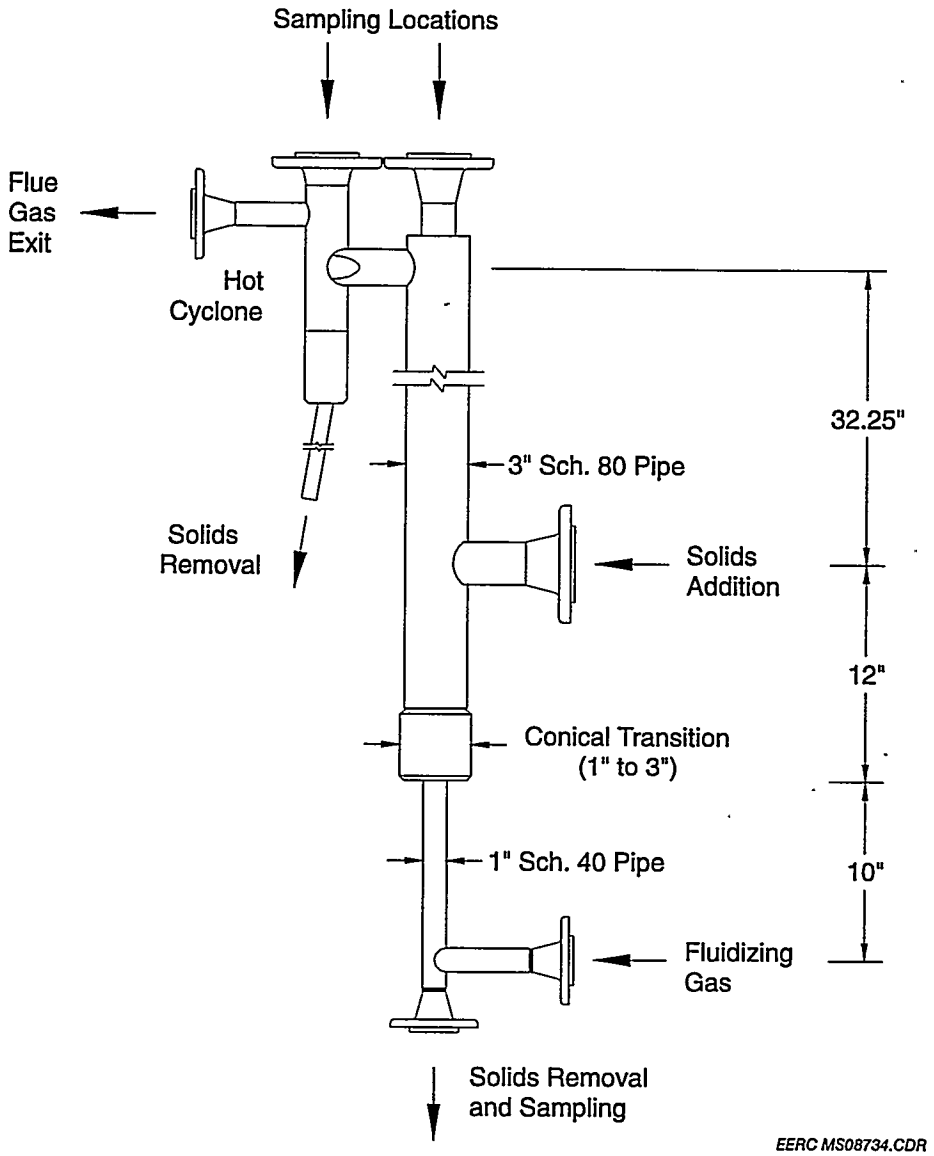

Figure 2. Side view of PFBR.

into the reactor. A bed material hopper empties directly into the common auger, without flow control. Each hopper is maintained at a pressure slightly higher than that in the combustor during operation. The hoppers can be isolated from the pressurized system so that they can be refilled during a test. At the bottom of each hopper is a plastic sight tube; in addition, the fuel and sorbent hoppers are equipped with sensors to alert the operator when the hoppers are empty and need to be refilled. A data acquisition and control system is used to monitor and record all critical pressures, temperatures, flow rates, and emissions. These critical data include the gas-flow rates, bed static pressure and differential pressures across the bed and cyclone, and eight different internal reactor temperatures. The air and nitrogen flow rates are controlled automatically to flow rate set points. The reactor pressure is automatically controlled to a pressure set point. The three ceramic heaters on the reactor may be controlled manually to a given heater temperature, or controlled automatically to maintain a desired gas temperature in each zone. Ports for alkali sampling probes or, alternatively, solid-sampling or gas-sampling

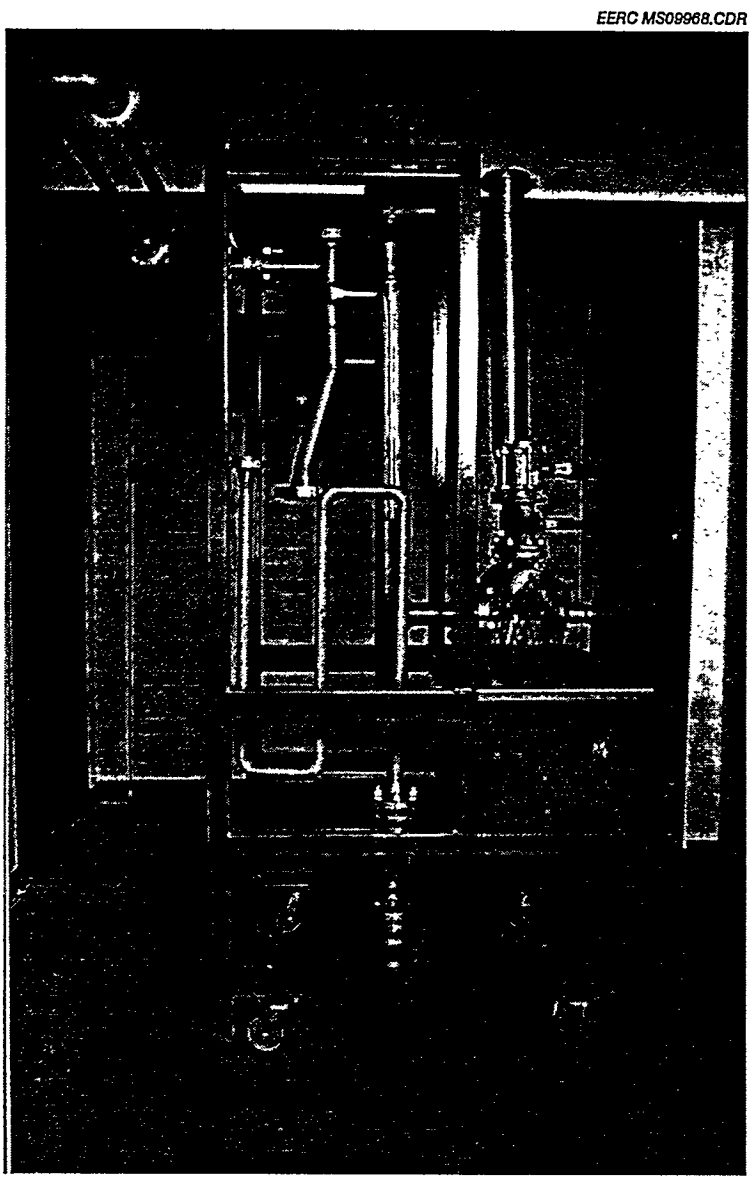

Figure 3. Photograph of PFBR.

probes are located at the top of the reactor and the top of the cyclone. An air-cooled deposition probe is located at the top of the reactor.

An alkali sampling probe is under construction and is expected to be ready for shakedown testing in July.

3.2 Shakedown Testing of Bench-Scale PFBR

Shakedown of the reactor, which commenced in 1993, is detailed in the topical report, "Advanced Power Systems, Topical Report Task No. 3.0," Contract No. DE-FC21-93MC30097. This year, additional shakedown followed the installation of a new backpressure control valve and the slurry feed system. The pressure tests with dry feed were conducted with Beulah lignite at a pressure of 150 psig and an average temperature

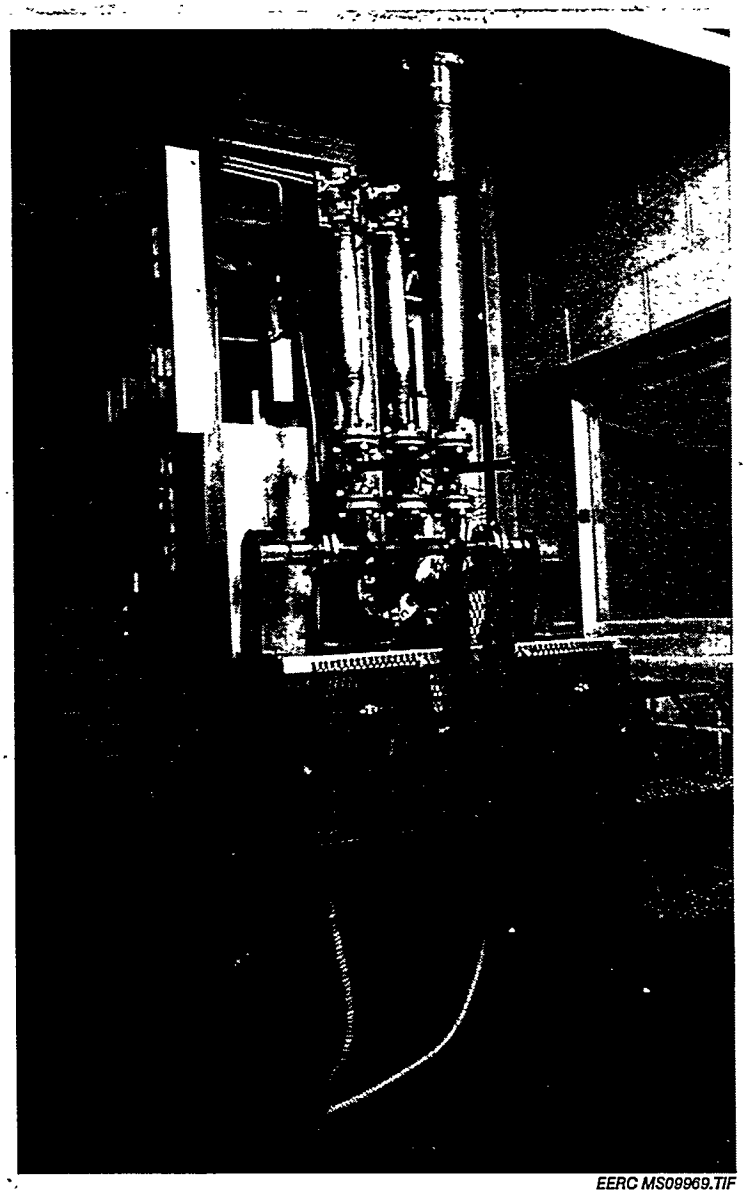

Figure 4. Photograph of PFBR in external heat jacket with auxiliaries installed.

of 1550°F. Start-up and shutdown procedures for pressurized operation were established. The slurry feed system was tested with Little Tonzana (Alaska) coal–water fuel (CWF) at 150 psig and 1550°F. The slurry feed pump is capable of delivering 3 to 8 lb/hr fuel against a reactor pressure of 150 psig. The feed rate is determined in part by the heat input of the fuel; the feed rate must be high enough to deliver enough heat to maintain the desired reactor temperature without exceeding it. While some heat can be made up with the external ceramic heaters, the heaters alone cannot supply full reactor temperature during pressurized operation. A second constraint on the minimum slurry feed rate is that the feed rate must be high enough to keep the material flowing into the reactor: if the feed rate is too low, the slurry will dry out and plug the feed line. The temperature distribution in the reactor was found to be much more uniform with the slurry feed than with a similar fuel fed dry.

3.3 Experimental

The first pressurized tests on the PFBR evaluated heavy metals partitioning and combustion chacteristics of three fuel–water mixtures. The three slurries were made of hot-water-dried (HWD) refuse-derived fuel (RDF), and HWD North Dakota lignite, and a blend of these two fuels. A test was also performed with the as-received Knife River lignite, referred to in this report as dry, as opposed to slurry, even though it was not dried prior to testing. The analyses of these fuels are shown in Table 1, along with the analysis of the Little Tonzona slurry used for shakedown testing.

A shakedown test with the dry Knife River test was conducted on June 16, 1994. During the test, the flue gas was continuously sampled for O_2, SO_2, NO_x, N_2O, HC, CO, and CO_2, to be compared to the flue gas emissions resulting from Knife River slurry combustion. No particulate sampling was performed for this test. Bed material and fly ash samples were taken.

The Knife River lignite slurry was tested on June 30, 1994; the RDF slurry and the blend will be tested during the last week in July. Continuous emissions sampling of the flue gas measured the levels of O_2, SO_2, NO_x, N_2O, HC, CO, and CO_2. The flue gas was also sampled for volatile organic carbons (VOC), and EPA Method 5 was used to measure particulate in the flue gas. Solid samples include fly ash and bottom ash, which will be analyzed for heavy metals and unburned carbon. The fluidizing gas was a mixture of air and nitrogen, preheated to about 650°F. Table 2 shows the operating data for the shakedown test with Knife River lignite, the shakedown test with Little Tonzona slurry, and the Knife River slurry test. The heat input for the Knife River slurry was about 38,000 Btu/hr, compared to 31,000 Btu/hr for the dry Knife River and 29,000 Btu/hr for the Little Tonzona slurry. All three tests were operated at similar temperature, velocity, and excess air levels. Figure 5 shows the temperature distributions for the three tests. The two slurries had very similar temperature distributions, while the dry fuel had a lower bed temperature and higher freeboard temperature.

Table 3 shows the emissions data for the three tests. It is important to remember that the emissions shown in ppm and percent will be low because of the make-up nitrogen added to the combustion air to maintain the desired velocity in the reactor. Figure 6 shows that the SO_2, NO_x, and N_2O emissions were relatively steady for the length of the test. Figure 7 compares the emissions, in lb/MM Btu, for the three tests. The SO_2 emissions were highest for the Little Tonzona slurry, followed by the Knife River slurry. The utilization of inherent alkali for sulfur capture was about 57% for the Little Tonzona slurry, 65% for the Knife River slurry, and 78% for the dry Knife River lignite. NO_x and N_2O emissions are greatly influenced by reactor temperature; the relatively high freeboard temperature for the dry Knife River test resulted in higher NO_x and lower N_2O emissions than either slurry test. Hydrocarbon emissions were quite low for all three tests.

4.0 FUTURE WORK

The remaining slurry tests will be completed during July and early August. As soon as construction of the alkali sampling probe is completed, the probe will be shaken down and parametric testing of in-bed sorbents for alkali control will begin.

TABLE 1

Moisture-Free Fuel Analyses

	Knife River Dry	Knife River Slurry	RDF Slurry	Lignite/ RDF Slurry	Little Tonzona Slurry
Proximate Analysis, %					
Volatiles	47.3	42.8	56.1	49.2	49.71
Fixed Carbon	41.2	467.0	32.8	40.9	40.05
Ash	11.4	10.3	11.1	9.9	10.24
Ultimate Analysis, %					
Hydrogen	4.4	4.6	7.2	5.8	4.39
Carbon	61.1	66.0	68.0	67.4	63.67
Nitrogen	0.9	0.9	0.5	0.8	0.75
Sulfur	1.6	1.5	0.1	1.0	1.42
Oxygen	20.5	16.7	13.1	15.0	19.53
Ash	11.4	10.3	11.1	9.9	10.24
Ash Composition, % as oxides					
Calcium, CaO	22.6	23.5	1.9	9.6	25.3
Magnesium, MgO	9.1	11.2	2.3	6.6	2.7
Sodium, Na_2O	3.2	0.9	0.4	0.7	0.2
Silica, SiO_2	25.1	22.3	41.8	37.7	27.6
Aluminum, Al_2O_3	9.7	10.7	36.0	24.7	20.5
Ferric, Fe_2O_3	3.6	5.3	2.6	5.8	7.2
Titanium, TiO_2	0.5	0.4	10.2	3.7	0.2
Phosphorous, P_2O_5	0.4	0.4	1.6	0.7	0.5
Potassium, K_2O	0.3	0.3	0.3	0.4	0.2
Sulfur, SO_3	25.4	24.9	3.0	10.1	15.5
Heating Value, Btu/lb	10,940	11,691	14,199	12,666	10,863
Solids content, %	NA[1]	55.5	45.6	56.7	53.7
Viscosity, cp	NA	500	500	500	500
Moisture content, %	31.7	NA	NA	NA	NA

[1] Not applicable.

TABLE 2

Summary of Process Data

Test No.	Knife River Dry	Knife River Slurry	Little Tonzona Slurry
Start Time	11:36	11:00	10:58
Stop Time	15:24	13:27	13:06
Date	06-16-94	06-30-94	06-22-94
Fuel Feed Rate, lb/hr	4.34	5.88	4.96
Fuel Feed Rate, Btu/hr	31,265	38,138	28,629
Reactor Pressure, psig	150.42	153.1	151.2
Reactor Pressure Drop, in. H_2O	13.87	11.4	11.5
Cyclone Pressure Drop, in. H_2O	14.53	4.4	10.9
Fluidizing Gas, scfm			
Air	11	11.26	10.23
Nitrogen	11.5	11.01	12.27
Total	22.5	22.27	22.5
Flue Gas			
O_2, %	4.8	4.5	4.8
CO_2, %	4.2	4.7	3.7
CO, lb/MM Btu	0.007	0.001	0.010
SO_2, lb/MM Btu	0.617	0.883	1.055
NO_x, lb/MM Btu	0.387	0.242	0.273
N_2O, lb/MM Btu	0.053	0.118	0.131
Hydrocarbons, lb/MM Btu	0.016	0.035	0.039
Excess Air, %	23.4	21.9	23.2
Sulfur Retention, %	80.0	65.0	60.0
FG SGV[1], ft/sec	2.95	2.94	2.91
Reactor Temperatures			
Preheater Exit	662	649	652
Plenum	927	813	943
0.25 in.	1394	1345	1396
1.75 in.	1419	1493	1459
3.5 in.	1409	1511	1461
5.0 in.	1415	1522	1474
7.0 in.	1426	1529	1476
9.0 in.	1442	1524	1472
11.0 in.	1462	NA[1]	NA
15.0 in.	1522	1568	1526
23.0 in.	1728	1642	1650
31.0 in.	1733	1616	1634
43.25 in.	1672	1556	1559
Average	1523	1551	1523
Cyclone Exit	1428	1432	1392

[1] Flue gas superficial gas velocity.

[2] Not available – slurry feed enters the reactor through this thermocouple port.

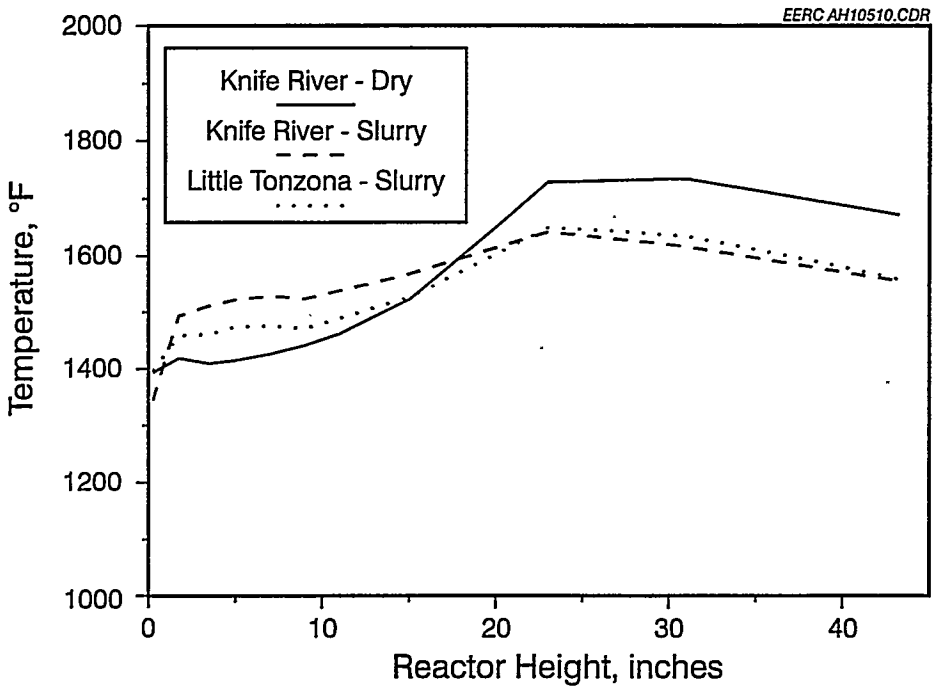

Figure 5. Temperature distributions for dry Knife River, Knife River slurry, and Little Tonzona slurry.

TABLE 3

Emissions Data

	Knife River Dry	Knife River Slurry	Little Tonzona Slurry
O_2, %	4.80	4.52	4.79
Excess Air, %	23.42	21.9	23.20
CO Content, ppm	2	1	3
CO Emission, lb/MM Btu	0.007	0.001	0.010
CO_2 Content, %	4.2	4.7	3.7
NO_x Content, ppm	73	53	44
NO_x Emission, lb/MM Btu	0.387	0.242	0.273
N_2O Content, ppm	10	27	22
N_2O Emission, lb/MM Btu	0.053	0.118	0.131
HC Content, ppm	1	1	0.3
HC Emission, lb/MM Btu	0.016	0.035	0.039
SO_2 Content, ppm	83	139	122
SO_2 Emission, lb/MM Btu	0.617	0.883	1.055
SO_2 Retention, %	80.0	65.0	60.0
Alkali-to-Sulfur Ratio	1.02	0.97	1.05
Alkali Utilization	78.5	67.3	57.1
Avg. Comb. Temp., °F	1523	1551	1523

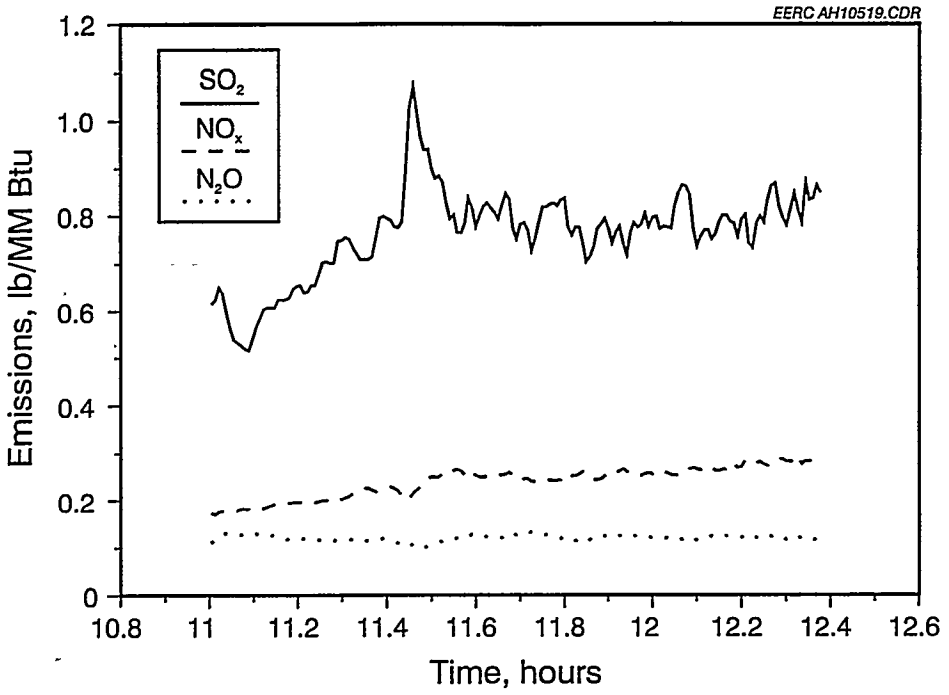

Figure 6. Flue gas emissions over time for the Knife River slurry.

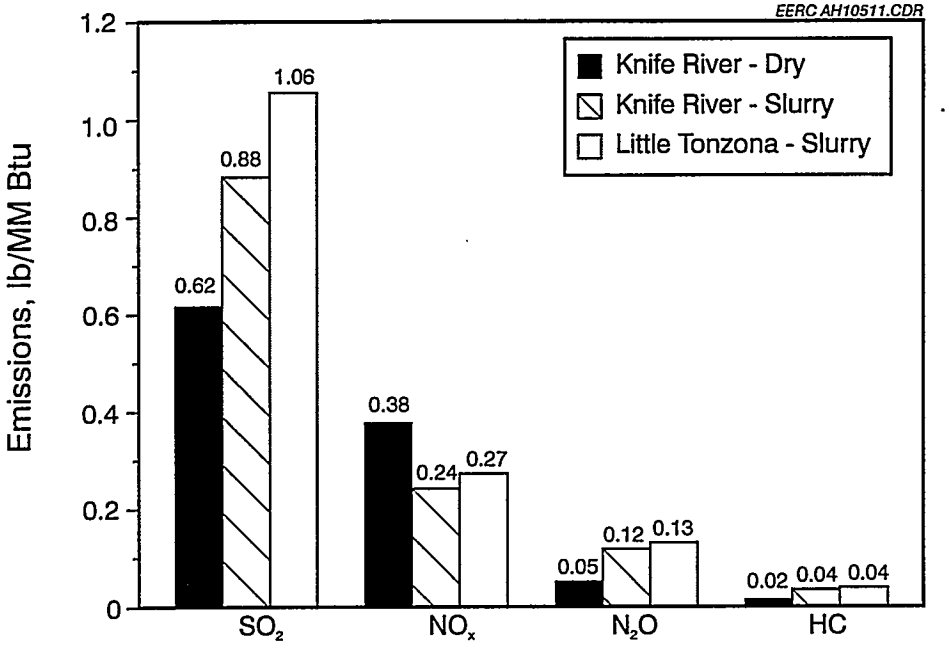

Figure 7. Comparison of flue gas emissions for three tests.

TASK 3.9

CATALYTIC TAR CRACKING

Prepared by:

Brian C. Young
Ronald C. Timpe

August 1994

TABLE OF CONTENTS

LIST OF FIGURES

LIST OF TABLES

TASK 3.9 CATALYTIC TAR CRACKING

1.0 INTRODUCTION

Tar produced in the gasification of coal is deleterious to the operation of downstream equipment including fuel cells, gas turbines, hot-gas stream cleanup filters, and pressure swing adsorption systems. Catalytic cracking of tars to smaller hydrocarbons can be an effective means to remove these tars from gas streams and, in the process, generate useful products, e.g., methane gas, which is crucial to the operation of molten carbonate fuel cells.

The need for on-line cracking of gasification tars is common to many types of gas stream cleanup. Aerosol tars are not readily removed from gas streams by conventional means and, as a consequence, often end up plugging filters or fouling fuel cells, turbines, or sorbents. Catalytic cracking of these tars to molecular moieties of C_{10} or smaller would prevent the problems commonly attributed to the tars. As an example, the moving Bourdon (fixed-bed) gasifier by virtue of its efficient countercurrent heat exchange and widespread commercial use may offer the lowest-cost integrated gasification combined cycle (IGCC) system if tar generation and wastewater contamination can be minimized. A project has been undertaken on catalytic tar cracking to evaluate the potential of selected catalysts to minimize tar accumulation and maximize char conversion to useful liquid and/or gaseous products.

2.0 OBJECTIVES

The objectives of this project arise from two fundamental questions concerning catalytic cracking of tar:

- Can gasification tar be cracked by synthetic nickel-substituted synthetic mica montmorillonite (NiSMM), zeolite, or dolomite material to a product slate that does not contaminate downstream equipment such as ceramic or candle filters, fuel cells, or turbines?

- Can gasification tars be cracked selectively by the catalysts mentioned above to produce a desired liquid and/or gas stream?

3.0 ACCOMPLISHMENTS

3.1 Materials and Method

Two low-rank coals (LRCs) were chosen for testing the tar cracking capability of NiSMM, dolomite and zeolite. North Dakota leonardite was selected as a LRC to be pyrolyzed to test the effect of NiSMM in cracking pyrolysis tar. The proximate analysis of the leonardite is shown in Table 1. Previous experience with this catalyst as an in-bed gasification catalyst for the steam–leonardite reaction indicated that it did not effectively increase the rate of gasification but seemed to promote the production of more methane

TABLE 1

Proximate Analysis of ND Leonardite and Beulah Lignite

Coal	Moisture, as-received wt%	Volatiles, moisture-free wt%	Fixed Carbon, moisture-free wt%	Ash, moisture-free wt%
Leonardite	42.1	49.9	37.6	12.2
Beulah – West Pit	30.2	44.8	47.6	7.6

than obtained from uncatalyzed gasification. The leonardite, however, is not an abundant fuel and therefore not a serious candidate for the remainder of the study. There are large reserves of lignite that are excellent candidates for gasification, as demonstrated by the Dakota Gasification Company at Beulah, North Dakota, which gasifies more than 14,000 tons of lignite per day. After the initial NiSMM tests with leonardite, Beulah West Pit lignite was the substrate gasified to provide the tar. The proximate analysis of Beulah West Pit lignite is also shown in Table 1. Pyrolysis and steam gasification was carried out in the integrated bench-scale gasifier (IBG), and the gas stream that passed through the catalyst bed was analyzed on-line using Fourier transform infrared spectrometry (FT-IR). In addition, the product gas was sampled periodically by collecting samples in gas bags for later analysis by gas chromatography (GC). A module for containing a catalyst bed was fabricated and flanged to the top of the IBG reactor. Operated in the fluidized mode, the fully instrumented IBG was used to pyrolyze and gasify coal. The gas and tar produced exited the reactor through the catalyst module containing a heated catalyst (NiSMM or dolomite) bed, passed through two water-cooled condensers, and was analyzed by on-line FT-IR. Trapped liquids were collected from the reactor following each test and were saved for later analysis. The catalyst was recycled to determine whether catalytic activity could be regained.

3.2 Integrated Bench-Scale Gasification

The integrated bench-scale gasifier (IBG) is a small batch process gasifier, with a charge capacity of nominally 70 g of coal. This unit provides data on the effects of bed fluidization, conversion of feedstock, reaction rate response to temperature, pressure, catalyst and feed gas composition and flow rate, and gaseous products, while providing sufficient quantities of conversion products for subsequent analysis. The top of the reactor has been fitted with a catalyst module through which the hot exhaust gas must pass before entering the series of two condensors. Although the module has no heaters of its own, it receives heat from the reactor and tends to remain predictably within 50°–100°C of the reactor. A typical catalyst charge to the module is 30–50 g. Gas flows uninterrupted through the system and through the heated FT-IR cell. Gas exiting the second condenser flows through the cell where it is analyzed. The data obtained indicate the effect on the tar by measuring the levels of methane in the gas stream. In this study, NiSMM and dolomite were tested for their effect on pyrolysis tar.

3.3 Results

North Dakota leonardite was heated in the IBG to 700°C in a 30% H_2 atmosphere and the gaseous products including tars were passed through a bed of NiSMM catalyst,

through a series of two traps and then through a heated FT-IR gas cell as described above. Experimentation with the NiSMM ceased when FT-IR spectra containing a strong band at 2055 cm^{-1} characteristic of nickel carbonyl, an extremely toxic gas, was observed. Since the molar absorptivity of nickel carbonyl is not known precisely, the graph of absorbance versus elapsed gasification time shown in Figure 1 includes the CO curve from the test with no catalyst as well as the traces assigned to nickel carbonyl.

Table 2 shows the operating parameters for steam gasification of Beulah West Pit lignite in the IBG at temperatures selected on the basis of potential operating temperatures of various gasifiers. The conversions shown are based on moisture- and ash-free (maf) proximate analysis values for volatiles and fixed carbon in raw coal sample. There is a clear conversion trend for temperature with 90 wt% conversion or above occurring at or above 700°C. Each reaction was carried out at the gasification temperature indicated until the production of CO_2 as monitored by FT-IR became negligible, generally 1 to 3 hours. The dolomite tended to decrepitate, producing fines, some of which blew over into the primary trap. The quantities of dolomite blown over did not correlate with temperature, but rather the fines tended to blow over with the occasional random increases in gas flow resulting primarily from uneven steam flow.

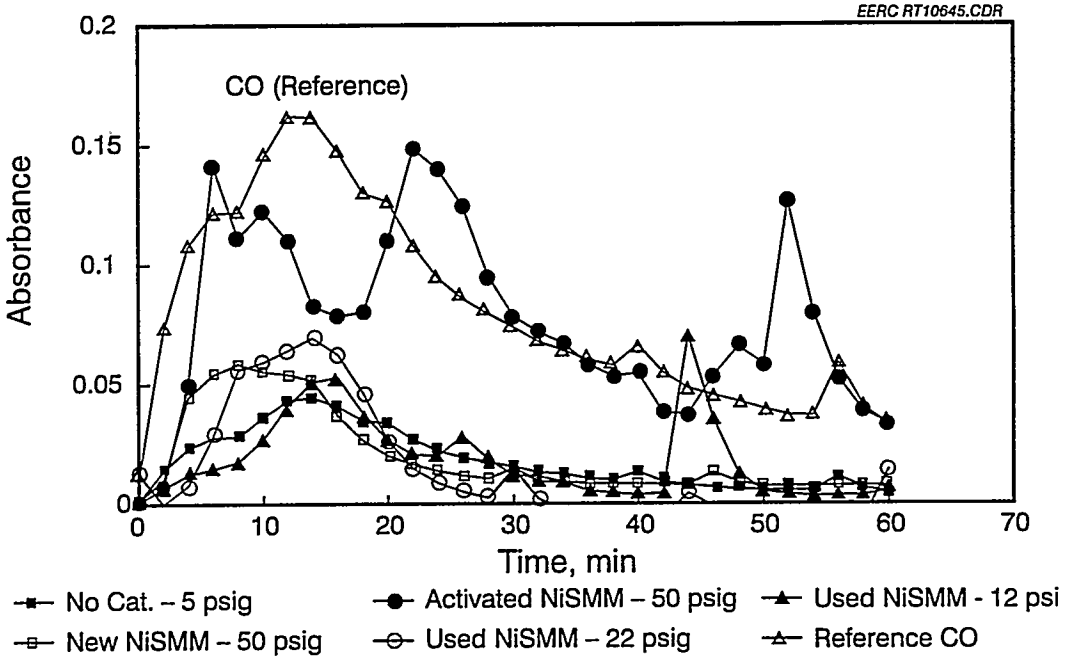

Figure 1. Gasification reactions showing FT-IR absorbance at 2055 cm^{-1} that may be nickel carbonyl. CO curve is shown for reference only.

TABLE 2

Conversion of Volatiles and Fixed Carbon to Tar and Gaseous Products under Steam Gasification Conditions at Various Temperatures

Run No.	Coal	Temperature, °C	Catalyst	Atm., g/min at 50 psig	Conversion, wt% (moisture-free)
IBG118	Beulah West Pit	850	Dolomite	Steam, 3-4	96
IBG119	Beulah West Pit	250	Dolomite	Steam, 3-4	16
IBG120	Beulah West Pit	550	Dolomite	Steam, 3-4	53
IBG121	Beulah West Pit	700	Dolomite	Steam, 3-4	90
IBG122	Beulah West Pit	400	Dolomite	Steam, 3-4	29

The tar collected from each of the tests listed in Table 2 will be determined when extraction of the tar from the liquids collected in the condensers has been completed. This information will be available in the next reporting period.

The methane content of the gaseous product normalized to the volatiles content of the coal from tests at each of the five gasification temperatures is shown in Figure 2. Pyrolysis methane was produced initially at temperatures above 500°C and dropped off after about 25 minutes into the run. Methane continued to be produced as a result of methanation reaction and catalytic cracking. Methane was not a product of the reaction carried out at 250°C, but substantial methane was produced at each of the other temperatures. Indeed, at 700°C, more methane relative to the volatiles content was produced than at 850°C.

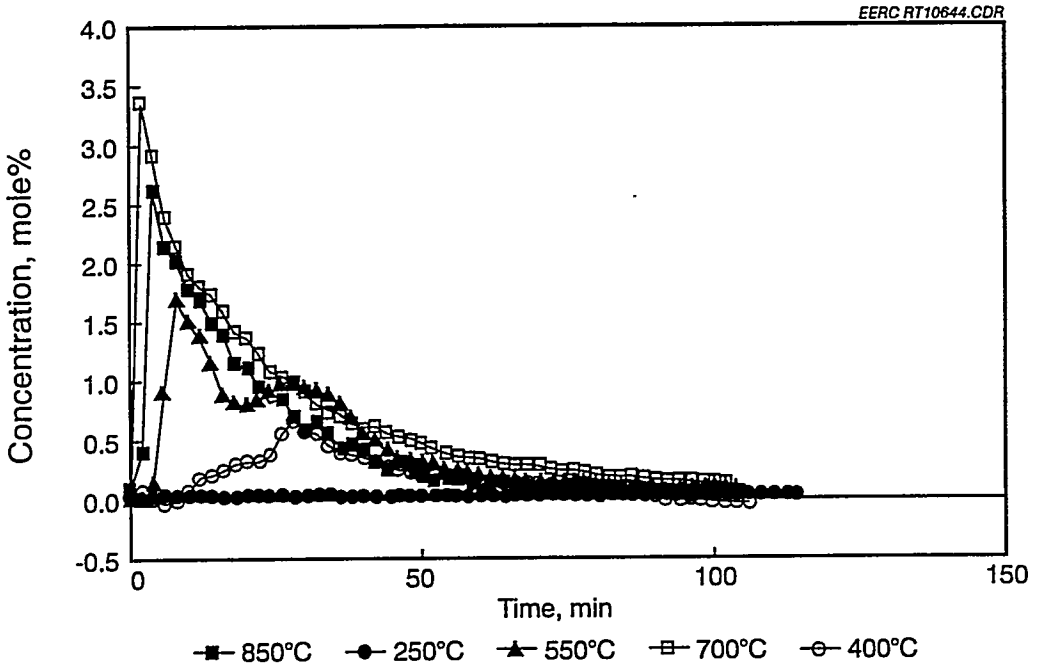

Figure 2. Methane concentration relative to tar production at each of five gasification temperatures.

The following paper was presented in June, 1994:

Timpe, R.C.; Kulas, R.W.; Hauserman, W.B.; Sharma, R.; Olson, E.S.; Willson, W.G. "Catalytic Gasification of Coal for the Production of Fuel Cell Feedstock," *In* Proceedings of the 10th World Hydrogen Energy Conference; Block, D.L.; Veziroglu, T.N., Eds.; Vol. 2, pp 843–852, 1994.

4.0 FUTURE WORK

- Complete the extractions of tar from trapped liquids.
- Evaluate X-2388 Engelhard zeolite as a lignite tar-cracking catalyst.
- Evaluate dolomite as a bituminous coal tar-cracking catalyst.
- Evaluate X-2388 Engelhard zeolite as a bituminous coal tar-cracking catalyst.

TASK 3.10

GAS SEPARATION AND HOT-GAS CLEANUP

Prepared by:

Michael L. Swanson

August 1994

TABLE OF CONTENTS

LIST OF FIGURES

TASK 3.10 GAS-SEPARATION AND HOT-GAS CLEANUP

1.0 BACKGROUND

Catalytic gasification of coal to produce H_2- and CH_4-rich gases for consumption in molten carbonate fuel cells is currently under development; however, to optimize the fuel cell performance and extend its operating life, it is desired to separate as much of the inerts (i.e., CO_2 and N_2) and impurities (i.e., H_2S and NH_3) as possible from the fuel gas before it enters the fuel cell. In addition, the economics of the integrated gasification combined cycle (IGCC) can be improved by separating as much of the hydrogen as possible from the fuel, since hydrogen is a high-value product. Researchers at the Energy & Environmental Research Center (EERC) are currently studying ceramic membranes as a method for accomplishing this gas separation and hot-gas cleanup. These membranes are operated at temperatures as high as 800°C and pressures up to 300 psig. These membranes have very small pore sizes which separate the undesired gases by operating in the Knudsen diffusion region of mass transport (30–50 Å) or in the molecular sieving region of mass transport phenomena (<5Å).

Technological and economic barriers which must be resolved before ceramic membranes are commercially viable include improved gas separation efficiency, membrane optimization, sealing of ceramic membranes to metal vessels, high burst strength of the ceramic material, pore thermal stability, and material chemical stability. Hydrogen separation is dependent on the temperature, pressure, pressure ratio across the membrane, and ratio of permeate flow to total flow. For gas separation under Knudsen diffusion, increasing feed pressure and pressure ratio across the membrane should increase the gas permeability, while decreasing the temperature and decreasing the permeate-to-total flow ratio should also increase the gas permeability. In the molecular sieving regime of mass transport, the inlet pressure and pressure ratio should have no effect on gas permeability, while increasing temperature should increase permeability.

2.0 OBJECTIVES

The selectivity of the ceramic membranes for removing the undesired gases while allowing the desired gases to be concentrated in the permeate stream must be determined. Specific questions to be answered during the year include:

- What are the effects of ceramic membrane properties (i.e., surface area, pore size, coating thickness) on permeability and selectivity of the desired gases?
- What are the effects of operating conditions (i.e., temperature, pressure, and flow rate) on permeability and selectivity?
- What are the effects of impurities (i.e., small particulate, H_2S, HCl, NH_3, etc.) on membrane performance?

3.0 ACCOMPLISHMENTS

Telephone conversations with Dr. Dave Edlund at Bend Research, Inc., have been held and information gathered concerning the prototype membrane module. This module is engineered to operate at 550 psig and 400°C with a safety factor of 5. The EERC engineering design group has reviewed the design of the Bend Research membrane module for pressure rating and has approved the vessel design for pressures up to 200 psig. The most cost-effective way to perform the tests is to conduct both the baseline separation efficiency tests using bottled gas and the impurity degradation tests using actual coal-derived fuel gas in the same equipment. Originally, it was proposed to build a separate test stand to conduct the separation efficiency tests using bottled gases. However, it was decided that this method would waste too many valuable resources duplicating similar capabilities. Modification of the EERC's continuous fluid-bed reactor (CFBR) presents the most cost-effective alternative.

Figure 1 shows the 4-lb/hr CFBR used for gasification tests with various coals. The unit was originally designed as a pyrolysis unit for a DOE mild gasification program, but it has been used since for gasification, pyrolysis, and combustion on a variety of projects. Although predominantly operated as a fluid bed, the unit has been operated as a fixed bed by using lower gas flow rates or larger particle sizes in the bed. The unit was intentionally designed to be flexible.

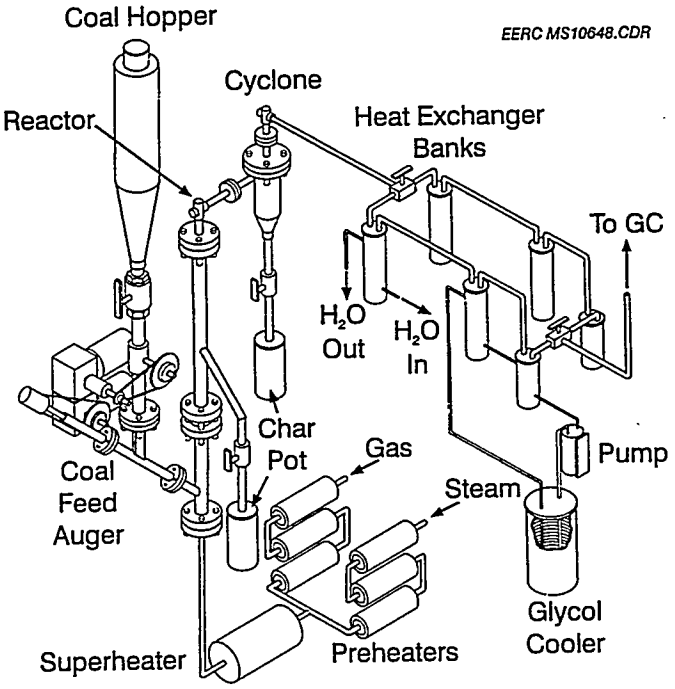

Figure 1. 4-lb/hr CFBR.

Gas used for fluidization is mixed in a gas manifold. Bottled gas, house nitrogen, house air, and any liquid desired (such as steam) are first preheated, then mixed, and heated to reaction temperature in a superheater (20 ft of 3/8-in. tubing coiled into an 18-in. ceramic fiber heater). Two bottled gases in combination with either house air or house nitrogen and a liquid can be used at the present time. Using more bottled gases in the feed gas mix would involve additional mass flow controllers.

The reactor was constructed of 316H stainless steel Schedule 80 pipe. The first (bottom) section is made of 3-in. pipe and is 33 in. in length. The next (top) reactor section is made of 4-in. pipe, 18.75 in. in length. The two sections are connected with a 316H weld reducer. The unit was designed such that the top of the fluid bed lies 33 in. above the coal injection point. A solids off-take leg at the top of the bed is the primary means of solids removal from the reactor. A ball valve facilitates the collection of product while the system is operating. The reactor currently has two ceramic fiber heaters to maintain the vessel's temperature and eliminate hot spots. Using external heaters allows the evaluation of internal and external heating methods for process development and scaleup. The reactor is capable of operation at a maximum of 155 psig and 840°C.

A 3-in.-diameter cyclone is used for solids removal from the gas stream. A ball valve allows the changing of the solids catch pot while the system is operating. The cyclone is heated with a ceramic fiber heater capable of operating at a temperature of 1650°F (900°C) and 200 psig. An 8-in.-long section of 2-in. 316H stainless steel Schedule 80 pipe is utilized as a pressure vessel to contain a fixed bed of zinc titanate sorbent to reduce the H_2S levels to less than 10 ppm and preferably to less than 1 ppm.

Three 4-in.-diameter vessels are used to remove all condensables from the gas stream. Two separate trains were installed: one for mass balance sampling and the other for heatup, unsteady-state conditions, and cool-down. The first condenser pot is indirectly cooled by water and typically cools the gas stream from 570°F (300°C) to 200°F (95°C). The next two condensers, also indirect, are glycol-cooled. The exit gas temperature is typically 50°F (10°C). A glass wool filter was used to capture aerosols passed through the condenser system. A wet scrubber neutralizes any chlorine still present in the gas stream, before sending the gas through a product gas meter.

A Genesis software package is used for process control and data acquisition. Pressure drop across the bed is measured by two transmitters, and thermocouples throughout the unit measure temperatures. Temperature and pressure readings are recorded every 30 seconds, and these data are directly transferred to Lotus spreadsheets.

Mass flow controllers for hydrogen, carbon monoxide, carbon dioxide, and nitrogen for supplying a clean gas stream from bottled gases are available at the EERC. It is proposed to utilize the continuous fluid-bed reactor as the mixing chamber and heater for the hot-gas source for the initial work. This testing would be accomplished without the presence of coal in the reactor. An on-line Foxboro 931C gas chromatograph together with a HP 5880 gas chromatograph will be utilized to measure gas compositions in this program. Initial tests will be performed to conduct short-term performance tests using the membrane to separate hydrogen from the mixed-gas stream. Subsequent tests will then look at the effects of impurities (such as H_2S, HCl, etc.) on the membrane performance using actual coal-derived fuel gases from the same CFBR equipment. The gas composition

of the coal-derived gas stream may be adjusted by adding some bottled gas to the gas stream entering the reactor.

Because of scheduling conflicts, testing of the Bend Research, Inc., membrane will not be started until late August or early September.

4.0 FUTURE WORK

Future work includes the following:

- Finish modifications to CFBR to conduct both the separation efficiency testing using bottled gases and the coal gas impurity degradation testing using actual coal-derived fuel gas.

- Conduct initial test sequence utilizing the Bend Research, Inc., membrane for producing hydrogen-rich fuel gas for fuel cell applications.

TASK 4.4

SULFUR FORMS IN COAL

Prepared by:

Steven B. Hawthorne
Ronald C. Timpe

August 1994

TABLE OF CONTENTS

LIST OF TABLES

TASK 4.4 SULFUR FORMS IN COAL

1.0 INTRODUCTION

Development of advanced fuel forms depends on having reliable quantitative methods for their analysis. Determination of the true chemical forms of sulfur in coal is a necessary element in developing more effective methods for reducing sulfur content. Past work at the EERC indicates that sulfur chemistry has broad implications in combustion, gasification, pyrolysis, liquefaction, and coal-cleaning processes.

Current analytical methods are inadequate for accurately measuring sulfur forms in coal. This subtask is concerned with developing methods to quantitate and identify major sulfur forms in coal based on direct measurement (as opposed to present techniques based on indirect measurement and difference values). The focus is on the forms that are least understood and for which the analytical methods are the poorest, i.e., organic and elemental sulfur. The development of improved measurement techniques for sulfatic and pyritic sulfur is also needed. A secondary goal is to understand the interconversion of sulfur forms in coal during thermal processing.

We have developed the first reliable analytical method for extracting and quantitating elemental sulfur from coal (1). This method has demonstrated that elemental sulfur can account for very little or as much as one-third of the so-called "organic" sulfur fraction. This method has disproved the generally accepted idea that elemental sulfur is associated with the organic fraction.

Standard (ASTM and similar) sulfur forms analysis (2) have been evaluated on a mass balance basis. (Note that these techniques have not been appropriately evaluated.) Standard HCl extraction (for sulfate) has been shown to give poor sulfur mass balance, and an improvement using formic acid has been developed (3). Standard HNO_3 extraction (for pyritic S) has also shown subquantitative mass balance. In addition, we have shown that HNO_3 radically changes the chemical structure of the coal (making subsequent forms analysis invalid). The common method of measuring iron to determine pyritic sulfur is questionable, since the stoichiometry of iron–sulfur compounds may not always be that of pyrite.

Two methods have been developed that show high potential to extract coal sulfur forms with sufficient selectivity to provide accurate forms data. Preliminary interpretations of the extraction data indicate that supercritical CO_2/10% methanol under pyrolysis conditions (450°C) selectively extracts true organic sulfur, but not sulfatic or pyritic sulfur. These extractions are performed on samples that have previously been extracted using our supercritical fluid extraction [SFE] method to remove elemental sulfur. Second, CO_2/H_3PO_4 appears to remove 80% of the total sulfur, including sulfatic, pyritic, and what we will call "easy" organic sulfur. Extraction methods used in attempts to remove sulfur, including the remaining 20%, have proven either to be ineffective or, in the case of peroxidation or molten caustic leaching, to lack economic and/or technical feasibility. This so-called "hard" organic sulfur appears to be immobile and unreactive with, or inaccessible to, mild reagents or extraction media.

This task focuses on the development of selective extraction methods that will allow the direct measurement of sulfur content in each form. Therefore, selective extraction methods are needed for the major sulfur forms in coal, including elemental, pyritic, sulfatic, and organic sulfur. This study is a continuation of the previous sulfur forms analytical methods development that resulted in the successful isolation and quantitation of elemental and sulfatic sulfur from coal. Super- and subcritical extractions with methanol or water with and without additives are investigated in an attempt to develop methods for pyritic and organic sulfur forms analysis in coal.

2.0 OBJECTIVES

The objective is to develop and validate analytically valid extraction and measurement techniques for all major sulfur forms in coal based on direct measurement. Secondary objectives are to investigate the transformation of sulfur forms and to determine potential processing implications of the extraction methods developed. For each of the extraction conditions, the major emphasis is on understanding the forms of sulfur removed (and/or transformed), with the primary goal of developing reliable analytical methodology.

Specific objectives for 1994 are to:

- Determine the effect of temperature and pressure with CO_2/H_3PO_4 and CO_2/methanol on the selectivity of extraction for the different sulfur forms in coal.

- Determine the effect of temperature and pressure with water on the selectivity of extraction for the different sulfur forms in coal. These investigations will both determine the potential analytical applications likely to be useful and will determine whether further investigations into coal sulfur removal as a processing method are warranted.

- Determine whether optimal conditions are generally applicable to different coals.

3.0 ACCOMPLISHMENTS

3.1 Sample Preparation

This study requires large quantities of elemental sulfur-free, elemental and sulfatic sulfur-free, and elemental, sulfatic, and pyritic sulfur-free coals. One hundred grams of elemental sulfur-free coal was prepared in 5-gram batches and the extracted residues were combined. This elemental sulfur-free coal was then divided into thirds, one of which was left intact, one was used to prepare elemental and sulfatic sulfur-free coal, and the last one-third was used to prepare elemental, sulfatic, and pyritic sulfur-free coal. Following is a brief description of the methods used for preparing these samples.

- One hundred grams each of elemental sulfur-free IBC-101 and IBC-107 were prepared by extracting each coal under mild SFE conditions (CO_2/10% methanol, 400 atm, 110°C, 100 min) as previously reported (1). Each extracted solid was

divided into three fractions as mentioned above. One fraction is for later extraction at 50°C, 250°C, and 450°C with supercritical CO_2/additives and with super- and subcritical H_2O. The second fraction is to be extracted with formic acid (HCOOH) to remove sulfate, and the third fraction is for extraction with the Canfield reagent (chromous acid) to remove sulfate and pyrite (inorganic sulfur).

- Elemental and sulfate sulfur-free coal was prepared by extracting elemental sulfur-free coal according to the method developed in this laboratory (3). In accordance with this procedure, elemental sulfur-free coal was extracted by boiling 4.8 N HCOOH, washed with water, filtered, and dried in an oven at 100°C for 2 hours. The sample was then stored under argon in plastic containers until used.

- Elemental, sulfatic, and pyritic sulfur-free coal samples were obtained by performing Canfield batch extractions (4) of inorganic sulfur from both IBC-101 and IBC-107 elemental sulfur-free coal samples.

- In this procedure, elemental sulfur-free coal was treated with chromous acid to reduce inorganic sulfur for removal as H_2S. The H_2S was collected as CuS in a liquid trap by purging the reaction vessel with N_2. The residue was collected on Whatman No. 1 filter paper and washed with formic acid to remove residual chromium, dried, and stored under argon in plastic containers until used.

3.2 Extraction

This study was based on background work successfully performed over the past three years, in which the investigations were designed to develop and evaluate extraction methods for their ability to provide reliable and accurate extraction of the various sulfur forms for direct analytical determinations. Sulfur extraction methods based on dynamic SFE under low-temperature (110°C, 400 atm) and pyrolysis conditions (450°C, 400 atm) on coal samples were developed and the results published over the past two years. Using CO_2/10% methanol (110°C, 400 atm) as an extraction fluid, elemental sulfur in coals was extracted quantitatively and selectively under dynamic conditions within 30 minutes. Under pyrolysis/dynamic SFE conditions using pure CO_2 with the addition of phosphoric acid, about 80% of the total sulfur was removed from two bituminous coal samples (IBC-101 and Indiana No. 3, respectively) regardless of whether the sulfatic sulfur or both the sulfatic and pyritic sulfur were removed prior to pyrolysis/SFE (Table 1). However, when pyrolysis/dynamic SFE was performed with CO_2/methanol, organic sulfur species appeared to be extracted preferentially, since only about 60% of the total sulfur was removed from the raw coal by pyrolysis/SFE using CO_2 modified with 10% methanol, while about 80% of the total sulfur was extracted if sulfatic and pyritic sulfur were removed prior to extraction. A test matrix to examine these results in more detail has been designed and will be executed next quarter.

Supercritical water extraction carried out at 450°C and 400 atm under static conditions for 15 min, followed by dynamic conditions for 15 min gave encouraging results with IBC-101 bituminous, as shown by Table 2. Approximately two-thirds of the total sulfur was removed, indicating that at least all or part of each major sulfur fraction of coal (pyritic, sulfatic, and organic) was removed. Under the same conditions, only about

TABLE 1

Pyrolysis/SFE Sulfur Removal from IBC-101 and Indiana No. 3 Using Supercritical CO_2/10% Methanol and CO_2/Phosphoric Acid

	Sulfur Removal on Total Sulfur Basis[1]			
	CO_2/MeOH		CO_2/Phosphoric Acid	
Coal Samples	IBC-101	Indiana No. 3	IBC-101	Indiana No. 3
Raw	62 ± 3	60 ± 7	82 ± 3	78 ± 9
Sulfate-Free	70 ± 1	72 ± 1	83 ± 13	85 ± 23
S_8- and SO_4-Free	68 ± 1	68 ± 2	81 ± 12	84 ± 7
SO_4- and FeS_2-Free	78 ± 1	76 ± 3	78 ± 13	81 ± 12
S_8-, SO_4-, FeS_2-free	81 ± 2	72 ± 4	80 ± 11	74 ± 10

[1] Standard deviations are based on triplicate 30-min extractions.

TABLE 2

Extraction of Sulfur from Coal (IBC-101) with Supercritical Water

Supercritical Extraction Conditions			
Static Conditions	Dynamic Conditions	S Reduction, %	C Reduction, %
15 min at 400 atm, 450°C	15 min at 400 atm, 450°C	65.3 ± 3.2	33.9 ± 0.9

one-third of the carbon was removed. Table 3 shows the initial data obtained by extracting IBC-101, IBC-106 and physically cleaned Indiana No. 3 with supercritical water under dynamic conditions, indicating that sulfur may be successfully extracted from coal with supercritical water. SFE with water makes up more than half of the work to be carried out in the remainder of this project.

4.0 FUTURE WORK

- Extract sulfur from elemental sulfur-free IBC-101 and IBC-107 using supercritical 10% CH_3OH/CO_2 and supercritical H_2O.
- Extract sulfur from elemental and sulfatic sulfur-free IBC-101 and IBC-107 using supercritical 10% CH_3OH/CO_2 and supercritical H_2O.
- Extract sulfur from elemental, sulfatic, and pyritic sulfur-free IBC-101 and IBC-107 using supercritical 10% CH_3OH/CO_2 and supercritical H_2O.
- Determine sulfur extracted from each of the coal samples.
- Examine the coal samples for coal matrix damage resulting from extraction.

TABLE 3

Removal of Sulfur under Sub- and Supercritical Water Extraction Conditions[1]

Sample ID	Extraction Temperature, °C	Extraction Pressire, atm	Purge Gas	S Removal as % of Total S
IBC-101	50	400	N_2	4.8
IBC-106	50	400	N_2	2.2
Indiana No. 3	50	400	N_2	3.2
IBC-101	250	400	N_2	16.8
1BC-106	250	400	N_2	18.8
Indiana No. 3	250	400	N_2	11.8
IBC-101	350	400	N_2	51.3
IBC-106	350	400	N_2	36.0
Indiana No. 3	350	400	N_2	38.2
IBC-101	450	400	N_2	73.0
IBC-106	450	400	N_2	71.4
Indiana No. 3	450	400	N_2	70.4
IBC-101	450	100	N_2	66.8
IBC-106	450	100	N_2	67.2
Indiana No. 3	450	100	N_2	82.6
IBC-101	450	400	Air	64.7
IBC-106	450	400	Air	74.1
Indiana No. 3	450	400	Air	70.3

[1] 30-min dynamic supercritical water extraction purged with N_2 or air.

5.0 REFERENCES

1. Louie, P.K.K.; Timpe, R.C.; Hawthorne, S.B.; Miller, D.J. *Fuel* **1993**, *72*, 225.

2. *Annual Book of ASTM Standards, Vol. 05.05, Gaseous Fuels: Coal and Coke*; American Society for Testing and Materials: Philadelphia, 1991.

3. Louie, P.K.K.; Timpe, R.C.; Hawthorne, S.B.; Miller, D.J. "Sulfur Removal from Coal by Analytical-Scale Supercritical Fluid Extraction (SFE) Under Pyrolysis Conditions," Presented at the Coal Utilization and the Environment Meeting, Orlando, FL, May 1993. Accepted by *Fuel*, in press.

4. Canfield, D.E.; Raiswell, R.; Westrich, J.T.; Reaves, C.M.; Berner, R.A. "The Use of Chromium Reduction in the Analysis of Reduced Inorganic Sulfur in Sediments and Shales," *Chemical Geology* **1986**, *54*, 149–155.

TASK 4.5

RESID AND BITUMEN DESULFURIZATION

Prepared by:

Edwin S. Olson

August 1994

TABLE OF CONTENTS

TASK 4.5 RESID AND BITUMEN DESULFURIZATION

1.0 INTRODUCTION

The sulfur content of many coals, crude oils, and bitumens results in serious problems in the utilization and processing of these resources, both as fuel and nonfuel materials. Emission regulations demand that cleaner fuels be utilized. The production of low-sulfur, low-metal petroleum coke (petcoke) is also being sought for the manufacture of needle cokes, carbon electrodes, metallurgical reductions, and fuels. Unfortunately, the feedstocks available for production of fuels and carbon products tend to have higher sulfur contents, e.g. the very large reserves of crude oil and bitumens that are available in South America with sulfur contents of greater than 3 wt%. Lower-value sour crudes are also an increasing problem for oil production in parts of the U.S.

Catalytic hydrodesulfurization can eliminate the sulfur from some feedstock materials, but the high metal content in these materials results in severe metal sulfide deposition that can poison the catalyst. Thus, new technologies and new catalysts are needed for effective desulfurization. Methods for removal of metals and nitrogen are also needed, since these form toxic or environmentally unacceptable species during utilization of the fossil materials. Chemical methods for removal of sulfur, nitrogen, and toxic metals from a liquid or soluble form of the feedstock will be easier than removal from a solid carbon matrix.

In a previous Energy & Environmental Research Center (EERC) project, molybdenum sulfide impregnated in a nickel-substituted synthetic mica montmorillonite (NiSMM) and in a hydrotalcite clay were demonstrated to be highly effective catalysts for hydrodesulfurization of coal-derived products. Further demonstrations of its activities and stability for desulfurization of petroleum resids and bitumens are needed. Currently used resid desulfurization catalysts experience severe deactivation as a result of plugging of the catalyst pores or sintering of the metal sulfides.

2.0 OBJECTIVES

The project will determine how effective the molybdenum-impregnated NiSMM catalysts and the molybdenum-exchanged hydrotalcite catalysts are for hydrodesulfurization of resids and bitumens. The activity and stability will be assessed to determine their potential for commercialization and patent protection.

A test matrix for comparison of the hydrodesulfurization activities of molybdenum-impregnated NiSMM with several other layered catalysts will be conducted. Effects of variables such as temperature, catalyst concentration, and hydrogen pressure will be studied. Substrates include a resid considered to be a precursor for petcoke. Model organosulfur compounds such as dibenzothiophene and aliphatic sulfides will also be tested to define the selectivity. Several runs will be performed with recovered catalysts to determine their stability. Recovered catalysts will be examined to determine if sintering occurred. The extent of hydrocracking will be determined, since this needs to be minimized for most of the substrates.

Molybdenum sulfide in a layered hydrotalcite matrix was another promising catalyst for removal of sulfur from coal liquids and model aromatic sulfides. Similar tests will be performed with an improved molybdenum-impregnated hydrotalcite.

3.0 ACCOMPLISHMENTS

Previous work at EERC was concerned with the development of catalysts for production and upgrading of coal liquids. Some of the catalysts developed in this program were also useful for hydrodesulfurization. The types of catalysts and supports investigated included zinc chloride–silica complexes (1), natural and synthetic clays (2–5), and zeolites (5).

In the current project, several of these catalysts were tested for desulfurization of a Venezuela bitumen product called "Orimulsion." These tests were conducted in a small batch reactor with hydrogen pressures of about 200 psi at a temperature of 390°C. Both the Orimulsion (a 70% bitumen–30% water emulsion) and the dry bitumen were used in tests. Catalysts were presulfided by heating with sulfur plus hydrogen at 400°C for 2 hr.

In a 1-hr test with the as-received emulsion, the NiSMM-supported molybdenum catalyst (presulfided) gave a product with 3.0% sulfur (dry basis), which is a 22% reduction in the sulfur content of the bitumen. The molybdenum terephthalate hydrotalcite (MoTPHT) catalyst gave a product with 3.6% sulfur (8% reduction). This catalyst is prepared as the sulfide and did not require the presulfiding step. A chromia-pillared clay containing the molybdenum catalyst (molybdenum–high-chromium-pillared clay [Mo–HCPC]) was presulfided and tested with the Orimulsion. This catalyst gave similar poor desulfurization activity (8% sulfur reduction). Presulfided commercial catalysts, AMOCAT and HDN-30, both removed 39% of the sulfur of the Orimulsion in the 1-hr batch hydrodesulfurization test. On this basis, we concluded that the EERC catalysts that previously showed desulfurization activities with coal liquids were far inferior to the commercial catalysts for desulfurization of the highly aliphatic bitumen.

Further testing was carried out with zeolite catalysts modified by metal impregnation and also by coating the zeolite with aluminosilicate as is done with fluid catalytic cracking (FCC) refining catalysts. The zeolite-supported nickel–molybdenum catalyst gave a 32% reduction of sulfur, and a similar zeolite-supported nickel–tungsten catalyst gave only a 22% sulfur reduction in 1-hr tests. However, the zeolite–aluminosilicate-supported nickel–molybdenum catalyst prepared at EERC gave 43% removal of sulfur in a 1-hr test. This catalyst is similar to that recently reported by a Canadian group (6). Further testing with Orimulsion for 3 hr gave 58% removal. When a dry fraction of the bitumen was hydrotreated with this catalyst, 73% of the sulfur was removed, to give a product with 1.0% (dry wt. basis) sulfur content.

A proprietary nickel catalyst supported on another oxide gave 38% removal of sulfur from the as-received Orimulsion in the 1-hr period. Reaction of the dry bitumen gave the same reduction in sulfur. Incorporation of molybdenum into this nickel oxide catalyst resulted in a slight increase in catalytic activity (41% sulfur reduction).

4.0 FUTURE WORK

The molybdenum-loaded nickel oxide catalyst and the nickel–molybdenum-loaded zeolite–aluminosilicate will be further tested with a resid. Further tests with recovered catalyst are in progress.

The use of an inexpensive catalyst for demetalation of the bitumen will be investigated. Conversion of nickel and vanadium to the sulfides can be effected by hydrogen sulfide generated in situ by hydrodesulfurization. Inexpensive iron or nickel catalysts on a stable, inexpensive support can release some (about 20%) of the organosulfur present in the bitumen and will rapidly collect the resulting deposits of metal sulfide. The processed bitumen will be further treated with the Ni–Mo zeolite catalyst and the vanadium and nickel recovered from the first-stage catalyst.

5.0 REFERENCES

1. Sharma, R.K.; Diehl, J.W.; Olson, E.S. "Hydrodesulfurization with a New Solid Acid Catalyst," *Processing and Utilization of High-Sulfur Coals III*; Markuszewski, R.; Wheelock, T.D., Eds.; Elsevier: Amsterdam, 1990; pp 735–743.

2. Olson, E.S.; Buchwitz, C.M.; Yagelowich, M.; Sharma, R.K. *Prepr. Pap.—Am. Chem. Soc., Div. of Fuel Chem.* **1993**, *38*, 156–162.

3. Olson, E.S.; Yagelowich, M.C.; Sharma, R.K. *Prepr. Pap.—Am. Chem. Soc., Div. Fuel Chem.* **1992**, *37*, 262–267.

4. Sharma, R.K.; Olson, E.S. "Catalytic Hydrodesulfurization with Hydrotalcites," in *Processing and Utilization of High-Sulfur Coals IV*; Dugan, P.R.; Quigley, D.R.; Attia, Y.A., Eds.; Elsevier: Amsterdam, 1991; pp 377–384.

5. Olson, E.S.; Sharma, R.K. "New Catalysts for Production of Snythetic Fuels," *In* proceedings of the Australian/U.S.A. Workshop on Low-Rank Coals; Billings, MT, May 23–24, 1991, EERC publication.

6. Diaz-Real, R.A.; Mann, R.S.; Sambi, I.S. *Ind. Eng. Chem. Res.* **1993**, *32*, 1354.

TASK 4.6

BIODESULFURIZATION

Prepared by:

Edwin S. Olson

August 1994

TABLE OF CONTENTS

TASK 4.6 BIODESULFURIZATION

1.0 INTRODUCTION

Conventional catalytic hydrodesulfurization involves high costs largely due to heavy metal deactivation of the catalysts. A potential lower-cost treatment is a microbiological or enzymatic desulfurization. Recent advances at the Energy & Environmental Research Center (EERC) at the University of North Dakota have improved our understanding of sulfur-specific microbial desulfurization pathways in *Rhodococcus* bacteria, but further work is needed to develop a technology based on biodesulfurization.

2.0 OBJECTIVES

The main focus in this task is the application of desulfurization enzymes to remove sulfur from crude oil, diesel fuel, or resid precursors for needle cokes. The most important question to be answered is how to utilize the *Rhodococcus* desulfurization complex in a nonaqueous solvent or medium, such as the oil itself. Successful application of nonaqueous enzymology to this problem will involve finding ways to stabilize the active conformations of the enzymes and to provide for easy recovery of the enzymes, perhaps in an immobilized-enzyme packed-bed reactor. Understanding the desulfurization activity will require that we determine what are the regulatory and mechanistic properties of the enzymes.

The proposed work will involve isolation and immobilization of the bacterial *(Rhodococcus)* enzyme systems that excise sulfur from thiophenic structures. Sulfur-specific microbial desulfurization has been shown to be an inducible trait that probably resides on the cell surface as a multienzyme cluster. Dead and broken cells exhibit the desulfurization activity; thus an immobilized cell-free system is plausible. Methods for dispersion and immobilization of enzyme clusters will be investigated. Immobilization is desired for ease in recovery and reuse and preparing packed column reactors for continuous processing. The critical task is to develop a system that is active in a nonaqueous solvent so that the reaction is not limited by the diffusion of sulfur compounds from the oil phase into an aqueous phase and so that phase separations at the end of the processing are eliminated. Attachment of stabilizing groups to the support matrix or to the enzymes may be required to achieve activity in the nonaqueous solvents. Both nonpolar and polar solvents will be investigated. It is also essential that we determine whether cofactors or other regulatory species are needed for functioning of the cell-free enzymes. Further information will be obtained on the nature of the pathways and desulfurization mechanisms and the inducers and inhibitors of the microbial activity via experiments with alternative sulfur substrates and inducers and with labeled substrates.

3.0 ACCOMPLISHMENTS

Microbial systems that desulfurize organosulfur compounds have potential use in removing sulfur from fossil fuels. Some organisms utilize a catabolic pathway that results in excision of the sulfur without converting organic carbon to carbon dioxide.

Dibenzothiophene (DBT) has been useful as a model compound to investigate the sulfur-specific behavior in bacterial systems. Intermediates corresponding to this thiophenic-ring scission (4S) pathway have been isolated and characterized (1).

The desulfurization of dibenzothiophene by *Rhodococcus rhodochrous* IGTS8 was recently demonstrated to proceed via two pathways that result in formation of either 2-hydroxybiphenyl or of 2,2'-dihydroxybiphenyl depending on whether growth or nongrowth conditions are used in the desulfurization experiments (2). Under nongrowth conditions, the DBT was converted to 2'-hydroxybiphenyl via the 2'-hydroxybiphenyl-2-sulfinate (analyzed as the cyclic sultine ester form). Under growth conditions, very little of the 2'-hydroxybiphenyl-2-sulfinate was converted to 2-hydroxybiphenyl, and instead most was oxidized to 2'-hydroxybiphenyl-2-sulfonate (analyzed as the sultone form), and 2,2'-dihydroxybiphenyl was the major product. The oxidation of the sulfinate to the sulfonate occurs spontaneously (nonenzymatically) in aqueous buffer exposed to air, but the sulfinate may also be oxidized in an enzyme-catalyzed reaction. These pathways are summarized in Figure 1. Further understanding of the details of the pathways and mechanisms of the various steps in the pathways are needed.

The initial reaction in the 4S pathway is the oxidation of dibenzothiophene to the sulfoxide (dibenzothiophene-5-oxide) (Reaction A). Further oxidation to the sulfone (dibenzothiophene-5,5-dioxide) also occurs. What is not known is whether the sulfoxide (Reaction B) or the sulfone (Reaction G) is the immediate precursor for the 2'-hydroxybiphenyl-2-sulfinate under nongrowth conditions and whether the sulfone can be converted directly to 2'-hydroxybiphenyl-2-sulfonate (Reaction E) under growth conditions. Is the sulfone an intermediate in the 4S pathway or a by-product?

When sulfone was fed to the bacterium under nongrowth conditions, 2'-hydroxybiphenyl-2-sulfinate and 2'-hydroxybiphenyl were produced (2). Since the sulfone is reduced back to the sulfoxide, whether the sulfoxide or the sulfone is the precursor of 2'-hydroxybiphenyl-2-sulfinate could not be distinguished in the earlier experiments.

This report describes the use of ^{18}O-enriched sulfone (dibenzothiophene-5,5-dioxide-$^{18}O_2$) to elucidate the pathway involving the sulfone. If prior reduction of the sulfone to sulfoxide occurred in the pathway (reverse of Reaction D), then loss of one labeled oxygen would be observed in the sultine and sultone intermediates.

The ^{18}O-labeled DBT sulfone substrate (98% isotopic purity) was utilized in the desulfurization experiment with the bacterium *Rhodococcus rhodocrous* (ATCC #53968) under nongrowth conditions. The supernatant from centrifugation of the culture medium was extracted with ethyl acetate, and GC analysis showed only starting sulfone and final product, 2-hydroxybiphenyl, and no sultine (cyclic form of the sulfinate) was present. From experiments with unlabeled sulfone, we know that all the sulfinic acid intermediate present in the culture medium is present in the open sulfinate form, but cyclizes to the sultine when the pH is lowered. The sultine can then be easily extracted with ethyl acetate and analyzed by GC. Therefore, the aqueous layer obtained after the initial extraction (from the experiment with ^{18}O-enriched substrate) was acidified and again extracted. GC/MS was performed to obtain the isotopic abundances for the peaks corresponding to sultine and sultone.

It must be pointed out that the cyclization to the sultine or sultone form displaces one oxygen from the sulfur; thus half of the label will be eliminated from each molecule of sultine. Thus the sultine molecules would contain a single-labeled oxygen if Reaction G were followed. If the pathway involving Reaction B were followed, half of the sultine molecules would be single-labeled and half unlabeled, as a result of the oxygen displacement. These projections assume no occurrence of exchange or disproportionation, which would decrease or increase the numbers of labeled oxygens on sulfur.

The mass spectrum of the sultine product showed molecular ions at m/e 218 and 216 (corresponding to single-labeled and unlabeled species, respectively) in the ratio 2.7. This greatly exceeds the ratio of 1 predicted for Pathway B. The ratio is consistent with Reaction G, and the much smaller number of unlabeled molecules must have been formed by exchange with water or disproportionation. The sultine mass spectrum shows a large fragment ion at m/e 190 resulting from loss of $C^{16}O$, and no peak at m/e 188, corresponding to loss of $C^{18}O$. Therefore, all of the ^{18}O must be attached to the sulfur, and none is on the phenolic carbon.

Thus the pathway must proceed directly from the sulfone to the sulfinate (Reaction G) rather than reduction of sulfone back to the sulfoxide intermediate. The reaction that forms the sulfinate from the sulfone is actually a reduction with respect to the sulfur. When the carbon–sulfur bond is cleaved, the electrons flow to the sulfur to form the sulfinate anion.

The cleavage reaction that involves formation of the sulfinate is similar to that in the electrochemical (3) and metal reduction of sulfones (4), except that hydroxyl is introduced at one aryl site in bacterial reaction, whereas hydrogen is added in the electrochemical and metal reduction reactions. The reactions of dibenzothiophenes with basic reagents, such as KOH, have been investigated. Attack of nucleophilic oxygen was reported to occur at the ring carbon at high temperatures in the presence of crown ether, resulting in the formation of 2'-hydroxybiphenyl-2-sulfinate (5). In the absence of crown ether, very small amounts of the sulfinate were formed, and attack at the sulfur occurred (5, 6).

In the bacterial system, the initial stage of the mechanism is more likely to involve addition of oxygen to the benzene ring via a hydroperoxyflavin cofactor. This type of mechanism has been described for oxygenase reactions, such as the salicylic acid and *p*-hydroxybenzoic acid oxygenase reactions that occur in other bacteria.

Formation of the sulfonate anion by simple addition of oxygen to the sulfinate anion would not be expected to change the number of labeled oxygens on the sulfur, and the sulfonate would be expected to be double-labeled. Cyclization of the sulfonate to the sultone involves loss of one of the oxygens on the sulfur. Thus one-third of the sultone would be double-labeled, and two-thirds would be single-labeled. But the sulfinate oxidation reaction might be more complex, and the labeling will provide some information on this oxidation.

The mass spectrum of the sultone exhibited the molecular ion peaks at 236, 234, and 232 in the ratio 5.6:3.2:1. Thus the sulfonic acid corresponding to the sultone must have been mostly triple-labeled. The obvious explanation for this fact is that the sulfinate undergoes a dimerization reaction and subsequently transfers labeled oxygen between

sulfur atoms as the sulfonic acid is formed (7). The sulfur that lost oxygen in the reaction of the dimer may eventually end up after subsequent oxidation as part of the unlabeled sultine that was observed.

The results not only prove that the sulfone is directly converted to the sulfinate, but also that the oxidation of the sulfinate to sulfonate follows accepted chemical mechanisms. A pathway involving Reaction E is, therefore, very unlikely to occur, since it would not produce triple-labeled sultone product.

The results would be more straightforward if the sulfinate were analyzed by conversion to a derivative that preserves both labeled oxygens attached to sulfur. The methyl sulfone derivative was prepared by treating the sulfinate with methyl iodide, and analysis of this derivative will be used to confirm the findings from the sultine derivative.

3.1 Enzyme Isolation/Immobilization

An important question to be answered in applying the *Rhodococcus* desulfurization system to oil desulfurization is how to utilize the enzyme complex most efficiently and cost-effectively. The sulfur compounds will, of course, be dissolved in the oil itself; thus the enzyme complex must not only function in the presence of excess amounts of hydrocarbons, but also must be readily recovered and reused. An immobilized-enzyme packed-bed reactor would be an ideal way to accomplish this goal. The use of reversed micelles containing the enzyme in the oil matrix is another alternative. Successful application of nonaqueous enzymology to this problem will involve finding ways to stabilize the active conformations of the enzymes in their immobilized or micelle form.

Initial work was performed to determine if cells can be ruptured and enzyme activity found in the resulting product fractions. Previous work by Ho suggested that the enzymes in the desulfurization complex exist in protrusions on the exterior of the bacterial cells. Their location should facilitate the preparation of crude enzyme fractions. Cells were washed free of DBT and hydroxybiphenyl by centrifugation from basal salt media, and pelleted cells were suspended in basal salt media for sonication. The sonication was performed with a VIRSONIC 475 sonicator with a series of ten 1-minute bursts at 80% power to achieve satisfactory rupturing of the cells. The initial dispersion of the ruptured cells exhibited high activity for DBT desulfurization (85% of initial activity). The sonicated product was centrifuged at 10,000 rpm. The supernatant contained only 10% of the activity of the sonicated product, whereas the insoluble ruptured cells exhibited 50% of the activity of the sonicated product.

Immobilization of the ruptured cells on a solid support was attempted. Sonicated cells were stirred with DEAE Sephadex A-25, and acetone was added to enhance the attachment of enzymes to the Sephadex gel. The gel complex was centrifuged and washed with acetone. DBT desulfurization tests with the gel complex in basal salt media showed that only 2% of the activity was retained.

Reactions of various organosulfur compounds were then carried out in organic solvents to determine if the organic media have an adverse effect on the enzyme activity. Pelleted cells were dispersed in organic solvents and tested for activity with DBT, DBTO, $DBTO_2$, sultine, and sultone. However, no hydroxybiphenyl product was detected for the

reactions in the organic solvents for any of the substrates. The organic solvents may cause some conformation change that destroys the activity.

The Sephadex gel complex was then prepared without use of the acetone. The activity of the resulting gel in basal salts medium was again low, indicating that some denaturing must be occurring as a result of attachment to the Sephadex. The activity of the gel complex in organic solvents was also zero.

An immobilized form of the desulfurization complex was also prepared with Celite diatomaceous earth. The activity of this form was also very low. The failure of these experiments to demonstrate significant activity indicates that the interactions with the solid support must be strong enough to inhibit the enzyme complex.

These preliminary experiments suggest that a stabilizer may be needed to utilize the enzymes in an immobilized form or in an organic solvent. Covalent attachment of polyethylene glycol chains to the enzymes is a possible solution for this problem.

3.2 Reversed Micelle Reactions

One way to utilize enzymes in chemical processing is to form a reversed micelle. The reversed micelle consists of an aqueous capsule system dispersed in a hydrocarbon solvent. The aqueous capsule system contains the enzyme and is stabilized by a surfactant at the aqueous–organic interface. The polar end of the surfactant is bound to the water in the micelle. The organic substrate must diffuse from the solvent phase through the interface to the enzymes in the micelle.

Reversed micelles were prepared by sonication in the presence of the surfactant, sodium dioctyl sulfosuccinate (AOT). Octane containing the DBT substrate was added after sonication as the organic solvent phase in the dispersion. After a reaction period of 2 days, 15% of the DBT was converted to hydroxybiphenyl, which was comparable to the reactions carried out in aqueous media.

3.3 Future Work

At the completion of this task, the activity and selectivity of modified and immobilized microbial desulfurization enzymes will be determined. The enzyme activities will be evaluated for dibenzothiophene and its metabolites and for actual samples including a resid, bitumen, and coal-derived liquid in a set of organic solvents.

Investigations of the activity of isolated and purified enzymes will inform us whether any regulatory species, metal ions, or other cofactors are required for enzyme functioning. If this is the case, methods will be devised for supplying these species in the cell-free system.

4.0 REFERENCES

1. Olson, E.S.; Stanley, D.C.; Gallagher, J.R. *Energy Fuels* **1993**, *7*, 159–164.

2. Gallagher, J.R.; Olson, E.S.; Stanley, D.C. *FEMS Microbiol. Lett.* **1993**, *107*, 31–36.

3. Simonet, J. In *The Chemistry of Sulfones and Sulphoxides*; Patai, S.; Rappoport, Z.; Stirling, C.J.M., Eds.; Wiley: New York, 1988; Chapter 22.

4. Rossi, R.A.; Bunnett, J.F. *J. Amer. Chem. Soc.* **1974**, *96*, 112.

5. Squires, T.G.; Venier, C.G.; Hodgson, B.A.; Chang, L.W. *J. Org. Chem.* **1981**, *46*, 2373–2376.

6. LaCount, R.B.; Friedman, S. *J. Org. Chem.* **1977**, *42*, 2751.

7. Kice, J.L.; Toth, B.R.; Hampton, D.C.; Barbour, J.F. *J. Org. Chem.* **1966**, *31*, 848.

TASK 4.7

DIESEL FUEL DESULFURIZATION

Prepared by:

Edwin S. Olson

August 1994

TABLE OF CONTENTS

TASK 4.7 DIESEL FUEL DESULFURIZATION

1.0 INTRODUCTION

Reductions in the maximum permissible sulfur content of diesel fuel to less than 0.05 wt% will require deep desulfurization technologies to meet these standards. In some refineries, a new hydrogenation catalyst may be required for diesel fuel production. The two treatments discussed in the previous tasks may achieve this level of sulfur reduction, depending on the nature of the compounds in the middle distillate feed for the diesel fuel.

2.0 OBJECTIVES

The extent to which a middle distillate feed can be desulfurized by immobilized desulfurization enzymes will be determined. In addition, the effectiveness of clay-supported molybdenum sulfide catalysts and clay-supported platinum catalysts in removing sulfur from the middle distillate cut will be determined.

3.0 ACCOMPLISHMENTS

Because of the late start date for the contract, work on this task has not been initiated.

Some of the major components of diesel fuel are dibenzothiophene and its alkyl derivatives. These components are desulfurized by the *Rhodococcus* enzymes. If the work proposed in Task 4.6 demonstrates that microbial desulfurization is feasible in an organic medium, the nonaqueous enzyme processing will be used for desulfurization of a diesel fuel. The amounts of both total sulfur and specific organosulfur compounds will be determined in these experiments.

Molybdenum sulfide dispersed on layered supports as described in Task 4.5 will be utilized for hydrotreatment of diesel fuel. Effects of variables such as temperature, catalyst concentration, and hydrogen pressure will be studied. Several runs will be performed with recovered catalysts to determine stability. Recovered catalysts will be examined to determine whether sintering occurred.

TASK 5.1

STABILITY ISSUES

Prepared by:

Chris M. Anderson
Ray A. DeWall
John J. Richter
Mark A. Musich

August 1994

TABLE OF CONTENTS

LIST OF FIGURES

LIST OF TABLES

TASK 5.1 STABILITY ISSUES

1.0 INTRODUCTION

The low-rank coal (LRC) upgrading technologies being developed include evaporative and nonevaporative drying and mild pyrolysis and gasification. An obstacle facing their development is the stability of the product with regard to dusting, moisture reabsorption, and spontaneous combustion. Because stability phenomena are often given only minor attention, the development of improved stability-testing methods was deemed a necessary and complementary component in the successful demonstration of upgrading technologies (1).

The Energy & Environmental Research Center (EERC), in an effort to establish new standards for dried products, has used various known methods as well as developing new methods to evaluate the propensity of lump western coals, raw and dried, to produce dust and absorb water. In 1993, three drying methods–air, hot water, and saturated steam–were used to generate low-moisture upgraded products. New indices for dust generation and friability were determined for assessing the effect of moisture removal and upgrading methodology on coal stability. Analysis of the dried coals using various strength tests indicated that the reduction in moisture made the lump coal unstable, yielding dust indices that were six times higher than those of the raw coal sample. Moisture reabsorption tests showed that air-dried products regained moisture, while hydrothermally dried products resisted moisture absorption (2).

2.0 OBJECTIVES

The near-term objectives are to continue to develop improved methods for evaluating the physical stability of raw and dried coal samples. Technique developments will be based on 1993 laboratory results for three selected coals. In addition, this year's program extended the coal matrix to include a selected North Dakota lignite, which will be used for multiple upgrading research development programs at the EERC. Objectives include the following:

- Continue to develop the modified Jameson cell (3) to determine more accurately the relative dustiness of LRCs and dried LRCs.
- Continue to correlate American Society for Testing and Materials (ASTM) and modified procedures and to understand how they relate to real-world applications.
- Conduct plant-site visits and coal sampling at coal mining and utility stations.
- Begin to investigate spontaneous combustion of raw and dried LRCs.

3.0 ACCOMPLISHMENTS

3.1 Coal Sample Section

Approximately 5440 kg of as-received lignite from the Beulah Mine (Knife River Coal Mining Company, Beulah, North Dakota) was obtained via truck and transferred to a bunker. A low-flow nitrogen purge was introduced to the bunker to prevent lignite degradation prior to utilization. The lignite sample was then used to supply several test programs, including stability evaluation.

Analysis of the as-received Beulah Mine lignite, including proximate, ultimate, heating value, sulfur forms, and ASTM ash x-ray fluorescence (XRFA) are presented in Table 1. Approximately (907 kg) of the lignite was classified into three size fractions. The samples were bagged and then stored in sealable barrels to preserve inherent coal moisture and prevent slacking.

In addition to the North Dakota lignite, three raw low-rank coals were dried using three different procedures and evaluated using various stability methods. All of the coals and coal samples used for the stability test program were sized to 12.7 × 4.75 mm via stage crushing and bottom sizing. This size range was determined to be representative of upgraded coals produced by drying and pyrolysis processes currently in stages of development ranging from bench through demonstration scale (4, 5).

TABLE 1

Beulah Mine Lignite Analysis (as-received)

Proximate, wt%	
Moisture	32.38
Volatile Matter	30.24
Fixed Carbon	31.04
Ash	6.34
Ultimate, wt%	
Hydrogen	6.71
Carbon	43.25
Nitrogen	0.61
Sulfur	0.78
Oxygen (difference)	42.31
Ash	6.34
Heating Value, Btu/lb	7436
Sulfur Forms, wt%	
Organic	0.34
Pyritic	0.40
Sulfatic	0.02

3.2 Durability Testing

3.2.1 Conveyor Test Loop

To evaluate the significance of the laboratory results from the ASTM D441 tumbler test, a test loop consisting of various conveyors was assembled to simulate conventional coal-handling operations. Figure 1 shows the conveyor test assembly. The main equipment used for test setup were four conveyors and a 76.2-cm diameter vibratory screen. The speed of the conveyors used ranged from 0.4 to 1.2 m/s, creating an estimated loop time of about 30 seconds. The loop features a drop area to simulate coal loadout station and transfer areas. Attached to the drop receiving tank is a real-time dust concentration analyzer to measure the level of fugitive or nuisance dust that occurs from dropping the coal sample 1.5 m. Each set of conveyor walls was elevated to keep the coal particles from escaping the system as the coal was being transferred.

The vibratory screening, used to remove –20 mesh material, is located directly after the drop area. This screening step inhibits the loss of additional fugitive dust and provides a method to contain the fines in one location. The preliminary test program was completed at three different residence times and compared to ASTM tumbler test results. A 15-min conveyor test involves transporting the coal 500 m and dropping the coal a total of 45 m. Raw Beulah lignite sized to 12.5 × 4.75 mm was used as the test sample for the conveyor and tumbler testing. The results, summarized in Table 2, illustrate that 15 min of transferring the coal sample with the conveyor test system was similar to a tumbler test using laboratory methods for friability and dust indices. Based on these results, the conveyor test assembly will complement laboratory test procedures in evaluating the durability of solid fuels, to include lump coals, aggregated, and agglomeration fuel types.

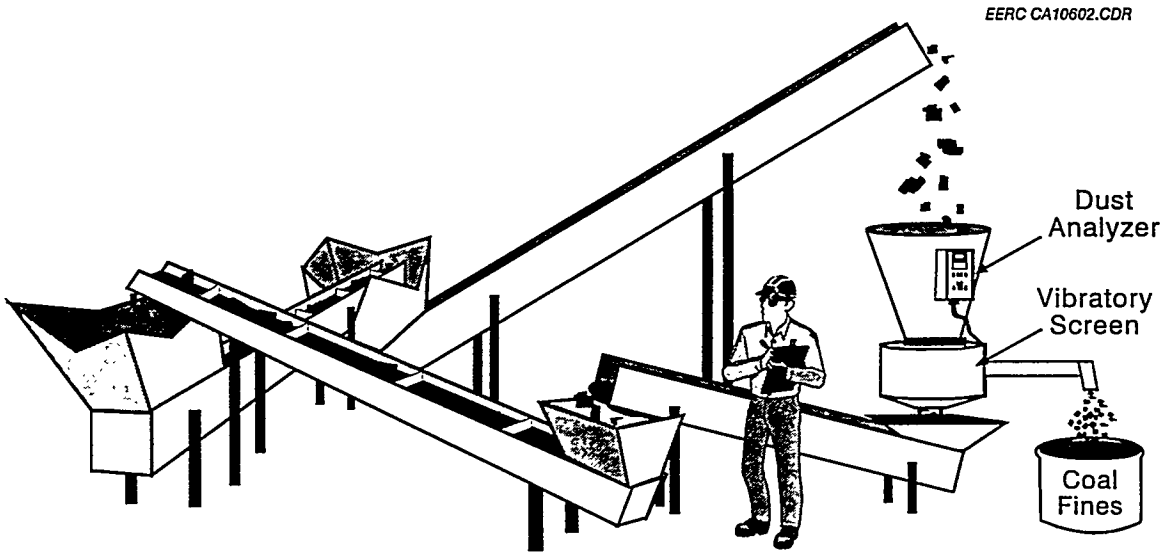

Figure 1. Conveyor test assembly.

3.2.2 Jameson Test Cell

The Jameson unit consists of an ASTM tumbler cell with an in-line dust collection system. The dust collection system includes a coal size inhibitor connected to a vacuum motor. Figure 2 illustrates the assembly. The vacuum pulls air across the tumbling bed of coal sample, simulating wind conditions at approximately 25 km/hr. Results are determined by sieve analysis, amount of dust collected by the vacuum, and the moisture content of periodic samples.

Earlier results on a subbituminous coal had indicated that for the three drying methods evaluated, the amounts of fines generated were not necessarily process-specific, but were more closely related to the moisture content of the individual fuel (2). Recent results from the testing of Knife River coal, illustrated in Figure 3, indicated that the raw coal generated less fines than the dried fuels. This relationship corresponds well to those results reported previously from tumbler and drop–shatter tests (2).

A comparison was made between the moisture loss results for the entire duration of Jameson cell testing on the coals. Moisture analysis indicated that for the three coals tested, the total moisture loss for the samples was 16.9% for Knife River, 15.9% for Colstrip, and 12.6% for Little Tonzona over the 180 minutes of Jameson cell testing. These results are within 5%–10% of the air-dry loss at 25°C as performed for proximate analysis. In addition, Jameson tests conducted on raw coals also indicated that fines

TABLE 2

Summary Information from Tumbler and Conveyor Tests Conducted on Raw Beulah Lignite Samples

	Tumbler Test		Conveyor, 15 min		Conveyor, 30 min		Conveyor, 60 min	
Moisture, wt%	32.3		32.3		32.3		32.3	
Revolutions	___	2400	___	30	___	60	___	120
Avg. size, mm	9.4	8.7	9.7	8.3	9.0	7.1	9.1	5.4
Size, mm	Cumulative Weight Percent Retained on Screen							
9.5	46.5	35.0	55.1	30.2	36.0	11.9	37.3	3.7
6.68	90.6	79.3	91.8	72.0	83.1	50.0	84.2	27.1
4.75	100.0	95.5	100	89.8	100.0	80.3	99.9	55.6
2.36	100.0	97.0	100	95.6	100.0	92.5	100.0	79.2
1.18	100.0	98.0	100	97.3	100.0	95.0	100.0	85.9
0.30	100.0	99.0	100	99.3	100.0	98.7	100.0	96.6
Friability Index, %	7.5		14.7		21.6		40.9	
Dust Index, %	1.0		0.7		1.3		3.5	

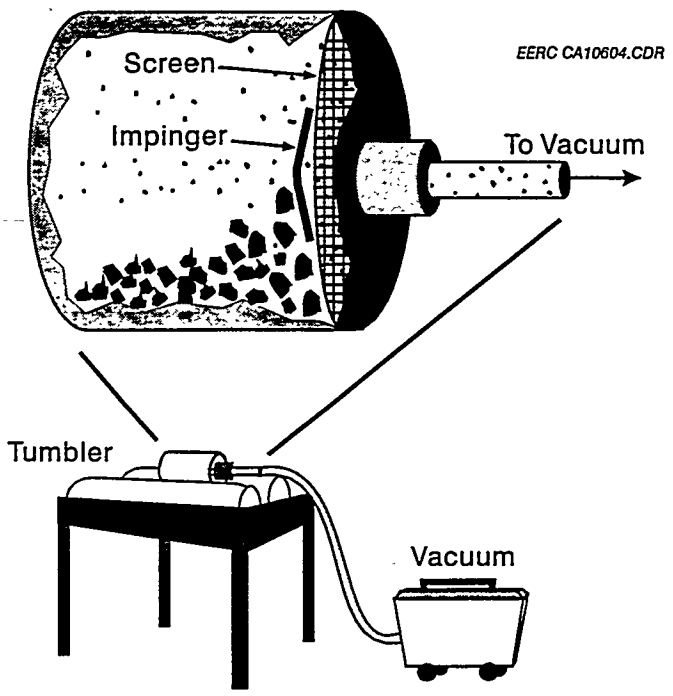

Figure 2. Jameson test assembly.

production depends on the relative humidity of the air being pulled by the vacuum, which in turn dries the coal. The higher the relative humidity, the less drying occurs to the raw coal, producing less fines.

An additional test was conducted on raw and dried fuels that were originally saturated with water and then tumbled. As Figure 4 illustrates, there was an initial suppression of the dust or fines generated; however, as tumbling continued, the saturated sample generated more fines then the original test sample. Initial moisture contents are indicated in parenthesis. These results will be evaluated further to aid in the development of effective water-based dust suppression additives for long distance hauling through a variety of climate conditions.

Preliminary tests were conducted on fuels with similar Hardgrove grindability index (HGI) and moisture contents to formulate some evaluation of the effect that HGI and moisture have on durability. The results indicated that the fines collected from the tumbling did not depend on the HGI but rather on the processing that was performed and moisture contents. For example, a comparison was made between a sample of hot-water dried (HWD) (HGI 69) and steam-saturated dried (SSD) (HGI 64) samples for Little Tonzona. The results indicated that despite having a lower HGI, the SSD coal generated 36% more dust than the HWD coal. This may be because of the flash drying that occurs during the recovery of SSD samples, which may further crack the coal particle, making it more friable.

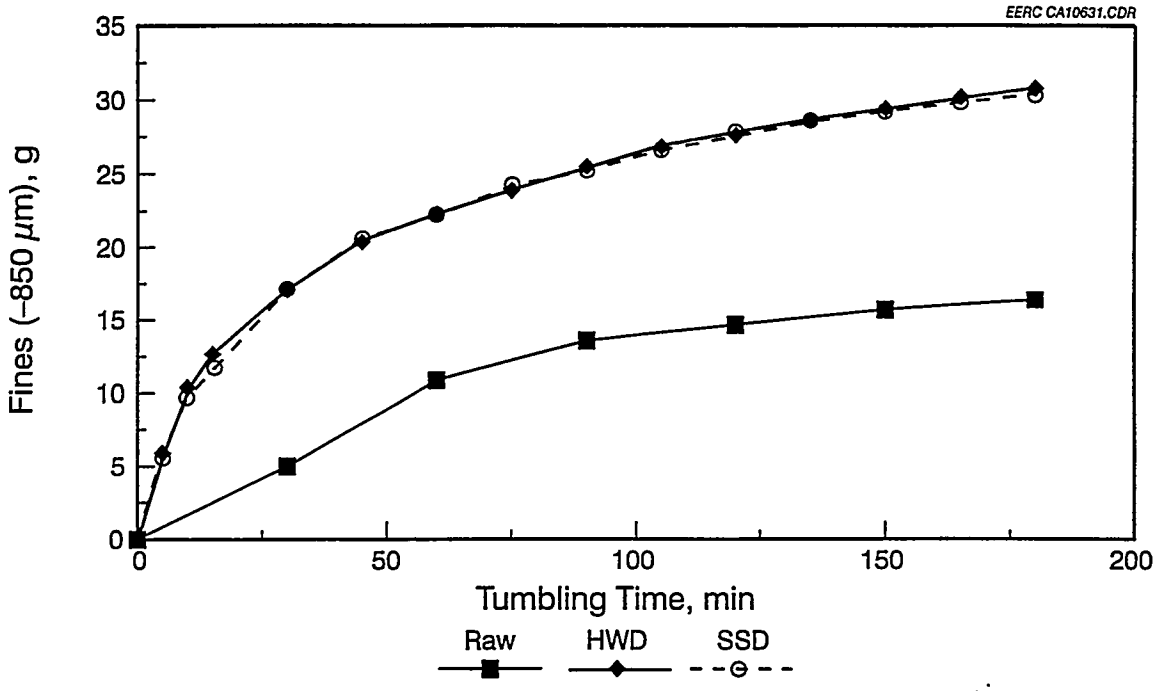

Figure 3. Jameson test results for various Knife River samples.

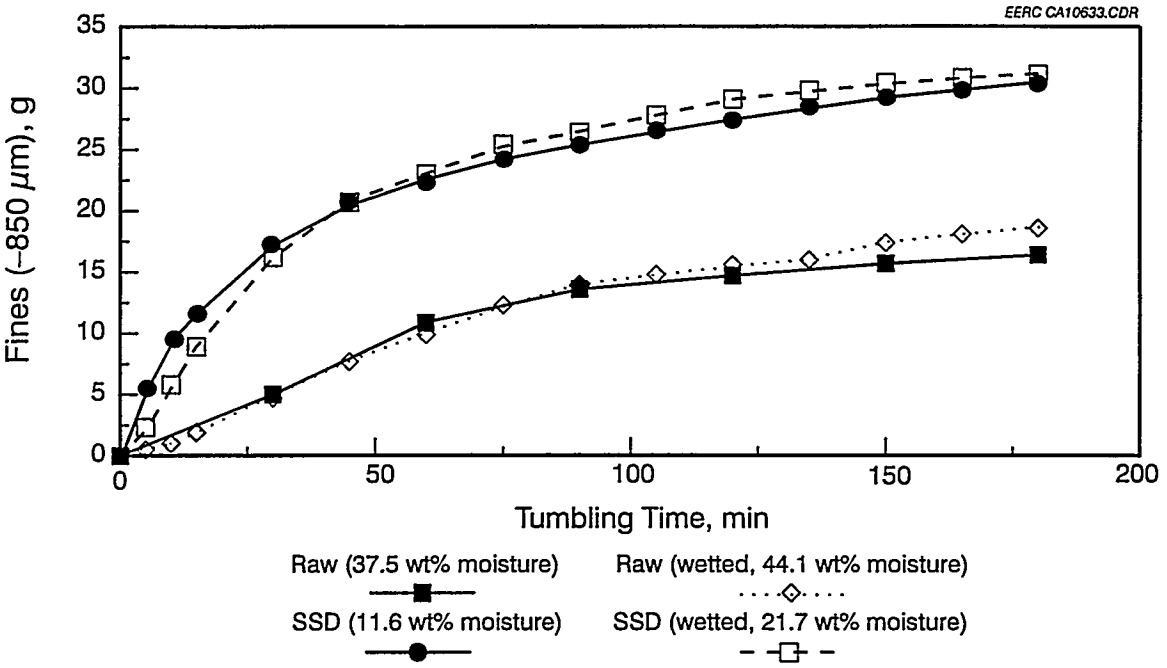

Figure 4. Jameson test results for saturated and unsaturated Knife River samples.

3.2.3 Self-Heating Tendencies of LRCs

For research on self-heating tendencies of LRC and products, the EERC is developing testing procedures following guidelines presented by the Bureau of Mines (6, 7, 8). The goal of the Bureau of Mines is to come up with a portable, inexpensive method to evaluate the self-heating tendencies of coal. After years of development, a test known as the sealed-flask test was identified.

The experimental procedure consists of placing a nitrogen-dried coal sample in 1-pint glass containers equipped with a gas sampling port and connected to a pressure-monitoring system. By monitoring pressure with pressure transducers for three to seven days, a minimum self-heating temperature can be calculated for the coal samples.

Using the Bureau base design, efforts focused on improvements to their system to enhance speed, accuracy, and reliability of self-heating testing while still keeping the unit cost down. Pressure transducers selected for the EERC were Setra® Model C-264 with a 4 to 20 mA output. These pressure transducers can be recalibrated and the span adjusted, whereas the Omega® transducers used by the Bureau do not allow for span adjustment and have a tendency to drift. The Omega® transducers also depend upon barometric pressure, having a range of 0–20 psig. The Setra® transducers have a range of 0–30 cm. of water column for determining pressure and are not affected by barometric pressure. A Genesis software package was used to continuously log pressure indications and present histories for each sample throughout the given test period. Similar to the Bureau of Mines testing, gas chromatography (GC) testing will be done on a sample of the gas removed from the glass container to determine the major gases produced during self heating. Gas will be analyzed using a Hewlett-Packard® Model 5880a GC with a refinery gas analyzer package used to detect selected gases in process gas samples.

Preliminary testing will consist of processing raw and value-added coal samples. Effects of particle size, moisture content, and other variables may be investigated as deemed necessary. The coarse samples will be pulverized, as needed, in a grinding mill and then sieved to obtain the desired size fractions. Additional sample preparation will include drying the samples to constant weight in a continuously nitrogen-purged oven set at 67°C. Predrying will be conducted to help minimize diffusion and exchange phenomena of carbon dioxide observed with LRCs. It has been shown that for LRCs, the moisture content of the coal is directly related to its carboxyl content, and these oxygen-containing groups can exert a controlling influence on the adsorbed water (9). Initial testing conducted with apparatus indicated a need for an improved method of sample containment after drying. Test methods recently developed at Pittsburgh Energy Technology Center (PETC) also indicated a need to minimize sample exposure to atmosphere. In addition, methods development may also include exposure of the dried samples to pure O_2 to speed up self-heating process (10).

3.2.4 Equilibrium Moisture

A humidity chamber will be used to determine equilibrium moisture contents of coal samples. This oven has the capability to determine equilibrium moisture content at 10°–60 °C at a constant relative humidity. The samples will remain in the humidity chamber until constant weight is achieved and then removed and completely dried in a

moisture oven to determine equilibrium moisture concentration. Raw coals and upgraded coals will be evaluated for equilibrium moisture as needed.

4.0 FUTURE WORK

- Continue to correlate laboratory durability test results with conveyor tests as they apply to commercial coal-handling operations. Complete test matrix with raw and dried Beulah lignite samples.

- Initial evaluation of self-heating tendencies on selected coal samples will be correlated with results from Bureau of Mines testing on bituminous coals.

- Equilibrium moisture testing at various temperatures and a constant relative humidity will be performed on raw and value-added samples.

5.0 REFERENCES

1. Grimes, W.R.; Cha, C.; Sheesley, D. "Future Research Needs of Western Coal," *In* Proceedings of the 6th Annual Coal Preparation, Utilization, and Environmental Control Contractors Conference; Pittsburgh, PA, Aug. 1990, pp 267–274.

2. Anderson, C.M.; Musich, M.A.; Young, B.C.; Timpe, R.C.; Olson, E.S.; Sharma, R.K. "Advanced Fuel Forms and Coproducts," semiannual report; DOE Contract No. DE-FC21-93MC30097, 1994.

3. Farrugia, T.J.; Ahmed, N.; Jameson, G.J. "A New Technique for Measuring Dustiness of Coal," *Journal of Coal Quality* **1989**, *2*, 55.

4. Willson, W.G.; Young, B.C.; Irwin, W. "Low-Rank Coal Drying Advances," *Coal* **1992**, *97* (8), 24–27.

5. Couch, G.R. *IEA Coal Research Reference: Lignite Upgrading*; May 1990.

6. Smith, A.C.; Lazarra, C.P. "Spontaneous Combustion Studies of U.S. Coals," Bureau of Mines RI 9079; 1987, 28 p.

7. Miron, Y.; Smith, A.C.; Lazarra, C.P. "Sealed Flask Test for Evaluating the Self-Heating Tendencies of Coals," Bureau of Mines RI 9330; 1990, 18 p.

8. Miron, Y. "Construction and Operation of a Sealed Flask Unit to Assess the Self-Heating Tendencies of Coal," Bureau of Mines RI 4913, 1993, 13 p.

9. Schafer, H.N.S. "Factors Affecting the Equilibrium Moisture Contents of Low-Rank Coals," *Fuel* **1972**, *51* (1), 4–9.

10. Fauth, D. "Spontaneous Combustion of Low-Rank Coal," Presented at 10th Annual Coal Preparation, Utilization, and Environmental Control Contractors Conference, Pittsburgh Energy Technology Center, July 1994.

TASK 5.2

VALUE-ADDED COPRODUCTS

Prepared by:

Brian C. Young

August 1994

TABLE OF CONTENTS

LIST OF FIGURES

LIST OF TABLES

5.2 SORBENT CARBON DEVELOPMENT

1.0 INTRODUCTION

Chars and other carbons, in granular or powdered form, are in high demand worldwide for environmental applications associated with energy production and by-product recovery. Carbons for gas-phase cleanup (sulfur gases, NO_x, and trace element removal) and liquid-phase cleanup (organics removal) sell for several hundred to several thousand dollars per ton, depending upon grade and end use. In general, these carbons have undergone an activation process, i.e., steam or CO_2. Commercial sorbent carbons are derived largely from coal and biomass sources, e.g., coconut shells and wood. Bituminous coals have been typically used for producing hard, large-pore-volume carbons for gas and vapor applications. Lignite carbons, with a hard, small-pore-volume texture, have been preferred in wastewater treatment. Information on the relative effectiveness of bituminous and lignite coal carbons is not readily available. Also, information is needed on the extent to which various preparation and metal ion impregnation procedures can alter structure, gas sorption capacity, and selectivity to develop low-cost supersorbents. Hence the need exists to develop methods to demonstrate the feasibility of utilizing lignites and allied materials (e.g., leonardite) as effective gas or vapor sorbents.

Activated carbon is used as an adsorbent in all aspects of fluids cleanup, including acid gas and toxic trace metals removal from combustion flue gases resulting from electrical generation and waste incineration, removal of heavy metal and organic contaminants of water, and removal of organic vapors from liquid fuel systems to prevent volatile organic emissions (VOCs). The cost of activated carbon produced from traditional feeds such as coconut shells, bones, and other carbonaceous material becomes prohibitive in the quantities required to satisfy all of these needs. An obvious substitute for these feeds is coal, which, because of its large reserves and availability, makes a much less expensive carbon source. Pyrolysis of coal, followed by activation with a reactant gas, has been shown to produce a satisfactory substitute for the activated carbon produced from the previously mentioned activated feedstocks. North Dakota has large reserves of lignite and leonardite (naturally weathered lignite) from which a useful activated carbon product (char) can potentially be manufactured. This project is directed toward producing activated carbon from a leonardite and lignite optimized for specific applications in gas and water cleanup.

2.0 OBJECTIVES

The primary objective of this study is to economically transform low-rank coals (LRCs) into effective sorbent carbons for gas- and liquid-phase contaminant removal.

Specific objectives for 1994 are detailed below.

- To determine the relative ranking of powdered and granulated carbons prepared from a lignite or leonardite with those of commercial carbons derived from bituminous coals or other raw materials for the sorption of sulfur-containing gases and mercury.

- To examine the effect of coal properties (e.g., rank, chemistry, ash content, and composition), metal ion impregnation, and carbon preparation and granulation (size enlargement) on gas-phase adsorption properties.

3.0 ACCOMPLISHMENTS

A new reactor used for carbonizing or carbonizing and activating feedstock is first described. The initial set of test matrices designed to determine the effect of temperature and steam activation on leonardite char is given next.

3.1 Kiln Reactor

The kiln reactor was assembled from a Cress Model X31TC kiln containing a stainless steel cylindrical vessel wrapped on the outside with stainless tubing. The kiln is rated for 2500°F (1370°C). The vessel, which has a capacity of 2700 $in.^3$ (44,480 cm^3), is designed to be operated in the fixed-bed mode. It has a distributer plate on the bottom through which gas, preheated by the kiln as it passes through the external coils on the vessel, enters to permeate the coal bed. The tars, oils, moisture, and effluent gases exit through the top of the vessel and pass through a series of two air-cooled condensers before being vented to the outside of the building.

3.2 Large TGA

A large capacity thermogravimetric analyzer (TGA) was built at EERC to carry out TGA experiments with larger quantities of material. The unit was built using a Cahn 1000 electrobalance and temperature controller and is interfaced to a microcomputer. In this study, the sample (limited by sample bulk) was loaded into a high-temperature stainless steel wire mesh basket, heated at 30°C/min in a flowing N_2 gas stream to target temperatures of 700°, 750°, 800°, or 850°C, and reacted with steam. Higher temperatures are not available on this instrument, so a tube furnace was used for activation at the higher temperatures.

3.3 Tube Furnace (TF)

A Lindberg Type 59344 furnace was used to activate the char at temperatures of 800°, 850°, 900°, 950°, and 1000°C after carbonization. The heating chamber is 19 in. long and accommodated the 1-in. OD Vycor tube, which was used as the reactor vessel when the char was activated.

3.4 Test Plan – Sorbent Preparation and Testing

Feed: Georesources Leonardite, received 6-10-94

Feed Size: −10 x +30 mesh

Carbonization conditions: Kiln vessel – Approximately 12 kg of feed at 480°C under N_2 for 1 hr.

Activation conditions: Test Plan 1 (Table 1), which was completed this quarter, shows the conditions for activating the carbonized leonardite (char) in the kiln. Upon determining optimum temperature at the given conditions, optimum steam activation time at that temperature was determined by repeating the test conditions for the series of activation times.

The activated char was characterized using the following:

- TGA proximate analysis
- SO_2 sorption at ambient temperature
- Iodine number

Properties of the char produced from leonardite according to the test plan are illustrated in Figures 1–5. Figure 1 shows the proximate analysis of raw leonardite, leonardite carbonized at 480°C, and carbonized leonardite, i.e., leonardite char, activated with steam at temperatures from 700° to 1000°C in 50°C intervals. The only trend seen in the figure is a decrease in volatiles. These volatiles at the higher temperature are probably not indigenous to the coal, but are surface-adsorbed gases occurring on exposure of the activated char to air. This being the case, the lower level of volatiles implies a less active char carbon.

Figure 2 shows SO_2 adsorption at ambient temperature by leonardite char activated at several temperatures. The char produced at 850°C shows the greatest SO_2 sorption capacity of those produced in the tube furnace. At activation temperatures higher than 850°C, a decrease in activity with increasing activation temperature is noted. The char activated at 800°C in the TGA shows the highest SO_2 sorption capacity of those activated

TABLE 1

Activation Conditions – Test Plan 1

Test No.	Sample Size, g	Reactor	Atmosphere	Temperature, °C	Time, min
1	10	TGA	N_2	700	10
2	10	TGA	N_2	750	10
3	10	TGA	N_2	800	10
4	10	TGA	N_2	850	10
5	50	TF	N_2	800	10
6	50	TF	N_2	850	10
7	50	TF	N_2	900	10
8	50	TF	N_2	950	10
9	50	TF	N_2	1000	10

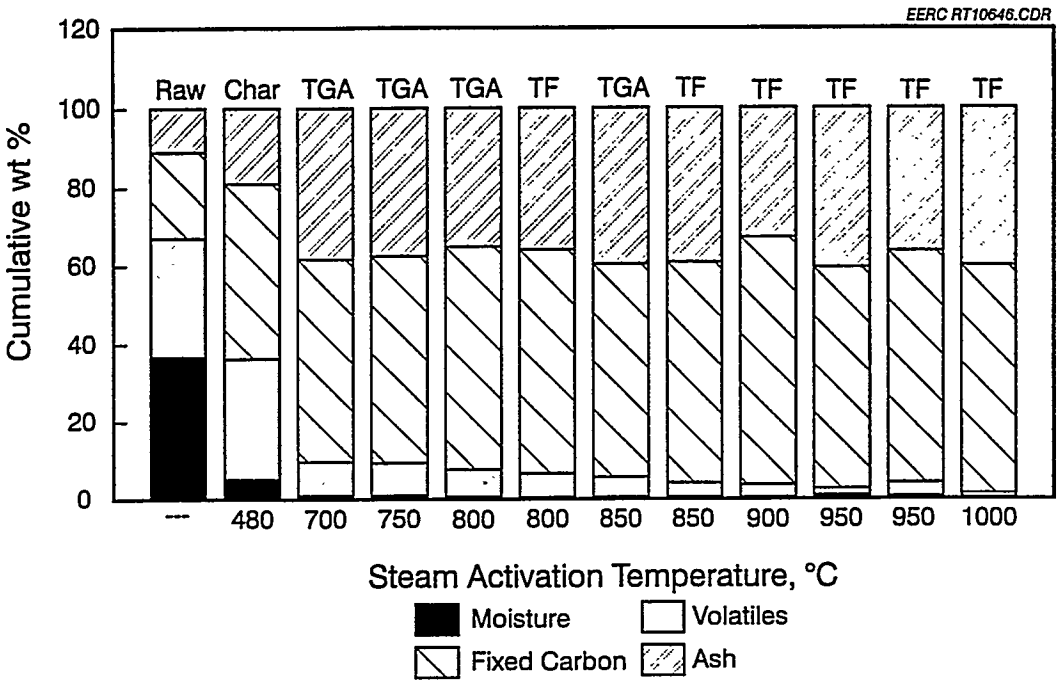

Figure 1. Proximate analysis of raw leonardite, leonardite carbonized at 480°C, and steam-activated carbonized leonardite.

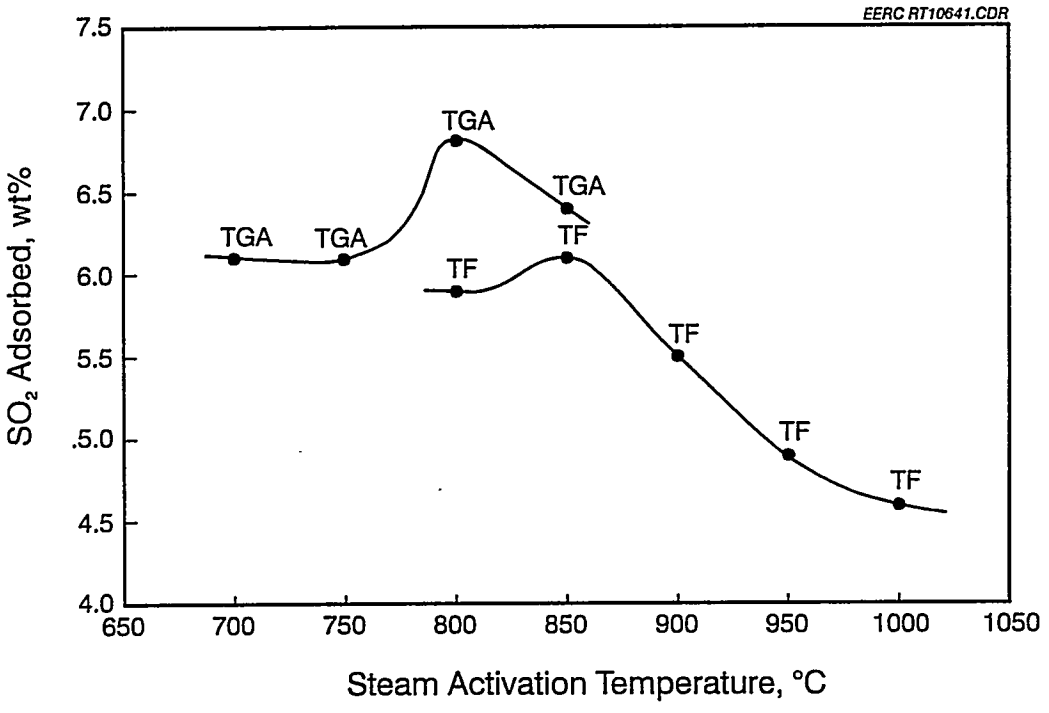

Figure 2. SO_2 adsorption from flowing gas containing 5000 ppm SO_2 in argon at ambient temperature.

in the TGA. Chars activated at 700°, 750°, and 850°C have similar sorption capacities when tested at ambient temperature.

Figure 3 shows SO_2 adsorption at 100°C. Char activated in the TGA shows maximum sorption capacity at 750°C followed by decreasing capacity with increasing temperature. Similarly, the char activated in the tube furnace had a maximum at 800°C followed by a slight decrease with temperatures up to 900°C and then a rapid decrease in sorption capacity up to 1000°C.

Since Figures 2 and 3 showed similar trends but apparently differed by a constant, the ratio of the SO_2 adsorption values at the two temperatures was plotted against activation temperature. Figure 4 shows the near linearity, with a slope of 0.0012/°C. For this set of tests, SO_2 adsorption can be predicted with reasonable accuracy using the following equation:

$$\%_{Amb}\ SO_2 = 2.79 \times \%_{100°C}$$

Figure 5 shows iodine adsorption as a function of activation temperature. The trend of iodine adsorption for the samples activated in the tube furnace is similar to the SO_2 sorption behavior, but those of the samples activated in the TGA exhibit a much steeper slope than those of the tube furnace. However, for SO_2, the slope of the TGA curve was markedly less than that of the tube furnace samples. It appears from this limited data set

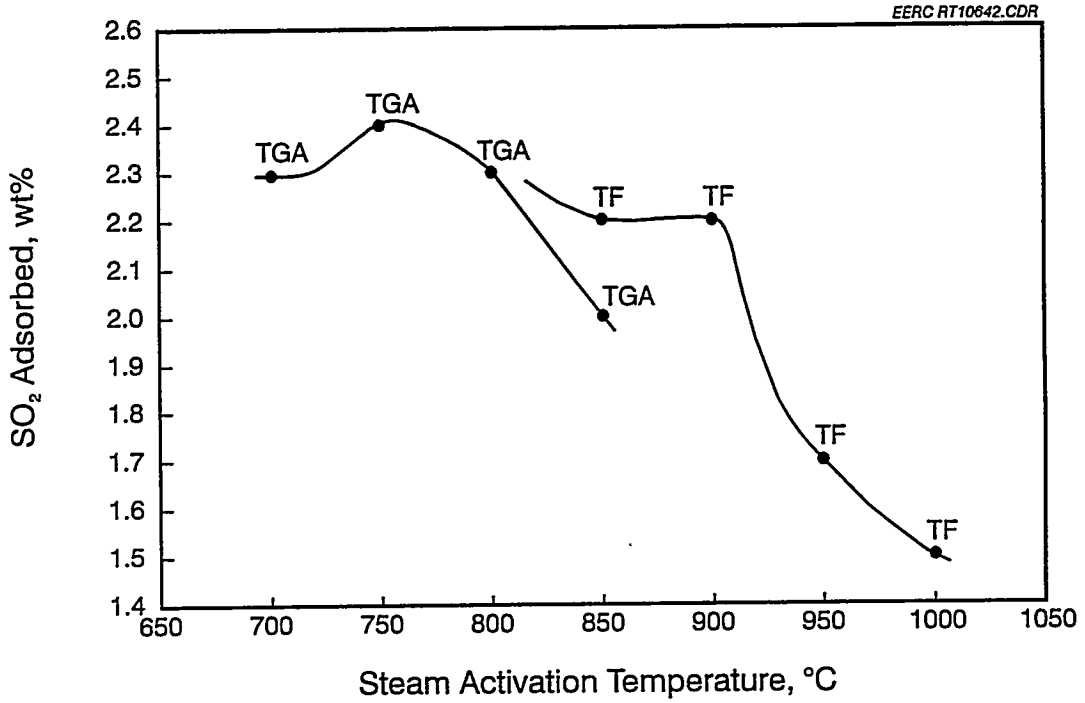

Figure 3. SO_2 adsorption from 5000 ppm SO_2 in argon at 100°C.

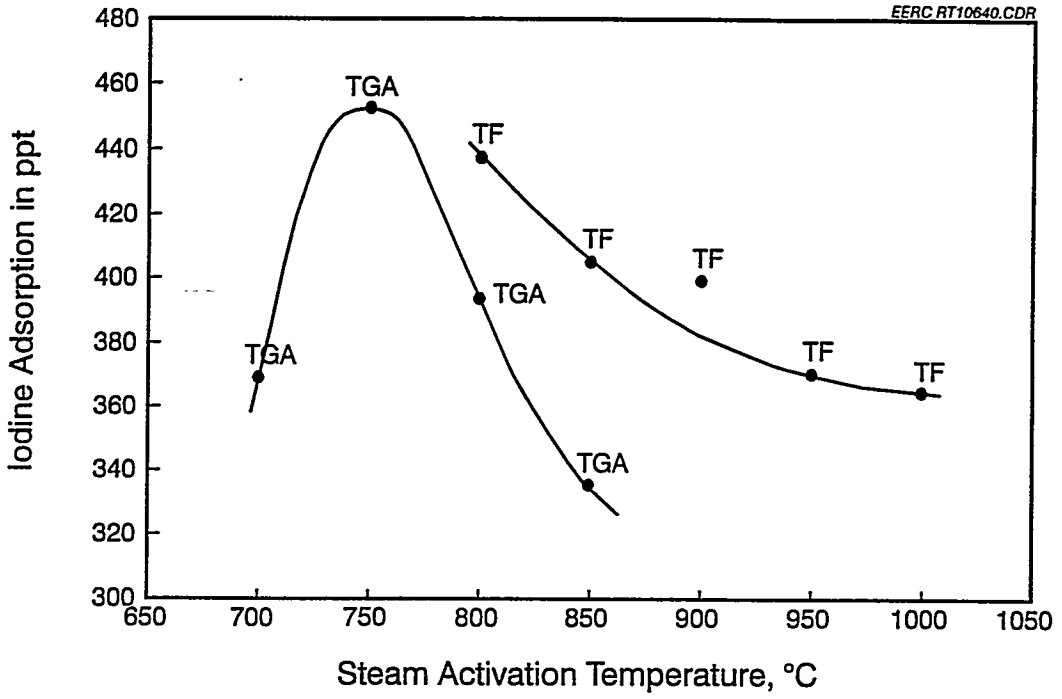

Figure 4. Ratio of SO_2 sorption capacity at ambient temperature to sorption capacity at 100°C versus steam activation temperature.

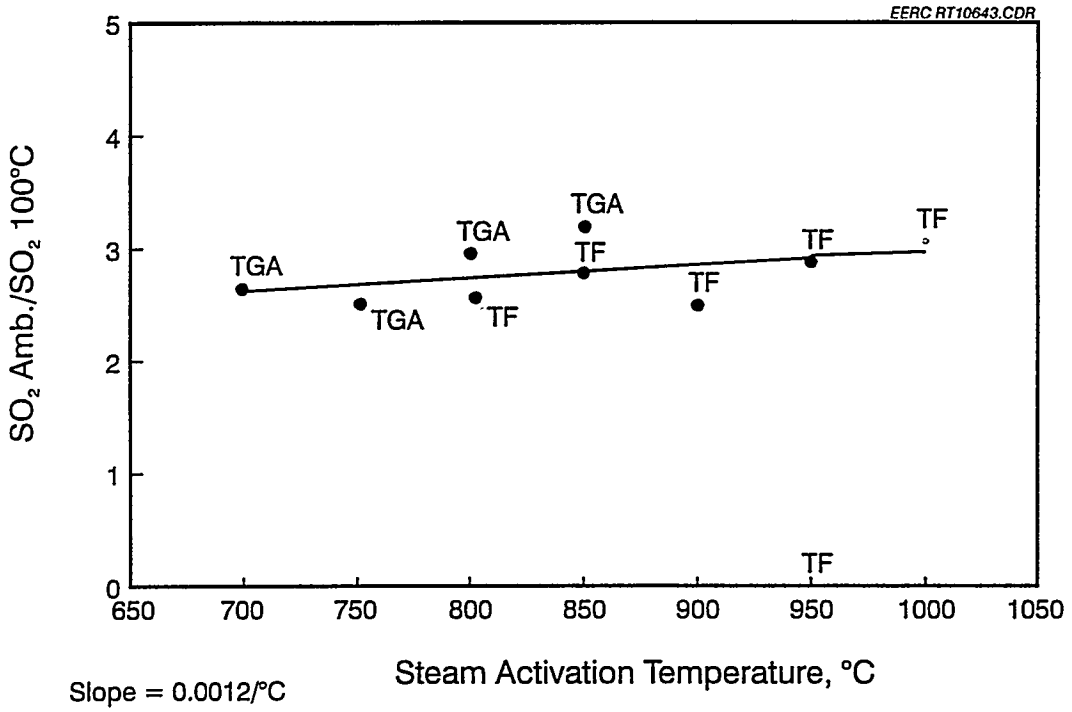

Figure 5. Sorptive capacity for I_2 of chars steam-activated at increasing temperatures.

that the iodine number gives a sharper focus with regard to optimum conditions for maximum sorption than does the SO_2 sorptive capacity. The maximum iodine numbers occurred on chars prepared in the TGA at 750°C and in the TF at 800°C. These are the same activation temperatures that produced the chars having the maximum SO_2 sorption capacities when SO_2 adsorption was measured at 100°C. Nevertheless, the maximum SO_2 capacities measured at ambient temperature occurred on chars activated at 800°C (TGA) and 850°C (TF) temperatures, i.e., chars activated at temperatures 50°C higher than those giving maximum SO_2 capacity when measured at 100°C or maximum iodine number. The iodine numbers calculated from single point determinations, which should lie between 600 and 1450 mg I_2/g C for a commercial active carbon, ranged between 320 and 460 mg I_2/g char for the leonardite char. Sorbent prepared from German brown coal by the method of Stadtwerke Dusseldorf was expected to adsorb up to 16 wt% SO_2, but in practice actually adsorbed 10–12 wt% (1). Marnet, et al. (2) gave similar properties for lignite char and gave SO_2-loading values for the sorbent of 10–15 wt%. GE-Mitsui-BF produces an activated coke that has a sorptive capacity of 6%–12% with a Brunaeur–Emmet–Teller (BET) surface area of 150–250 m^2/g (3). The large difference between the sorptive capacities of the activated leonardite chars and those reported for commercial materials is probably related to the high mineral content of the leonardite. An investigation of the effect of mineral matter reduction on sorption capacity is proceeding.

3.5 Physical Cleaning

Washability testing was performed on raw leonardite and leonardite char prepared in the kiln reactor at 450°C under flowing N_2. The results, shown in Table 2, indicate that physical cleaning will reduce the ash in either the raw or carbonized leonardite by more than 55% with 72%–75% recovery of the feed (db) in the float fraction.

3.6 Summary

- Leonardite carbonized at 480°C produces char with highest SO_2 sorptive capacity and highest number when activated with steam between 750° and 850°C.

TABLE 2

Washability – Leonardite

	Specific Gravity	Weight, g	Solids, wt%	Dry, g	Solid Recovery, wt%	Ash, wt%	Ash Reduction, %
Raw	--	150.0	64	96.5	--	22	--
Float	1.40	112.8	60	68.0	72	9	56
Sink	1.40	31.7	83	26.2	28	54	--
Char (K3)	--	150.0	93	140.2	--	24	--
Float	1.60	112.8	92	104.1	75	11	55
Sink	1.60	36.8	96	35.4	25	62	--

- Reduction of inert mineral material (ash) in the leonardite (or carbonized leonardite) should result in an increase in SO_2 uptake on a mg SO_2/g char basis.

- Measured differences in activity between chars activated at the same temperature in the TGA versus the TF probably result from differences in heating characteristics of the two reactor configurations; i.e., the sample in the TGA receives no heat via conduction from the reactor wall, resulting in more uniform sample heating than the sample in the TF, which is heated primarily by conduction from direct contact with the wall.

- The difference in SO_2 uptake at ambient vs 100°C is probably a result of the relatively large amount of physisorption occurring on the cooler surface caused by bonding that is too weak to retain the sorbate in the presence of increased thermal energy.

- German reports of char preparation show SO_2 uptake of 10%–15% at 70°–90°C. It is difficult to get the details of their measurement method to know exactly how our results compare, although their reported face values are at least a factor of 4 above the values we obtain at 100°C.

4.0 FUTURE WORK

- The leonardite will be cleaned by chemical and physical–chemical methods, the goal being to observe effects of cleaning-induced porosity, ash content, and composition on carbon adsorption capacity.

- Carbon from the uncleaned and cleaned feedstocks will be activated by pyrolysis in inert or steam atmospheres.

- Gas-phase SO_2 adsorption capacity for the prepared powdered carbons will be thermogravimetrically measured using simulated combustion or gasification flue gas streams.

- Mercury sorption will be measured via spectrophotometric analysis.

- Select powdered carbons will be agglomerated (tableted) with appropriate binders and then subjected to similar gas-phase adsorption testing.

5.0 REFERENCES

1. Bewerunge, J.; Ritter, G. "The Use of Lignite Coke for Flue Gas Cleanup in Refuse Incineration Plants," Paper presented at GVC Conference on Disposal of Special Refuse by Incineration, Baden-Baden, Dec. 4–6, 1989.

2. Marnet, C.; Kassebohm, B.; Asmuth, P. "Use of Lignite Coke for Reduction of NO_x after Flue Gas Desulfurization," *In* Proceedings on the 4th Biennial Lignite Symposium on the Technology and Utilization of Low-Rank Coals; Dallas, TX, May 18–21, 1987.

3. Tsuji, K.; Shiraishi, I.; Dague, R.F. "The Activated Coke Process for Combined SO_x/NO_x/Air Toxics Reduction," Presented at the 6th International Symposium of Integrated Energy and Environmental Management, Air and Waste Management Association, New Orleans, LA, March 10–12, 1993.

TASK 5.3

EVALUATION OF CARBON PRODUCTS

Prepared by:

Edwin S. Olson

August 1994

TABLE OF CONTENTS

TASK 5.3 EVALUATION OF CARBON PRODUCTS

1.0 INTRODUCTION

Inverse gas chromatography (GC) and liquid chromatography (LC) methods can be used to determine surface energies or adsorption characteristics. Free energies; enthalpies and entropies of adsorption; acidic or basic characteristics (strengths) and distribution (quantitation); hydrophobicity parameters; sorbent polarities; and deformation polarizabilities will be determined for carbon samples produced in this and other projects.

2.0 OBJECTIVES

The objective of this task is to set up inverse GC instrumentation and obtain a set of measurements useful for determining the thermodynamic properties of chars and carbons from LRCs with respect to adsorption of mercury, sulfur dioxide, and other probe species. The long-range goal is the development of a model for low-rank char porosity and surface energies that relate to its stability and effectiveness for sorption of polar and nonpolar substrates.

3.0 ACCOMPLISHMENTS

Because of the late start date for the contract, work on this task has not been initiated.

Instrumentation for gas and liquid injection of probe molecules into the heated char-packed column and appropriate detection of eluted probes will be assembled. A variety of probes will be utilized to determine the thermodynamic properties of carbons, including polar and nonpolar probes for determining surface hydrophobicities and polarity parameters, which can be related to earlier work with other carbons. Methods for determining adsorption energies of SO_2 and Hg will then be investigated. This technique is not appropriate for determining irreversible chemical bonding, as in the sulfur- or copper sulfide-loaded char for binding mercury.

TASK 5.4

STABLE AND SUPERCRITICAL CHARS

Prepared by:

Edwin S. Olson

August 1994

TABLE OF CONTENTS

TASK 5.4 STABLE AND SUPERCRITICAL CHARS

1.0 INTRODUCTION

The use of chars and carbons as absorbents and catalyst supports could be expanded if their stability to reactive gases were improved. The purpose of this task is to develop methods for applying surface coatings of boron carbide, silicon carbide, and titanium carbide on the char. Formation of these composites will increase stability and improve structural strength and, consequently, resistance to abrasion.

2.0 OBJECTIVE

The first objective of this task is to develop methods for coating LRC chars and carbons by chemical vapor deposition (CVD) to produce high-surface-area composites that are inert to reactive atmospheres. The proposed coating layers will be formed from elements known to form extremely hard and stable carbide materials.

The second objective is to determine the feasibility of using supercritical extraction to prepare an activated carbon with a very high surface area.

3.0 ACCOMPLISHMENTS

Because of the late start date for the contract, work on this task has not been initiated.

High-porosity chars will be produced for coating with inexpensive precursor reagents by vapor deposition methods. Low-rank coals (LRCs) will be utilized because of their large distribution of micro-, meso-, and macropore structures. Composite coating methods will be adapted from carbon fiber work: for boron composites, 1) CVD with boron trichloride and hydrocarbon to produce boron carbide with the composition BC_3 which deposits as a layer and 2) reactive CVD with boron trichloride and hydrogen to produce a thin film of boron carbide with the composition B_4C.

A novel technique will be explored for developing a very large micropore structure in the coal (specific surface area of 2000 m^2/g). This technique employs supercritical solvent extraction of some of the coal material, followed by stabilization of the highly porous structure so that it does not undergo the collapse normally observed when the pressure is brought back to ambient. The technique may involve careful release of pressure at the supercritical point of the solvent, as in the preparation of aerogel precursors or introduction of a stabilizing agent under pressure with a high-pressure liquid chromatograph (HPLC) injection device. The stabilizing agents can be carbon cross-linking agents or boron, silicon, and titanium compounds to stabilize the micropore structure.

The inertness (stability) of the composite carbons containing these protective layers will be investigated by thermogravimetric analysis (TGA) methods in air, hydrogen, and carbon monoxide. Surface areas and pore sizes will be determined, and data on the

composition of the layers (fresh and after activation or use) will be obtained by infrared and Raman spectroscopy, x-ray diffraction (XRD), and electron spectroscopy for chemical analysis (ESCA).

TASK 5.5

BRIQUETTE BINDERS

Prepared by:

Edwin S. Olson

August 1994

TABLE OF CONTENTS

TASK 5.5 BRIQUETTE BINDERS

1.0 INTRODUCTION

Coal briquetting is valuable for compacting coal fines for storage and shipping as well as for the production of smokeless fuels and cokes. Carbonization of the coal briquette produces a carbon form useful for catalyst supports or adsorbent. Many kinds of binders have been used to achieve the desired strength in the briquette. Synthetic polymers have been investigated because of their strength and water insolubility, but cost is a major factor. Basically, less expensive but equally effective binders are still needed.

Recent advances in processing of lignocellulosic material to give some inexpensive intermediates provide us with an opportunity to devise an inexpensive polymeric binding material for making coal briquettes. The recent environmental interest in pyrolysis conversion of plastic waste to usable feedstocks has generated some unique gels that will be investigated for the preparation of briquette binders. Markets are urgently needed for products resulting from both of these technologies.

2.0 OBJECTIVE

The objective of the proposed work is to produce high-strength coal briquettes using inexpensive binders derived from waste plastic pyrolysis tars and from lignocellulose hydrolysates.

3.0 ACCOMPLISHMENTS

New materials and methods were investigated for producing inexpensive adhesive materials from waste materials and very inexpensive mildly processed biomaterials. Pellets were pressed from the coals and chars mixed with the potential binders under various conditions and were compression-tested for strength and for moisture uptake. The subsequent section discusses the preparation of various binders from 1) biomaterials and 2) plastic waste materials.

3.1 Biomaterials

Lignin has been utilized for some time as a binder for briquetting. In this project, the use of lignin with other binder components was investigated for a low-rank Wyodak coal (Knife River) and char products from two coals. For a basis of comparison, dried Knife River coal was ground with lignin (10% binder) and pelleted. The cold-pressed pellet cracked and lacked strength. However, the hot-pressed pellet exhibited a very high compression strength (236 lb/in^2). Previous tests with as-received coal gave pellets that cracked during drying as a result of expulsion of the large moisture content. When no binder was used with the Knife River coal (hot-press), the pellet had very low strength (6 psi).

Conversion of lignin to a Novolak resin (Novolignin) was accomplished by condensation of lignin with formaldehyde to cross-link the phenolic rings in the lignin

macromolecules. This tarry material was mixed with Knife River coal (at 10% binder concentration) and oven-dried. The dried product was ground with cross-linker (hexamethylene tetramine), magnesium oxide, and lubricant (calcium stearate) and cold-pressed into tablets. These components gave a moderately low-strength pellet in the compression test (75 psi). The Novolignin was also converted to an aqueous suspension, which was mixed with coal (at 10%), dried, and mixed with the above pelleting materials. A similar-strength pellet was obtained.

A pellet was also produced from the Knife River coal and phenol Novolak (10%) by hot pressing, but this had a lower strength (59 psi), and the pellet with 5% Novolak binder had a very low strength. The Novolak binder (10%) with cold pressing gave a much lower-strength pellet (28 psi). But the strength was substantially improved by curing the cold-pressed pellet at 150°C (194 psi). The coal was then pelleted with a mixture of phenol Novolak (5%) and lignin (10%). The hot-pressed pellet had a very high compression strength (198 psi). The cold-pressed pellet was less stable (56 psi) even with heat curing. Increasing the amount of Novolak in the composition to 10% improved the strength considerably (141 psi).

A char product from low-rank coal (TRW Gravimelt process) was mixed with Novolak (5%) and the cross-linking and lubricant components, then hot-pressed into pellets. The pellet prepared from the char exhibited very high compression strength (257 psi). A very fine char from bituminous coal (TRW Gravimelt Process) was also mixed with Novolak and hot-pressed. The pellets from the bituminous char were too fragile to be even tested for compression strength.

3.2 Coal-Derived Binders

A coal-derived binder was also tested with the Wyodak coal and the two char products. The intermediate low-severity liquefaction product from a low-rank coal (low-severity Wyodak [LSW]) was utilized directly as the binder. The hot-pressed pellet from the coal and LSW (10%) was moderately strong (76 psi), but the char pellets were too fragile for testing.

3.3 Waste Plastic Products

Thermal processing of plastic waste containing polyethylene terephthalate (PET) from bottles and tape results in a highly viscous gel consisting of aromatic polymers and oligomers. Formation of this material appears to be a major problem for plastic waste recycling, and there is no market for this dark, viscous product. Various mixtures of plastics representative of collected wastes have been pyrolyzed at the Energy & Environmental Research Center (EERC) and some of the products from that project were available for this study.

The pyrolysis product from a mixture of 50% polystyrene and 50% PET was used as-received for binding coal. In addition to the aromatic gel materials, the pyrolysis product contained some volatiles, such as styrene, that may have been stripped off or reacted during pelleting or curing. The coal used was Knife River lignite. At a 15% binder concentration, the pellet had a relatively low strength (40 psi).

The product from pyrolysis of a tape containing PET was also utilized. This product had a slight pine odor and contained no styrene. Formation of the pellet with lignite at 15% binder composition was carried out. However, again the pellet had low compression strength (36 psi).

Several attempts were made to prepare binders from polystyrene packing foam. Finely ground foam was mixed with the Knife River coal at 10% concentration. The pellet was very fragile and could not be tested. Similar results were obtained with the two char samples described above. It is likely that the polystyrene is not able to sufficiently coat the coal particles to provide effective binding.

To generate a better dispersion of the polystyrene for coating the coal particles, the foam was dissolved in solvent and stirred into the Knife River coal (7.5% binder). The pellet was formed by hot pressing. The effectiveness of this binder was demonstrated by its very high compression strength (425 psi).

The solution of the polystyrene foam was mixed with the two char samples at 10% concentrations. The pellet from the bituminous char had a very high compression pressure (233 psi), and the pellet from the low-rank char also had a very good strength (192 psi). This was the first case where the bituminous char showed a high strength.

4.0 CONCLUSIONS

Waste plastic materials have been successfully utilized to prepare high-strength binders for coal and chars. Novolac binders generally did not give high-strength pellets, possibly because of the brittleness of the resin after curing. When lignin was used alone or with the Novolac, high-strength binders were also formed. Methods for formulating and pressing out pellets from the desired binders with a low-rank coal were worked out in this quarter.

5.0 FUTURE WORK

Methods for cross-linking the olefinic pyrolysis products and other waste plastic materials are being examined. Further investigation of pellets that are prepared with a carbon product instead of coal are currently under way.

TASK 5.6

CARBON MOLECULAR SIEVES

Prepared by:

Edwin S. Olson

August 1994

TABLE OF CONTENTS

TASK 5.6 CARBON MOLECULAR SIEVES

1.0 INTRODUCTION

Separations of gas components can be effected by molecular sieves made from carbons by developing a pore-size distribution in the subnanometer range. The required pore-size distribution can be achieved by filling the numerous larger pores in a coal char with a liquid phase, which is a good precursor for carbons when thermally activated. This technique will be performed with some recently available materials from waste and coal pyrolysis.

2.0 OBJECTIVE

The objective of this task is to examine the feasibility of preparing microporous composite carbons from inexpensive or waste products that exhibit high selectivity properties suitable for gas separations. Although many tarry and polymeric materials have been investigated previously, the pore-filling materials utilized in this project will be unique.

3.0 ACCOMPLISHMENTS

Because of the late start date for the contract, work on this task has not been initiated.

New methods for synthesis of carbon molecular sieves will be investigated. New types of organic pore fillers will be cross-linked inside high-porosity low-rank coal (LRC) chars and the products tested for gas separation capabilities. Precursor materials include the following:

- Low-severity liquefaction products
- Mild gasification tars
- Plastic pyrolysis tars (from polyethylene terephthalate bottles)

Cross-linking agents include methylal and furfural derivatives. Following thermal activation of the pore-filled char, the selectivity will be determined for a propane–propylene mixture. Later studies will determine selectivity of oxygen separation from air.

TASK 5.7

COAL CHAR FUEL EVAPORATION CANISTER SORBENT

Prepared by:

Ted R. Aulich
Ames A. Grisanti
Curtis L. Knudson

August 1994

TABLE OF CONTENTS

LIST OF FIGURES

LIST OF TABLES

TASK 5.7 COAL CHAR FUEL EVAPORATION CANISTER SORBENT

1.0 INTRODUCTION

Automobile evaporative emission canisters contain activated carbon sorbents that trap and store fuel vapors emitted from automobile fuel tanks during periods of hot ambient temperatures and after engine operation. When a vehicle is started, combustion air is pulled through the canister, and adsorbed vapors are removed from the sorbent and routed to the intake manifold for combustion along with fuel from the tank. The two primary requirements of an effective canister sorbent are that 1) it must be a strong enough adsorbent to capture all fuel vapors that contact it, and 2) it must be a weak enough adsorbent to release the captured vapors in the presence of the airflow required by the engine for fuel combustion. Most currently available commercial canister sorbents are made from wood, which is reacted with phosporic acid and heat to yield an activated carbon with optimum pore size for gasoline vapor adsorption.

Although current EPA regulations regarding automobile fuel vapor emissions are concerned primarily with evaporation due to ambient or engine operation temperatures, regulations are being prepared that will require capturing refueling emissions, which are generated by displacement of fuel vapors (present in the head space of a partially empty tank) with liquid fuel. Meeting these regulations, which are scheduled to be initiated in 1998 and phased in over the next two years, will involve the use of "on-board" refueling emission canisters. Because of size, aerodynamic, and weight considerations important for optimum mileage, the mandated addition of refueling emission canisters to automobiles will create a need for sorbents that can meet higher vapor capacity and loading rate requirements. Work is ongoing at Westvaco Corporation in Charleston, South Carolina, and Dow Chemical Company in Midland, Michigan, to develop more efficient activated carbon and synthetic polymeric sorbents, respectively, for automotive applications.

The primary objective of Task 5.7 is to evaluate the use of lignite char as an automobile fuel evaporation canister sorbent. The performance of a steam-treated lignite char from American Norit Company will be measured against the performance of 1) a commercial sorbent obtained from a canister purchased at a local auto parts store, 2) a recently patented synthetic polymeric sorbent obtained from Dow Chemical, and 3) three steam-treated peat-derived sorbents from American Norit. The secondary objectives of Task 5.7 are to investigate 1) whether the performance of any of the sorbents is affected by the presence of ethanol in gasoline at a concentration of 10 volume percent (vol%), and 2) whether any of the sorbents has a preference for adsorption of ethanol vapors over gasoline vapors. These investigations will involve comparing the adsorbing and desorbing capacities of the sorbents with unleaded regular "base" gasoline to the capacities of the sorbents with E10 fuel, a blend of 90 vol% base gasoline with 10 vol% ethanol. The motivation for the work with E10 fuel was provided by comparison of Energy & Environmental Research Center (EERC) data on evaporative emission compositions with data from other researchers using sealed housing for evaporative determination (SHED) test methodology. While the EERC data showed that the ethanol concentration in an evaporative emission from an E10 blend should be about 13 weight percent (wt%), published SHED test results for ethanol concentration in E10 evaporative emissions ranged from 2–20 wt% (1–5). One possible explanation for these differences may involve canister performance with E10 fuels.

2.0 ACCOMPLISHMENTS

The EERC evaporation canister sorbent test system was designed based on published designs of Westvaco Corporation and Dow Chemical Company sorbent test systems (6–8). The EERC system, shown in Figure 1, was designed to test sorbents for adsorbing and desorbing capacity using vapors from normal butane, gasoline, or any other desired gas or volatile liquid. The Task 5.7 test program calls for intitial shakedown testing with normal butane, followed by testing with locally purchased gasoline.

As shown in Figure 1, the test system is built around two sorbent beds connected in series. The first (primary) sorbent bed contains the sorbent being tested, and the second (secondary) bed contains a sorbent (whatever material is available) used to collect "breakthrough" vapors from the primary bed. The output of the secondary bed is passed through a 10-cm path length, 50-cc gas cell mounted in the sample compartment of a Bomem Model B-100 Fourier transform infrared spectrometer (FT-IR), which is used to monitor the output of the secondary bed. Vapors (which in the initial series of tests were generated from a tank of certified pure normal butane) are delivered at a constant rate to the primary sorbent bed using a calibrated mass-flow controller. The primary bed volume is approximately 25 cc, which can contain about 7–10 g of sorbent, depending on sorbent density. The temperature of the primary bed is maintained at 25°C by a controlled temperature bath that uses ethylene glycol as the circulating heat-transfer fluid. The secondary bed volume is approximately 50 cc, and its temperature is allowed to vary with ambient conditions. The mass-flow controller delivers the test vapor (or nitrogen, which is

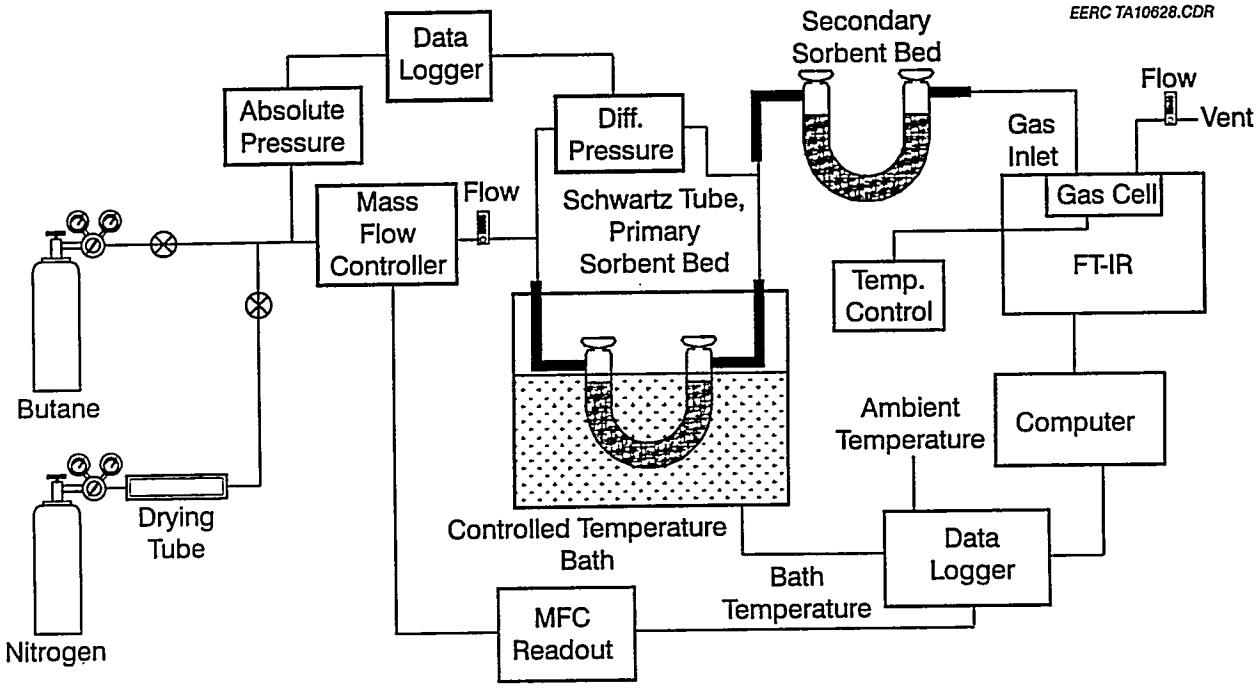

Figure 1. Sorbent test aparatus.

used as a purge or carrier gas) to the apparatus. The inlet pressure to the mass-flow controller is monitored using an electronic pressure transducer. Gas flow to the sorbent bed is also monitored with a floating ball-type flow indicator, used as a backup check on the normal butane mass flow. The sorbent bed pressure drop is monitored with an electronic differential pressure transducer. The temperature of the circulating ethylene glycol temperature bath and the ambient temperature are also monitored througout each test. The temperature of the FT-IR gas cell is maintained at 25°C using an electronically controlled heater. Another floating ball-type flow indicator is used to monitor the outlet gas flow on the downstream side of the FT-IR gas cell. All electronically monitored temperature, pressure, and flow rate readings are converted to digital signals by a data logger and input to a personal computer. The FT-IR and data logger are controlled by a personal computer, which is programmed to collect and store data at timed intervals. The following is a description of the test procedure used to compare sorbents based on their butane adsorption and desorption capacities.

The sorbent to be tested is dried for four to six hours in an oven at 100°C. The weight of the empty primary sorbent bed container (a glass Schwartz tube—see Figure 1) is determined using an analytical balance and recorded. The test sorbent is loaded into the Schwartz tube to a predetermined volume such that the portion of the tube containing the sorbent is completely immersible in the controlled temperature bath. The weight of the filled tube is then recorded and the tube is sealed and immersed in the 25°C controlled temperature bath. The secondary sorbent bed is then filled with nontest sorbent, weighed, sealed and connected to the system as shown in Figure 1. The complete flow system is purged with nitrogen at a flow rate of 190 standard cubic centimeters per minute (sccm) for 2 minutes. The computer is then programmed to collect data at 20-second intervals and data collection begins. At 100 seconds into the test, the input gas is switched from nitrogen to normal butane and a timer is started. The normal butane flow is maintained at 50 sccm for 30 minutes. The test sorbent-containing Schwartz tube is then removed from the temperature bath and the outside of the tube is wiped to remove ethylene glycol from the temperature bath. The inside of the tube is examined for condensation, and if water vapor or other nonsorbent materials are observed, the test is aborted. If no condensation or other nonsorbent material is observed, the weight of the tube (with sorbent and adsorbed material) is recorded. The secondary sorbent bed is also removed, examined and weighed. If desorption capacity testing is to be performed, the two sorbent beds are placed back in the test system; however, the primary sorbent bed is positioned in the flow system "backwards" to ensure that nitrogen purge flow through the sorbent is reversed. Nitrogen flow at 50 sccm is initiated and maintained 30 minutes, after which the two sorbent-containing tubes are removed and their weights recorded. Table 1 lists butane adsorption and desorption capacity test conditions.

Sorbents tested using *n*-butane vapor include material extracted from a new canister (for 1992 Ford vehicles) purchased at a local autoparts store and materials obtained from American Norit and Dow Chemical. Sorbent from the Ford canister was extracted after cutting the canister in half with a saw. The American Norit materials included three steam-treated, peat-derived sorbents and one steam-treated lignite-derived sorbent, and the Dow sorbent was a synthetic polymeric material. Typically, three tests were done, one after the other, with each sorbent. Several sorbents were tested up to six times. The resulting data are summarized in Table 2, which lists average conditions and average adsorption and desorption data for each sorbent tested, along with the number of tests performed with each sorbent.

TABLE 1

Test Conditions

Parameter	Value
Nitrogen Flow Rate	50 sccm
n-Butane Flow Rate	50 sccm
Adsorption Time	30 min
Desorption Time	30 min
Primary Sorbent Bed Weight (average)	8 g
Primary Sorbent Bed Temperature	25°C
Average Ambient Temperature	21°C

3.0 CONCLUSIONS

Figure 2, which compares the sorbents on the basis of grams butane adsorbed per grams sorbent, shows that the Dow XU-43546 adsorbed the most material over a 30-minute period, with the Ford canister sorbent and a Norit peat adsorbing slightly less. Figure 3, which compares the sorbents on the basis of grams of butane desorbed per grams butane adsorbed, shows that the Dow and Ford canister materials were the best "desorbers," followed very closely by the Norit lignite. In comparing the desorption data, it is important to remember that airflow through a canister properly installed on an operating vehicle will be much higher than the airflow used in these preliminary tests, which means that the desorption/adsorption ratios reported here are probably minimum values.

These preliminary butane adsorbing/desorbing data indicate that while the lignite char is comparable to the Dow and commercial canister sorbents in desorption capacity, it fared poorly in adsorbance capacity under the conditions employed for these tests. A better indication of lignite performance as a fuel evaporation canister sorbent will be provided in upcoming tests with gasoline vapors. Regardless of how the gasoline testing goes, the high desorbing capacity of the lignite char warrants further study of lignite-derived materials as sorbents for other vapor-capturing applications in which the vapor molecules have physical (pore size-related), chemical, or concentration characteristics that may make them more suitable for lignite adsorbance and desorbance. Possibilities may involve gas streams that contain alcohols, glycols, and/or phenols, or gas streams with low pollutant concentration which, historically, have been expensive to treat (9). The test system designed for the work reported here will work well in evaluating lignite performance as a sorbent in other applications.

TABLE 2

Average *n*-Butane Adsorption/Desorption Data

Sorbent	Adsorbed Butane/ Sorbent (g/g)	Desorbed/Adsorbed (g/g)	Ambient Temp., °C	Bath Temp., °C	Pressure Differential, in. H_2O	Number of Tests, Adsorbed	Number of Tests, Desorbed
92 Ford	0.367	0.581	22.05	25.39	0.22	5	3
SorboNorit 3 Peat	0.296	0.339	18.14	25.47	0.22	6	3
Norit RB3 Peat	0.295	0.270	21.10	25.57	0.22	8	5
SorboNorit B3 Peat	0.267	0.309	23.81	25.20	0.22	3	3
Norit GD Lignite	0.157	0.548	22.12	25.43	0.23	8	6
Dow XU-43546	0.422	0.575	21.30	25.26	0.23	6	3
Relative standard deviations							
92 Ford	0.032	0.057	0.067	0.014	0.047		
SorboNorit 3 Peat	0.011	0.045	0.112	0.018	0.047		
Norit RB3 Peat	0.297	0.072	0.095	0.010	0.046		
SorboNorit B3 Peat	0.088	0.029	0.041	0.001	0.699		
Norit GD Lignite	0.418	0.253	0.066	0.008	0.038		
Dow XU-43546	0.235	0.016	0.078	0.007	0.543		

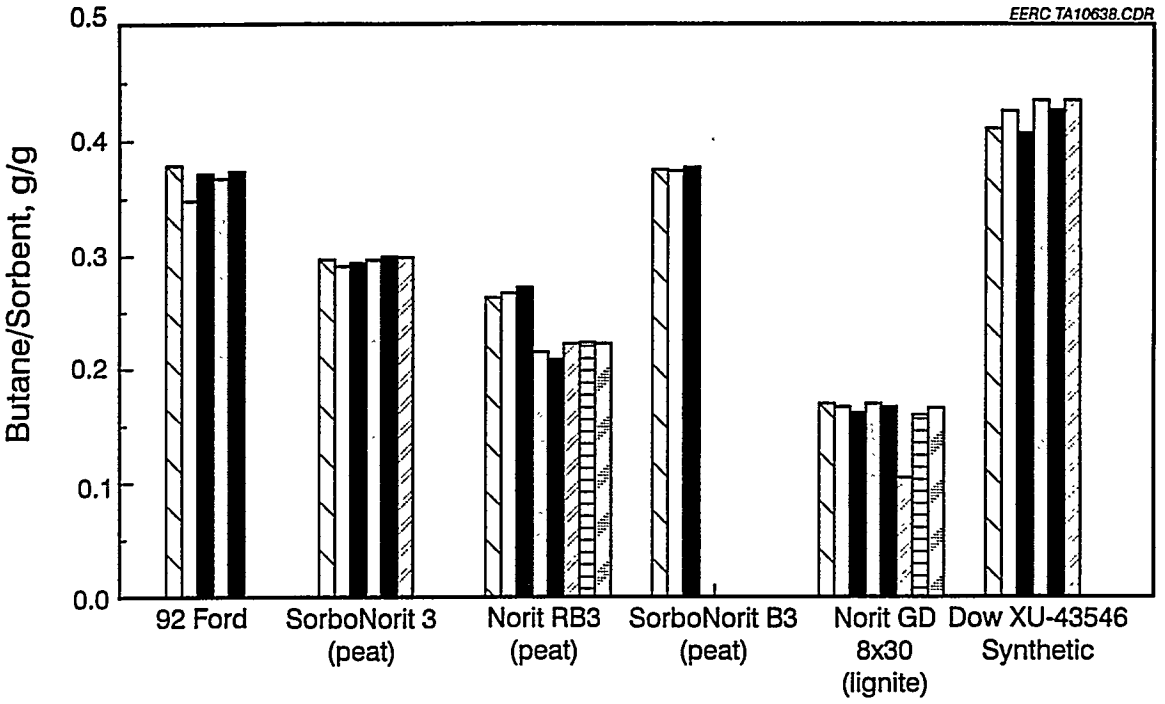

Figure 2. Grams *n*-butane adsorbed per gram of sorbent.

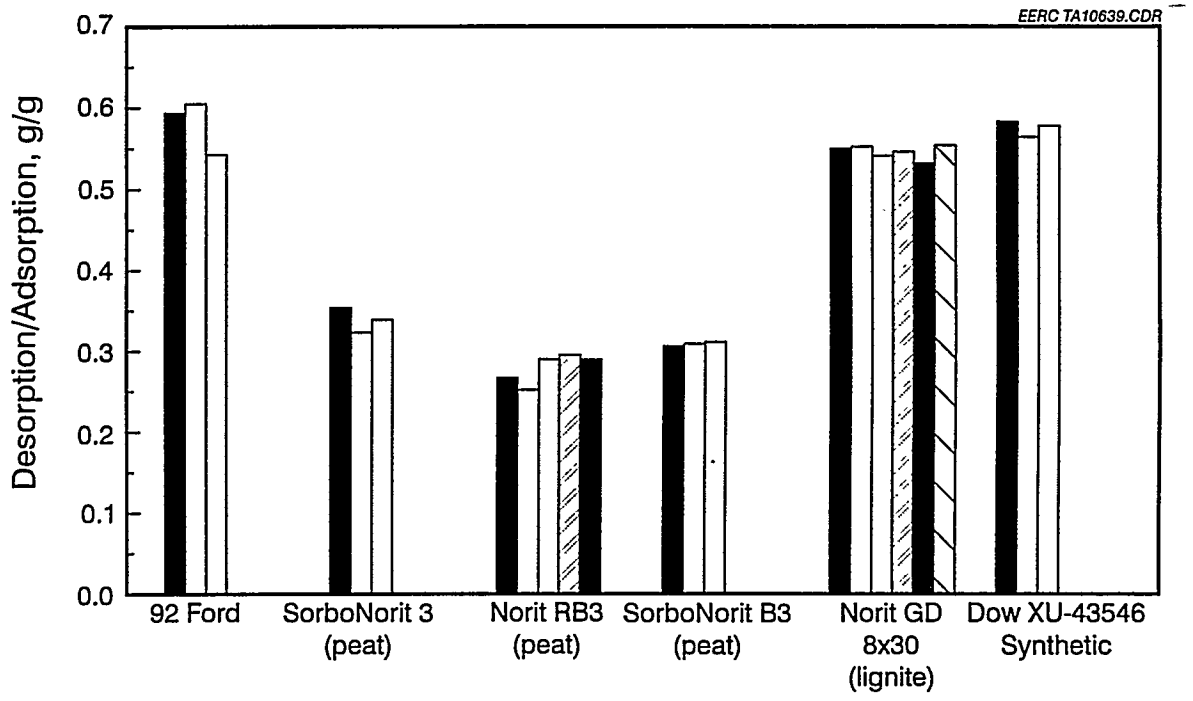

Figure 3. Grams *n*-butane desorbed per gram of *n*-butane adsorbed.

4.0 FUTURE WORK

Upcoming work will include comparing the sorbents on the basis of capacity to adsorb and desorb gasoline vapors, including vapors from a base gasoline and vapors from base gasoline blended with ethanol at a concentration of 10 volume percent (E10). In addition, if time is available, tests will be performed in which sorbents are compared on the basis of gasoline working capacity, which is a sorbent bed's adsorption/desorption capacity after it has been subjected to several (at least 10) load-and-purge cycles. During a load-and-purge cycle, a sorbent bed is loaded to saturation capacity and then desorbed at a specific airflow rate for a specific time. Gasoline working capacity is the most definitive criterion for fuel canister sorbent evaluation, because it most accurately predicts how well a canister will work in the real world.

5.0 REFERENCES

1. Stump, F.D.; Knapp, K.T.; Ray, W.D. "The Seasonal Impact of Blending Oxygenated Organics with Gasoline on Motor Vehicle Tailpipe and Evaporative Emissions," *J. Air Waste Manage. Assoc.*, **1990**, *40*, 872.

2. Stump, F.D.; Knapp, K.T.; Ray, W.D.; Burton, C.; Snow, R. "The Seasonal Impact of Blending Oxygenated Organics with Gasoline on Motor Vehicle Tailpipe and Evaporative Emissions, Part 2," SAE Paper No. 902129, 1990.

3. Furey, R.L.; King, J.B. "Evaporative and Exhaust Emissions from Cars Fueled with Gasoline Containing Ethanol or Methyl *tert*-Butyl Ether," SAE Paper No. 800261, 1980.

4. Lang, J.M.; Black, F.M. "Impact of Gasohol on Automobile Evaporative and Tailpipe Emissions," SAE Paper No. 810438, 1980.

5. Naman, T.M.; Allsup, J.R. "Exhaust and Evaporative Emissions from Alcohol and Ether Fuel Blends," SAE Paper No. 800858, 1980.

6. Johnson, H.R.; Williams, R.S. "Performance of Activated Carbon in Evaporative Loss Control Systems," SAE Paper No. 902119, 1990.

7. McDaniel, R. "Westvaco Technical Lab Procedures—Butane Working Capacity," Westvaco Corporation, Chemical Division: Washington Street, Covington, VA 24426; Jan. 10, 1992.

8. Dow Polymeric Adsorbent XU-43546 Technical Data Sheet, Butane Adsorption Capacity Test; Dow Chemical Company: Midland, MI 48674.

9. Ruhl, M.J. "Recover VOCs via Adsorption on Activated Carbon," *Chemical Engineering Progress* **1993**, *89* (7), 37–41.

TASK 5.8

DEVELOPMENT OF A COAL BY-PRODUCT CLASSIFICATION PROTOCOL FOR UTILIZATION

Prepared by:

Edward N. Steadman
Debra F. Pflughoeft-Hassett

August 1994

TABLE OF CONTENTS

TASK 5.8 DEVELOPMENT OF A COAL BY-PRODUCT CLASSIFICATION PROTOCOL FOR UTILIZATION

1.0 INTRODUCTION

A large volume of fly ash is produced that does not meet current American Society for Testing and Materials (ASTM) specifications for cement and concrete but could be used for other applications. In many cases, coal ash is required to meet ASTM specifications even when they are clearly inappropriate for the application (i.e., structural fill).

Creating a classification system for fly ash that facilitates the use of performance-based specifications for use applications will broaden the utilization options for coal ash, avoiding disposal costs and providing opportunities for industry to develop new products and expand the use of coal ash in existing products. The inadequacy of the current classification system is one of the major technical barriers to increased coal by-product utilization. This project is ideally suited to the Energy & Environmental Research Center (EERC) multidisciplinary approach and involves personnel from several groups.

2.0 OBJECTIVES

The goal of this project is to develop a classification system for fly ash based on parameters that relate to performance specifications of engineering and construction applications. The new classification system will provide a means to evaluate the suitability of coal ash for use in certain products that currently have no reality-based standards or classifications.

3.0 ACCOMPLISHMENTS

In order to keep this task within the available budget, it was decided to limit the scope of work to a single use application. The application selected was structural fill. Recent work by ASTM Committee E50 on Pollution Prevention has proposed a standard practice for use of coal ash for structural fill. EERC coal ash researchers have worked on preparing this standard practice. The development of criteria for coal ash to be used in this application will facilitate the use of this standard once it has been approved by ASTM.

A preliminary set of requirements for coal ash to be deemed acceptable in use applications was developed. The initial criterion is an environmental screening test. For structural fill, other criteria will include several physical properties such as compaction, handling specifications, and density.

4.0 FUTURE WORK

A flow chart for classification criteria will be developed. Appropriate test procedures will be evaluated for validity. Where required, new test methods or modifications will be recommended.

TASK 5.9

USE OF COAL ASH IN RECYCLED PLASTICS AND COMPOSITE MATERIALS

Prepared by:

Edward N. Steadman
Debra F. Pflughoeft-Hassett

August 1994

TABLE OF CONTENTS

TASK 5.9 USE OF COAL ASH IN RECYCLED PLASTICS AND COMPOSITE MATERIALS

1.0 INTRODUCTION

Coal fly ash has been used as an inert filler in paints, plastics, and other manufactured products. Unfortunately, the properties of coal ash have not been considered for use to upgrade these materials or to produce a unique material. Coal ash exhibits a broad range of characteristics that appear to have the potential to be used beneficially in plastics and other composite materials. The EERC currently has a program to investigate the thermal destruction of plastics for several major industrial companies. Some baseline investigations of the use of coal ash in plastics, particularly recycled plastics, would benefit from the contacts already established and information being generated regarding the inorganic constituents in plastics.

2.0 OBJECTIVES

The goal of this research is to determine the potential for coal ash to serve as a functional filler in plastics and other composite materials, with special emphasis on recycled plastics.

3.0 ACCOMPLISHMENTS

Several conventional coal combustion by-products were evaluated for potential use in plastic–ash tile. A boiler slag was selected for these experiments, based primarily on appearance and anticipated ease of handling. It was determined that two tiles would be produced. One would use the unground boiler slag, and the second would be produced with ground boiler slag.

Lists of plastic types and typical post-consumer streams were obtained. Evaluation of these materials continues.

4.0 FUTURE WORK

Laboratory evaluations of the boiler slag will be performed. These evaluations will include evaluation of particle size, hardness, and chemical composition. Sample preparation will begin.

A single post-consumer plastic stream will be identified for use in the formulation of a plastic–ash tile. Samples of this stream will be obtained or mimicked in the laboratory. Thermal properties will be evaluated. Mold release agents needed to allow molding of the plastic–ash will be identified and obtained.

TASK 6.1

CORROSION OF ADVANCED STRUCTURAL MATERIALS

Prepared by:

John P. Hurley
Jan W. Nowok

August 1994

TABLE OF CONTENTS

LIST OF FIGURES

TASK 6.1 CORROSION OF ADVANCED STRUCTURAL MATERIALS

1.0 INTRODUCTION

The study of viscosity began in 1687 with Sir Isaac Newton and, up to now, the record shows little light shed on the molecular basis of viscosity in liquids, particularly in multicomponent aluminosilicates, such as those derived from coal ashes (1). Interest in the viscosity of ash slags today stems from practical applications such as fluxing propensities, corrosion of refractories, sinterability of coal ashes, and high-temperature deformation of silicate binders in SiC composites used in candle filters. Therefore, the description of melt morphology has become an important factor in understanding the dynamics of mass transport in slags. However, mass transport depends upon the temperature of critical viscosity, T_{cv}, at which a slag changes its flowing characteristics from Newtonian to Bingham plastic. In Bingham plastic slags, viscosity increases with progressive phase transformation. The degree of crystallinity of slag is directly proportional to the amount of cooling, though not necessarily linearly below T_{cv} (2).

A considerable amount of literature now exists regarding the rheology of Bingham plastic solutions such as suspensions (i.e., a combination of liquid plus rigid particles), the viscosity of which depends critically on composition, temperature, and shear rate and on particle abundance, size, size distribution, and shape. For simple systems, the effects of crystals on viscosity can be evaluated. In the case of ash slags, an estimation of slag viscosity in the Bingham plastic region is more complicated, since 1) crystallization usually causes changes in the composition of remaining slags, and 2) the cooling rate may additionally cause a sudden change in the sequence of crystallization. It is suggested here that for the viscosity of ash slag in the Bingham plastic region, it is the interplay of these two factors that primarily controls the slag flow characteristics.

It is the aim of this project to define the phase equilibria in ash slag and apply them in understanding the corrosion of refractories and creep phenomena in binders.

2.0 VISCOSITY AND ITS PRACTICAL APPLICATION

In an attempt to explain the viscosity–temperature relationship of silicate glasses, a structural model, based on the variation of the degree of polymerization and, further, on a selective separation of solid material from the melt, has been proposed (1). The degree of polymerization can be described by the proportion of nonbridging oxygens to tetrahedrally coordinated cations (NBO/T). NBO is an oxygen atom bound to only one silicon atom, $Si\text{-}O^-$, and to a nontetrahedral cation. For silicate melts, the NBO-to-Si ratio may range from 0 for highly polymerized melts (pure SiO_2) to 4 (SiO_4^{4-}) for highly depolymerized melts (3). Thus, NBO is a measure of the melt's depolymerization and may provide information on viscosity and diffusivity (Stokes–Einstein or Eyring equations) mechanisms in slags. The depolymerization process of melts is caused by the alkali and alkaline-earth elements content.

Viscosity sensitivity to the activity of slag constituents based on iron has been explored, in particular, its dependence on oxygen partial pressure. Ferrous iron can depolymerize a slag depending on the CO/CO_2 and H_2/H_2O ratios in the flue gas which, in

turn, controls the oxygen partial pressure. High CO content, formed at the SiC/slag interface during the oxidation of silicon carbide, may further reduce Fe^{2+} ions to metallic iron and control the formation of iron silicides at the interface. It seems to be important to establish the link between the oxygen partial pressure and viscosity and phase transformation in ash slags. A further speculation is that the partial pressure of oxygen may control the diffusion of oxygen in a slag and the corrosion rate of SiC. It is expected that the mechanism of SiC/slag corrosion under combustion conditions will differ from that under gasification conditions. Also, the creep behavior of silicates depends strongly on the partial pressure of oxygen (4, 5).

To establish the link between viscosity and phase transformation means to determine and/or predict crystalline phases which may form near the temperature of critical viscosity. Previous attempts to predict the identity of stable phases have been based on free energy minimization techniques (6). They involved calculations of free energies for all possible phases derived from major and minor oxides in multicomponent systems, ignoring constraints imposed by chemical equilibria. The chemical equilibria of the entire nucleation–growth process include 1) growth of nuclei as a result of a large excess of appropriate species in a slag and 2) dissolution of some nuclei into a slag (Ostwald ripening) in a case of a limited content of appropriate species (7). Consequently, nuclei with low free energies, as determined from thermodynamic data, with the limited content of appropriate components may either fall toward the ripening stage or participate in the heterogenous nucleation of phases with higher free energies and larger components content (2). To alleviate this problem we have proposed to apply free energy-composition phase diagram rather than temperature-composition phase diagram and free energy of mixing (2). Details of this method will be discussed in the final report. Knowledge of viscosity and phase transformation will allow slagging propensity of ash slags to be defined.

3.0 ON THE CRYSTALLINITY, PROBABILITY OF OCCURRENCE, AND RHEOLOGY OF ASH SLAGS

The great sensitivity of slag viscosity to the precipitated crystalline-phase content may be a useful qualitative indicator of the mechanism of phase transformation near T_{cv}. Figure 1 illustrates viscosity variation with time in Rochelle slag for several temperatures near the temperature of critical viscosity. Viscosity increases because each precipitated solid introduces mechanical interactions and resistance of the slag to flow. The significance of this test is that there is a temperature near T_{cv} at which some formed crystalline phases undergo frictional degradation, and the viscosity of the slag slowly decreases.

Generally, viscosity moderately increases with increasing solid-phase content, but the basic mechanics are not well understood.

4.0 MODIFICATIONS TO THE HOT-GAS REACTION FURNACE

Experiments to perform a 500-hr corrosion test of the prototype candle filter produced by the Third Millennium Corp. in the hot-gas reaction furnace (HGRF), so far have met

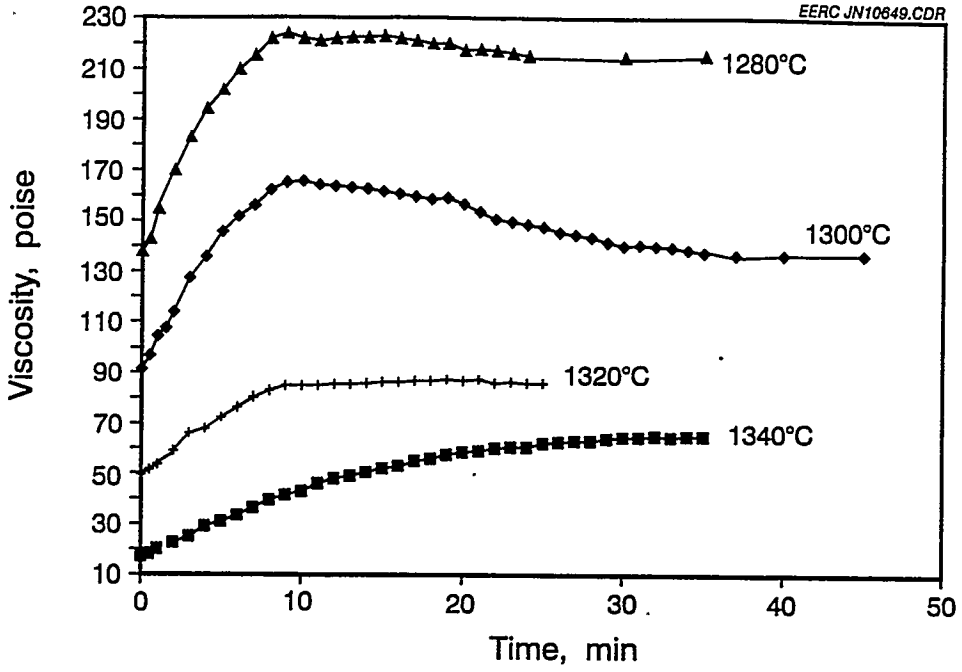

Figure 1. Viscosity of Rochelle ash slag measured in air.

with very limited success. After the last attempt, which lasted only 20 hr, the end cap seal on the mullite retort of the reactor failed because of the condensation of aqueous sulfuric acid. Also a factor in the seal failure was the 3.5-psi back pressure produced by the filter at 900°C by the gas-flow rate of 10 L/min. In later testing, the mullite retort also failed because of the combination of mechanical, thermal, and chemical stresses induced during its use. Observation of the inside of the retort showed a thin white film had been deposited from the test runs. It was initially thought to be deposition of sodium sulfate from the molten salt vaporizer in the reactor. Analysis of a sample of this film by x-ray diffraction and Auger electron spectroscopy showed the film to be composed of an amorphous silicon compound. Thus, it was assumed that the white film was a silicon polymer generated upon decomposition of the silicon-based high-temperature sealant that serves to seal the end caps of the retort.

It is because of these, as well as a host of other problems, that the reactor has undergone the modifications described below.

4.1 Redesign of End Caps with Gasketed Flanges

The retort end caps have been redesigned to accept a thermocouple, which will be monitored by the data acquisition system. Thus, the system will report any decrease in end cap temperature below the dew point to prevent aqueous condensation of sulfuric acid. The end caps were also designed with flanges to accept a high-temperature gasket material. The flanges thus separate the gaskets from direct radiation from inside the furnace to prevent their subsequent decomposition. The new end caps were designed with

ports to accept an adjustable pressure relief valve to prevent the hazards of possible overpressure of the retort from occlusion of the exhaust port, gas regulation system failure, or accidental overpressure. The materials for construction of the new end cap and fittings are all of 316 stainless steel.

4.2 Installation of Thermocouple Inside Salt Vaporizer

Because of the temperature gradients induced by the cold inlet gases passing through the vaporizer, the salt temperature is lower than that indicated by the process the thermocouple located above the vaporizer just outside the retort. This causes salt to sublime from a solid rather than evaporate from a liquid. For this reason, a 24-in. B-type thermocouple was placed directly inside the vaporizer in contact with the salt. Type B was selected because of its composition: 30% rhodium and 70% platinum, which gives it a rating for use up to 1750 degrees Celsius. The higher temperature rating and composition should give the thermocouple extended life in the corrosive molten salt. After exiting the vaporizer, the thermocouple is fed through the inlet end cap and out to the furnace temperature controller input, of the vaporizer zone. Thus, the temperature in the vaporizer zone will be directly controlled by the furnace power supply through feedback from this thermocouple.

4.3 Design of Thermocouple Probe for Filter Assembly

A thermocouple probe has been built to measure and provide feedback of the temperature inside the filter assembly also. This thermocouple is a 60-in. K-type with a $^1/_{16}$-in 316 stainless steel sheath, sealed and protected from the corrosive gas stream by a $^1/_8$-in outer sheath of pure alumina. This probe is inserted inside the test filter through the exhaust tube of the filter assembly and is passed out of the reactor through the exhaust port. This thermocouple is then connected to the input of the temperature controller for this zone. Thus, as in the case of the salt vaporizer, the internal temperature of the test filter itself will be monitored and controlled. Operation of this thermocouple also confirmed the existence of a temperature gradient in the reactor retort. The original thermocouple for the filter zone, again located just outside the retort, indicated a lower temperature by approximately 50 degrees Celsius, depending on gas flow and water vapor content.

4.4 Design of Vapor Condensation Probe

Because no existing equipment could be dedicated to detect volatilization of salt from the molten salt vaporizer or the passage of these vapors through test filters, a vapor condensation probe was designed. The probe has been designed to be inserted inside the test filter through the filter assembly exhaust tube. This probe is constructed from two 60-in.-long $^1/_4$-in 316 stainless steel tubes with a small holder on the end to attach substrate coupons. These tubes serve as water inlet and outlet to cool the coupon holder. A $^1/_{16}$-in K-type thermocouple inserted through the inlet tube serves to monitor the temperature of the coupon holder. The purpose of the probe is to condense volatiles present in the gas stream onto a platinum coupon held in place by the coupon holder. The platinum coupon can be removed for leaching the condensates for chemical analysis by flame atomic absorption (AA) spectroscopy. The detectability limit of the AA ranges from about 0.5–1.0 mg per liter of leachate, which corresponds to approximately 25 micrograms of condensate on a $^1/_2$-in.^{2} platinum coupon.

4.5 Installation of a Mass-Flow Controller

Because of the accuracy limitations of the rotameters used to mix the simulated combustion gas for the reactor, a precision mass-flow controller and readout device were purchased. The gas-flow rate of 10 L/min, which was chosen as a flow rate for the HGRF, is not arbitrary. The flow rate is defined by the gas mixture composition as it relates to the lower limit in measuring capability of trace gases in the mixture. For these experiments, the smallest gas flow we must meter is for the 5000-ppm sulfur dioxide requirement for the simulated combustion gas. The highest-precision rotameter in the gas mixer will allow a lower limit of approximately 50 cc/min for sulfur dioxide. Thus, the balance in gas flow for a 5000-ppm mix equates to a total flow of 10 L/min. At this flow rate, large quantities of gas are required, resulting in experiment interruption for gas cylinder replacement and higher run pressures than are desirable. Also, this high flow rate causes temperature gradients in the furnace and may tend to splatter molten salt in the salt vaporizer.

Because of these complications, a Type 1259c mass-flow controller and a Type 247c four-channel readout were purchased from MKS Instruments Inc. The readout is capable of metering up to three additional Type 1259c controllers. The 1259c controller was calibrated specifically for a sulfur dioxide flow of 0–10 cc/min., with an accuracy of 0.15% of full scale. This controller will replace the rotameter used for sulfur dioxide only; the rest of the gases will still be metered with the existing rotameters. Using the combination of mass flow controller and rotameters, at 5000 ppm sulfur dioxide, the flow rates can be reduced to at least a factor of 10 in the range of 500 to 1000 cc/min total gas flow. This will result in significant savings in cost for gases and downtime, while at the same time producing a more reproducible combustion gas mixture.

4.6 Redesign of Steam Boiler into an Evaporator

Installation of the MKS mass-flow controller has also reduced the mass flow requirement of water vapor by ten times. Boiling the water, it turns out, is not necessary to produce the water vapor requirement. The calculated evaporation rate for a water vapor molar function of 0.15 at 1 L/min total flow is 4.5 cc/hr. This can be produced by heating a flask of water slightly above room temperature and bubbling the gas mixture through. Previously, the boiling water proved difficult to regulate and created a possible overpressure hazard in the boiler flask and retort. The evaporator flask does not become pressurized and has been proven to be easier to regulate without the need for refilling.

4.7 Replacement of Mullite Retort with Fe–Ni–Cr Alloy

As mentioned earlier, a combination of mechanical, thermal, and chemical stresses caused failure of the mullite retort during testing. This retort has since been replaced by a retort of an Fe–Ni–Cr alloy of the same dimensions, 6 in. ID and 72 in. long. The alloy, designated RA 330, was obtained from Rolled Alloys, Temperance, Michigan. This is the same alloy used in the construction of the filter holder assembly, and has been shown to be highly resistant at 900°C to combustion gases. The replacement of the mullite with this alloy has allowed welding of the end cap directly to the tube, thereby eliminating the silicon adhesive seal and the problems associated with its decomposition.

5.0 FUTURE WORK

Our future work will try to establish the relationship between the viscosity of ash slag and oxygen partial pressure, as well as phase transformation, and relate them to the corrosion of silicon carbide and creep process of binders. Additionally, we intend to determine the relationship between viscosity and diffusivity of major constituents in ash slags, mainly, nonbridging oxygen during the sintering process of mullite at various partial pressures of oxygen observed in liquid metals (8, 9).

6.0 REFERENCES

1. Nowok, J.W.; Hurley, J.P. "Local Structure of a Lignitic Coal Ash Slag and Its Effect on Viscosity," *Energy & Fuel* **1993**, 7, 1135–1140.

2. Nowok, J.W. "Viscosity and Phase Transformation in Coal Ash Slags near and below Temperature of Critical Viscosity," *Energy & Fuel*, accepted for publication (Nov. 1994).

3. Mysen, B.O. "Structure and Petrology–Important Properties of Silicate Melts Relevant to Natural Magmatic Liquids," In *Silicate Melts*; Scarfe, C.M., Ed.; Mineralogical Association of Canada, 12, 1986, 180–209.

4. Jaoul, O.; "Multicomponent Diffusion and Creep in Olivine," *J. Geoph. Res.* **1990**, *95*, 17,631–17,642.

5. Jaoul, O,; "High-Temperature Deformation of Diopside Crystal. 3. Influence of PO_2 and SiO_2 Precipitation," *J. Geoph. Res.* **1994**, *99*, 9423–9439.

6. Harvie, C.E.; Greenberg J.P.; Weare, J.H. *Geochim. Cosmoch. Acta* **1987**, 51, 1045–1057.

7. Bartels, J.; Lembke, U.; Pascova R.; Gutzov, J.; *J. Non-Crystal. Solids* **1991**, 136, 181–188.

8. Nowok, J.W. "Analysis of Atomic Diffusion in Liquid Metals at Melting Temperatures in Capillary-Like Media," *Acta Metall. Mater.*, accepted for publication, 1994.

9. Nowok, J.W. "A Universal Relation between Diffusion, Viscosity, and Surface Tension in Liquid Metals in Capillary-Like Media," *Scripta Metall. Mater.* **1993**, 29, 931–935.

Viscosity and Phase Transformation in Coal Ash Slags near and below the Temperature of Critical Viscosity.

Jan W. Nowok

Fuels and Materials Science, University of North Dakota Energy & Environmental Research Center, PO Box 9018, Grand Forks, North Dakota 58202-9018

The phase transformation of multicomponent aluminosilicates on liquidus curves becomes an important parameter in the prediction of the slag behavior upon cooling. Three major factors are taken into consideration: 1) thermodynamic driving forces for a selection of stable phases on liquidus curves, such as free energies of components at various temperatures, 2) the effect of free energy of mixing on the tendency to phase segregation in liquid solution on cooling, and 3) free energy change at the solid–melt interface and entropy of fusion and their effects on the morphology of the crystalline phase(s). In order to identify the solid phase(s) crystallized from ash slag it is proposed first, to calculate major binary free energy composition diagrams based on major oxides in ash and secondly, to select phase(s) with the free energy and composition constrained by free energy diagrams. It is postulated that the free energy of the solid–melt interface plays a significant role in the selection of crystal size; the small ΔG^{int} constrains the formation of fine crystallites, while the large ΔG^{int} indicates the formation of large crystals in a slag. It is quite apparent that the low ΔG^{int} contributes to lowering the activation energy of nucleation. Both examples, the nucleation of fine crystallites and the growth of large crystals, are evident in Beulah and Illinois No. 6 ash slags. In ash slags the phase transformation may occur either by nucleation or by spinodal decomposition, both of which are recorded in Beulah and Gascoyne ash slags. The spinodal decomposition causes a sharp increase of slag's viscosity. The differential thermal analysis (DTA) technique shows endotherms in Pittsburgh No. 8 and Gascoyne White ash slags, on heating, near and above the temperature of critical viscosity that are assigned to the dissolution of solid phases into the melt and anomalous in melt thermal conductivity, respectively.

Introduction

The viscous properties of coal ash slags are of considerable importance in the description of their slagging tendencies in boilers. Providing a complete description of slag rheology requires the study of viscous flow, both in Newtonian and non-Newtonian regions. Non-newtonian behavior of ash slags is represented by Bingham plastic melts, which are well evidenced in colloidal suspensions. In Bingham plastic slags, viscosity increases with progressive phase transformation and is higher than that in Newtonian melts with similar compositions. Phase transformation in coal ash slags is usually noticed near the temperature of critical viscosity, T_{cv}. The temperature of critical viscosity has been defined as the temperature at which the viscosity of molten slag changes on cooling from that of a Newtonian fluid to that of a Bingham plastic.[1] It is very difficult to predict the viscosity of these slags, since no single parameter such as composition is sufficient to apply in the description of their flow.

The key issues relating to an understanding and description of phase transformation in coal ash slags and its effect on viscosity are as follows:

1) The thermodynamics of phase transformation

2) Solid–melt interface phenomena

3) The morphology of crystallizing phases and its connection with the viscosity of slags

Generally, phase transformation may proceed by a variety of structural mechanisms: nucleation and crystal growth, spinodal decomposition[2,3] and phase separation.[4]

The objective of this work was to derive more fundamental and comprehensive information about the dominant cause of the viscosity increase in ash slags below T_{cv}. Based on thermodynamic considerations, we evaluated 1) conditions for the formation of stable phases during cooling process of slag, 2) the morphology of precipitates, and 3) the relationship between phase transformation and viscosity.

Viscosity and Structural Changes in Ash Slags

In an attempt to explain the viscosity–temperature relationship of silicate–aluminosilicate melts, structural models based on variations in the degree of polymerization and, further, on a selective crystallization of solid material from the liquid have been proposed.[5,6] The degree of

polymerization can be described by the proportion of nonbridging oxygens per tetrahedrally coordinated cations (NBO/T) and calculated from the chemical composition of the silicate–aluminosilicate systems. NBO is an oxygen atom bound to only one silicon atom, $Si\text{-}O^-$ and to a nontetrahedral cation (Na^+, Ca^{2+}, etc.). For silicate melts, NBO/Si may range from 0 for highly polymerized melt (pure SiO_2) to 4 (SiO_4^{4-}) for highly depolymerized melts.[7] The depolymerization process of melts is caused by alkali and alkaline-earth elements content. Substitution of Al^{3+} and Fe^{3+} for Si^{4+} in tetrahedral coordination results in a lowering of alkali and alkaline-earth elements content and a simultaneous increase in melt viscosity. The sensitivity of viscosity to melt composition allows the relationship between both variables in the Newtonian region to be defined.[8–11]

As the temperature drops, a critical temperature is reached, below which the relationship is no longer linear (Figure 1). Much of the deviation is caused by phase transformation.[12,13] Furthermore, if the viscosity is measured at a high shear rate, such as that used in the Newtonian region, the remaining melt and formed crystalline phases undergo shear thinning, and the apparent viscosity may increase, since the higher shear rate accelerates phase transformation (see below).

The viscosity of slag near T_{cv} depends on the volume fraction of dispersed solid assemblies (u), their shapes, the viscosity of "residual slag" (η_r), and the mutual hydrodynamic interaction of the solid–melt and fractional process:[14]

$$\eta_{mixt} = \eta_r(1 + cu + du^2) \qquad (1)$$

where c and d are constants related to the shape of dispersant and solid–melt interaction, respectively.

A differential thermal analysis (DTA) technique was employed to investigate phase transformation in ash slags, particularly near the temperature of critical viscosity. Two amorphous ash slags were tested: Pittsburgh No. 8 and Gascoyne White. The amorphous ashes were obtained by melting coal ash at 1500°C, homogenizing the ash melt by stirring with a platinum rod, and quenching at room temperature. The glasses were ground to a particle size of < 38μm. The DTA measurements were performed using a DuPont 2100 instrument at a heating

rate of 8°C/min. The tests were run in the temperature range of 25° to 1500°C. Our earlier reported DTA data showed that all amorphous ashes crystallized below 1100°C.[15] Figures 2 and 3 illustrate the DTA curves of Pittsburgh No. 8 and Gascoyne ash slags on heating, along with the changes in viscosities. A strong endothermic peak in Pittsburgh No. 8 and a broad peak in Gascoyne samples near T_{cv} can be assigned to different mechanisms of solid-phase dissolution into the melt. The extremely endothermic peaks detected above 1300°C for the Pittsburg No. 8 and Gascoyne seem to offer support for the concept of changes in thermal conductivity of slags initiated by the fluctuation of heat flux in the slags that can be, but not necessarily correctly, related to phase transformation. No significant changes in viscosity occur above this temperature.

The most important changes in the size and shape of DTA curves are caused by a sudden change in the thermal properties of samples on heating or cooling that usually occurs as the samples undergo transformation. If there is a good contact between the platform and pan as well as between the pan and sample, the return of the DTA to baseline is fast, and the DTA curves are more representative.[16] If the contact becomes less perfect, the heat transfer across the sample pan and the pan platform is low and DTA curves may be recorded at a higher-than-baseline temperature. This anomaly has been noticed in Colstrip ash slag during crystallization (Figure 4). The recorded endothermic peak resulting from the high resistance of contacts does not pertain to the melting of any phase. However, the DTA endothermic peaks recorded near T_{cv} in Figures 2 and 3 confirm that they can be applied in explanation of the melting of solid phases. It seems likely that the broad endothermic peak in Gascoyne ash slag is a product of fractional fusion. Fractional fusion is considered to be an infinite number of infinitely small equilibrium fusion events, usually occurring at either a peritectic or eutectic invariant point.[17] Powder x-ray diffraction (XRD) patterns show the presence of gehlenite ($Ca_2[Al,Fe]_2SiO_7$), and merwinite ($Ca_3MgSi_2O_8$) crystalline phases. It seems possible that the fractional fusion in Gascoyne ash slag can be approximated by changes in composition along the liquidus curve.

To understand the structural complexity of slag rheology near and below T_{cv} we will first discuss the thermodynamics of phase transformation in solutions such as ash slags.

Thermodynamic Driving Force for the Solidification of Melts

The formation of Bingham plastic melt below T_{cv} is the result of two individual processes: the formation of new phases and their growth. Many complex solutions consist primarily of ternary mixtures in which other ingredients are often present only in small amounts. To identify major phase diagrams which become unstable below T_{cv} and undergo the phase transformation with the formation of stable crystalline phases, the first step is to define the smallest number of components that can describe the system. The second step is to consider possible routes for phase transformation, either by nucleation and growth process or by a spinodal decomposition.[18]

In simple component systems such as pure oxides, all phases (melts and solids) have the same composition, and equilibrium involves temperature as a variable. Phase transformation can occur when the free energies of melt and solid are equal (Figure 5). The driving force for this process is assigned to the free energy difference between liquid and solid phases, which increases with an increase in supercooling temperature. If Component 2 is added into the pure liquid of Component 1, the chemical potential and activity of Component 1 is reduced, and the temperature where a solid first appears is depressed.[19] It follows that the lowest free energy of a solid phase on a liquidus curve is not achieved at the expected temperature range, T_m and T, but at T^{sol} and T' (Figure 5). The driving force for phase transformation is attributed to the free energy difference between solution and solid phase (or phases).

At the equilibrium state, the chemical potential of any melt component in solution (sol) and in corresponding crystalline phase (s) are the same. Thus, we may write:[20]

$$\mu_i^{sol} = \mu_i^{s} \qquad (2)$$

To determine the phase equilibria in ash slag, one needs to know the phase diagrams. Depending on the complexity of the system, a phase diagram contains, two, three, or more components (anorthite, diopside, albite, etc.). Any point within a phase diagram specifies both a composition and a temperature. We propose to replace the phase diagrams by free energy composition diagrams. The approach used here is essentially the traditional method of metallurgists used to describe the changes of thermodynamic properties of alloys. Thus, to determine the phase equilibria in ash slag, one must be familiar with the following:

1) Free energy composition diagrams of liquid solutions of major components in ash slag near the temperature of critical viscosity, which may correspond to the liquidus curve

2) Mixing properties of the liquid and solid solutions

3) Free energies of solid phases at various temperatures

For the sake of simplicity, let us consider the case where the Components 1 and 2 form ideal solutions over the entire composition range. The free energy of this solution is represented by:[19,21,22]

$$\Delta G^{sol}(T) = x_1 G_1(T) + x_2 G_2(T) + \Delta G^M \quad (3)$$

and:

$$\Delta G^M = \Delta H^M - T\Delta S^M \quad (4)$$

where x_1 and x_2 are the mole fractions of Components 1 and 2, respectively. For random mixing, the enthalpy of mixing ΔH^M is either zero such as in garnets,[23] positive, as in crystalline solid solution series,[24] or negative, as in glasses and melts.[25] For systems with Al/(Al+Si)<~0.5, enthalpies of mixing become more endothermic as A_nAlO_3 is substituted for SiO_2 (where A represents the alkali/alkaline-earth ion). The ΔH^M increase becomes more pronounced with the increasing basicity of alkali and alkaline-earth elements. Also, at Al/(Al+Si)> 0.5, the enthalpy of mixing is changed to exothermic values.[19] Generally, the enthalpy of mixing arises from the interactions between nearest neighbors in solution. The changes of ΔH^M with composition are rather small, less than 15 kJ/mol, in magnitude. The entropy of mixing, ΔS^M, and free energy of mixing, ΔG^M, of one mole of solution are given by the following:

$$\Delta S^M = -R[x_1 \ln x_1 + x_2 \ln x_2] \quad (5)$$

$$\Delta G^M = RT[x_1 \ln x_1 + x_2 \ln x_2] + \Delta H^M \quad (6)$$

where R is the gas constant equal to 8.314 J/Kmol.

As a solution is cooled down, the strong chemical interactions between components in a melt appear near equilibrium, which may lead to the formation of stable solid phase(s). Obviously, the stable solid phase on an X_1–X_2 phase diagram may crystallize if its free energy intersects the free energy of the liquid solution (Figure 6). The rate of configurational rearrangements is low in high-

viscosity solution and high in low-viscosity solution; in aluminosilicate systems these trends are reflected in the increase of enthalpies of mixing.

Free Energy-Composition Phase Diagram and Nucleation Process in Aluminosilicate Systems

In the classical theory of crystallization, the phase transformation begins from the formation of solid-phase nuclei. During the first step of nucleation, nuclei of new phases are always metastable and become stable if they continue to grow up to critical sizes. The number of new phases in aluminosilicates is controlled by the structural changes in the solution and results from the shifts in the chemical equilibrium.[26] Urbain et al. have suggested that the phase transformation that occurs along the liquidus reflects composition-dependent changes in liquid structure that persist far above the liquidus.[27] To continue our consideration, we have to assume that the solid phase that appears on the liquidus curve is in thermodynamic equilibrium with its clusters in a melt. This may happen in aluminosilicate slags with slow relaxation times.[28,29] During phase transformation, the composition of the solution is modified so that it lowers the liquidus temperature. In this case, the solute depresses the liquidus temperature, and the composition of the solution may cross a new phase diagram. The less usual case is that in which solute raises the liquidus temperature.

For the sake of simplicity, let us assume that the solution is an ideal mixing of anorthite–diopside–albite, which composition matches that of ash slags. The free energy of mixing of the ideal solution is calculated based on mole % of all oxides in anorthite–diopside–albite join. All minor oxides in ash slags such as potassium, titanium phosphorus, and others are assumed to remain in the solution. In some cases they may promote the nucleation process or can be incorporated into crystalline phases as chemical defects if they match some crystallographic rules such as formation of solid solution. They should not significantly change the structure of major phases, and consequently the free energy, on disordering. Calculated $\Delta G^{mol}(T)$ composition diagrams at 1400 K for an anorthite–diopside–albite join is illustrated in Figure 7. This system is not truly ternary, but will be considered so for the sake of discussion. The free energy of the

supercooled ideal solution is constantly decreasing with anorthite content; also, albite causes further decrease in the free energy of the ideal solution.

The first confusing thing to notice about this system is that a melt of any composition can crystallize to produce a solid phase of the same composition. In fact, in this type of system, there is equilibrium segregation of clusters in liquid solution between two components, anorthite and diopside, which can be described by the equilibrium segregation coefficient, k^*. In a theory for segregation coefficients in solidification from melts, the k^* can be predicted from the entropy and enthalpy of mixing.[30] If we plot the free energy of mixing ΔG^M versus composition we may receive information how mixing process affect the selection of stable phases on liquidus curves (Figure 8). Indeed, the free energy composition diagram corresponds to the anorthite–diopside phase diagram[31] (Figure 8). In the evaluation of ΔG^M we have also included heat of mixing for anorthite–diopside join experimentally determined by Navrotscy et al.[25] The proposed free energy composition diagram and free energy of mixing composition plot seem to provide more information on the ideal solution behavior during crystallization in the presence of a third phase, like albite, than the binary-phase diagram. It shows that the eutectic range can be shifted to lower diopside content with the increase of albite concentration. An alternative way to examine the free energy composition diagram is to search for other individual phases with appropriate free energies and compositions on the liquidus curve constrained by the free energy phase diagram. One of the best examples is akermanite ($Ca_2MgSi_2O_7$) with a free energy of the solid phase (–2949.0 kJ/mol at 1400°C) intersecting the liquidus curve in the appropriate composition range. Here an invariant point is reached, and at a fixed temperature the following reaction is proposed to occur:

$$2CaO{\cdot}MgO{\cdot}Al_2O_3{\cdot}4SiO_2 = \underset{\text{akermanite}}{2CaO{\cdot}MgO{\cdot}SiO_2} + \underset{\text{in solution}}{Al_2O_3{-}2SiO_2} \qquad (7)$$

The appearance of Al_2O_3 and SiO_2 in the solution will cause a decrease in nonbridging oxygen content and simultaneously an increase in the viscosity of remaining melt. Crystallization of solid phases with plagioclase compositions were earlier noted in the anorthite–diopside–albite system and can be predicted from traditional phase diagrams.[32]

A quite different type of system is albite–anorthite ($NaAlSi_3O_8$–$CaAl_2Si_2O_8$) which shows essentially no change in free energy of mixing with composition (Figure 9). Consequently, there is no segregation of calcium-rich and sodium-rich phases; therefore, the melt crystallizes as a solid solution with a composition of plagioclase feldspars.[32]

Figure 10 shows the free energy change in mullite–larnite systems with added nepheline. It is obvious that the stable phases that may crystallize from the ideal solution are anorthite and gehlenite of which the free energy of solid phases (–3131.7 kJ/mol and –3065.6 kJ/mol, respectively) intersects the liquidus line. The fluctuation of chemical composition in the mullite–larnite diagram by added nepheline may better adopt the chemical composition of the ideal solution to that of anorthite and gehlenite. We may write the following reactions:

$$2CaO{\cdot}3Al_2O_3{\cdot}3SiO_2 = \underset{\text{gehlenite}}{2CaO{\cdot}Al_2O_3{\cdot}2SiO_2} + \underset{\text{in solution}}{2Al_2O_3{-}2SiO_2} \quad (8)$$

$$2CaO{\cdot}3Al_2O_3{\cdot}3SiO_2 = \underset{\text{anorthite}}{CaO{\cdot}Al_2O_3{\cdot}2SiO_2} + \underset{\text{in solution}}{CaO{-}2Al_2O_3{-}SiO_2} \quad (9)$$

The thermodynamic behaviors of the three ideal solutions discussed are characteristic of processes occurring in ash slags, in which crystallization of solid phases may also cause an increase in polymerization of residual melts. Considerable disagreement between theory and experiments may occur if precipitated phases react with the remaining oxides in the solution and form new phases with low melting temperatures. The best example is the nepheline–silica join: the melting temperature of nepheline is 1800 K and the $Na_2O \cdot Al_2O_3 \cdot 2SiO_2$–$SiO_2$ join reduces the melting temperature of the solution to 1390 K.

As a consequence of phase transformation, the free energy of the system changes to

$$\Delta G^{sol}(T) = x'\Delta G'(T) + x^s\Delta G^s(T) + \Omega\Delta G^{int}(T) \quad (10)$$

where $\Delta G'(T)$ is a free energy of solution with a new composition, $\Delta G^s(T)$ is a free energy of solid-phase crystallized from solution, x' and x^s are mole fractions, $\Delta G^{int}(T)$ is a free energy of solid–melt interface (positive value) and Ω is a constant value that depends on the interface shape (sphere, flat surface). In this context, ΔG^{int} can be applied to consider a solid–melt interface both in crystal–melt and nucleus–melt systems (this property will be discussed separately. However, for the nucleation process, it is convenient to use the activation energy defined as[33] follows:

$$\Delta G^* = 16\pi\gamma^3/3(\Delta G^{sol}-\Delta G^s)^2 = \beta(\Delta G^{int})^3/(\Delta G^{sol}-\Delta G^s)^2 \quad (11)$$

where γ is a solid–melt interfacial tension and β a constant value. It can be shown that nucleation will dominate if nuclei have the minimum activation energy. The most effective way to minimize ΔG^* is by the formation of nuclei with the smallest interfacial energy, ΔG^{int}, and/or the largest, $\Delta G^{sol} - \Delta G^s$.

Table 3 lists major thermodynamical properties of selected silicate and aluminosilicate melts which may appear on liquidus curves during crystallization of ash slags. The thermodynamic data were taken from available literature.[34,35] Table 4 lists major mineral phases noted in some ash slags crystallized below the temperature of critical viscosity. The consequence of the availability of CaO, Al_2O_3, and SiO_2 oxides in slags is the precipitation of calcium-rich phases. Slags were quenched in water from temperatures around T_{cv}.

Recently, it has been shown that metastable phases that may coexist with stable phases on diagrams often grow steadily prior to the nucleation of stable phases, mostly when the supercooling or cooling rate is high.[36–38] In the supercooled melt of anorthite, anorthite never nucleates as the first phase, even when anorthite is the only stable phase. At temperatures from 1350° to 1200°C, corundum or mullite nucleates as the first phase; below 1250°C pseudohexagonal and pseudo-orthorhombic anorthite phases nucleate prior to anorthite.

It is evident from the above discussion that for any ash slag of known composition we need to identify the limited number of phase diagrams that can exist in ash slag in order to select solid phase(s) with an appropriate free energy (or energies) on liquidus curves. Previous attempts to predict the identity of stable phases have been based on free energy minimization techniques.[39] They involved calculations of free energies for all possible phases derived from major and minor oxides in multicomponent systems, ignoring constraints imposed by chemical equilibria. The chemical equilibria of the entire nucleation–growth process include 1) growth of nuclei as a result of a large excess of appropriate species (clusters) in a slag, and 2) dissolution of some nuclei into a slag (Ostwald ripening) in case of a limited content of appropriate species.[40] Consequently, nuclei with low free energies, as determined from thermodynamic data, with the limited content of

appropriate components may either fall towards the ripening stage or participate in the heterogenous nucleation of phases with higher free energies and larger components content.

Impurities and Heterogenous Nucleation in Ash Slags

Little is known concerning the activity of impurities in ash slags such as TiO_2 and other minor oxides. In many glasses they appear to be effective in inducing internal nucleation.[41] This may happen if there are stronger attractive forces between impurities and silicate and/or aluminosilicate species in a melt, leading to the formation of metastable nuclei. The free energy of metastable nuclei may then be lower than other phases with major components. However, the relatively high concentrations of some components in a slag aggravate the mass transport of low concentrations of ions to metastable nuclei. Consequently, they may either promote phase transformation of major components in a slag by reducing ΔT and simultaneously ΔG (compare to Figure 5) by heterogenous nucleation of major components or dissolve into a slag. Figure 11 illustrates an example of heterogenous nucleation of dendritic crystals on an impurity in Illinois No. 6 ash slag.

Spinodal Decomposition

Spinodal decomposition is indeed an interesting transformation mechanism that arises from thermodynamic instabilities of composition in supercooled melts. This does not require a nucleation process.[41] Large fluctuations of composition are needed to create new phases, and this is associated with a reduction of free energy. This transformation occurs by a continuous change of free energy from one phase to another. This requires coexisting phases to be structurally similar to one another.[42] Phase transformation within the region outside the spinodal decomposition involves a nucleation and growth process. Figure 12 illustrates the phase morphology of spinodal decomposition noted in Beulah ash slag during its cooling to room temperature after viscosity was measured . Figure 13 shows the droplet morphology of spinodal decomposition noted in Colstrip amorphous ash sintered in air at 1100°C for 15 hr.

Solid–Melt Interface

In the preceding section, we discussed the thermodynamic principles of phase transformation, ignoring the thermodynamics of the solid–melt interface and their effect on the

stability and morphology of crystals. Various viewpoints have been considered concerning conditions for selecting the stable interface shape. One, essentially thermodynamic in origin, is considered here. Let us consider the behavior of a pure system such as a liquid oxide. The liquid–crystal interfacial energy can be estimated from undercooling data, assuming they reflect homogeneous nucleation.[43] Thus, the entropy of the liquid phase should not be lower than that of the stable crystalline phase, which may occur if the fictive temperature T is higher than the critical supercooled temperature. If T is equal to the critical supercooled temperature, the entropy and heat capacity of the glassy phase are equal to those of the crystalline phase. As a consequence, phase transformation will not occur.

In order to obtain an estimate of ΔG^{int} we follow the treatment of other authors. The free energy difference between the liquid phase and the isotropic crystal in pure systems can be estimated either from Turnbull or Battezzatti and Garrone relations:[43,44]

$$\Delta G^{int} = \Delta H_m(T_m - T)/T_m - \Delta C_p[(T_m - T) - T\ln(T_m/T)] \quad \text{(Turnbull)} \quad (13)$$

$$\Delta G^{int} = \Delta H_m(T_m - T)/T_m - \Delta S_m[(T_m - T) - T\ln(T_m/T)] \quad \text{(Battezzatti)} \quad (14)$$

where ΔH_m is the heat of fusion (positive value), T_m is a melting temperature, ΔS_m is the entropy of fusion, and $T_m > T$. The temperature difference $(T_m - T)$ represents the supercooling temperature. We expect that the ΔG^{int} of a solid–liquid interface in a solution such as ash slag will differ from above equations by the selection of supercooling temperature, $(T_m^{sol} - T)$ (Figure 5). Both equations are useful for the calculation of interface free energy in pure systems such as minerals and oxides.

The interface free energy required to stabilize the solid–melt interface for further crystal growth for selected aluminosilicates and oxides at 1400 K, are listed in Table 3. The results suggest that negative values of ΔG^{int} do not allow the phase transformation to occur, while the positive values of ΔG^{int} do favor a high-stability solid–melt interface. Additionally, the low ΔG^{int} values should facilitate the nucleation process (compare with Eq. 11) and allow the formation a large number of nuclei in the melt—fayalite, pseudowollastonite, high sanidine, and quartz seem to be the best examples. On the other hand, solid phases with a high ΔG^{int} such as anorthite, fosterite, gehlenite, larnite, spinel, and corundum may nucleate slowly under high-supercooling conditions and grow to large crystals during phase transformation of a solution.

Strong evidence of the ΔG^{int} effect on the morphology of crystals of is noted in Beulah ash slag (Figure 14). Note, that the large value of ΔG^{int} for $MgO \cdot Al_2O_3$ (spinel) facilitates the growth of large isomorphous $(Fe,Mg)O \cdot Al_2O_3$ crystals, when the smaller value of ΔG^{int} proceeds to the crystallization of relatively smaller $2CaO \cdot Al_2O_3 \cdot SiO_2$, gehlenite crystals. Figure 15 shows the crystal morphology in Illinois No. 6 ash slag after viscosity was measured in a CO/CO_2 (60/40) atmosphere and the slag quenched in water. The small crystallites represent the $FeO \cdot SiO_2$ phase, fayalite, with a small ΔG^{int} value, and the large crystals belong to $CaO \cdot Al_2O_3 \cdot 2SiO_2$ (anorthite) with a higher ΔG^{int}.

The crystal morphology is also controlled by several variables, i.e., temperature distribution, solute distribution, transport processes such as diffusion, and convective mixing of matter and heat flow. The temperature difference at a solid–melt interface may cause the precipitation of dendritic to spherulitic forms at higher cooling rates.[45] The spherulitic forms growth is more often noted in liquid metals with high entropy change at melting temperatures if other mentioned parameters are constants.[46] This results from the disparity in growth rates between the low-index planes and the faster growing high-index planes.[47] In liquids with high entropy of fusion, the growth becomes more "spikey" if these materials are cooling very fast.[48]

In real systems there is always microfluctuation of thermodynamic state variables (temperature, concentration) at any location in a melt. Thus, the crystal–melt interface is subject to a spatially fluctuating driving force that can manifest itself as a perturbation in a crystallite's shape. It can be readily shown that the fluctuations of heat transport at the crystal surface provides conditions for dendritic growth such as that noted in Illinois No. 6 ash slag (Figure 11).

Viscosity of Ash Slags and Phase Transformation

A change of slag composition during phase transformation must also be followed by a sudden viscosity change (Figure 16). A sudden increase in viscosity is assigned to a phase transformation resulting from both a nucleation and a spinodal decomposition. In the model discussed, the response of a slag to physical perturbation caused by nucleation and the formation of a liquid phase with a different viscosity consists of an instantaneous increase in shear stress. Figure 17 plots shear stress–shear rate ratio versus temperature for a Beulah slag. A good linear portion of

Newtonian viscous flow is noted only for low shear rates, below 16 rotations per minute (rpm). The phase transformation in Beulah slag arising at the about temperature of critical viscosity has the ability to dissipate energy and instantaneously raise the shear stress. This effect was not noted in model glass NBS 711 (Figure 18). The results raise the question of whether high shear rates may promote phase transformation in a slag.

Summary and Conclusions

Thermodynamic considerations of phase transformations in multicomponent systems, along with the corresponding discussion on the viscosity–phase transformation relationship, demonstrate that the viscosity trajectory of ash slag is intimately related to the concomitant microstructure. In order to tailor the viscosity of ash slag near and below the temperature of critical viscosity, phase equilibria (described as the variation of free energy with slag composition) are needed to provide guidance in the selection of the appropriate stable solid phase(s). Actually, silicate and aluminosilicate melts are composed of clusters (structural units) that do not correspond to the chemical composition of slags as expressed by equivalent oxides. To calculate phase diagrams, one is forced to apply free energies of pure minerals rather than of oxides, because phase equilibria are controlled by structural rearrangements of clusters before and on liquidus curves and not by silicon, oxygen, and other ions. Free energy changes, free energy of mixing, enthalpy, and entropy of fusion provide valuable insight into the estimation of early stages of phase transformation and slag morphology. It is believed that solid–melt interfacial free energy may control the morphology of precipitates in multicomponent aluminosilicates such as ash slags.

Acknowledgements

The author thanks the U.S. Department of Energy for its support under Contract No. DE-FC21-86MC10637.

References

(1) Winegartner, E.C. *Coal Fouling and Slagging Parameters*; ASME: Fairfield, NJ, 1974; p 6.

(2) McGahany, V.; Tomozowa, M. *J. Non-Cryst. Solids*, **1989**, *109*, 27.

(3) Kreidl, N. *J. Non-Cryst. Solids*, **1991**, *129*, 1.

(4) Filipovich, V.N. In *Phase Separation in Glasses*; Mazurin, O.V., Porai-Koshits, E.A., Eds.; Amsterdam: North-Holland, 1984; p 15.

(5) Sage, W.L.; McIlroy, J.B. *J. Engin. Power*, **1960**, *April*, 145.

(6) Nowok, J.W.; Hurley, J.P.; Stanley, D.C. *Energy & Fuels*, **1993**, *7*, 1135.

(7) Mysen, B.O. In *Silicate Melts*; Scarfe, C.M., Ed.; Mineralogical Association of Canada, 1986, p 180.

(8) Urbian, G.; Bottinga, Y.; Richet, P. *Geochim. Cosmoch. Acta*, **1982**, *46*, 1061.

(9) Hoy, H.R.; Roberts, A.G.; Wilkins, D.M. In *Chemistry of Coal Utilization*; Elliot, M.A. Ed.; 1965, p 444.

(10) Kalmanovitch, D.P. Frank, M. In *Mineral Matter and Ash Deposition from Coal*; Bryers, R.W.; Vorres, K.S. Eds.; United Eng. Trustees Inc., 1990, p 89.

(11) Jung, B.; Schobert, H.H. *Energy & Fuel*, **1992**, *6*, 387.

(12) Simmons, J.H.; Mills, S.A.; Napolitano, A. *J. Am. Ceram. Soc.*, **1974**, *57*, 109.

(13) Nowok, J.W.; Hurley, J.P.; Steadman, E.N. In *The Impact of Ash Deposition on Coal Fired Plants*," in press.

(14) Goldsmith, H.L.; Mason, S.G. *Rheology, Theory and Applications*; New York: Academic Press, 1967.

(15) Nowok, J.W.; Benson, S.A.; Steadman, E.N.; Brekke, D.W. *Fuel*, **1993**, *72*, 1055.

(16) Crighton, I.S.; Wilburn, F.W. *Thermochimica Acta*, **1992**, *203*, 1.

(17) Presnall, D.C. In *The Evolution of the Igneous Rocks*; Yoder, H.S. Jr., Ed.; Princeton, NJ: Princeton U Press, 1979; p 59.

(18) Rao, C.N.; Rao, K.J. *Phase Transitions in Solids*; New York: McGraw-Hill, Intern. Book Comp., 1978, p 81.

(19) Navrotsky, A. In *Silicate Melts: Their Properties and Structure to Problems in Geochemistry, Petrology, Economic Geology*; Scarfe, C.M., Ed.; Mineral Association of Canada, 1986, p 130.

(20) Richardson, F.D. *Physical Chemistry of Metals in Metallurgy*, London: Academic Press, 1974; Vol. 1, p 127.

(21) Rao, Y.K. In *Phase Diagrams. Materials Science Technology*; Alper, A.M., Ed.; New York: Academic Press, 1970; Vol. 1, p 1.

(22) Navrotscy, A. "Thermodynamic Modeling of Geological Materials: Minerals, Fluids and Melts," *Reviews in Mineralogy*, **1987**, *17*, 35 .

(23) Geiger, C.A.; Newton, R.C.; Kleppa, O.J. *Geochim. Cosmoch. Acta*, **1987**, *51*, 1755.

(24) Newton, R.C.; Charlu, T.V.; Kleppa, O.J. *Geochim. Cosmochim. Acta*, **1980**, *44*, 933.

(25) Navrotsky, A.; Zimmermann, H.D.; Hervig, R.L. *Geochim. Cosmochim. Acta*, **1983**, *47*, 1535.

(26) Mazurin, O.V. *J. Non-Cryst. Solids*, **1991**, *129*, 259.

(27) Urbain, G.; Bottinga, Y.; Richet, P. *Geochim. Cosmochim. Acta*, **1982**, *46*, 1061.

(28) Uchino, Takashi; Sakka, Tetsuno; Ogata, Yukio; Iwasaki, Matae *J. Phys. Chem.*, **1993**, *97*, 9642.

(29) Taylor, M.; Brown, G.E. Jr. *Geochim. Cosmoch. Acta*, **1979**, *43*, 61.

(30) Rosenberger, F. *Fundamentals of Crystal Growth I*; Berlin: Springer-Verlag, 1979, p 399.

(31) Muan, A. In *The Evolution of the Igneous Rocks*; Yoder, H.S., Jr., Ed.; Princeton: Princeton NJ: Princeton U Press, 1979, p 77.

(32) Ehlers, E.G. *The Interpretation of Geological Phase Diagrams*; San Francisco: Freeman and Company, 1972, p 82.

(33) Porter, D.A.; Easterling, K.E. *Phase Transformations in Metals and Alloys*; New York: Van Norstrand Reinhold, 1981, p 186.

(34) Robie, R.A.; Hemingway, B.S.; Fisher, J.R. "Thermodynamic Properties of Minerals and Related Substances at 298.15 K and 1 Bar Pressure and at Higher Temperatures," Geological Survey Bulletin 1452, Washington, DC, 1979.

(35) Barin, I. *Thermochemical Data of Pure Substances*; Wiesbaden: VCH, 1993.

(36) Kirkpatrick, R.J.; Kuo, I.C.; Melchior, J. *Am. Mineral.*, **1981**, *66*, 223.

(37) Kirkpatrick, R.J.; Pelly, B.H.; Kuo, L.C. *Am. Mineral.*, **1983**, *68*, 1095.

(38) Abe, Toshiya; Tsukamoto, Katsuo; Sunayawa, Ichiro *Phys. Chem. Minerals*, **1991**, *17*, 473.

(39) Harvie, C.E.; Greenberg, J.P.; Weare, J.H. *Geochim. Cosmoch. Acta*, **1987**, *51*, 1045.

(40) Bartels, J.; Lembke, U.; Pascova, R.; Schmeltzer, J.; Gutzow, I. *J. Non-Crystal. Solids*, **1991**, *136*, 181.

(41) McMillan, P.W. *Glass–Ceramics*; London: Academic Press, 1979, p 40.

(42) Jantzen, C.M.F.; Herman, H. In *Phase Diagrams*; Vol. V, Alper, A.M., Ed.; New York: Academic Press, 1978, p 127.

(43) Kelton, K.F. *Solid State Physics*, **1991**, *45*, 75.

(44) Clavaguera-Mora, M.T.; Clavaguera, N. *J. Mater. Res.*, **1989**, *4*, 906.

(45) Sunagawa, I. In *Materials and Science of the Earth's Interior*; Sunagawa, I., Ed.; Tokyo: Terra Scientific Publications, 1984, p 63.

(46) Jackson, K.A. In *Solidification*; Metals Park, OH: American Society for Metals, 1971, p 141.

(47) Kurz, W.; Fisher, D.J. *Fundamentals of Solidification*; Switzerland: Trans Tech Publication, 1984, p 40.

(48) Miller, C.E. *J. Crystal Growth*, **1977**, *42*, 357.

LIST OF FIGURES

LIST OF TABLES

TABLE 1

Composition of Pittsburgh No. 8 Ash Slag (wt% as equivalent oxide)

Oxide	SiO_2	Al_2O_3	Fe_2O_3	TiO_2	CaO	MgO	Na_2O	K_2O
Wt%	50.9	20.7	17.3	1.1	5.3	1.5	0.0	2.7

TABLE 2

Composition of Gascoyne White Ash Slag (wt% as equivalent oxide)

Oxide	SiO_2	Al_2O_3	Fe_2O_3	TiO_2	CaO	MgO	Na_2O	K_2O
Wt%	35.2	11.5	9.8	1.5	27.6	7.5	6.7	0.1

TABLE 3

Thermodynamic Properties of Selected Silicates–Aluminosilicates and Oxides

Mineral Composition	Mineral	T_m,K	Free Energy at T_m, kJ/mol	Heat of Fusion at T_m, kJ/mol	Entropy of Fusion at T_m, J/(Kmol)	ΔG^{int} at 1400 K, kJ/mol (Turnbull)
$NaAlSi_3O_8$	Albite	1391	–2880.3	59.3	NA[1]	–0.4
$CaAl_2Si_2O_8$	Anorthite	1830	–2842.5	81.0	44.52	18.8
$MgSiO_3$	Clinoenstatite	1830	–1058	61.5	NA	14.3
$CaMgSi_2O_6$	Diopside	1664	–2219.2	77.4	77.14	10.3
$MgSiO_3$	Enstatite	1850	–960.0	75.3	40.71	16.8
Fe_2SiO_4	Fayalite	1490	–989.3	92.1	61.86	5.5
Mg_2SiO_4	Forsterite	2163	–1146.6	71.1	32.76	24.6
$Ca_2Al_2SiO_7$	Gehlenite	1866	–2780.0	100	NA	24.9
$FeTiO_3$	Ilmenite	1640	–817.9	90.8	54.76	12.3
Ca_2SiO_4	Larnite	2403	–1280.2	71.1	29.60	28.6
$CaTiSiO_5$	Sphene	1670	–1822.1	123.8	74.02	18.5
$MgAl_2O_4$	Spinel	2400	–1172.9	196.6	81.66	78.9
Mn_2SiO_4	Tephroite	1620	–1200.8	89.6	55.39	11.3
$CaSiO_3$	P-Wollastonite	1817	–1115.7	27.4	30.85	5.8
$KAlSi_3O_8$	H. Sanidine	1473	–2856.2	61.5	41.75	3.0
Na_2SiO_3	Sodium-met.	1362	–1095.6	51.8	NA	–1.4
$MgTiO_3$	Geikelite	1903	–966.9	90.3	47.49	22.4
α-Al_2O_3	Corundum	2327	–928.3	111.0	47.73	32.7
Fe_2O_3	Hematite	1895	–360.0	NA	NA	NA
SiO_2	Quartz	1983	–608.3	9.6	4.79	1.8

[1] Not applicable.

TABLE 4

Cystalline Phases Resulting from Phase Transformation of Ash Slags Rich in Calcium Around the Temperature of Critical Viscosity

Ash Slag	B/A	CaO/SiO_2	MgO/SiO_2	T_{cv}, °C	Mineral Phases
Anaconda Utah	0.33	0.33	0.05	1380	$CaAl_2Si_2O_8$ (Anorthite)
Beulah	0.65	0.71	0.15	1250	$Ca_2Al_2SiO_7$ (Gehlenite)
Baukol Noonan	0.73	0.95	0.28	1220	$Ca_2Al_2SiO_7$ (Gehlenite) $Ca_2MgSi_2O_7$ (Akermanite)
Gascoyne White	1.07	1.59	0.44	1220	$Ca_3MgSi_2O_8$ (Merwinite) $Ca_2Al_2SiO_7$ (Gehlenite)

TABLE 5

Composition of Illinois No. 6 Ash Slag from Points Indicated on Micrograph (wt% as equivalent oxide)

Analyzed Points	SiO_2	Al_2O_3	TiO_2	Na_2O	K_2O	CaO	MgO	FeO	Mineralogical Composition
1	33.4	15.5	0.0	0.3	0.3	41.7	0.3	8.3	$(Fe,Ca)O \cdot Al_2O_3 \cdot 2SiO_2$
2	25.1	5.0	2.2	0.0	5.3	9.2	0.9	52.5	$FeO \cdot SiO_2$
Ash Slag	40.9	18.6	1.1	0.0	2.3	17.5	0.7	18.9	

TABLE 6

Composition of Beulah Ash Slag from Points Indicated on Micrograph (wt% as equivalent oxide)

Analyzed Points	SiO_2	Al_2O_3	TiO_2	Na_2O	K_2O	CaO	MgO	FeO	Mineralogical Composition
1	2.0	22.1	1.9	0.5	0.0	1.4	11.7	60.4	$Fe(Mg)O \cdot Al_2O_3$
2	34.5	10.9	0.4	0.9	0.0	44.8	4.7	3.8	$2(Ca,Fe,Mg)O \cdot Al_2O_3 \cdot SiO_2$
3	33.7	12.3	2.1	4.8	1.8	21.4	5.3	18.6	$2(Ca,Fe,Mg)O \cdot Al_2O_3 \cdot SiO_2$
4	0.0	50.6	0.2	0.0	0.0	0.4	19.4	29.4	$(Mg,Fe)O \cdot Al_2O_3$
Ash Slag	38.0	15.3	1.6	5.8	0.7	22.4	5.1	10.9	

TABLE 7

Composition of Beulah Ash Slag (wt% as equivalent oxide)

Oxide	SiO_2	Al_2O_3	Fe_2O_3	TiO_2	CaO	MgO	Na_2O	K_2O
Wt%	27.5	16.0	16.3	1.6	24.8	5.9	8.7	0.1

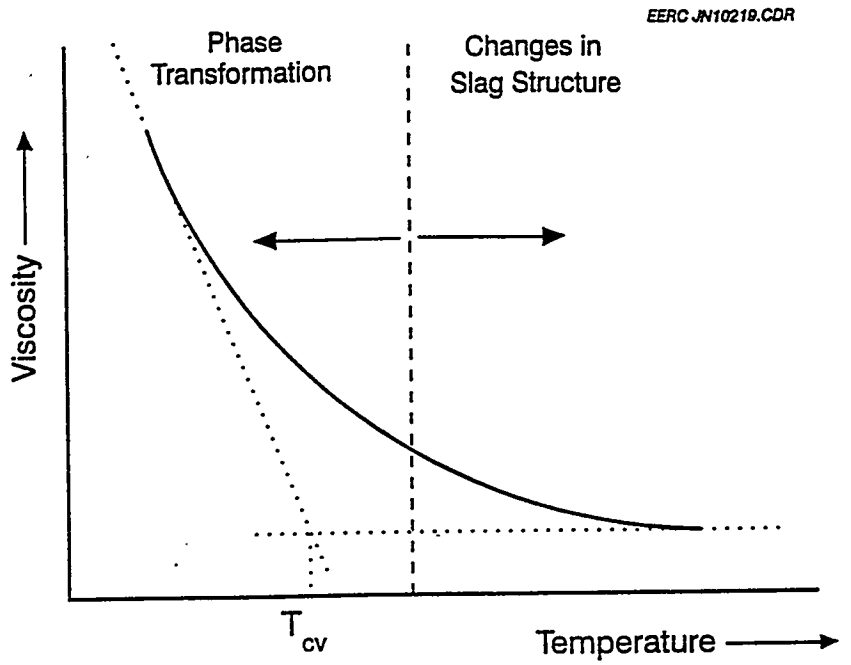

Figure 1

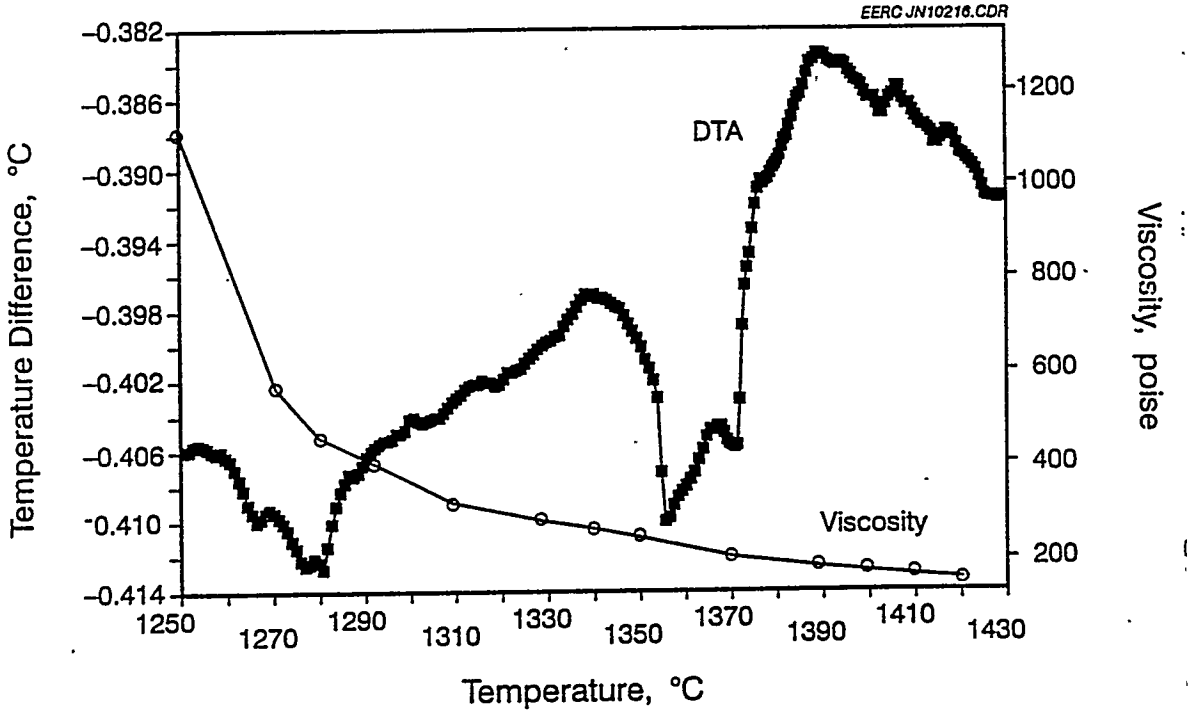

Figure 2

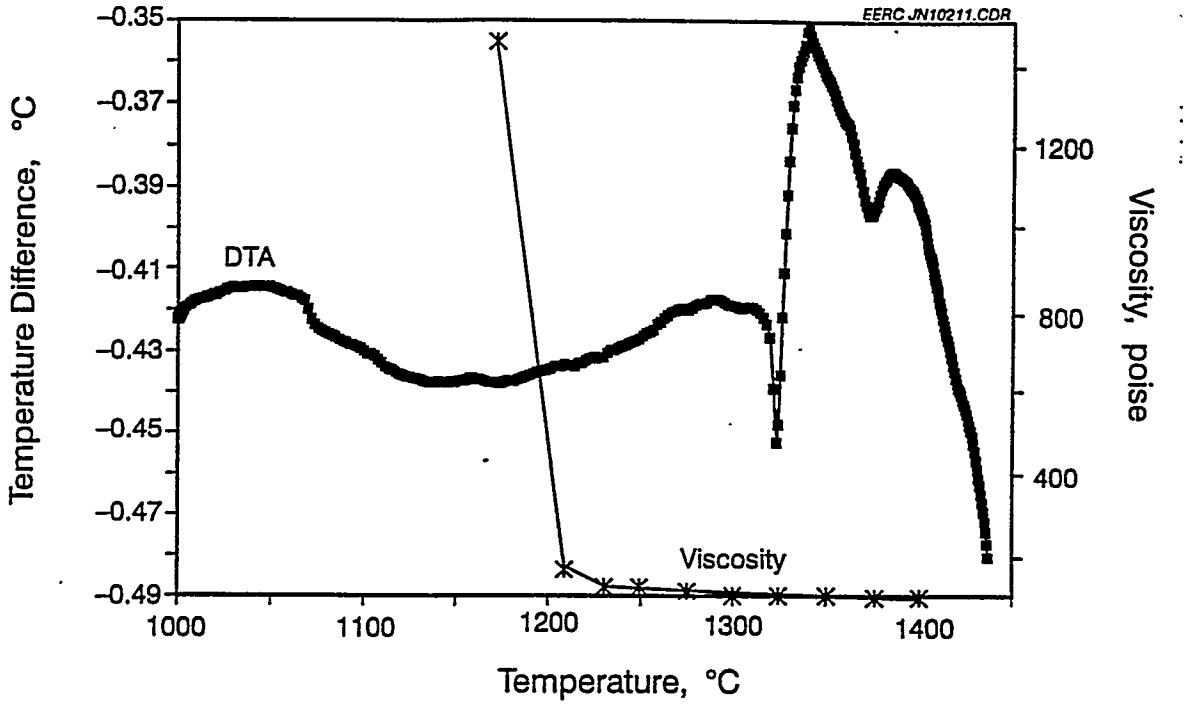

Figure 3

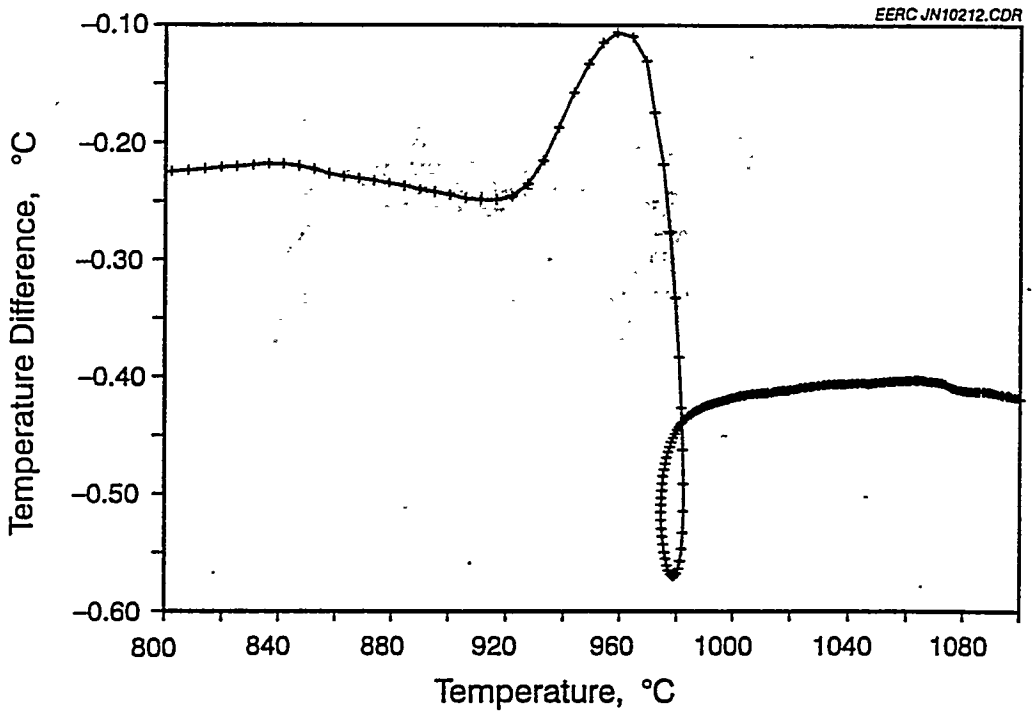

Figure 4

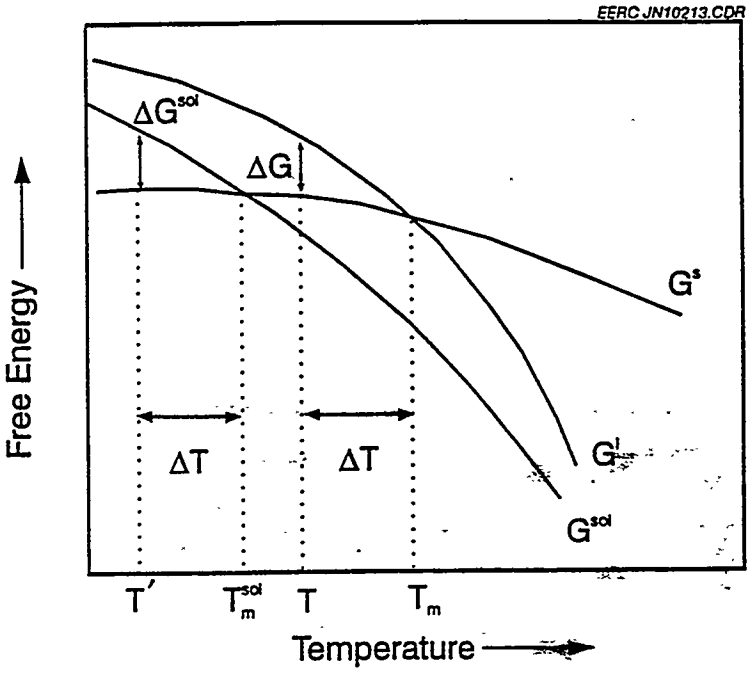

Figure 5

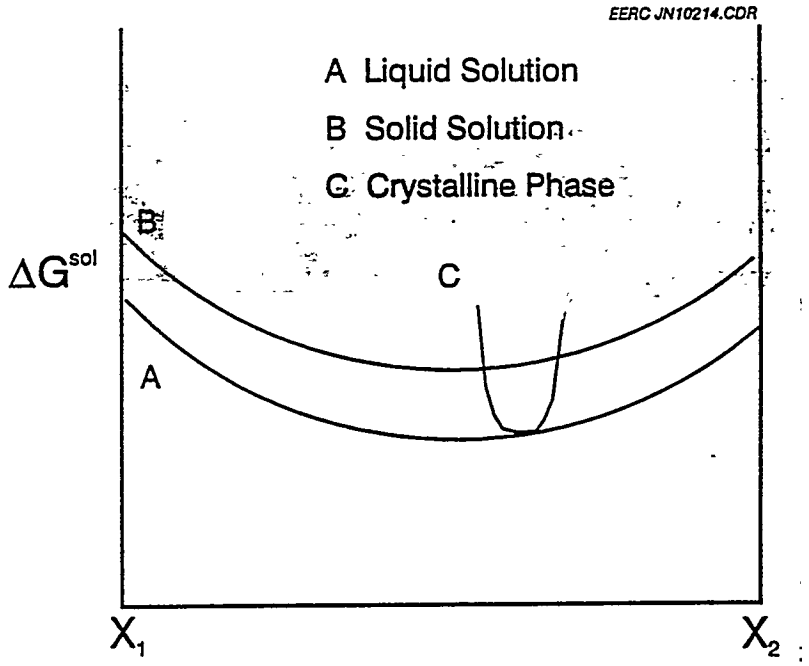

Figure 6

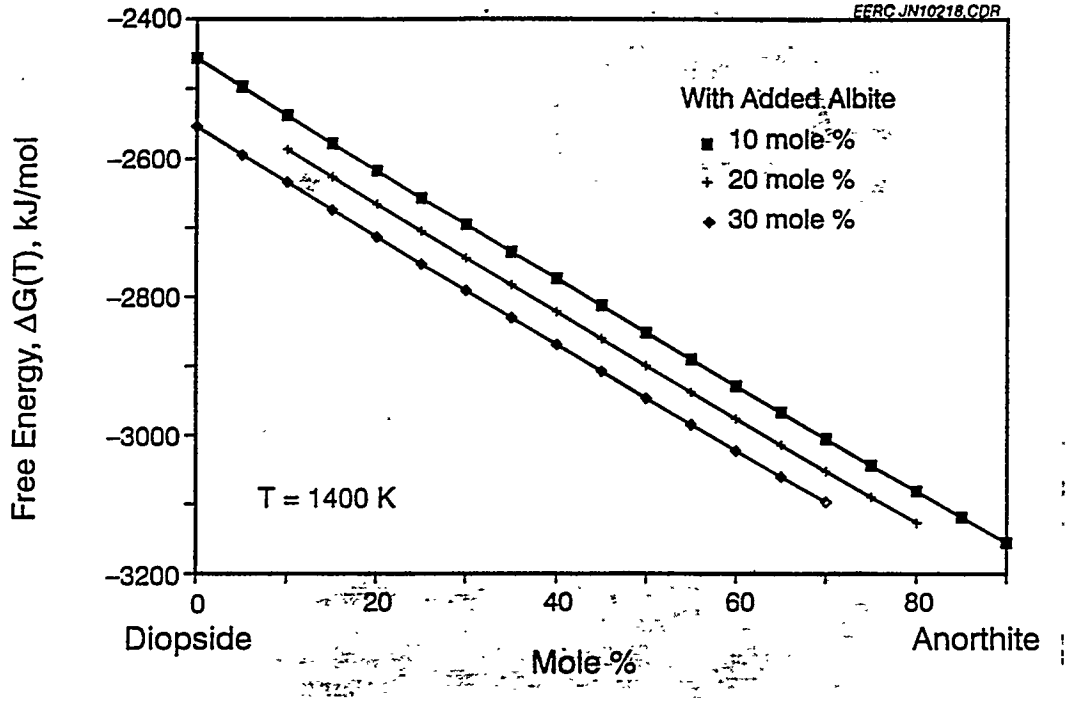
EERC JN10218.CDR
Free Energy, ΔG(T), kJ/mol
-2400
-2600
-2800
-3000
-3200
With Added Albite
10 mole %
20 mole %
30 mole %
T = 1400 K
0
20
40
60
80
Diopside
Mole %
Anorthite

Figure 7

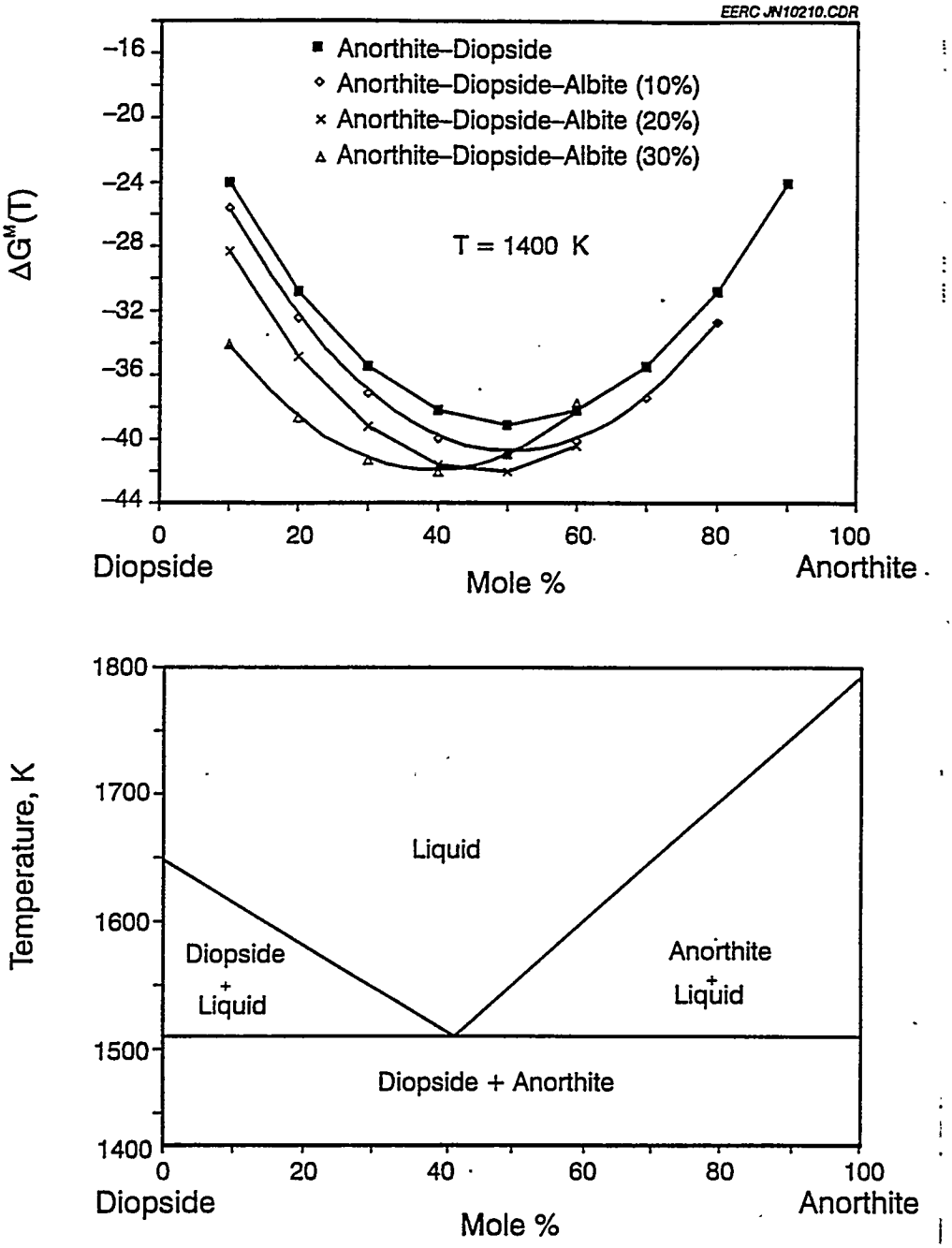
EERC JN10210.CDR
Anorthite–Diopside
Anorthite–Diopside–Albite (10%)
Anorthite–Diopside–Albite (20%)
Anorthite–Diopside–Albite (30%)
T = 1400 K
ΔG^M(T)
−16
−20
−24
−28
−32
−36
−40
−44
0
20
40
60
80
100
Diopside
Mole %
Anorthite
Temperature, K
1800
1700
1600
1500
1400
Liquid
Diopside + Liquid
Anorthite + Liquid
Diopside + Anorthite
0
20
40
60
80
100
Diopside
Mole %
Anorthite

Figure 8.

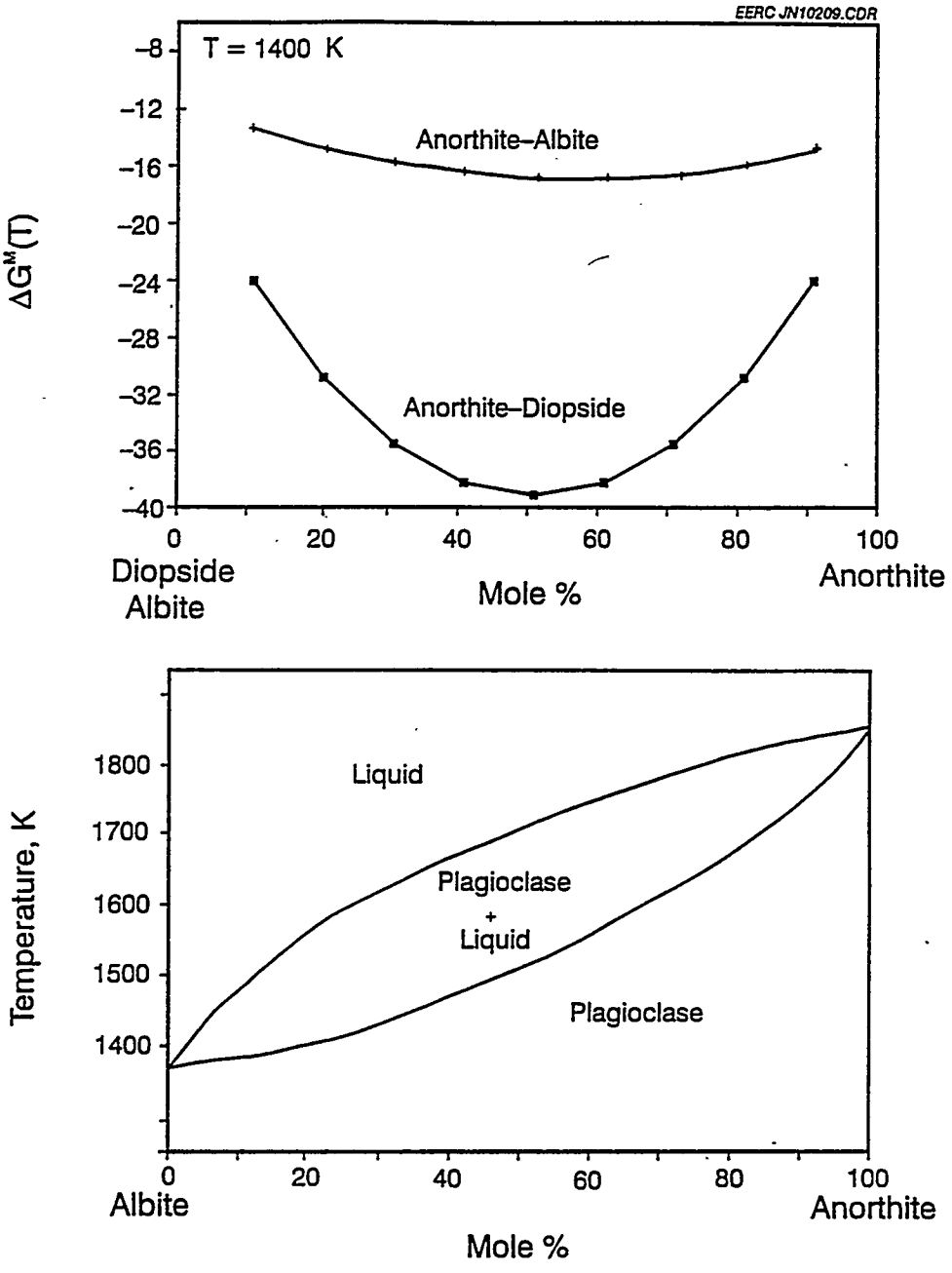
EERC JN10209.CDR
T = 1400 K
Anorthite–Albite
Anorthite–Diopside
$\Delta G^M(T)$
-8
-12
-16
-20
-24
-28
-32
-36
-40
0
20
40
60
80
100
Diopside
Albite
Mole %
Anorthite
Liquid
Plagioclase
+
Liquid
Plagioclase
Temperature, K
1800
1700
1600
1500
1400
Albite
Mole %
Anorthite

Figure 9

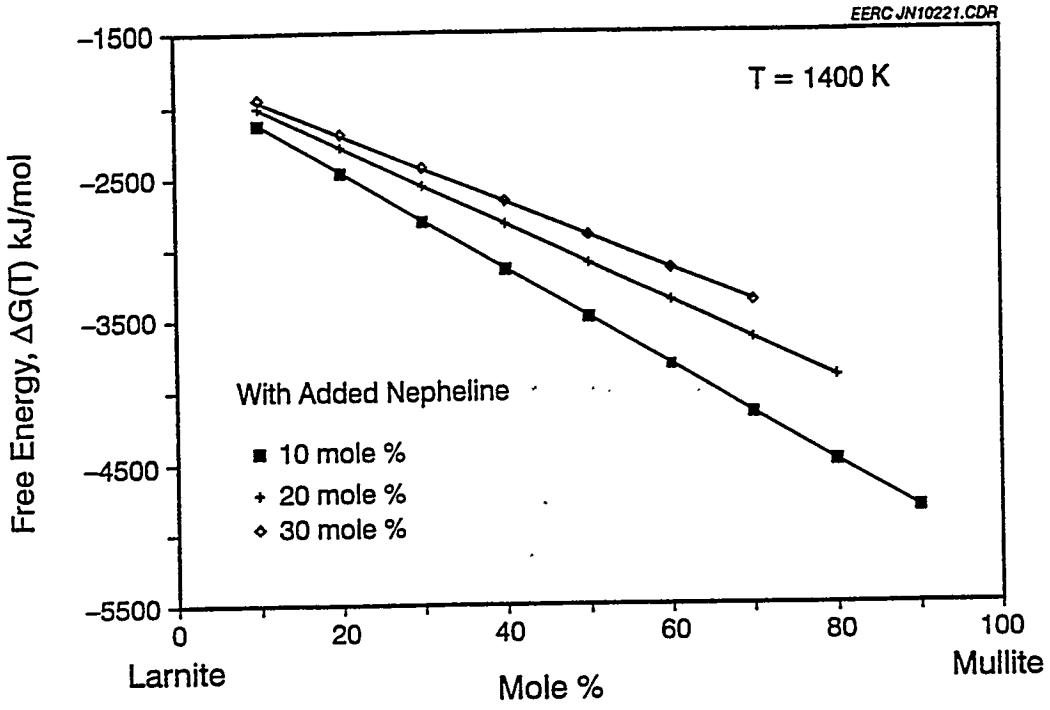

Figure 10

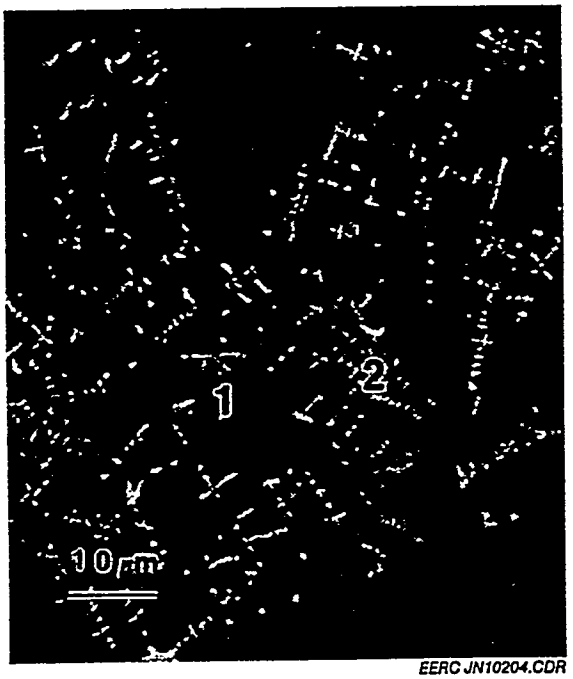

Figure 11

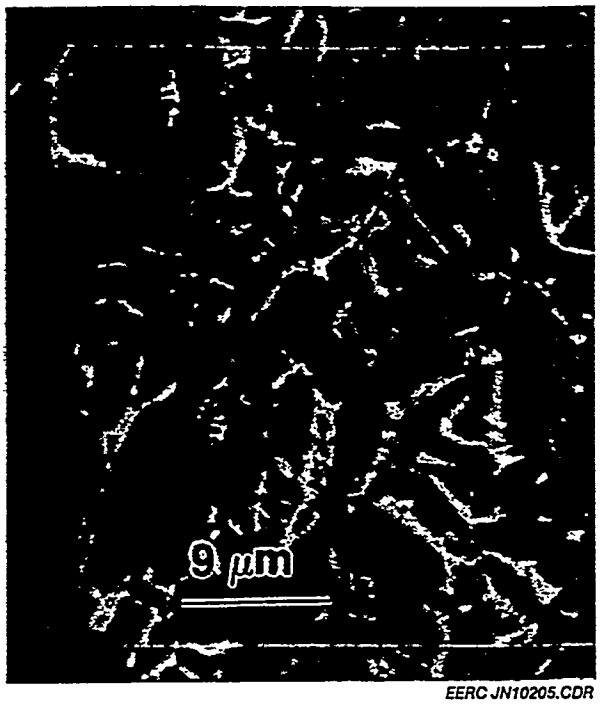

Figure 12

Figure 13

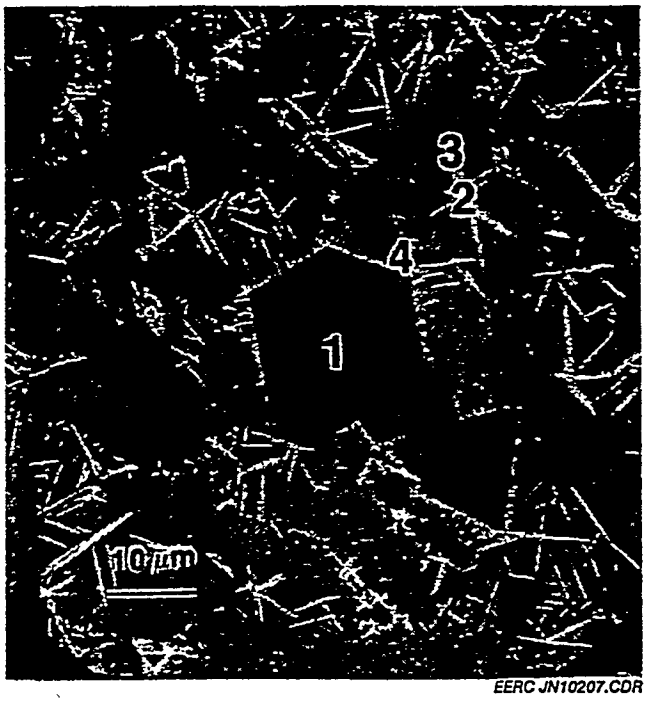

Figure 14

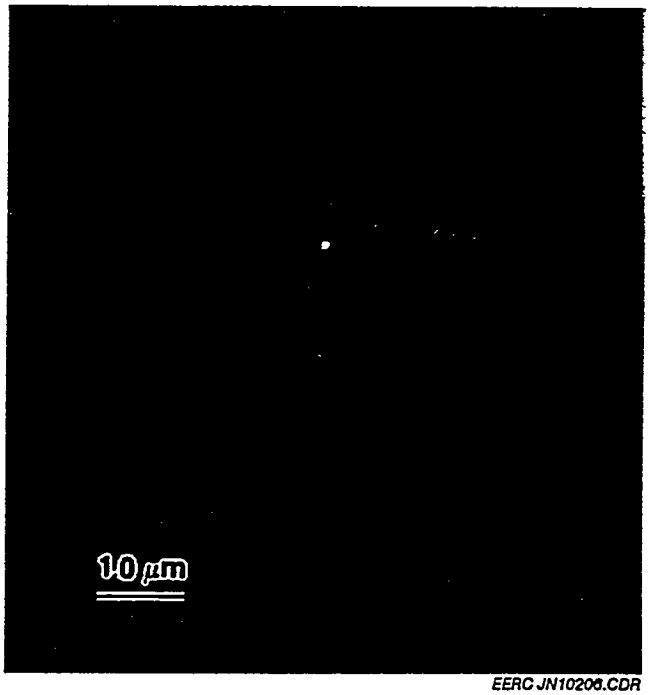

Figure 15

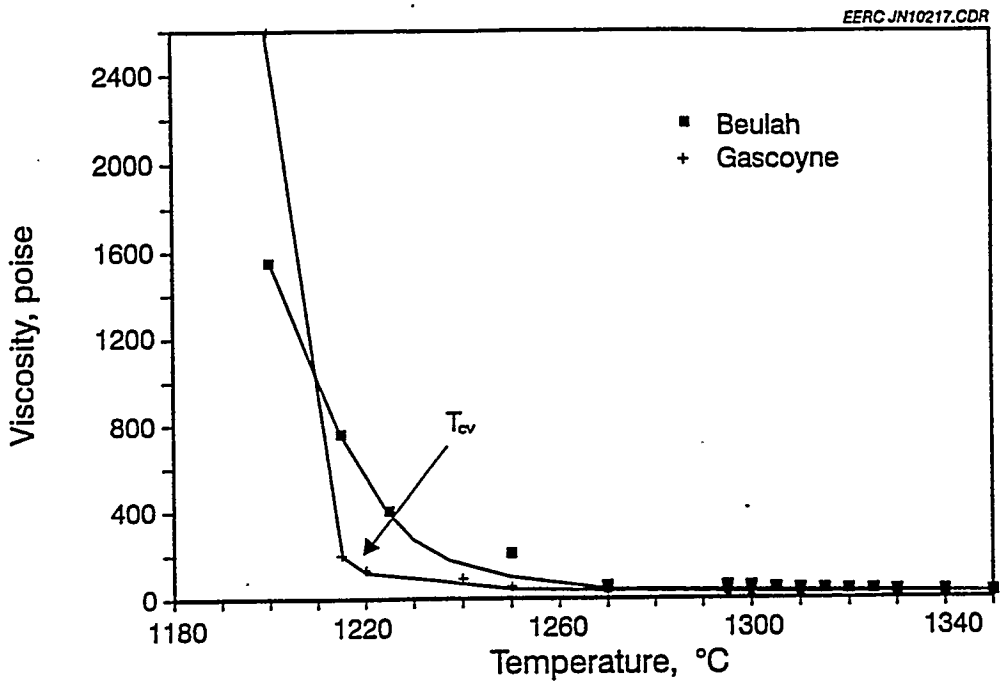

Figure 16

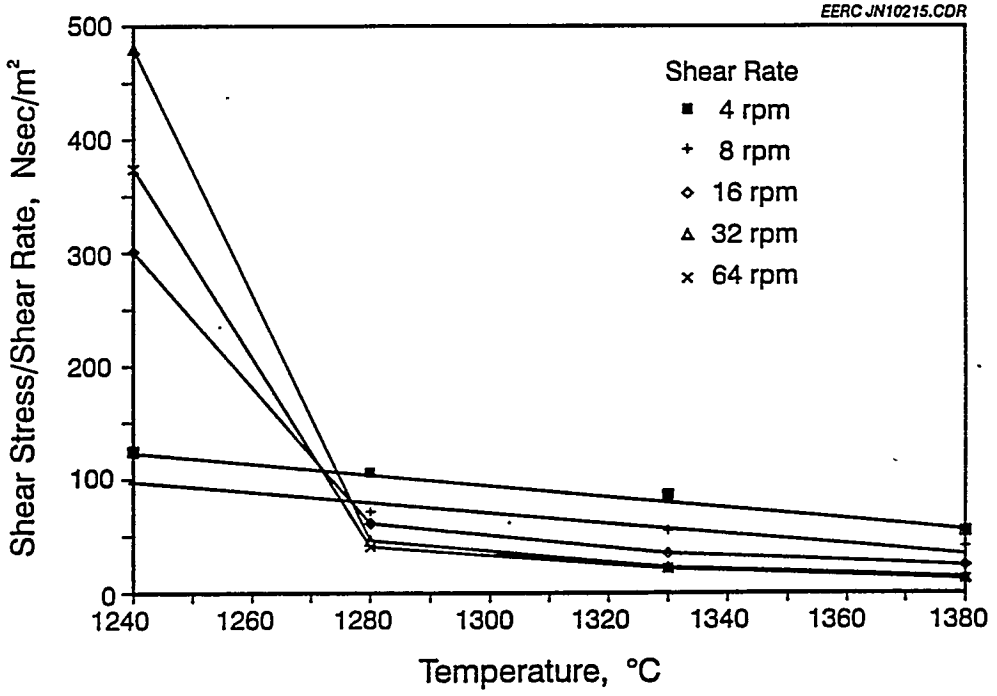

Figure 17

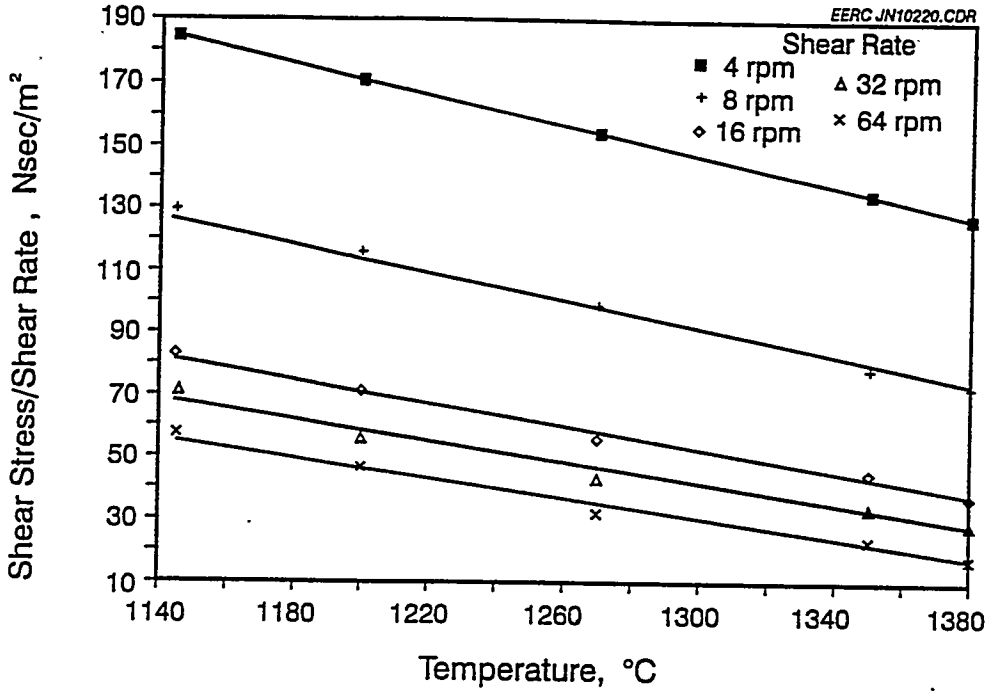
EERC JN10220.CDR
Shear Rate
4 rpm
8 rpm
16 rpm
32 rpm
64 rpm
Shear Stress/Shear Rate , Nsec/m²
190
170
150
130
110
90
70
50
30
10
1140
1180
1220
1260
1300
1340
1380
Temperature, °C

Figure 18

TASK 6.2

JOINING OF ADVANCED STRUCTURAL MATERIALS

Prepared by:

John P. Hurley
Jay A. Bieber

August 1994

TABLE OF CONTENTS

TASK 6.2 JOINING OF ADVANCED STRUCTURAL MATERIALS

1.0 INTRODUCTION/OBJECTIVES

To fully utilize the potential of ceramic materials in structural applications, economical and practically efficient commercial methods must be developed to assemble, or join, the components of the structure. Once an effective method is found, it will be possible to construct and test the suitability of large ceramic structures, such as high-temperature heat exchangers and other components used in combustion and energy engineering.

To determine the current state-of-the-art of ceramic joining research, a preliminary literature search was performed on ceramic welding and joining using the Applied Science and Technology Index CDROM Database from the HW Wilson Company. This database covers technical literature published between 1986 and 1993. Forty articles were found under the subject heading Ceramic Materials/Joining. The particular emphasis of this search was to obtain material on techniques of electrical joining of silicon carbide (SiC). Very little work at all appears to have been done in this area in the past several years. Only a very few articles were found on various techniques of joining SiC, none on electrical joining. A number of articles, however, have been published recently on the joining of silicon nitride and several in particular on electrical joining. Most of the work published in the area has been done by K. Okuda and others in Japan (1–5).

In the so-called "electrical joining method," joints or welds are made by passing electric current through the joint to be made between two ceramic pieces. Heat is created in the joint by the resistance of the joint to the current forced through it from a high-voltage power supply. Heat produced in this way, called Joule heating, can produce extremely high temperatures. At the Diahen Corporation in Osaka, Japan, K. Okuda and others are using this method to join silicon nitride ceramics. In this procedure, the joint of the parts to be bonded is coated with a joining agent, which becomes electrically conductive at high temperatures. The joint is then heated to 700°–800°C, with a preheating gas of propane and oxygen. Tungsten electrodes, 2 mm in diameter, are then reciprocated along this joint. These electrodes deliver 6,600 V with a maximum current of 1 ampere from a 60-Hz, high-voltage supply. The joining agent then melts and reacts with the ceramic; after the joint has cooled to room temperature, the joint is complete. The entire process is done in the ambient atmosphere. The joint layer consists of a glassy substance, which may limit the high-temperature strength of the joints. High-temperature four-point flexure tests indicated a strength of 300 MMPa at 800°C.

2.0 ACCOMPLISHMENTS

Although no literature has yet been located describing electrical joining of SiC, since some level of success has been achieved with this technique on silicon nitride, SiC is also a good candidate, possibly a better one. This is because the electrical resistance of silicon carbide is many orders of magnitude lower than that of silicon nitride. At 1000°C, silicon nitride has a specific resistance of 2×10^3 ohm-cm, whereas SiC at 1100°C is 5×10^{-2} ohm-cm (6).

Thus far, only a preliminary experiment has been done in this laboratory to test the feasibility of electrical joining of silicon carbide. An attempt was made to join two washers made of Hexoloy SA from the Carborundum Company without the aid of any joining agent. A syncrowave 250 constant-current AC/DC arc welding power source from Miller Electric Mfg. Co. of Appleton, WI, was used as a supply. The unit was configured for use as a tungsten inert gas (TIG) welder with argon gas. The SiC washers were clamped together in the ground clamp of the welder. The welding gun was fitted with a 2-mm tungsten electrode. This power supply has a high-voltage, high-frequency circuit; which was used as the source for igniting the main arc. With the high voltage on, the electrode was brought near the joint between the washers, at which point a 1-in. arc was established. This arc was held for approximately 2 min before the main arc was established. This may have preheated the joint enough to decrease conductivity, allowing the main arc to form. The current on the main arc was set to 300 amperes. This made the sample extremely hot, at which point the washers began to immediately decompose into a white silica fume and carbon. At this point, approximately 5 seconds after the main arc formation, the arc was extinguished. Upon examination, the joint between the washers where the arc formed was seen to be thoroughly fused. The rest of the washer, however, was severely fractured in the process, probably from thermal expansion.

3.0 FUTURE WORK

This experiment has, nonetheless, shown that it may be possible to electrically weld or join silicon carbide under more carefully controlled and optimized conditions. Further, options and experiments are currently under consideration for the joining of silicon carbide. As mentioned earlier, this was just a preliminary test; much more research and experimentation must be done to determine the applicability of this method.

4.0 REFERENCES

1. Kohyama, M. et al. "Electric Discharge Welding of Ceramics," *Yogyo Kyokaishi* **1986**, *94*, 1197–200.

2. Okuda, K. et al. "Electrical Joining Method of Ceramics," *In* Proceedings of the Fall Meeting of the Ceramic Society of Japan; Ceramic Society of Japan, Tokyo, Japan, 1988 pp 467–68.

3. Ebata, Y. et al. "Electrical Joining of Silicon Nitride Ceramics," *J. Ceram. Soc. Japan* **1989**, *97*, 88–90.

4. Moore, T.J. "Feasibility Study of the Welding of SiC," *J. Am. Ceram. Soc.* **1985**, *68* (6), C151–C153.

5. Okuda, K.; Takai, H.; Nishi, T. "Electrical Joining of Silicon Nitride Ceramics," *J. Am. Ceram. Soc.* **1993**, *76* (6), 1459–65.

6. Samsonov, G.B. *Plenum Press Handbook of High Temperature Materials;* Plenum Press: New York, 1964; No. 2 Properties Index, p 147.

TASK 7.2

RESOURCE DATA EVALUATION

Prepared by:

Joseph H. Hartman

August 1994

TABLE OF CONTENTS

LIST OF FIGURES

LIST OF TABLES

TASK 7.2 RESOURCE DATA EVALUATION

1.0 INTRODUCTION

The Resource Data Evaluation subtask of the U.S. Department of Energy (DOE) base program represents an Energy & Environmental Research Center (EERC) initiative to promote the integration of geographic information system (GIS) technologies with other ongoing and planned EERC research in the areas of resource utilization, remediation, land use planning, and regulatory and policy assessment. Significant demand for GIS-based information already exists for energy resource evaluation, interpretation of remote sensing data, environmental assessment at the state and local levels, and use in strategic planning. Through sound data-taking procedures and wise data management policies, a GIS approach can serve an integral function in permitting cross-disciplinary uses of information by many EERC researchers. The use of GIS methodologies will expand the potential for interaction between the researcher, governmental agencies, and private companies.

The objective of this task is to determine the appropriate platform and approach upon which to develop GIS applications for optimizing resource evaluation and integrating this information with related areas of interest.

To review, GIS specifically refers to computer-based methodologies that manipulate, analyze, and portray information derived or summarized from specific geographically referred observations. The geographic reference can be any number of earth-based coordinate systems (e.g., latitude and longitude) or generalized to any number of political (e.g., counties) or other types of boundaries (e.g., zip codes). Different types of information are effectively layered, each layer representing a vector-based map with associated discrete attribute information (Hartman, 1994). For example, the map portrayal of the interpreted occurrences of a particular coal bed throughout its extent might include political boundaries, selected cultural features, the geology of the region, and the specific surface and subsurface coal observations being investigated. The political aspect of the map could consist of several layers including federal, state, county, and township boundaries. Cities of a certain population range, roads of a certain type, and drainage systems of a certain size could be added to provide potential market and environmental considerations. Subsurface water interests could be applied if considered potentially significant. The geologic map could consist of layers representing selected geologic contacts and occurrence of relevant marker beds. The portrayal of the coal occurrences of a particular coal bed could be keyed to 1) surface versus subsurface observations, 2) coals greater than a certain thickness, 3) coals with selected analytical properties, or 4) estimates of coal reserves. As each data type is represented by a different database or file, data can be edited and integrated with existing databases.

2.0 ACCOMPLISHMENTS

Activities associated with Task 7.2, Resource Data Evaluation, commenced during the first quarter of the project year. These activities included tasks associated with the development and implementation of GIS databases and construction of digitized files for research pertaining to energy studies. Database design and use was undertaken for two

EERC projects: 1) coal occurrence in Bowman and adjacent counties in the Fort Union Coal Region of southwestern North Dakota and 2) energy resource utilization concerns for selected sites in Alaska. Both projects involved the development of GIS applications using Atlas GIS® 2.0 by Strategic Mapping, Inc., and Access® by Microsoft Corporation. The EERC continues to use coal-related databases designed in Q&A® 4.0 by Symantec Corporation. However, the advantages of GIS technology are more fully realized through fully relational database designs, where files can be maintained in various environments (such as those specifically associated with Atlas GIS® and those in Access®) and directly linked to provide seamless implementation of queries and table (report) construction.

In the Bowman County area, the North Dakota project involved approximately 700 surface and subsurface geological observations related to coal bed stratigraphy (Figure 1). The digitized records in Atlas GIS® were shared through a dBase® (by Borland International, Inc.) file format with attributes maintained in Access®. Previously, the

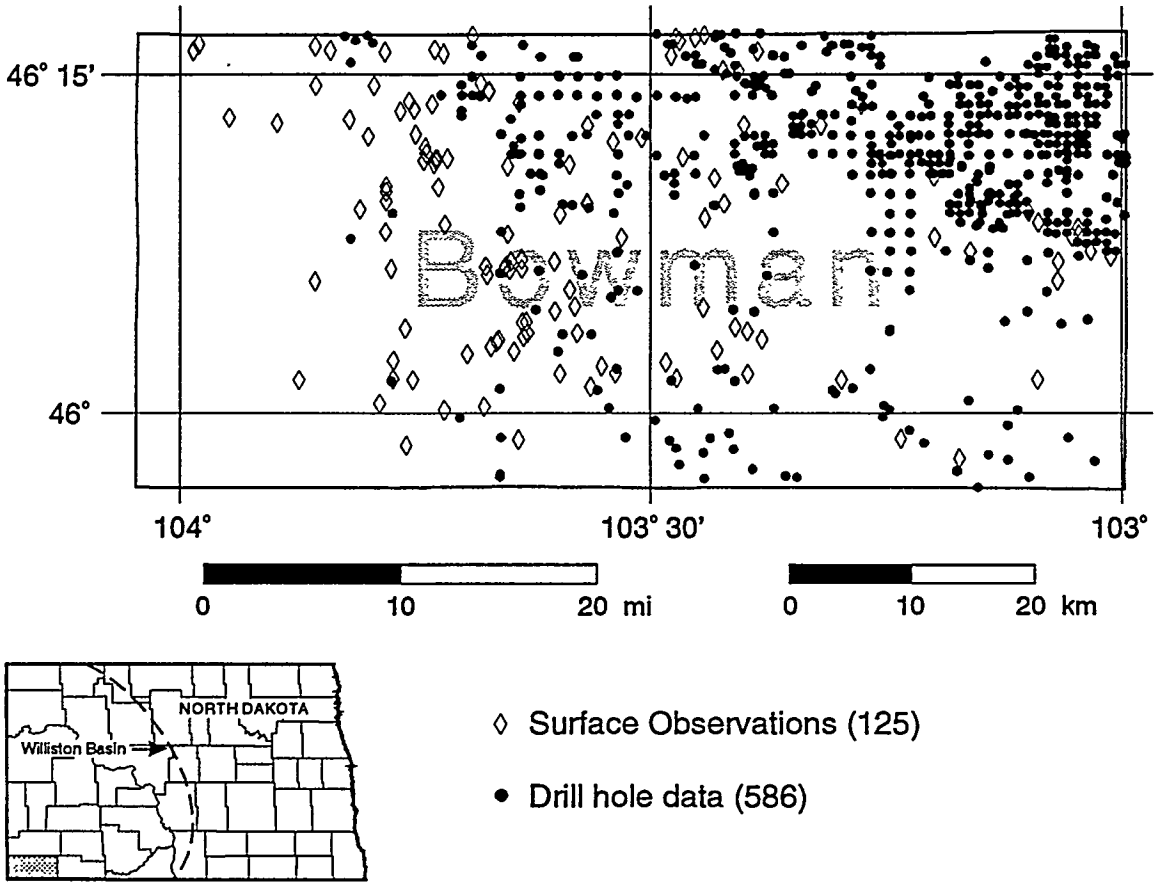

Figure 1. Distribution of geological observations (M-numbers) in Bowman County, North Dakota. Numerous subsurface and surface coal-related observations have been made in Bowman County. The density of data increases from west to east, away from the drainage of the Little Missouri River, where predominantly nonbearing strata of uppermost Cretaceous and lowermost Paleocene age are exposed. The surface mines near Gascoyne are the largest coal-producing operations in southwestern North Dakota.

graphical depiction of coal-bearing stratigraphic geologic sections was accomplished via a multistep procedure involving Q&A®, a DOS editor, such as Norton Commander® by Symantec Corporation, and a modified public domain program known as STRATCOL/STRATA. With the use of a relational data manager, such as Access®, the procedure to produce a graphic representation of a geologic column can be greatly simplied for the general user. The revised procedure, however, does require a number of programming steps to facilitate this approach. The following discussion illustrates the type of database management and programming considerations followed to simplify the production of a selected type of graphical image.

Previous discussions on the management of coal-related geologic observations (Hartman, 1992) have reviewed Q&A® database file structure. Two databases were maintained for geologic observations, MNOS and UNIT files. In Access®, the functioning of these two files can be combined into one database. More importantly, the implementation of the UNIT file can be altered significantly by relating specific UNIT fields in a one-to-many relationship. This relationship is well documented in Figure 2 (Summary Subform), where a summary of the units in a particular measured section

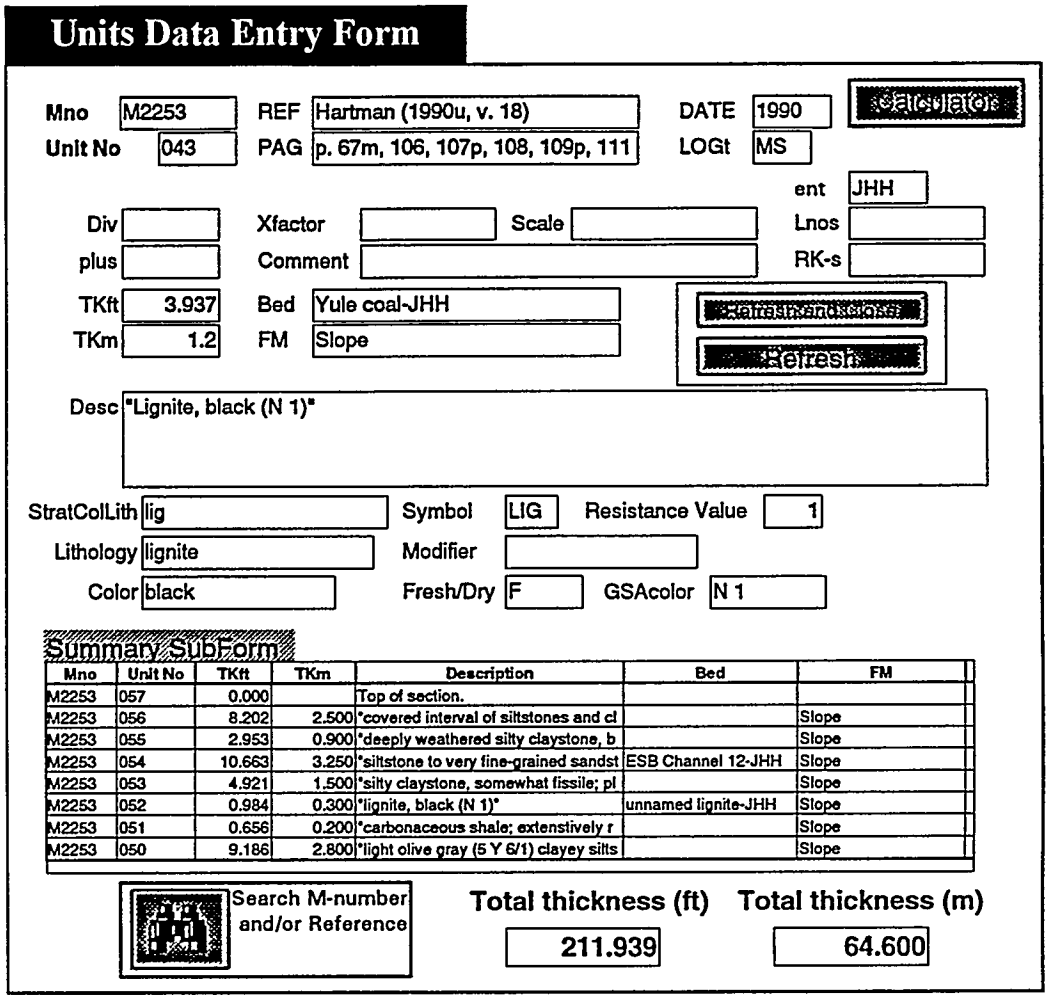

Mno	Unit No	TKft	TKm	Description	Bed	FM
M2253	057	0.000		Top of section.		
M2253	056	8.202	2.500	"covered interval of siltstones and cl		Slope
M2253	055	2.953	0.900	"deeply weathered silty claystone, b		Slope
M2253	054	10.663	3.250	"siltstone to very fine-grained sandst	ESB Channel 12-JHH	Slope
M2253	053	4.921	1.500	"silty claystone, somewhat fissile; pl		Slope
M2253	052	0.984	0.300	"lignite, black (N 1)"	unnamed lignite-JHH	Slope
M2253	051	0.656	0.200	"carbonaceous shale; extenstively r		Slope
M2253	050	9.186	2.800	"light olive gray (5 Y 6/1) clayey silts		Slope

Figure 2. Units Data Entry Form. The UNIT table, containing the field entries describing the observations for a particular geologic unit, are entered in this form design. The summary subform displays a selected number of unit descriptions and related information. Important abbreviations include TKft (thickness feet) and TKm (thickness meters) (see text for additional discussion).

TABLE 1

Geologic Section M2253

```
M2253
  056     2.500     8.202   COV    3
  055     0.900     2.953   BEN    2
  054     3.250    10.663   ETA    3                ESB Channel 12-JHH
  053     1.500     4.921   SH2    3
  052     0.300     0.984   LIG    1                unnamed lignite-JHH
  051     0.200     0.656   CM4    1 plants
  050     2.800     9.186   SH2    3
```

(M2253) can be depicted simultaneously. Previously, in Q&A®, a separate report would have to have been written to tabulate this subform information. The entry of information to produce a graphic file is as before. A primary lithology is entered into the field "StratColLith," and fields "Symbol" and "Resistance Value" are automatically filled by reference to a lookup table. To produce a data file in Q&A® for graphic image construction, a report (from the Report Module) would have been written that would contain the appropriate columnar data to load into STRATCOL/STRATA. Table 1 represents a portion of a UNIT file (Units 50 to 56) for measured Section M2253 (see also Figure 4). The second column (e.g., 2.500) represents the metric thickness of the unit, while the third column gives the thickness in feet. The fourth column is the graphic symbol name (e.g., COV = covered interval), while the fifth column is the resistance value for the weathering profile. Two descriptive fields are available to add comment to the unit. In the example in Table 1, fossil information is included in Column 6, while names of key beds are reported in Column 7. A precise spacing between columns (fixed format) is required for use by STRATCOL/STRATA. The same file must be generated by Access®, but can be accomplished directly and more simply for the uninitiated user through the use of an Access® custom toolbar and associated programming.

In Access®, the buttons on the custom toolbar (as shown in Figure 3) activate associated macros, which in turn, run the proper modules. The toolbar can be set to be present on the screen at all times in UNIT applications. By clicking on the "Run StratOut(DH) Macro" button, the following module is run:

```
Function StratOut_DH ()

On Error GoTo ExitThisFunction DoCmd OutputTo A_Report, "StratCol Report
(DH)", A_Formattxt

Exit Function

ExitThisFunction:
   Exit Function

End Function
```

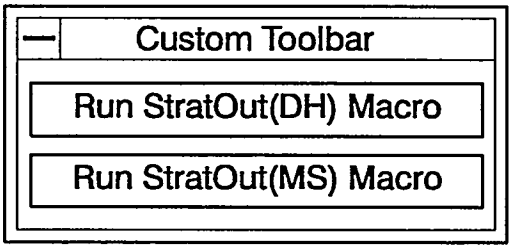

Figure 3. Access® custom toolbar for the construction of geologic columns.

If no error is detected, such as not finding the M-number requested (see below) or the process is canceled, a report (A_Report) is written in a form (StratCol Report), which is exported in a text format (A_Formattxt). Depending on the type of geologic column to be printed in STRATCOL/STRATA, either drill hole (DH, representing measurements from the top down) or measure section (MS, representing measurements from the bottom up), the user clicks the appropriate toolbar button. The following code was written as the control source for an "unbound text box" in the "StratCol Report (DH)" report for fixing the format in the data file for use in STRATCOL/STRATA.

```
=Format([Unit_no],"@@@@@") & "  " & Format([TKm],"0000.000")
& "  " & Format([TKft],"0000.000") & "  " & [Symbol] & Space(4) &
[Resistance Value] & Space(16) & [Bed]
```

After the button is clicked, the programming is activated and the user is prompted for the name (and path, if necessary) of the data file to be created. Next, the user is prompted to fill in a value for the parameter requested by the underlying query. In this case, the parameter value is the M-number (Figure 2), and the data file is then automatically created. The extra steps formerly required in Q&A® to produce a specific report and eliminate unwanted leading headers and trailing blank lines at the end of the data file are unnecessary. This method for creating STRATCOL/STRATA data files also has the advantage of being available to create a data file for any M-number at anytime while in the UNIT database. The resulting output from STRATCOL/STRATA is shown in Figure 4.

The Alaskan project incorporated data into Access® from a number of sources, as well as digitizing a number of natural resource features (e.g., coal and gas basins) and political boundaries (Figure 5). Location data were derived in part from U.S. Geological Survey Geographic Names Information System (GNIS) USGeoData. Using magnetic tape media, 25,000 Alaskan place names, locations, and map and civil divisions were downloaded into a Q&A® database and decoded for general use. Relevant project place names and their position, fixed by latitude and longitude, were transferred to Atlas GIS® for graphical output. Attribute files maintained in Access® included given information on site power generation (e.g., electrical, diesel) and relative costs. Cultural–census information was derived from TIGER files from the U.S. Census. GIS file manipulation resulted in graphical output of site locations (with energy consumption), major coal basins and fields, and indigenous ethnic and general population structure on a digitized map of Alaska. Figure 4 represents a map of potential gas fields in Alaska, along with proposed natural gas pipelines. All of these activities and products were implemented to support the decision-making process in considering additional, more site-specific studies and to draw general and detailed conclusions on coal availability.

STRAT3 OUTPUT: SECTION M2253

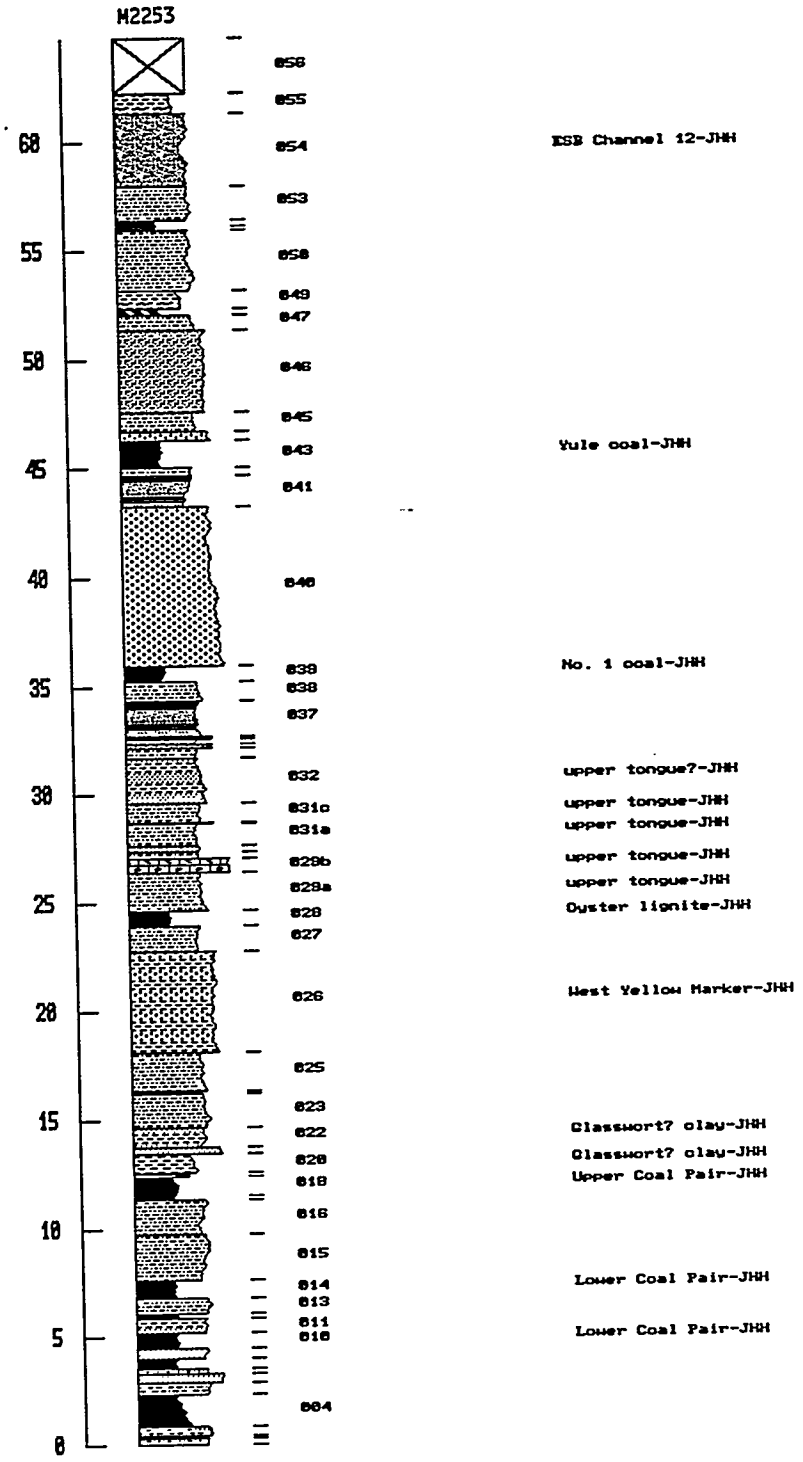

Figure 4. Geologic Section M2253. This geologic column is produced from the program STRATCOL/STRATA and is a measured section of 64.6 m in length. The symbols making up the units of the column describe the lithology of the rock; a black fill represents a lignite, dot patterns represent sandstone or sandy textures, and dashes and lines represent claystones, shales, or clayey textures. Named or significant beds are labeled to the right.

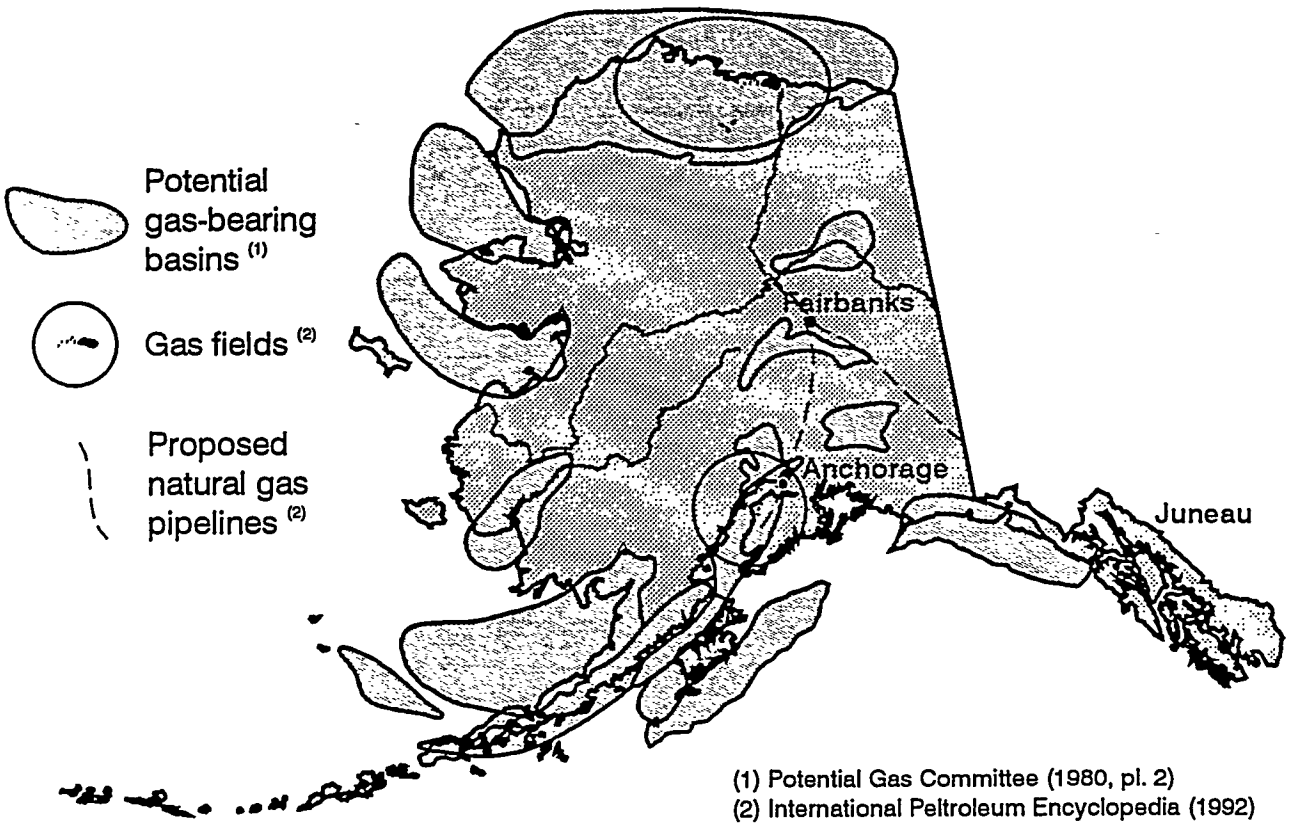

Figure 5. Natural gas resources of Alaska. A number of large potential gas-bearing basins are present in Alaska. Producing gas fields are shown as small dots bounded by an ellipse in the area of the North Slope and southwest of Anchorage.

3.0 REFERENCES

Data User Services Division, 1991, Alaska TIGER/Line Census Files, 1990: Washington, D.C., U.S. Department of Commerce, Bureau of the Census, Compact Disc.

International Petroleum Encyclopedia, 1992, International Petroleum Encyclopedia: Tulsa, PennWell Publishing Co., 358 p.

Potential Gas Committee, 1980, Natural Gas Map of Alaska: Golden, Potential Gas Agency, Colorado School of Mines, plate 2.

GEONAMES for Alaska, 1990, U.S. Geological Survey, National Mapping Division, Geographic Names Information Service, USGeoData (magnetic media).

Hartman, J.H., 1992, Coal science: Earth resource evaluation and management: Semiannual technical report for the period July through December 1991, DE-FC21-86MC10637: EERC publication.

Hartman, J.H., 1994, Resource Data Evaluation, *in* Resource Characterization and Residuals Remediation: Topical Report Task 1.0, for the period January through December 1993, DE-FC21-93MC30097: EERC publication, p. 12–34.

TASK 8.3

USTI NAD LABEM COAL-UPGRADING PROGRAM

Prepared by:

Brian C. Young

August 1994

TASK 8.3 USTI NAD LABEM COAL-UPGRADING PROGRAM

1.0 INTRODUCTION/OBJECTIVES

The major political changes occurring in Eastern Europe and the Czech Republic in particular since 1989 have engendered a dramatic reappraisal of the use of energy and its impact on the environment. The Czech Republic is highly dependent on coal, although a significant portion of the country's energy needs are derived from nuclear power. It has over 5000 million tons of recoverable coal reserves, consisting mainly of lignite and subbituminous coal (3500 Mt) and hard or bituminous coal (1870 Mt) (1). A substantial amount of the coal is low grade, having not only a high ash but also a high sulfur content. For the Most and Sokolov regions, the respective ash content ranges are 26 to 44 wt% and 24 to 32 wt%, and the respective sulfur content ranges are 0.5 to 3.0 wt% and 0.7 to 6.0 wt%.

Although the current production of lignite and subbituminous coal is estimated at over 100 million tons per year and bituminous coal at about 20 million tons per year, production has been declining (1). However, a strong economic incentive exists to use indigenous fuels. Upgrading or beneficiating the coal is a potential option for improving the efficiency of coal use as well as its environmental acceptability.

Usti nad Labem is one of the cities in the Northern Bohemia region of the Czech Republic that is very dependent on the use of coal. An industrial city, it contributes significantly to the high pollution levels of the "Black Triangle" region, which includes other cities of the Czech Republic, Poland, and the former East Germany. A critical concern for Usti nad Labem is substantial pollution resulting from to emissions of sulfur dioxide, nitrogen oxides, and particulate. These emissions come from three large district heating systems that supply 80% of the city's heating energy demand, as well as from small residential coal-fired stoves. The city has eight heating plants (total output of 910 MW), about 100 local block boilers (125 MW total), and approximately 7400 small domestic boilers and stoves. Domestic heating uses some 7.4 million tons of raw lignite and 600,000 tons of lignite briquettes, as well as 640,000 tons of bituminous coal in a year. Combined, the power plants and large heating plants use 36 million tons per year of pulverized lignite, whereas the local boilers use 1.1 million tons per year (2).

The upgrading of low-grade coals may involve one or more techniques for the removal or reduction of minerals, moisture, or combustion pollution precursors (e.g. sulfur). These techniques may include washing, oil agglomeration, ion exchange, hot-water drying, thermal treatment for moisture reduction, and briquetting. Depending on the type and grade of coal, coal-cleaning costs, including the cost of the disposal of wastes, can be high. However, there are several advantages of beneficiation, namely, improved consistency of feedstock quality, enhanced heating value of the fuel, reduced inorganic content (minerals, atomically dispersed cations) resulting in less wear, corrosion, and deposition as well as lower emissions and reduced transport, handling, and storage costs for a specific power plant output (3).

The Usti nad Labem coal-upgrading program is divided into two activity areas:

- A review of cost-effective upgrading technologies to reduce emissions of sulfur dioxide, nitrogen oxides, and particulate associated mainly with the combustion of low-rank coals (lignite and subbituminous). This activity is being undertaken by the EERC with significant assistance from the North Bohemia Economic Association (NBEA, Mr. Z. Krivsky, Executive Director). The EERC will also interact with Gilbert/Commonwealth. Inc.

- A limited technical investigation by EERC, which will involve physical cleaning and tableting of selected Czech coals.

The specific objectives of the program are as follows:

- To review cost-effective upgrading technologies for low-rank coals as a means to reduce the gaseous and particulate pollutants in the Czech Republic

- To undertake a brief experimental study on up to six Czech coals to examine the potential for their upgrading by physical cleaning and tableting

2.0 ACCOMPLISHMENTS

The scope of work has been determined by the EERC, and the role of NBEA has been accepted by Mr. Z. Krivsky. A contract between the EERC and NBEA has been finalized. Correspondence has been initiated regarding coal samples, coal usage in various systems, coal characteristics, and project status with NBEA and Gilbert/ Commonwealth. Mr. Krivsky has visited selected coal mines and has sent samples of two coals, a North Bohemia lignite and a bituminous coal from Ostrava used for smokeless fuel. Requests for the four additional coals along with background information have been made.

2.1 Scope of Work

2.1.1 Review of Upgrading Technologies

Information to be procured from the Czech Republic as well as the United States for low-rank coal technologies will cover at least the following:

- Coal upgrading

- Evaporative and nonevaporative thermal drying

- Pyrolysis/mild gasification

- Lump fuel combustion emissions control for residential and district heating systems

- Coal aggregation

2.1.2 Technical Investigation

Bench-scale evaluations are to include the following steps:

- Coal sizing for six coals
- Washability (float–sink) testing
- Dry coal cleaning on at least two coals
- Pyrolysis of two bench-scaled cleaned coals
- Tableting of two pyrolyzed and two cleaned coals
- Bench-scale combustion testing on four tablet types

3.0 FUTURE WORK

Future work is planned as follows:

- Assess information on upgrading technologies for low-rank coals

- Analyze and physically clean Czech coal samples using the bench-scale methods of dense-media (washability) and dry magnetic separation

4.0 REFERENCES

1. Couch, G.R. "Coal Prospects in Eastern Europe," *In* Proceedings of the Energy and Environment: Transitions in Eastern Europe Conference; Prague, 1992, Vol. 1, p 22–31.

2. Krivsky, Z. Private communication, June 1994.

3. Couch, G.R. *Lignite Upgrading*, IEA Coal Research: London, 1990; IEACR/23.